

UC Santa Cruz

UC Santa Cruz Electronic Theses and Dissertations

Title

Probing Dark Matter and New Physics With MeV Gamma-Ray Telescopes

Permalink

<https://escholarship.org/uc/item/17n7857p>

Author

Morrison, Logan Andrew

Publication Date

2021

Copyright Information

This work is made available under the terms of a Creative Commons Attribution License, available at <https://creativecommons.org/licenses/by/4.0/>

Peer reviewed|Thesis/dissertation

UNIVERSITY OF CALIFORNIA
SANTA CRUZ

**PROBING DARK MATTER AND NEW PHYSICS WITH MEV
GAMMA-RAY TELESCOPES**

A dissertation submitted in partial satisfaction of the
requirements for the degree of

DOCTOR OF PHILOSOPHY

in

PHYSICS

by

Logan Morrison

December 2021

The Dissertation of Logan Morrison
is approved:

Professor Stefano Profumo, Chair

Professor Michael Dine

Professor Howard Haber

Peter F. Biehl
Vice Provost and Dean of Graduate Studies

Copyright © by

Logan Morrison

2021

Table of Contents

List of Figures	vi
List of Tables	xi
Abstract	xiii
Dedication	xiv
Acknowledgments	xv
1 Introduction	1
2 Precision Gamma-Ray Constraints for Sub-GeV Dark Matter Models	4
2.1 Introduction	4
2.2 Theoretical Framework and its Validity	10
2.2.1 Low-energy QCD degrees of freedom	11
2.2.2 ChPT Applicability	13
2.2.3 Microscopic Models	16
2.2.4 Matching	18
2.3 Searching for MeV Dark Matter with Future Gamma Ray Telescopes . .	21
2.3.1 Gamma-ray constraints	22
2.3.2 Cosmic Microwave Background Constraints	25
2.3.3 Higgs portal model constraints	28
2.3.4 Dark photon model constraints	31
2.3.5 Results	32
2.4 Conclusions	34
3 Hunting for Dark Matter and New Physics with (a) GECCO	37
3.1 Introduction	37
3.2 The Galactic Explorer with a Coded Aperture Mask Compton Telescope	39
3.2.1 Instrument concept	40
3.2.2 Operating principles and performance	42

3.2.3	Instrument Sensitivity	43
3.3	Searches for Annihilating and Decaying Sub-GeV Dark Matter	50
3.3.1	Indirect Detection Constraints and Projections	50
3.3.2	Model-independent projections	55
3.3.3	Model Example: Higgs Portal	61
3.3.4	Model Example: Dark Photon	66
3.3.5	Model Example: Right-Handed Neutrino	69
3.4	Searches for Light Primordial Black Hole Evaporation	74
3.5	Exploring the Origin of the 511 keV Line	77
3.6	Discussion and Conclusions	82
4	Direct Detection of Hawking Radiation from Asteroid-Mass Primordial Black Holes	88
4.1	Introduction	88
4.2	MeV gamma-ray telescopes.	92
4.3	Photons from evaporating PBHs.	95
4.4	Results and discussion	102
4.5	Summary & conclusions.	103
5	Hazma: A Python Toolkit for Studying Indirect Detection of Sub-GeV Dark Matter	105
5.1	Introduction	105
5.2	Structure of <code>hazma</code>	110
5.3	Particle physics framework	114
5.3.1	Scalar Mediator	117
5.3.2	Vector Mediator	121
5.3.3	Computing Particle physics quantities	124
5.4	Building Blocks of MeV Gamma-Ray Spectra	129
5.4.1	Monochromatic Gamma Rays	130
5.4.2	Final State Radiation	131
5.4.3	Radiative Decay Spectra	134
5.4.4	Continuum Gamma-Ray Spectra in <code>hazma</code>	141
5.5	Gamma Ray Spectra from DM annihilation	144
5.6	Electron and Positron Spectra from DM annihilation	151
5.7	Gamma Ray Limits	156
5.8	Cosmic Microwave Background limits	162
5.9	Conclusion	166
A	Installation	168
B	Basic Usage	170
B.0.1	Using the Built-In Models	170
B.0.2	Subclassing the Built-In Models	177


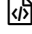
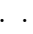

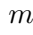
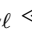
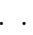

C	Advanced Usage	182
C.0.1	Adding New Gamma-Ray Experiments	182
C.0.2	User-Defined Models	185
D	Multi-particle phase space integration: rambo	195
E	Gamma-ray Spectra from many final state particles: gamma_ray	201
	Bibliography	207


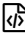














List of Figures

2.1	The effective area as a function of energy for past, existing, and planned telescopes under consideration in our study. The effective area of MAST is not shown since it is significantly larger than for other telescopes ($6.5 \times 10^4 \text{ cm}^2$ to $1.2 \times 10^5 \text{ cm}^2$ for $E_\gamma = 10 \text{ MeV}$ to 1000 MeV).	8
2.2	Illustration of DM masses m_{DM} and mediator masses m_M for which the leading-order chiral perturbation theory calculations in this paper can be considered reliable.	15
2.3	Prospects for future gamma-ray telescopes, and phenomenological constraints, for the Higgs portal case; the left panels assume a mediator mass half the mass of the DM, while the right panels assume a mediator mass equal to 1.5 times the DM mass. The lower panels show the future telescope prospects normalized to GECCO's (a smaller value on the y axis corresponds to a <i>tighter</i> constraining capability). In computing the CMB constraint we conservatively assume a kinetic decoupling temperature of $10^{-6} m_\chi$	30
2.4	Vector mediator constraints, for a mediator mass $m_V = 3m_\chi$. The right panel shows the ratio of the projected constraints from a given future telescope relative to those for GECCO (shown with a brown line in the left panel).	31
3.1	GECCO design concept: a) with mask in stowed position and notional spacecraft bus; b) with mask in deployed position; c) cutaway. [183] . . .	40
3.2	Backgrounds in the Compton-Mask combined analysis. The signal event is shown in blue, while the background event is shown in dark red. Dashed lines show the photons' incident direction, while the dotted lines show the reconstructed direction of Compton-scattered photons. The rings illustrate the solid angle of background acceptance. The red arc shows the intersection of the reconstructed event circle with the Mask position for signal events. [183]	47
3.3	A (preliminary) comparison of instrumental sensitivities with GECCO's projected sensitivity, as calculated via Eq. (3.1), see the text for details.	49

3.4	Projected constraints on annihilation into different final states (solid lines). To account for the unknown systematics of GECCO, the surrounding bands show how the projections would change if the background photon counts were a factor of 25 higher than the fiducial value. The shaded regions show constraints from existing gamma ray data. The dashed black line shows the CMB constraint assuming the DM annihilation are p -wave and have a kinetic decoupling temperature of $10^{-6} m_\chi$; higher kinetic decoupling temperatures would give weaker constraints. The dot-dashed line gives the CMB constraint for s -wave DM annihilations.	58
3.5	Constraints on the DM particle's lifetime for decays into different final states (solid lines). To account for the unknown systematics of GECCO, the surrounding bands show how the projections would change if the background photon counts were a factor of 25 higher than the fiducial value. The CMB constraint on decays into e^+e^- is taken from Ref. [220]. While constraints for the $\mu^+\mu^-$ final state are not provided, we estimate they lie around $10^{24} - 10^{25}$ s since the subsequent muon decays produces electrons with energy $\sim 1/3m_\chi$. The constraint for decays into $\gamma\gamma$ lies below the axis range.	59
3.6	Constraints on the thermally-averaged DM self-annihilation cross section in the Milky Way for the Higgs portal model (solid lines). To account for the unknown systematics of GECCO, the surrounding bands show how the projections would change if the background photon counts were a factor of 25 higher than the fiducial value. The case where the indirect detection signal comes from annihilations into mediators (SM particles) is shown on the left (right). The thin red dotted lines are contours of constant coupling strength. The orange region in the right panel is a conservative exclusion region from experiments besides gamma-ray telescopes. The CMB constraint was computed assuming a kinetic decoupling temperature of $10^{-6} m_\chi$; taking this to be higher would weaken the constraint.	67
3.7	Projected constraints on the dark matter annihilation cross section for the dark photon model from GECCO (solid lines). To account for the unknown systematics of GECCO, the surrounding bands show how the projections would change if the background photon counts were a factor of 25 higher than the fiducial value. As before, the bands correspond to increasing or decreasing the background model by a factor of 25. The light blue shaded region shows the combined constraints from COMPTEL, EGRET, FERMI and INTEGRAL. The orange region shows the region excluded by BaBar and LSND. We show the contour yielding the correct dark matter relic density with the dotted black line.	84

3.8	Projected constraints on the RH-neutrino lifetime (solid lines). To account for the unknown systematics of GECCO, the surrounding bands show how the projections would change if the background photon counts were a factor of 25 higher than the fiducial value. The area shaded in light blue is excluded by current observations, as in the previous plots. We also show, with dot-dashed contours, the mixing angle corresponding to parameter space shown in the figure.	85
3.9	GECCO's 5σ discovery reach for detecting Hawking radiation from evaporating primordial black hole dark matter (solid lines). To account for the unknown systematics of GECCO, the surrounding bands show how the projections would change if the background photon counts were a factor of 25 higher than the fiducial value. The blue region shows existing constraints, the strongest of which comes from COMPTEL data [83]. We assume a monochromatic mass function.	86
3.10	Left: the GECCO sensitivity to 511 keV individual point source on the plane defined by the number of sources contributing to the signal at the Galactic Center (assumed to all contribute the same 511 keV luminosity), versus the distance of the closest such source; we also indicate with vertical dashed lines the distance to the closest MSP, Wolf-Rayet star, and LMXB, and with horizontal dark green bands the estimates for the total number of MSP and Wolf-Rayet stars potentially contributing to the signal. Right: predictions for the 511 keV flux from a variety of nearby astrophysical objects, based on a signal scaling proportional to mass over distance squared. The horizontal dashed and solid lines correspond to GECCO's point source sensitivity best-case and conservative case. . . .	87
4.1	The effective area, as a function of energy, of existing and proposed MeV gamma-ray telescopes. Thin lines mark existing telescopes and thick lines mark proposed ones. The effective area of MAST (not shown) ranges from $\sim 7 \times 10^4 - 10^5 \text{ cm}^2$ over $E_\gamma = 10 \text{ MeV} - 60 \text{ GeV}$. 92	
4.2	Photon emission from light black hole evaporation. We consider Hawking temperatures of 20, 3, 0.3 and 0.06 MeV (from top left to bottom right), corresponding to masses $M = 5.3 \times 10^{14}, 3.5 \times 10^{15}, 3.5 \times 10^{16}, 1.8 \times 10^{17}$ grams. The thick blue lines show the spectra computed in this work; the dashed red curves correspond to the primary (thin lines) and secondary-plus-primary (thick lines) output from BlackHawk. We also show contributions from π^0 decay (magenta dotted lines) and from final state radiation off of electrons and muons (dot dashed yellow and magenta lines) and charged pions (dotted green lines). The upper-left panel shows the results from MacGibbon and Weber [171] as a dashed black line. In the two lower panel we also show what results from adopting the geometric optics approximation for the grey-body factors. . . .	94

4.3	New bounds on the PBH abundance based on COMPTEL observations of the Milky Way. Assuming the PBHs follow an Einasto rather than NFW distribution gives a slightly stronger bound. Existing bounds collected in Ref. [130] from INTEGRAL observations of galactic diffuse emission [162], CMB [197, 75], EDGES 21 cm [73], Voyager 1 [49], the 511 keV gamma-ray line [95, 160], the extragalactic gamma-ray background [64] and dwarf galaxy heating [151] are also shown.	98
4.4	Discovery reach for PBHs with future MeV gamma ray telescopes. In the top row, the PBH density is assumed to track an Einasto density profile (left) and an NFW profile (right) fit to the Milky Way's DM distribution. In the lower panels we consider the Draco dwarf spheroidal and M31 as targets. For all targets we assume a 5° circle around the central region.	99
5.1	Overview of the hazma workflow, showing different starting points for analyzing sub-GeV dark matter models and possible outputs. The light green boxes show different types of models the user can analyze. After a model has been instantiated (purple box), various functions can be called to compute the outputs in the dark green boxes.	110
5.2	Structure of hazma. At the core of hazma are modules for computing gamma-ray and positron spectra: <code>decay</code> , <code>positron_spectra</code> and <code>gamma_ray</code> hazma comes with predefined models located in the <code>scalar_mediator</code> and <code>vector_mediator</code> modules.	112
5.3	Annihilation branching fractions for the scalar mediator model. The coupling $g_{S\chi\chi}$ between the DM and mediator is set to one. The rows correspond to the Higgs portal and heavy quark UV completions and the columns are for a light (left) and heavy (right) mediator.  	125
5.4	Annihilation branching fractions for the vector mediator model. The coupling $g_{S\chi\chi}$ between the DM and mediator is set to one. The rows correspond to a kinetically mixed mediator and a mediator with couplings only to quarks, and the columns are for a light (left) and heavy (right) mediator.  	126
5.5	Final state radiation spectrum for dark matter annihilating into $\mu^+\mu^-$. The curves correspond to the scalar (blue curve) and vector (orange curve) models, with the indicated center of mass energies. The Altarelli-Parisi spectrum from Eqn. (??) is also shown (dashed black curve), illustrating the limiting behavior of the spectra as $m_\ell \ll Q$.  	134
5.6	Final state radiation spectrum for dark matter annihilating into $\pi^+\pi^-$. The blue curve corresponds to the scalar-mediator model and the orange to the vector-mediator case. The dashed black curve shows the Altarelli-Parisi spectrum. The panels are labeled with the annihilation's center of mass energy.  	135

5.7	Contributions to the charged pion radiative decay spectrum in the pion's rest frame. The decay $\pi^+ \rightarrow \mu^+ \nu_\mu$ followed by radiative muon decay is plotted in orange. The other curves show the spectra for $\pi^+ \rightarrow \ell^+ \nu_\ell$, where the photon is produced via initial/final state radiation from the lepton or emission from virtual hadronic states. The total spectrum completely overlaps with the orange curve.  	141
5.8	Spectra from DM annihilation into Standard Model particles for scalar-mediator models. The two-mediator final state is kinematically forbidden. The black curve is the total spectrum as seen by an instrument with 5% energy resolution. The labeled colored curves are the spectra for individual final states, and the vertical dashed line marks the photons' energies in the $\gamma\gamma$ final state. The rows correspond to Higgs portal and heavy quark coupling patterns. The DM mass is fixed to the indicated value in each column.  	145
5.9	Spectra from DM annihilation into mediators for scalar-mediator models. Curves are only shown when $E_{\text{CM}} \geq 2m_S$, and are labeled with the corresponding mediator mass. The spectra have not been convolved with an energy resolution function since the SS final state does not produce gamma-ray lines.  	146
5.10	Spectra from DM annihilation into Standard Model particles for vector-mediator models. The two-mediator final state is taken to be kinematically forbidden. The black curve is the total spectrum as seen by an instrument with 5% energy resolution. The rows correspond to the case where the mediator kinetically mixes with the photon and where it couples only to quarks. The vertical dashed line indicates the energy of the photon in the $\pi^0\gamma$ final state.  	147
5.11	Spectra from DM annihilation into mediators for vector-mediator models. The labels and colors indicate the value of m_V for each curve.  	148
5.12	Positron spectra for DM annihilating into Standard Model final states. Results for the scalar model with Higgs portal couplings are shown in the top row and for the vector model with a kinetically-mixed mediator in the bottom. The grey vertical dashed line indicates the location of the monochromatic $\bar{\chi}\chi \rightarrow e^+e^-$ final state. The total spectrum (black curve) is convolved with a 5% energy resolution function.   .	153
5.13	Positron spectra for DM annihilating into two mediators.   .	154
5.14	Efficiency of energy injection into the CMB by dark matter annihilation. The top panels are for the vector model with kinetic mixing and two possible values for mediator couplings to quarks only. The bottom row shows f_{eff}^X for the scalar mediator with Higgs portal and heavy quark-type couplings. The DM-mediator coupling is fixed to one in all panels. Note that the curves for different mediator masses have some overlap.  	164

List of Tables

2.1	Target regions and \bar{J} factors for different detectors' measurements of the diffuse gamma-ray flux, as well as the target used to project the discovery reach of planned telescopes. All \bar{J} factors were computed assuming the same Einasto profile (see text for details). See Ref. [145] for COMPTEL, Ref. [224] for EGRET and Ref. [7] for Fermi-LAT.	26
3.1	\bar{J} and \bar{D} factors for various circular targets, in units of $\text{MeV}^2 \text{cm}^{-5} \text{sr}^{-1}$ and $\text{MeV cm}^{-2} \text{sr}^{-1}$ respectively. The dark matter profile parameters are taken from the Ref. [92] (GC, NFW), Ref. [92] (GC, Einasto), Ref. [99] (Draco, NFW), and Ref. [126] (M31, NFW). For the Milky Way, we use the values from Table III of Ref. [92]. The Einasto profile parameters are adjusted within their 1σ uncertainty bands to maximize the \bar{J} and \bar{D} factors. For all other targets we use the parameters' central values. The distance from Earth to the Galactic Center is set to 8.12 kpc [4, 92]. For reference, the angular extents of the $1'$ and 5° regions are $2.658 \times 10^{-7} \text{sr}$ and $2.39 \times 10^{-2} \text{sr}$ respectively.	56
3.2	\bar{J} and \bar{D} factors for observing regions in the Milky Way used by past experiments, in units of $\text{MeV}^2 \text{cm}^{-5} \text{sr}^{-1}$ and $\text{MeV cm}^{-2} \text{sr}^{-1}$ respectively. The regions are specified in Galactic coordinates. We again use the NFW profile parameters from Table III of ref. [92].	57
3.3	Predicted brightness of a 511 keV signal assuming a scaling proportional to mass over distance squared for a variety of astrophysical targets (see main text for references to the quoted masses, distances, and fluxes).	82

4.1	\bar{J}_D factors for various circular targets and the COMPTEL observing region from Ref. [145]. The DM profile parameters are taken from the indicated references. For the Milky Way targets, we use the values from Table III of Ref. [92]. The Einasto profile parameters are adjusted within their 1σ uncertainty bands to maximize \bar{J}_D . For all other targets we use the parameters' central values. The distance from Earth to the Galactic Center is set to 8.12 kpc [4, 92]. For reference, the angular extent of a 5° region is 2.39×10^{-2} sr.	96
5.1	Figures of merit for the detectors used in <code>hazma</code>. Note that the effective area is only used in <code>hazma</code> for projecting limits for e-ASTROGAM.	158
5.2	Target regions and data references (first column) for detectors included in <code>hazma</code>. The J -factors for COMPTEL, EGRET and Fermi-LAT are taken from [109] and the value for e-ASTROGAM is from ref. [71]. All assume an NFW profile for the galactic DM distribution [71].	159

Abstract

Probing Dark Matter and New Physics With MeV Gamma-Ray Telescopes

by

Logan Morrison

The indirect detection of dark matter particles with mass below the GeV scale has recently received significant attention. Future space-borne gamma-ray telescopes, including All-Sky-ASTROGAM, AMEGO, and GECCO, will probe the MeV gamma-ray sky with unprecedented precision, offering an exciting test of particle dark matter in the MeV-GeV mass range. While it is typically assumed that dark matter annihilates into only one Standard Model final state, this is not the case for realistic dark matter models. In this work we analyze existing indirect detection constraints and the discovery reach of future detectors for the well-motivated Higgs and vector-portal models, a right-handed neutrino model and astroid-size primordial black holes. We showcase a new code, `hazma`, developed specifically for computing constraints for each of these models. We show how to leverage chiral perturbation theory to compute the dark matter self-annihilation cross sections into final states containing mesons, the strongly-interacting Standard Model dynamical degrees of freedom below the GeV scale. We find that future telescopes could probe dark matter self-annihilation cross sections orders of magnitude smaller than those presently constrained by cosmic microwave background, gamma-ray and terrestrial observations.

To my wife Madelyn,
for putting up with me for ten years of physics.

Acknowledgments

This work was partly supported by the U.S. Department of Energy grant number de-sc001010. First, I want to thank my collaborators Adam Coogan, Alexander Moiseev and Stefano Profumo for all the hard work they put into these projects with me. I want to thank my committee, Stefano Profumo, Michael Dine and Howard Haber, for reviewing my thesis. I acknowledge with gratitude early collaboration on the projects in Chapters 2,3 and 5 with Francesco D'Eramo. Francesco D'Eramo was the first to put forward the idea of using chiral perturbation theory in the context of accurately calculating the annihilation and decay products of MeV dark matter. He was also responsible for several of the early calculations, part of the writing of the text, and for overall educating us all on numerous topics in chiral perturbation theory. I thank Michael Peskin, for useful discussions regarding IR-divergences. I thank Eulogio Oset and Jose Antonio Oller for clarifying some points about unitarized chiral perturbation theory.

Chapter 1

Introduction

One of the most pressing unsolved problems in physics is the origin of dark matter, a substance that makes up 80% of all matter and 25% [249] of the total energy in our universe. To date, we have only detected the presence of dark matter through its gravitational influence on other massive objects. In order to determine the properties of dark matter, it is crucial to develop additional means of observing dark matter.

The leading theoretical framework for describing dark matter has been the so-called Weakly-Interacting Massive Particle (WIMP) for the last few decades. The WIMP paradigm postulates that the dark matter has an Electro-weak scale mass and interacts with the Standard Model (SM) through the weak force. This framework is theoretically well-motivated as we expect new-physics (NP) near the EW scale (for example, because of the Hierarchy Problem; see [176] for a review and how supersymmetry can solve the problem while also yielding a suitable dark matter candidate.) However, many ground- and space-based experiments have already been performed to detect WIMPs,

each yielding null results. These include several direct [29, 80, 68, 19, 14, 11, 110, 112] and indirect [26, 3, 140] detection experiments. In light of the failures to detect WIMPs, attention is increasing towards alternative dark matter models.

A particular exciting alternative is sub-GeV dark matter, where the dark matter has a mass of between a few MeV and hundreds of MeV. Several new space-based telescopes are currently under development and are ideally suited to detect debris from MeV-scale dark matter decays or annihilations. These telescopes include AMEGO [179], AS-Astrogam [203], and GECCO [184], among others [138, 21, 101, 248]. However, before deploying these experiments, significant work needs to be done on the theoretical side to predict the expected signals from dark matter decays and annihilations.

In this thesis, we present several simplified models of MeV dark matter. Due to asymptotic freedom, Quantum Chromodynamic (QCD) 's coupling constant increases as the typical momentum transfer decreases. Near energy scales on the order of a GeV, the QCD coupling becomes order one, the theory becomes non-perturbative. The QCD degrees of freedom confine to baryons and meson at these energies. Thus, to describe dark matter interactions with strongly-interacting particles, the interactions must be described in terms of baryons and mesons. In the early 1980s, Leutwyler and Gasser [124, 123] developed a theoretical framework for describing interactions among mesons and baryons known as Chiral Perturbation Theory. A simple procedure has been developed to translate models describing quarks and gluon interactions to Chiral Perturbation Theory to describe the same interactions with mesons and baryons (see [206] for a recent review). We utilize Chiral Perturbation Theory and the techniques

mentioned above to derive realistic dark matter models with mesons. In addition, we use accurate decay spectra of muons, charged pions, and neutral pions to compute photon and positron emission from dark matter decays and annihilations.

This thesis is organized as follows. Chapter 2 describes our theoretical framework for describing dark matter interactions with meson and leptons and provides the estimated experimental reach for new MeV telescopes. Chapter 3 focuses on the GECCO telescopes and lays down a case for why GECCO is ideal for detecting MeV-scale dark matter. Chapter 4 expands on the motivation for MeV telescopes by showing their prospects of detecting Hawking radiation and constraining the fraction of dark matter consisting of primordial black holes. Finally, in Chapter 5, we showcase Hazma, a new python package developed explicitly for studying new physics at MeV-scale.

Chapter 2

Precision Gamma-Ray Constraints for Sub-GeV Dark Matter Models

This chapter was adapted from “Precision gamma-ray constraints for sub-GeV dark matter models”, published August 20, 2021 in the Journal of Cosmology and Astroparticle Physics, Volume 2021. This work was done in collaboration with Adam Coogan and Stefano Profumo with significant contributions from Francesco D’Eramo.

2.1 Introduction

The paradigm of Weakly-Interacting Massive Particles (WIMPs), a class of dark matter particle candidates with weak-scale mass and charged under Standard Model weak interactions, is extraordinarily compelling. WIMPs are found in myriad extensions to the Standard Model of particle physics, their relic abundance from the Early Universe is often very close to the observed abundance of dark matter in the Uni-

verse, and the fact that they share weak interactions with the Standard Model makes them in principle discoverable through a broad array of experimental techniques (for a recent review see e.g. Ref. [23]).

In the last few decades, the “natural” scales for the cross sections relevant to the detection of WIMP dark matter have been targeted by numerous experimental searches. In particular, direct dark matter detection – the search for the minuscule energy deposition that a WIMP would impart to a nucleus in a low-background detector – has ruled out large swaths of parameter space for WIMPs that interact through, for example, the exchange of Standard Model Z bosons or Higgs bosons, in a broad WIMP mass range between a few GeV and up to several TeV. WIMPs have failed to appear at colliders, where they are searched in the form of missing energy/momentum. Finally, the pair-annihilation cross section expected for a thermal relic from the early universe and weak-scale mass has been extensively searched for with gamma-ray as well as cosmic-ray space-borne experiments, generally with null results (though some controversial possible “detections” are still debated).

The WIMP paradigm for thermal production in the early universe – the notion that the particle species making up the dark matter was once in thermal equilibrium with Standard Model particles, subsequently falling out of chemical equilibrium and “freezing out” with the right relic density – is actually not unique to the weak scale and to weak interactions (see e.g. the “WIMP-less miracle” described in Ref. [115]). Assuming the existence of new force mediators, lighter particles, much below the Lee-Weinberg limit [163] (which states that particles with neutrino-like weak interactions

would be produced with an excessively large density if their mass were much lighter than a few GeV) provide perfect WIMP-like dark matter candidates from the standpoint of production, as well as for that of possible detection.

An interesting range for the mass of such light, WIMP-like dark matter candidates is the MeV scale. The direct detection of MeV dark matter is challenging, since the recoil energy is well below the threshold sensitivity of most current detectors. New ideas on how to experimentally search for MeV dark matter scattering have however been investigated [153]. This area, as well as the related question of how other cosmological and collider constraints circumscribe the target parameter space, continues to witness intense activity (see e.g. [157, 96, 153, 165]).

The indirect detection of MeV-scale WIMP-like dark matter particles – the detection of the debris of dark matter annihilation or decay – is an especially promising and timely arena. On the one hand, new telescopes will quite literally revolutionize the relevant energy range for indirect MeV dark matter detection (as well as for other searches for new physics, such as radiation from the evaporation of light primordial black holes, see e.g. [83]), as we describe below. On the other hand, from a theoretical standpoint, the lack of specific observational facilities has been responsible for somewhat of a gap in the understanding of the details of the photon spectrum to be expected from the annihilation or decay of MeV dark matter, especially compared to what is known and established for “traditional” WIMP candidates.

As with WIMPs, the annihilation of MeV-scale dark matter can produce identifiable and sometimes unmistakable features in the electromagnetic spectrum. Gamma

rays from WIMPs in the 0.5 MeV to 250 MeV mass range would lie predominantly in the range $\mathcal{O}(0.1 \text{ MeV to } 100 \text{ MeV})$, which includes the prominent neutral pion decay peak centered at $\sim 70 \text{ MeV}$. This energy window was last explored by COMPTEL [223] and EGRET [139] in the 1990s, leading to a couple order-of-magnitude gap (in terms of spectral energy density point source sensitivity) relative to the $\gtrsim 1 \text{ GeV}$ and x-ray portions of the electromagnetic spectrum (see fig. 2.1). Several experiments have been proposed to close this gap: GAMMA-400 [122, 105], Advanced Compton Telescope (ACT) [45], Advanced Energetic Pair Telescope (AdEPT) [141], PANGU [248, 247], GRAMS [21, 20], MAST [101], AMEGO [179, 62, 150]¹ and All-Sky ASTROGAM [172] (a scaled-back version of e-ASTROGAM [18]).² Another promising telescope is the Galactic Explorer with a Coded Aperture Mask Compton Telescope (GECCO), which encapsulates at once the principles of a Compton telescope and of a coded-aperture mask telescope [184]. GECCO's performance in the search for dark matter and new physics was recently explored in Ref. [82]. We show the approximate anticipated effective areas of the various telescopes under consideration here in fig. 2.1.

The calculation of indirect gamma-ray constraints on models of sub-GeV dark matter presents several important technical challenges that have not been simultaneously addressed in previous studies [129, 31, 109, 40, 158, 72]. Firstly, in realistic dark matter models the dark matter typically annihilates into more than one final state. In

¹See also <https://asd.gsfc.nasa.gov/amego/>

²We do not project discovery reach for ACT since the energy-dependent effective area is not available in the literature. We also do not consider GAMMA-400 further since its effective area is significantly lower than Fermi's, and a previous study already assessed its discovery reach for dark matter annihilating into photon pairs [105], finding it to be a factor of ~ 1.5 times more sensitive than Fermi for 2 years of observing time.

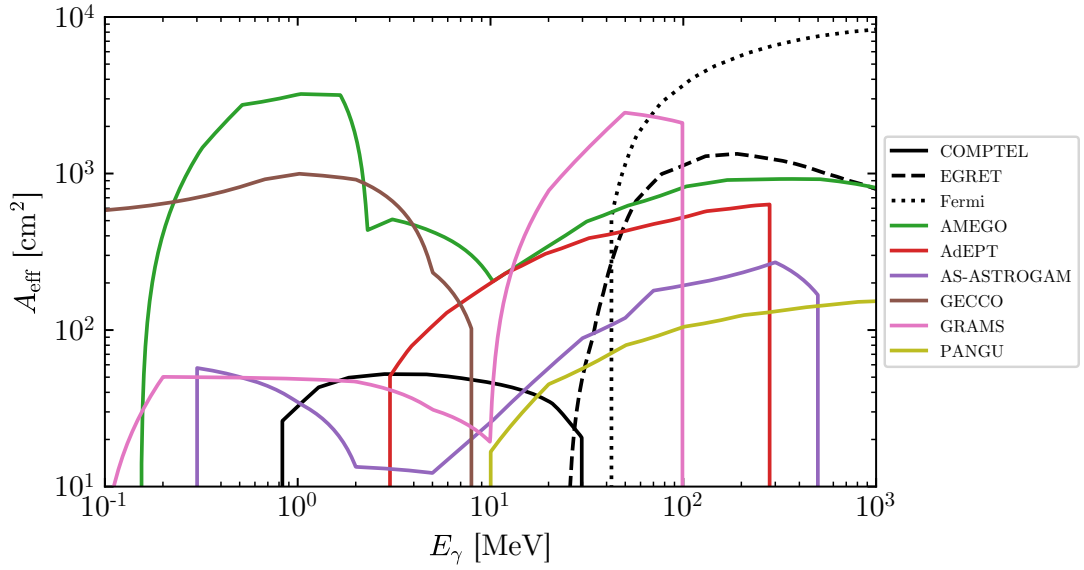


Figure 2.1: The effective area as a function of energy for past, existing, and planned telescopes under consideration in our study. The effective area of MAST is not shown since it is significantly larger than for other telescopes ($6.5 \times 10^4 \text{ cm}^2$ to $1.2 \times 10^5 \text{ cm}^2$ for $E_{\gamma} = 10 \text{ MeV}$ to 1000 MeV).

this case, unlike what holds for mass scales of ~ 10 GeV or more, where perturbative QCD is an adequate theoretical tool, since QCD confines below $\Lambda_{\text{QCD}} \sim 1$ GeV the relevant final-state degrees of freedom for MeV dark matter are light mesons. Annihilation branching fractions in such models can be computed using *chiral perturbation theory* (ChPT), the effective field theory of mesons. A second issue concerns the spectrum of final-state radiation off of charged annihilation final states (including pions, muons and electrons). This is often handled using the Altarelli-Parisi approximation [17], but in actuality depends on the spin of the mediator and radiating particles. Lastly, computing photon spectra for models that annihilate into charged pions requires assessing that particle’s complex radiative decay chain.

In this work, we derive effective Lagrangians describing the interactions of sub-GeV dark matter with light mesons. In particular, we focus on two well-motivated dark matter models (containing mediators that mix with the Higgs and photon) and explain how to match the mediator’s interactions with quarks and gluons onto interactions with mesons using ChPT. We then use these Lagrangians and the final-state radiation and radiative decay spectra computed in our previous paper [84] to find the gamma-ray constraints on these models and project which annihilation cross sections could be probed by the aforementioned planned telescopes. Additionally we explore how these complement cosmic microwave background and other constraints. This study thus acts as a companion to our previous work [84], wherein we computed annihilation spectra and presented plots of the annihilation branching fractions for these models (figs. 3 and 4), but did not explain the ChPT matching procedure or derive detailed model

constraints/projections.

The remainder of this paper is organized as follows. In section 2.2 we provide an overview of the parton-level Lagrangian for the models we consider and a discussion of the applicability and validity of chiral perturbation theory for given dark matter and mediator masses. We then describe the specific microscopic models we consider, and the matching between parton-level and hadronic-level Lagrangians. Section 2.3 assesses the discovery reach for planned MeV gamma-ray telescopes, and compares with bounds from existing gamma-ray and cosmic microwave background data as well as non-astrophysical observations. Finally, section 5.9 concludes.

2.2 Theoretical Framework and its Validity

Our analysis considers extensions of the Standard Model (SM) defined in terms of microscopic Lagrangians just above the confinement scale $\Lambda \sim 1$ GeV. We posit that there is a dark matter particle χ with sub-GeV mass and a mediator that couples the dark and visible sectors. At the GeV scale the relevant fundamental SM degrees of freedom are the photon, light leptons (e, μ), gluons and light quarks (u, d, s). Letting M represent the mediator, the Lagrangians for such models takes the form

$$\mathcal{L} = \mathcal{L}_{\text{SM}} + \mathcal{L}_{\text{DM}} + \mathcal{L}_{\text{M}} + \mathcal{L}_{\text{Int(M)}}, \quad (2.1)$$

where the second and third pieces are the free terms for the DM and mediator and the fourth contains mediator-SM and mediator-DM interaction terms. We assume that χ is a (Dirac) fermion and a SM gauge singlet, so that it cannot couple directly to SM fields

in a renormalizable manner.

At the energy scale for annihilations of such DM particles, quarks and gluons are not the right strongly-interacting dynamical degrees of freedom. Instead, we must match eq. (2.1) onto one defined in terms of light *mesons*. In the rest of this section, we describe the framework for performing this matching, its range of validity, the particular DM models we consider and how to perform their matching in detail.

2.2.1 Low-energy QCD degrees of freedom

Since the strong interaction is confining below ~ 1 GeV, the relevant degrees of freedom in the MeV range are pions and other mesons. As was known since about 1980, these degrees of freedom can be described by an effective field theory (EFT) called *chiral perturbation theory* (ChPT), which is derived by treating the pions as pseudo-Goldstone bosons under the chiral symmetry group $SU(3)_L \times SU(3)_R$ [124, 205, 238]. The expansion parameter of the EFT is p/Λ_{ChPT} , where p is the characteristic momentum scale of the process in question and $\Lambda_{\text{ChPT}} \sim 4\pi f_\pi \sim 1$ GeV is the cut-off scale for ChPT; $f_\pi \approx 92$ MeV is called the pion decay constant. At a fixed order in the EFT expansion parameter, we restrict the number of derivatives on meson fields since $\partial_\mu \sim p_\mu$. Thus, at leading order (i.e. at order $(p/\Lambda_{\text{ChPT}})^2$), the most general ChPT Lagrangian density consistent with chiral symmetry is:

$$\mathcal{L}_{\text{ChPT}} = \frac{f_\pi^2}{4} \text{Tr} \left[(D_\mu \Sigma)(D^\mu \Sigma)^\dagger \right] + \frac{f_\pi^2}{4} \text{Tr} \left[\chi^\dagger \Sigma + \Sigma^\dagger \chi \right]. \quad (2.2)$$

There are a number of items in this Lagrangian density that need explaining: First, Σ is the Goldstone matrix transforming under $(L, R) \in \text{SU}(3)_L \times \text{SU}(3)_R$ as $\Sigma \rightarrow R\Sigma L^\dagger$. Explicitly, Σ is given by the exponential of a 3×3 matrix containing pions, kaons and the η :³ $\Sigma = \exp(i\Phi/f_\pi)$, with Φ given by

$$\Phi = \begin{pmatrix} \pi^0 + \frac{1}{\sqrt{3}}\eta & \sqrt{2}\pi^+ & \sqrt{2}K^+ \\ \sqrt{2}\pi^- & -\pi^0 + \frac{1}{\sqrt{3}}\eta & \sqrt{2}K^0 \\ \sqrt{2}K^- & \sqrt{2}\bar{K}^0 & -\frac{2}{\sqrt{3}}\eta \end{pmatrix} \quad (2.3)$$

The covariant derivative acting on the Goldstone matrix, D_μ , contains the $\text{SU}(3)_L$ and $\text{SU}(3)_R$ up, down and strange quark currents gathered into 3×3 matrices ℓ_μ and r_μ . These are taken to be $\mathcal{O}(p)$. The chiral currents transform under $(L, R) \in \text{SU}(3)_L \times \text{SU}(3)_R$ as $r_\mu \rightarrow Rr_\mu R^\dagger$ and $\ell_\mu \rightarrow L\ell_\mu L^\dagger$. These transformation rules restrict the form of the covariant derivative to

$$D_\mu \Sigma = \partial_\mu \Sigma - ir_\mu \Sigma + i\Sigma \ell_\mu, \quad (2.4)$$

which results in an object that transforms as Σ under chiral transformations: $D_\mu \Sigma \rightarrow R(D_\mu \Sigma)L^\dagger$. The second term in the leading order chiral Lagrangian encodes the masses of the mesons. The χ field is taken to be a spurion field responsible for chiral symmetry breaking. The spurion field transforms in the same way Σ does (namely $\chi \rightarrow R\chi L^\dagger$) and is counted as $\mathcal{O}(p)$. The expansion of χ around its vacuum expectation value is

$$\chi = 2B_0(M_q + s + ip), \quad (2.5)$$

³Note that what we refer to as the η is technically the η_8 . The physical η is instead a mixture of η_8 and η_1 , the field associated with the (anomalous) $U_A(1)$ symmetry. However, since $\eta = \eta_8 \cos \theta - \eta_1 \sin \theta$ and $\theta \approx -11^\circ$ we ignore this subtlety [249].

where s and p are scalar and pseudoscalar up, down and strange quark currents and M_q is the quark mass matrix. With no external fields, the quark mass matrix breaks chiral symmetry. The constant B_0 is related to the expectation value of the quark condensate via $B_0 = -\langle \bar{q}q \rangle / 3f_\pi \sim 2.3 \text{ GeV}$.

2.2.2 ChPT Applicability

Before moving on to describing the dark matter and mediator interactions with mesons, we would like to briefly explain the regime of validity of chiral perturbation theory. As the magnitude of the meson momentum p becomes comparable to Λ_{ChPT} , loop diagrams from the leading-order Lagrangian and tree diagrams from the next-to-leading order Lagrangian contribute comparably to tree-level diagrams from the leading order Lagrangian, signaling a breakdown in the effective theory.

However, the convergence of ChPT is actually disrupted at a lower scale than Λ_{ChPT} by hadronic resonances such as the scalar $f_0(500)$ [191] and the vector meson ρ . These induce significant interactions between hadrons produced by DM annihilation or mediator decay at center-of-mass energies of $p \gtrsim 500 \text{ MeV}$. The ρ and other vector resonances can be included in extensions of chiral perturbation theory [102]. The $f_0(500)$ cannot be incorporated in this framework, but can instead be accounted for using chiral unitary techniques in meson-meson scattering [191], which can be extended to compute corrections to cross sections for DM annihilation processes like $\text{DM DM} \rightarrow \pi\pi$. However, determining the impact on final state radiation processes like $\text{DM DM} \rightarrow \pi\pi\gamma$ is much more technically challenging. We leave this for future work, restricting the present

analysis to the narrow but well-controlled $p \leq 500$ MeV part of parameter space.

These considerations imply that the analysis in Ref. [158] pushes leading-order ChPT beyond its range of validity. That study focuses on final states containing an η meson and a π^0 or $\pi^+\pi^-$. The center of mass energies for these final states with all particles produced at rest are $p_{\pi^0\eta} \sim 680$ MeV and $p_{\pi^+\pi^-\eta} \sim p_{\pi^0\pi^0\eta} \sim 825$ MeV, well beyond the scale at which resonances must be taken into account. For example, the strength of final state interactions for $DM DM \rightarrow \pi^0\eta$ is related to the elastic $\pi^0\eta \rightarrow \pi^0\eta$ scattering cross section by the Watson final state theorem [236]. This amplitude is dominated by exchange of the $f_0(500)$ and $a_0(980)$ scalar resonances [39], with little contribution from leading-order ChPT.⁴ As another example, the final state interactions relevant for $DM DM \rightarrow \pi\pi\eta$ with $J^{PC} = 0^{-+}$ are the same as for the process $\eta' \rightarrow \pi\pi\eta$. The value for the branching fraction computed with leading-order ChPT is only 3% of the measured value [108]. Successfully predicting the experimentally-measured Dalitz plot parameters requires combining next-to-leading order large- N_c ChPT with a unitarization procedure to account for final state interactions.

The diagram in fig. 2.2 shows in detail the range of validity of this work, with the red region indicating where leading order ChPT calculations cannot be trusted due to resonances and/or convergence issues with ChPT. The dashed lines indicate parameter space for which the mediator can decay invisibly and the DM can annihilate into the mediator. In the green region, the DM annihilation cross sections are well-described by leading-order ChPT. In the blue one, ChPT cannot be used to compute

⁴Note that the $f_0(500)$ is instead denoted by $\sigma(560)$ in Ref. [39].

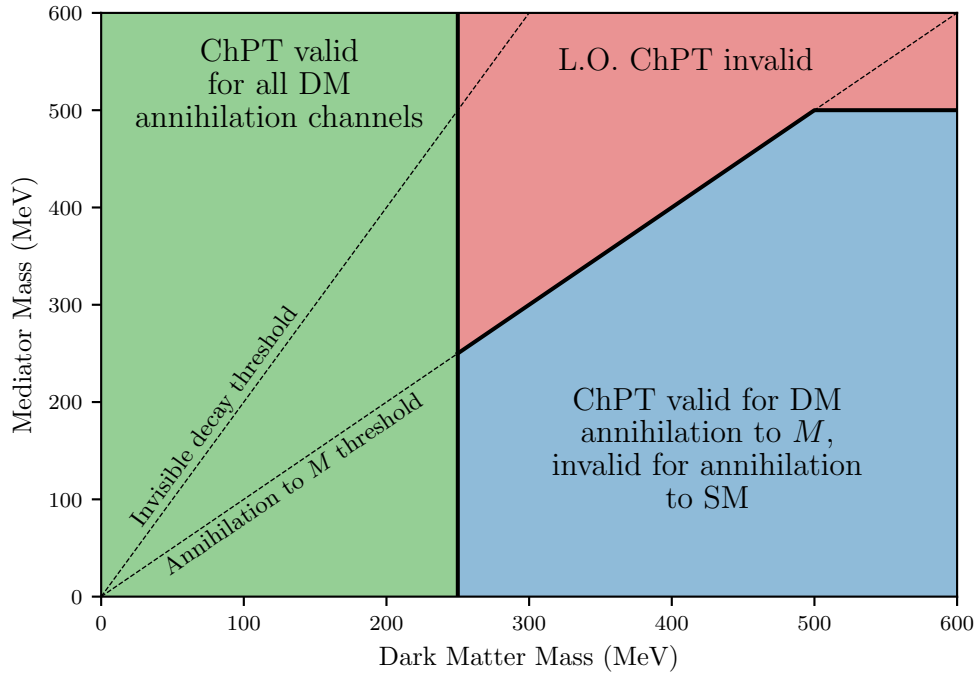


Figure 2.2: Illustration of DM masses m_{DM} and mediator masses m_M for which the leading-order chiral perturbation theory calculations in this paper can be considered reliable.

the cross section for annihilation into SM final states. However, annihilation of the dark matter into mediators followed by their subsequent decay can be accurately treated using ChPT in this region.

As a consequence of this analysis, we neglect annihilation and mediator decays into strange mesons K^+ , K^0 and η . Producing kaons in appreciable numbers in DM annihilations requires $m_K < m_{\text{DM}} < m_M$; alternatively, producing them through annihilation into mediators followed by mediator decay requires $2m_K < m_M < m_{\text{DM}}$. Both these parts of parameter space are within the red region of Fig. 2.2. The η mass, $m_\eta = 547 \text{ MeV}$, is also outside the range of validity for a leading order ChPT analysis, and will be neglected throughout. The strange quark and associated couplings will thus be ignored in this work, though they are an important input for any chiral perturbation theory analysis beyond leading order.

2.2.3 Microscopic Models

We consider two choices for the mediators, a (real) scalar mediator S and a vector mediator V . The free Lagrangian for the scalar mediator reads

$$\mathcal{L}_S = \frac{1}{2}(\partial_\mu S)(\partial^\mu S) - \frac{1}{2}m_S^2 S^2, \quad (2.6)$$

with the following interaction Lagrangian:

$$\mathcal{L}_{\text{Int}(S)} = -S \left(g_{S\chi} \bar{\chi}\chi + \frac{g_{Sf}}{\sqrt{2}} \sum_f y_f \bar{f}f \right) + \frac{S}{\Lambda} \left(g_{SF} \frac{\alpha_{\text{EM}}}{4\pi} F_{\mu\nu} F^{\mu\nu} + g_{SG} \frac{\alpha_s}{4\pi} G_{\mu\nu}^a G^{a\mu\nu} \right). \quad (2.7)$$

In the expression above, we assume that the interactions of the scalar S with SM fermions is mediated by Yukawa interactions, where $y_f = \sqrt{2}m_f/v_h$ and $v_h = 246$ GeV is the vacuum expectation value of the SM Higgs (this choice is motivated by the framework of minimal flavor violation [58, 87]). We also included non-renormalizable operators describing effective interactions of the mediator S with the low-energy gauge boson degrees of freedom, photons and gluons; these interactions are invariably generated by integrating out heavier degrees of freedom including those responsible for ensuring gauge invariance of the theory at high energy.

In what follows, we fix the parameters g_{Sf} , g_{SF} and g_{SG} assuming the Higgs portal scenario, where a quartic coupling $\lambda H^\dagger H S^2$ induces a mixing of the mediator S with the SM Higgs boson. In this case, indicating with θ the relevant mixing angle, $g_{Sf} = -\sin\theta$, $g_{SF} = 5\sin\theta/6$ and $g_{SG} = -3\sin\theta$ (see [174] for details), and the effective mass scale $\Lambda = v_h$.

In the case of a vector mediator, the free mediator Lagrangian reads

$$\mathcal{L}_V = -\frac{1}{4}V_{\mu\nu}V^{\mu\nu} + \frac{1}{2}m_V^2 V_\mu V^\mu, \quad (2.8)$$

with interaction terms

$$\mathcal{L}_{\text{Int}(V)} = V_\mu \left(g_{V\chi} \bar{\chi} \gamma^\mu \chi + \sum_f g_{Vf} \bar{f} \gamma^\mu f \right) - \frac{\epsilon}{2} V^{\mu\nu} F_{\mu\nu}. \quad (2.9)$$

In the expression above, the sum over fermions includes all light degrees of freedom, $f \in \{e, \mu, u, d, s\}$, while ϵ is a kinetic mixing parameter. Notice that upon $A_\mu \rightarrow A_\mu - \epsilon V_\mu$ the kinetic mixing term disappears, and the charge assignments in turn change, e.g. $g_{Vf} \rightarrow g_{Vf} - \epsilon e Q_f$, where Q_f is the electric charge of fermion f . In what follows,

we posit that the interactions with SM fermions be only originating from said kinetic mixing, and thus $g_{Vf} = -\epsilon e Q_f$.

2.2.4 Matching

In this section we demonstrate the procedure of matching various terms from the Lagrangians defined at energies above Λ_{QCD} onto the chiral Lagrangian. In particular, we will be interested in matching the following terms:

$$S\bar{q}\mathbf{G}_{Sq}q, \quad SG_{\mu\nu}^a G^{\mu\nu,a}, \quad V_\mu\bar{q}(\mathbf{G}_{Vq})\gamma^\mu q \quad (2.10)$$

where S and V_μ are the scalar and vector mediators, $q = \begin{pmatrix} u & d & s \end{pmatrix}$ and $\mathbf{G}_{Sq}, \mathbf{G}_{Vq}$ are 3×3 coupling matrices. Below, we provide the details for matching each of the above terms onto the Chiral Lagrangian.

$S\bar{q}\mathbf{G}_{Sq}q$

The term $S\bar{q}\mathbf{G}_{Sq}q$ closely resembles the quark mass term: $\bar{q}M_qq$. In fact, we match the former and latter terms onto the chiral Lagrangian using the same technique. Recall that the quark mass terms are matched onto the chiral Lagrangian by introducing a spurion field χ transforming as $\chi \rightarrow R\chi L^\dagger$ under chiral transformations. Then, we form a chiral invariant using $\text{Tr}[\chi\Sigma^\dagger + \text{h.c.}]$. χ then is used to break chiral symmetry by setting it to its vacuum state $\chi = 2BM_q$. Thus, the mass term is matched as follows:

$$-\bar{q}M_qq \rightarrow \frac{f_\pi^2}{4} \text{Tr}[\chi\Sigma^\dagger + \text{h.c.}], \quad \chi = 2BM_q. \quad (2.11)$$

Generalizing by adding interaction terms of the form $S\bar{q}G_{Sq}q$, with G a 3×3 matrix, we change χ to:

$$\chi \rightarrow 2B(M_q + SG_{Sq}) \quad (2.12)$$

In the Higgs portal model, we have scalar Yukawa interactions with $G_{Sq} = -g_{Sf}M_q/v_h$.

These, together with the quark mass terms, are therefore matched as:

$$-\sum_{i=3}^3 \left(1 + g_{Sf} \frac{S}{v_h}\right) m_q \bar{q}_i q_i \rightarrow \frac{f_\pi^2}{4} \text{Tr} \left[\chi \Sigma^\dagger + \text{h.c.} \right], \quad \chi = 2BM_q \left(1 + g_{Sf} \frac{S}{v_h}\right). \quad (2.13)$$

$$\frac{\alpha_s}{4\pi} \frac{S}{\Lambda} G_{\mu\nu}^a G^{\mu\nu,a}$$

Terms of the form $\frac{\alpha_s}{4\pi} \frac{S}{\Lambda} G_{\mu\nu}^a G^{\mu\nu,a}$ frequently arise when integrating out heavy quarks. For example, this term arises in the Higgs portal model when integrating out the top, bottom and charm quarks at one-loop. The matching of $SG_{\mu\nu}^a G^{\mu\nu,a}$ onto the chiral Lagrangian is performed by utilizing the trace anomaly [97, 69]. The trace anomaly relates the divergence of the dilatation current $\partial^\mu d_\mu$ to the gluon kinetic term and quark mass operators. The key insight in matching $\alpha_s G^2$ onto the chiral Lagrangian is that $\partial_\mu d^\mu$ is RGE-invariant [131]. In Ref. [69], it was shown that, at leading order in perturbation theory, $\frac{\alpha_s}{4\pi} \frac{S}{\Lambda} G_{\mu\nu}^a G^{\mu\nu,a}$ can be written as:

$$\frac{\alpha_s}{4\pi} \frac{S}{\Lambda} G_{\mu\nu}^a G^{\mu\nu,a} = -\frac{2}{\beta_0} \frac{S}{\Lambda} \left[\partial_\mu d^\mu - \sum_{q=u,d,s} m_q \bar{q}q \right] \quad (2.14)$$

where $\beta_0 = 11 - \frac{2}{3}N_f$ is the leading order β -function for the QCD coupling constant with N_f flavors. Since $\partial_\mu d^\mu$ is RGE-invariant, it is matched onto the chiral Lagrangian

by simply computing the divergence of the scale current using the chiral Lagrangian:

$$\partial_\mu d^\mu = -\frac{f_\pi^2}{2} \text{Tr} \left[(D_\mu \Sigma)(D_\mu \Sigma)^\dagger \right] - 2f_\pi^2 B_0 \text{Tr} \left[M_q (\Sigma + \Sigma^\dagger) \right] \quad (2.15)$$

We can match $m_q \bar{q}q$ onto the chiral Lagrangian using techniques described above. The result is:

$$\frac{\alpha_s}{4\pi} \frac{S}{\Lambda} G_{\mu\nu}^a G^{\mu\nu,a} \rightarrow \frac{f_\pi^2}{\beta_0} \frac{S}{\Lambda} \text{Tr} \left[(D_\mu \Sigma)(D_\mu \Sigma)^\dagger \right] + \frac{3f_\pi^2 B_0}{\beta_0} \frac{S}{\Lambda} \text{Tr} \left[M_q (\Sigma + \Sigma^\dagger) \right] + \dots \quad (2.16)$$

where the (\dots) contains terms with more than one S coming from matching

$-2S/(\beta_0 \Lambda) m_q \bar{q}q$ and $g_{Sf}(S/v_h) \bar{q}q$ onto the chiral Lagrangian. These are irrelevant for this study so we omit them.

$V_\mu \bar{q} G_{Vq} \gamma^\mu q$

External vector currents are matched onto the chiral Lagrangian through the covariant derivative:

$$D_\mu X = \partial_\mu X - i r_\mu X + i X \ell_\mu \quad (2.17)$$

where r_μ and ℓ_μ are right-handed and left-handed currents. Given a quark vector current $V^\mu J_\mu = G_{Vq} V^\mu \bar{q} \gamma^\mu q$, we can identify:

$$r_\mu = \ell_\mu = G_{Vq} V_\mu + \dots \quad (2.18)$$

where the \dots represent other currents (such as the electromagnetic currents.)

There are additional terms outside of the chiral expansion that are necessary for our studies. Wess, Zumino [239] and Witten [244] showed the existence of an additional

term in the chiral Lagrangian which gives rise to the neutral pion's decay into two photons:

$$\mathcal{L}_{\pi^0\gamma\gamma} = -\frac{e^2}{32\pi^2}\epsilon_{\mu\nu\rho\sigma}F^{\mu\nu}F^{\rho\sigma}\frac{\pi^0}{f_\pi} \quad (2.19)$$

where $F_{\mu\nu}$ is the photon field strength tensor and $\epsilon_{\mu\nu\rho\sigma}$ is the 4-dimensional Levi-Civita symbol. In the case of kinetic mixing model, the shift of the photon field $A_\mu \rightarrow A_\mu - \epsilon V_\mu$, results in the following vector-photon-pion coupling:

$$\mathcal{L}_{\pi^0\gamma\gamma} \rightarrow -\frac{e^2}{32\pi^2}\epsilon_{\mu\nu\rho\sigma}F^{\mu\nu}F^{\rho\sigma}\frac{\pi^0}{f_\pi} - \frac{\epsilon e^2}{16\pi^2}\epsilon_{\mu\nu\rho\sigma}F^{\mu\nu}V^{\rho\sigma}\frac{\pi^0}{f_\pi} \quad (2.20)$$

Hence, we pick up an additional $V\gamma\pi^0$ coupling which gives important contributions to the dark matter annihilation spectrum when annihilations into two-pion channels are forbidden.

2.3 Searching for MeV Dark Matter with Future Gamma Ray Telescopes

We now turn to assessing the prospects for future MeV gamma-ray telescopes to explore the parameter space of dark matter for the Higgs portal and dark photon portal models. After briefly summarizing how to compute the gamma-ray yield from dark matter annihilation, we describe the calculation of constraints from existing gamma-ray telescopes, the cosmic microwave background and other particle physics observations. We then discuss our results for the anticipated performance of future MeV gamma-ray telescopes.

2.3.1 Gamma-ray constraints

Gamma rays can be produced through three mechanisms when dark matter self-annihilates: direction photon production and radiation from and radiative decays of final state particles.⁵ Photons from the first mechanism are simple to account for, contributing delta function spectra in the cases considered in this work ($\gamma\gamma$ in the Higgs portal model and $\pi^0\gamma$ for the dark photon model). The spectrum of final-state radiation is dependent on the details of the mediator's couplings to the final-state particle and whether the particle is a scalar or fermions, so its accurate calculation requires the effective Lagrangians provided above. Analytic expressions for these spectra were presented in eqs. 4.8 - 4.11 in our previous work [84]. There we also provide the radiative decay spectra of the neutral pion (eq. 4.20), muon (eq. 4.21) and charged pion (eqs. 4.22 - 4.25, which critically includes the process $\pi^+ \rightarrow \mu^+\nu_\mu$ followed by subsequent radiative muon decay). Summing these three spectral components weighted by their branching fractions as computed with the effective Lagrangians above gives the total spectrum from DM annihilation, $\frac{dN}{dE_\gamma}|_{\bar{\chi}\chi}$.

This spectrum can be combined with an assumed spatial distribution of DM to give the gamma-ray flux from DM annihilations in an astrophysical target subtending solid angle $\Delta\Omega$:

$$\frac{d\Phi}{dE_\gamma}\Big|_{\bar{\chi}\chi}(E) = \frac{\Delta\Omega}{4\pi} \frac{\langle\sigma v\rangle_0}{2f_\chi m_\chi^2} \bar{J} \frac{dN}{dE_\gamma}\Big|_{\bar{\chi}\chi}(E). \quad (2.21)$$

⁵Dark matter annihilations also produce photons indirectly through astrophysical processes involving the annihilation products, such as synchrotron radiation in regions with magnetic fields and inverse-Compton scattering of cosmic microwave background photons. This so-called secondary emission spectrum is challenging to compute accurately given the substantial astrophysical uncertainties involved [76, 78, ?] and we thus neglect it here.

$\langle\sigma v\rangle_0$ is the thermally-averaged, present-day DM annihilation cross section in the target region. The \bar{J} factor accounts for the amount of DM in the target, and depends on the square of the DM density ρ since annihilations consume pairs of DM particles:

$$\bar{J} \equiv \frac{1}{\Delta\Omega} \int_{\Delta\Omega} d\Omega \int_{\text{LOS}} dl \rho(r(l, \psi))^2, \quad (2.22)$$

f_χ accounts for the statistics of the DM, taking value 1 when it is self-conjugate and 2 otherwise. Since we assume the DM is a Dirac fermion, $f_\chi = 2$. In reality, a detector with finite energy resolution does not measure the flux in eq. (2.21) but rather the flux smoothed by an energy resolution function $R_\epsilon(E|E')$:

$$\left. \frac{d\Phi_\epsilon}{dE_\gamma} \right|_{\bar{\chi}\chi}(E) = \int dE' R_\epsilon(E|E') \left. \frac{d\Phi}{dE_\gamma} \right|_{\bar{\chi}\chi}(E') \quad (2.23)$$

The resolution function gives the probability a gamma ray with true energy E' is reconstructed with energy E , and can generally be approximated as $\mathcal{N}(E|E', \epsilon(E') E')$, with energy-dependent width parameter $\epsilon(E)$ [54].

Existing measurements of the gamma-ray flux from the Milky Way by the Imaging Compton Telescope (COMPTEL) [223], the Energetic Gamma Ray Experiment Telescope (EGRET) [139], the Fermi Large Area Telescope (Fermi-LAT) [24] and INTEGRAL/SPI [48] constrain DM models. In lieu of attempting to model the astrophysical MeV gamma-ray background, we adopt the simple constraint-setting approach of requiring that the smoothed flux from DM annihilation integrated over each of a given detector's energy bins not exceed the measured flux plus twice the upper error in the bin: $\Phi_\epsilon^{(i)}|_{\bar{\chi}\chi} < \Phi^{(i)}|_{\text{obs}} + 2\sigma^{(i)}$, where i indexes the bins. We have checked that setting a constraint using a χ^2 test statistic yields similar results.

Several missions with capabilities in the MeV are in the proposal, planning, or construction phase. Here, we consider the following: AdEPT [138], AMEGO [179], All-Sky-ASTROGAM [172], GECCO [184, 82], MAST [101], PANGU [248, 247] and GRAMS [21, 20]. These are each characterized by an energy-dependent effective area $A_{\text{eff}}(E)$ and energy resolution $\epsilon(E)$. For all telescopes we assume an observation time of 3 years, $T_{\text{obs}} = 9.5 \times 10^7 \text{ s} = 1095 \text{ d}$.

Determining the reach of future telescopes requires adopting a background flux model $\frac{d\Phi}{dE_\gamma}|_{\text{bg}}$ so the expected photon counts from DM annihilation and astrophysical processes in a target can be compared. A flux $\frac{d\Phi}{dE_\gamma}$ can be converted to photon counts at a detector over an energy range $[E_{\text{low}}, E_{\text{high}}]$ using

$$N_\gamma = T_{\text{obs}} \int_{E_{\text{min}}}^{E_{\text{max}}} dE A_{\text{eff}} \frac{d\Phi}{dE_\gamma} \quad (2.24)$$

By substituting $\frac{d\Phi_\epsilon}{dE_\gamma}|_{\bar{\chi}\chi}$ and $\frac{d\Phi}{dE_\gamma}|_{\text{bg}}$ into this equation we can construct the signal-to-noise ratio by maximizing over the energy range:

$$\text{SNR} \equiv \max_{E_{\text{min}}, E_{\text{max}}} \frac{N_\gamma|_{\bar{\chi}\chi}}{\sqrt{N_\gamma|_{\text{bg}}}}. \quad (2.25)$$

We estimate that a DM model is discoverable if $\text{SNR} > 5$.

Note that since the DM's mass is not identifiable under the background-only hypothesis, a full data analysis must compensate for the look-elsewhere effect using the methods of e.g. Ref. [132].⁶ We leave this more involved analysis for future work, but point out that except for the case where DM annihilates into pairs of photons the

⁶Detection significances must also be corrected slightly to account for the fact that $\langle\sigma v\rangle_0$ is non-negative, the so-called Chernoff correction to Wilks' theorem [?].

spectrum would be spread across multiple energy bins in a realistic analysis, reducing the trials factor correction to detection significances. The effect could also be mitigated by splitting the dataset (at the cost of a $\sqrt{2}$ reduction in SNR), and if a strong-enough annihilation signal is detected it could be confirmed by observing other targets such as M31 and Draco.

Since the \bar{J} factor scales with the DM density squared, it is advantageous to select small, DM-rich targets for DM searches. We use the inner $10^\circ \times 10^\circ$ region of the Milky Way as a target for the purposes of projecting the discovery reach of future telescopes. There is substantial uncertainty in modeling the baryonic and DM mass distributions in the Milky Way, which translates into factor of $10^{-1} - 10^1$ uncertainties in the \bar{J} factor for the Galactic Center. We fix the DM distribution to the Einasto profile from Table III of Ref. [92], with the parameters adjusted within their 1σ error bands to maximize \bar{J} . For consistency the constraints from existing gamma-ray observations are derived using this same profile.

As a background model we adopt the one developed in Ref. [31] specifically for searches in our target region. The model combines spectral components computed using the GALPROP cosmic ray propagation code [226] as well as an analytic power-law component required to closely fit COMPTEL galactic center observations.

2.3.2 Cosmic Microwave Background Constraints

Dark matter annihilation around the time of CMB formation can inject ionizing particles into the photon-baryon plasma (see e.g. Ref. [219]). The resulting changes

Detector	Latitude	Longitude	$\Delta\Omega$ (sr)	\bar{J} ($\text{MeV}^2 \text{cm}^{-5} \text{sr}^{-1}$)
COMPTEL	$ b < 20^\circ$	$ l < 60^\circ$	1.433	1.04×10^{30}
EGRET	$20^\circ < b < 60^\circ$	$ l < 180^\circ$	6.585	9.062×10^{27}
Fermi-LAT	$8^\circ < b < 90^\circ$	$ l < 180^\circ$	10.817	1.601×10^{28}
Planned	$ b < 5^\circ$	$ l < 5^\circ$	3.042×10^{-2}	3.99×10^{31}

Table 2.1: Target regions and \bar{J} factors for different detectors' measurements of the diffuse gamma-ray flux, as well as the target used to project the discovery reach of planned telescopes. All \bar{J} factors were computed assuming the same Einasto profile (see text for details). See Ref. [145] for COMPTEL, Ref. [224] for EGRET and Ref. [7] for Fermi-LAT.

in the residual ionization fraction and baryon temperature, modifying the CMB temperature and polarization power spectra, particularly at small scales. The changes depend on the energy per unit volume per unit time imparted to the plasma, quantified with the DM annihilation parameter

$$p_{\text{ann}} \equiv f_{\text{eff}}^{\chi} \cdot \frac{\langle \sigma v \rangle_{\text{CMB}}}{m_{\chi}}. \quad (2.26)$$

The thermal average is taken at the time of CMB formation. In the case of s -wave annihilation, $\langle \sigma v \rangle_{\text{CMB}}$ is equal to the present-day thermally averaged annihilation cross section, $\langle \sigma v \rangle_0$. For p -wave annihilation, $\langle \sigma v \rangle_{\text{CMB}} = \langle \sigma v \rangle_0 (v_{\text{CMB}}/v_0)^2$, where we take the present-day DM velocity to be $v_0 = 220 \text{ km s}^{-1}$ in the Milky Way. The DM velocity at recombination depends on the kinetic decoupling temperature. While the DM velocity is thermal before kinetic decoupling, it redshifts more quickly afterwards, giving [109]

$$v_{\text{CMB}} = \sqrt{3T_{\chi}/m_{\chi}} \approx 2 \times 10^{-4} \left(\frac{T_{\gamma}}{1 \text{ eV}} \right) \left(\frac{1 \text{ MeV}}{m_{\chi}} \right) \left(\frac{10^{-4}}{x_{\text{kd}}} \right)^{1/2}, \quad (2.27)$$

where $x_{\text{kd}} \equiv T_{\chi}/m_{\chi} \approx 10^{-4} - 10^{-6}$ and we take $T_{\gamma} = 0.235 \text{ eV}$. This means that while the CMB bounds on $\langle \sigma v \rangle_0$ are quite stringent for s -wave annihilation, they are much weaker for p -wave annihilation since v_{CMB} is much smaller than v_0 . The quantity f_{eff}^{χ} encapsulates how efficiently DM annihilations inject energy into the plasma. It is obtained by integrating the e^{\pm} and photon spectra per DM annihilation weighted by energy injection efficiency factors [217]. This quantity can be computed in `hazma` (see sec. 8 of Ref. [84]).

In the constraint plots below, we use the most recent Planck constraint on the DM annihilation parameter [?], $p_{\text{ann}} < 4.1 \times 10^{-31} \text{ cm}^3 \text{ s}^{-1} \text{ MeV}^{-1}$.

2.3.3 Higgs portal model constraints

There are numerous terrestrial constraints on our Higgs portal model (see e.g. Ref. [157]), and in particular the coupling $\sin\theta$. The most important here are the upper limit on the invisible Higgs branching fraction, bounds on several rare visible and invisible meson decays processes and limits on light particle production at beam dumps.

For the first process, the invisible Higgs branching fraction can be computed from the microscopic interaction Lagrangian and compared with current constraint of $\text{Br}(h \rightarrow \bar{\chi}\chi) < 0.19$ from the CMS detector at the Large Hadron Collider [?]. In our analysis the DM mass is much smaller than the Higgs mass, so this constraint is independent of m_χ .

The scalar mediator gives a contribution to flavor-changing neutral currents (FCNCs) that cause rare B and K -meson decays. These proceed via $B \rightarrow K S$ and $K \rightarrow \pi S$, followed by subsequent decay of the mediator into leptons or DM particles. We follow the analysis in Appendices A and C of Ref. [96] to compute constraints on our model from Belle measurements of $\text{Br}(B^+ \rightarrow K^+\ell^+\ell^-)$ [?], KTeV's upper limits on $\text{Br}(K_L \rightarrow \pi^0\ell^+\ell^-)$ [?, ?], BaBar's upper limit on $\text{Br}(B^+ \rightarrow K^+\bar{\nu}\nu)$ [?] and E949's measurement of $\text{Br}(K^+ \rightarrow \pi^+\bar{\nu}\nu)$ [?, ?].

The CHARM beam dump searched for electrons, muons and photons produced by the decays of light particles created in collisions between a 400 GeV proton beam and a copper target [?]. Since no such decays were detected, the number of decays in the detector volume is constrained to be less than 2.3 at the 90% confidence level [?].

We follow the analysis in Ref. [?] to impose this constraint.

The complementarity between these terrestrial constraints and indirect detection constraints and projections in the $(m_\chi, \langle\sigma v\rangle)$ plane depends on whether the DM annihilates invisibly or visibly. In the first case, corresponding to a mediator mass smaller than the dark matter mass, the cross section $\langle\sigma v\rangle$ is proportional to $g_{S\chi}^4$: $\sin\theta$ plays no role in indirect detection. The only requirement in this case is that there is *some* $\sin\theta$ value consistent with terrestrial observations, and that it is large enough that the mediator’s decay length is below the parsec scale. This is the case for all DM masses we will consider.

If instead the DM annihilates into SM final states (i.e. the mediator mass is larger than the DM mass), the annihilation cross section scales as $g_{S\chi}^2 \sin^2\theta y^2$, where $y \ll 1$ is the Yukawa coupling of the final state particles. The Yukawa strongly suppresses the indirect detection signal, and large values of $g_{S\chi}$ and $\sin\theta$ are required to give detectable signals (see the dashed red line in the right panel of fig. 2.3). We translate terrestrial constraints into the $(m_\chi, \langle\sigma v\rangle)$ plane as follows. For fixed m_χ , each point in this plane defines a range of $\sin\theta$ and corresponding $g_{S\chi}$ values. The largest-possible value of $\sin\theta$ is 1 and the smallest value corresponds to $g_{S\chi} \sim 4\pi$. We thus check at each point whether there is *some* value of $(\sin\theta, g_{S\chi})$ in this range that is consistent with terrestrial constraints. If there is not, that point is excluded, and we highlight it in orange in our final constraint plots (fig. 2.3).

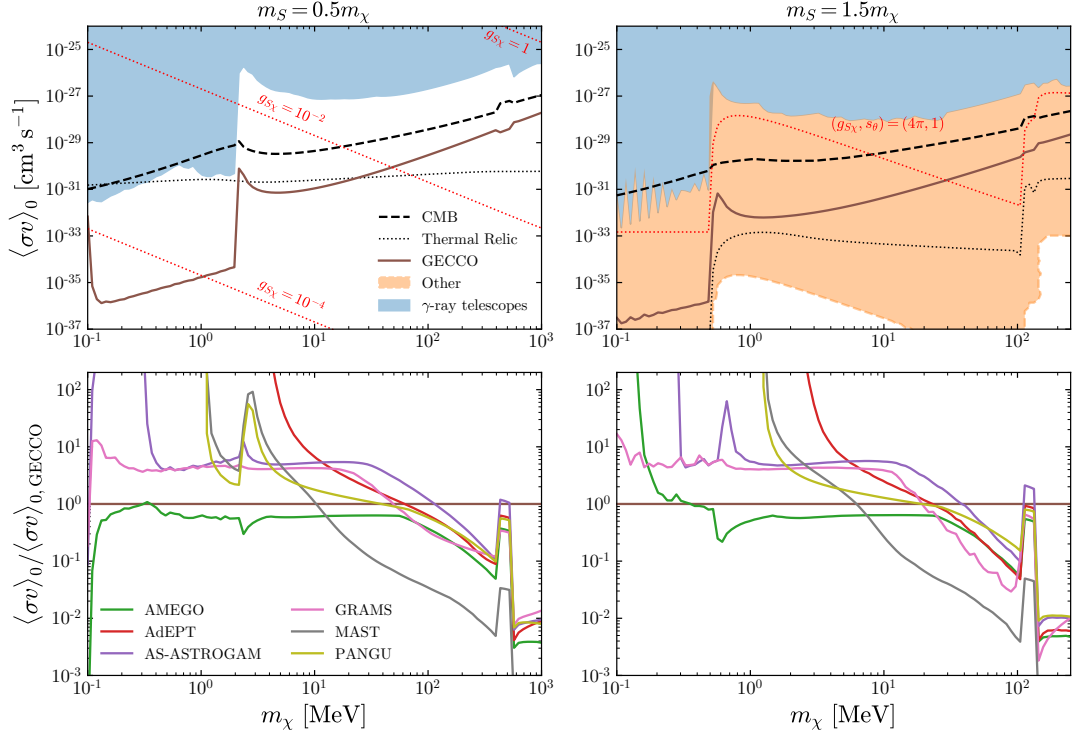


Figure 2.3: Prospects for future gamma-ray telescopes, and phenomenological constraints, for the Higgs portal case; the left panels assume a mediator mass half the mass of the DM, while the right panels assume a mediator mass equal to 1.5 times the DM mass. The lower panels show the future telescope prospects normalized to GECCO’s (a smaller value on the y axis corresponds to a *tighter* constraining capability). In computing the CMB constraint we conservatively assume a kinetic decoupling temperature of $10^{-6} m_\chi$.

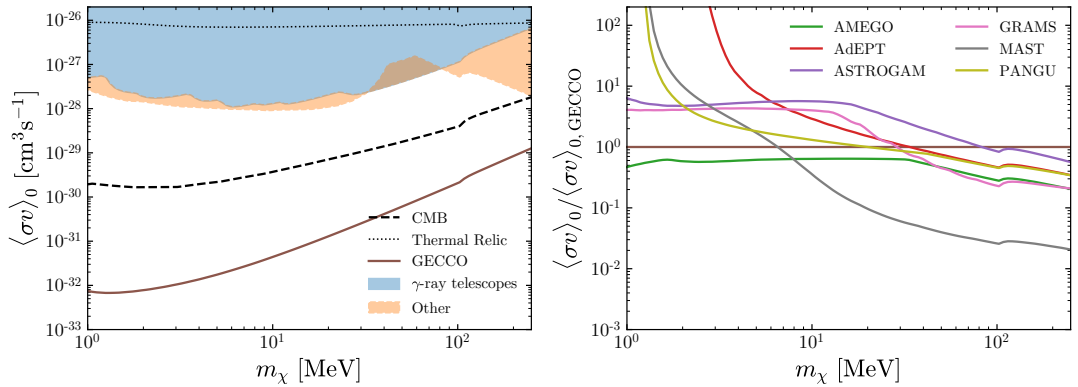


Figure 2.4: Vector mediator constraints, for a mediator mass $m_V = 3m_\chi$. The right panel shows the ratio of the projected constraints from a given future telescope relative to those for GECCO (shown with a brown line in the left panel).

2.3.4 Dark photon model constraints

We choose here to focus on the regime where the mediator is heavier than the dark matter mass, and assume $3m_\chi = m_V$. This choice enables us to re-use previously-calculated constraints from non-astrophysical experiments. The strongest constraints on dark photon models for the masses we are interested in come from the B -factory BaBar [164] and beam-dump experiments such as LSND [12]. Studies using the datasets of these experiments were able to constraint the dark photon model by searching for dark photon production and subsequent decay into dark matter (see, for example Ref. [33, 164, 155]); in the case of BaBar, the relevant process is $\Upsilon(2S), \Upsilon(3S) \rightarrow \gamma + V \rightarrow \gamma + \text{invisible}$, while the relevant process for LSND is $\pi^0 \rightarrow \gamma + V \rightarrow \gamma + \text{invisible}$. We adapt here the constraints computed in Ref. [15, 155] (see Fig.(201) of Ref. [155] for the constraints and the text and references therein for

details). These references take $\alpha_D = g_{V\chi}^2/4\pi = 0.5$ and we do the same in order to consistently compare their constraints with our gamma-ray constraints. This value is conservative for the phenomenological constraints. Lowering α_D will strengthen the phenomenological constraints (for example, taking $\alpha_D = 10^{-3}$ will strengthen the constraints by an order of magnitude; see Ref. [15]). However, the gamma-ray constraints will be unaffected.

2.3.5 Results

Figure 2.3 shows the current and projected limits on the scalar mediator (Higgs portal) model. In the left panels, the DM pair annihilates preferentially to the scalar mediator, which, in turn, decays to kinematically-available final states according to the corresponding Yukawa coupling. A prominent feature of the gamma-ray constraints lines (including from existing telescopes) appears at the electron threshold, corresponding to a dark matter mass being four times the electron mass (since the mediator's mass is half that of the dark matter, and to decay into electron-positron pairs its mass must be twice the mass of the electron). The other visible features, at higher DM masses, correspond to the muon and pion thresholds.

Since the mixing angle θ is virtually unconstrained in the invisible decay case (left panels), phenomenological constraints are weaker, in general, than existing gamma-ray constraints. Also, notice that because of the velocity suppression of the pair-annihilation cross section in this model, CMB limits are weak compared to the expected cross section from thermal production.

The anticipated performance of future MeV gamma-ray telescopes is shown with the brown line for GECCO in the upper panel, and in the lower panel for all other future telescopes under consideration, relative to GECCO (a smaller ratio corresponding to tighter constraints). While the relative sensitivity of telescopes such as GRAMS, All-Sky ASTROGAM, and AMEGO are within a factor of a few for several decades in DM mass, the sudden appearance of muons in the annihilation final state, and the corresponding final-state radiation, samples in a non-trivial way the effective area of telescopes as a function of energy in the DM mass range between the muon and pion threshold. This produces the sudden sensitivity decrease for virtually all telescopes compared to GECCO in that DM mass range, visible as a box-shaped feature.

Broadly, we find that as soon as the mediator decay to e^+e^- opens up, future MeV telescopes will definitely be sensitive to thermally-produced MeV dark matter for light scalar mediators where the dark matter pair annihilates preferentially invisibly.

The situation is markedly different for heavier scalar mediator. Generally, most parameter space is, in this case, ruled out by phenomenological constraints. While in principle future MeV telescopes will be sensitive to this case as well (as shown by the red-dotted line being *above* the brown line in the top, right panel), it will be critical for the DM mass to exceed the electron threshold, and/or the muon threshold. Again, though, future MeV telescope will outperform CMB constraints as well as, naturally, existing gamma-ray telescopes.

The case of dark matter annihilation via kinetically-mixed vector mediators weighing *more* than the dark matter is shown in fig. 2.4. Current gamma-ray telescopes

do not provide any meaningful constraint, given current phenomenological constraints, as shown by the orange shaded region extending beyond the blue shaded region in the left panel. Additionally, for all but the heaviest masses CMB constraints are the strongest for this case, where the pair-annihilation cross section is *not* velocity suppressed. Nonetheless, our analysis indicates that future MeV gamma-ray telescopes such as GECCO (whose projected sensitivity is shown with a brown line in the left panel) will out-perform CMB constraints by between 1 and 2 orders of magnitude, thus being slated to probe meaningful portions of open parameter space.

Compared with other gamma-ray telescopes, GECCO's performance is similar, albeit slightly inferior, to AMEGO's, but better than All-Sky ASTROGAM up to 100 MeV masses, and better than even MAST up to almost 10 MeV. Again, smaller cross section ratios (shown in the y -axis) indicate more constraining power.

2.4 Conclusions

This study aimed at filling a few gaps in the reliable analysis of indirect detection prospects for annihilating dark matter in the MeV mass range. The key analytical results we presented were the matching of parton-level interactions between Higgs portal and dark photon mediators onto meson-level ones, which were obtained by means of chiral perturbation theory. We clarified the range of validity of our leading-order chiral perturbation theory treatment as a function of the dark matter and mediator mass. We then compared current constraints from the CMB, terrestrial experiments and existing

and past gamma-ray telescopes with the anticipated performance of planned telescopes. Our gamma-ray constraints/projections and CMB ones were derived by computing annihilation branching ratios using the meson-level interactions we derived, and applying our previous analysis of the final-state radiation and radiative decay spectra for light meson and lepton final states [84].

We focused on invisibly- and visibly-annihilating Higgs-portal mediator models. For the former, future gamma-ray telescopes will explore large swaths of yet-unexplored parameter space (including that preferred by thermal dark matter production), while for the latter, typically the existing phenomenological constraints will prevent exploring new models. For the dark photon mediator case, we found that new MeV gamma-ray telescopes will enhance the constraints on the dark matter self-annihilation cross section by 1 to 2 orders of magnitude beyond the values currently constrained by CMB observations.

While the landscape of WIMP searches in the traditional GeV - TeV range appears to offer faltering returns for dark matter discovery, our study illustrates how future MeV gamma-ray detectors provide very promising prospects over several orders of magnitude in the dark matter mass. With improved observational tools, improved theoretical tools are in order. This paper addressed some of the shortcomings in the current understanding of how to reliably compute gamma-ray spectra, and elucidated how, with the technique of chiral perturbation theory, the discovery of an anomalous gamma-ray spectrum might be tied to a parton-level Lagrangian, potentially offering important guidance to illuminating the nature of physics beyond the Standard Model

of particle physics.

Chapter 3

Hunting for Dark Matter and New Physics with (a) GECCO

This chapter was adapted from “Hunting for Dark Matter and New Physics with (a) GECCO ” which was posted to arXiv (2101.10370) 25 January 25, 2021 and is currently being submitted to Physical Review Letters D. This work was done in collaboration with Adam Coogan, Alexander Moiseev, and Stefano Profumo.

3.1 Introduction

It is in not an overstatement that the MeV gamma-ray energy range remains one of the least explored frontiers in observational astronomy, with important implications for the understanding of high-energy astrophysical phenomena. With the most recent data dating back several decades, the photon band in between hard x-rays and the gamma rays detectable with the Fermi Large Area Telescope quite literally offers

some of the richest opportunities for discovery across the electromagnetic spectrum. It is therefore not a surprise that much activity has resumed in recent years around a next-generation MeV telescope. Without attempting to be exhaustive, a partial list of such missions under consideration, in no special order, includes AdEPT [138], AMEGO [179], eASTROGAM [229]¹, MAST [101], PANGU [248, 247] and GRAMS [21, 20].

The scientific significance of a new space-borne observatory in the MeV range includes a very broad range of topics such as identifying the hadronic versus leptonic nature and the acceleration processes underpinning jets outflows, studying the role of magnetic fields in powering the jets associated with gamma-ray bursts, pinning down the sources of gravitational wave events, understanding the electromagnetic counterparts of astrophysical neutrinos. Lower energy phenomena will also be clarified by new capabilities in the MeV: for instance, cosmic-ray diffusion in interstellar clouds, and the role cosmic rays play in gas dynamics and wind outflows, as well as nucleosynthesis and chemical enrichment via the study of nuclear emission lines.

Here, we focus on a proposed mid-size class mission, the Galactic Explorer with a Coded Aperture Mask Compton Telescope (GECCO) and consider its capabilities in the search for new physics beyond the Standard Model. We describe GECCO in some detail in the following section 3.2. We then explore GECCO's potential in searching for dark matter annihilation and decay for dark matter particle masses in the MeV range in section 3.3; in discovering the products of Hawking evaporation of primordial black holes in section 3.4 (see also Ref. [83]); and in identifying the origin of the 511 keV

¹This has since been scaled back to All-Sky-ASTROGAM [172].

emission line from the Galactic Center (section 3.5).

3.2 The Galactic Explorer with a Coded Aperture Mask Compton Telescope

The Galactic Explorer with a Coded Aperture Mask Compton Telescope (GECCO) is a novel concept for a next-generation γ -ray telescope that will cover the hard x-ray to soft γ -ray region, and is currently being considered for a future NASA Explorer mission [183]. GECCO will conduct high-sensitivity measurements of the cosmic γ -radiation in the energy range from 50 keV to ~ 10 MeV and create intensity maps with high spectral and spatial resolution, with a focus on the separation of diffuse and point-source components. Its science objectives are focused on understanding the nature, composition and fine structure of the inner Galaxy, discernment of the origin of the positron annihilation 511 keV line, identification and precise localization of gravitational wave and neutrino events, and resolving Galactic chemical evolution and sites of explosive elements synthesis by precise measurements of nuclear lines topography. As we show in this study, GECCO's observational capabilities will be of paramount importance for e.g. disentangling astrophysical and dark matter explanations of emission from the Galactic Center and potentially providing a key to discovering as-of-yet unexplored dark matter candidates [184].

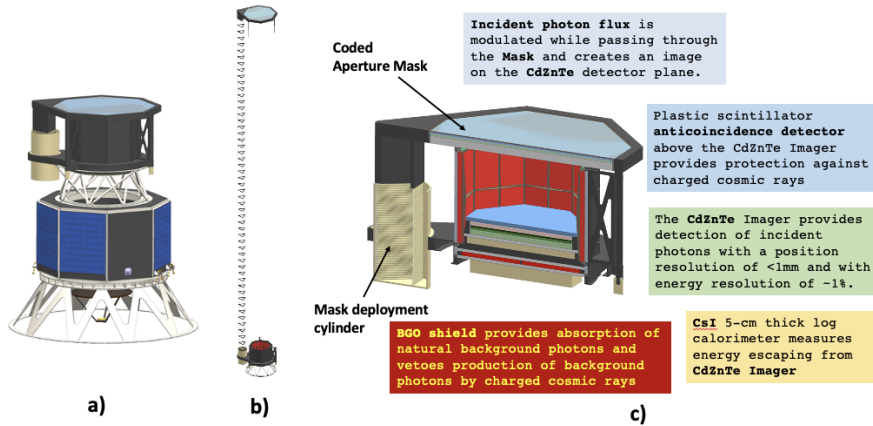


Figure 3.1: GECCO design concept: a) with mask in stowed position and notional spacecraft bus; b) with mask in deployed position; c) cutaway. [183]

3.2.1 Instrument concept

In many aspects, GECCO inherits from both SPI and IBIS of INTEGRAL [243], combining the scientific capabilities of both of them and focusing on effective and improved suppression of various backgrounds to enhance sensitivity. The unique concept of GECCO combines the advantages of two techniques: (i) the high angular resolution possible with coded-mask imaging, and (ii) a Compton telescope mode providing high-sensitivity measurements of diffuse radiation.

GECCO has an octagon shape with a medium diagonal of ~ 90 cm. The instrument is based on a novel CdZnTe imaging calorimeter and a deployable coded aperture mask. It also utilizes a heavy-scintillator (BGO) shield, a CsI calorimeter, and a plastic scintillator anti-coincidence detector (fig. 3.1). Learning the lessons from INTEGRAL's design and operation, background suppression is implemented in GECCO

(but not limited to) by the following:

1. The instrument design and material choice have been optimized to reduce secondary (background) photons produced by the instrument activation caused by charged cosmic rays;
2. The mechanical structure has been designed with predominant use of composite (non-metal) materials, for the same purpose;
3. Efficient active shielding of the detecting area;
4. Use of Low-Earth (550-600 km) equatorial orbit (<5 degrees declination) to minimize the time spent in the South Atlantic Anomaly, as well as to maximize geomagnetic cutoff on the spacecraft orbit.

The CdZnTe imaging calorimeter operates in GECCO as a standalone Compton telescope [46]. The angular resolution for a Compton telescope has intrinsic limitations on the order of a degree (depending on the scatterer material and incident photon energy) due to a Doppler broadening of the incident photon direction induced by the velocity of the electron where the Compton scattering occurred. A coded-aperture mask can provide potentially as high as desired angular resolution, depending on the distance between the coded mask and the focal plane detector, at the expense of a reduced field of view. This distance is constrained by available space, in turn usually limited by the launcher shroud dimensions.

An attractive option to increase the distance between the mask and the detector is to deploy the coded mask after reaching orbit; however in this configuration the

instrument aperture will be exposed to side-entering background radiation, which can potentially decrease the signal-to-noise ratio. GECCO has a coded mask deployable to 20 meters and solves the problem of side-entering background by selecting the events whose Compton-reconstructed direction points to the coded mask location. This is a unique feature of GECCO which greatly improves its angular resolution while maintaining a high signal-to-noise ratio.

Another promising approach to increase the instrument sensitivity is to exploit a coded mask capability of nearly-perfect subtraction of the uniform background, or any other background with known structure.

The BGO shield effectively protects the CdZnTe imaging calorimeter from side-entering photons, both natural and artificial, i.e. produced in the spacecraft by incident cosmic rays. It also serves as a powerful gamma-ray burst monitor.

The coded-aperture mask is covered by a plastic scintillator detector which vetoes secondary photons which can be created by cosmic rays in the mask material. Another thin plastic scintillator detector is placed on top of the CdZnTe imaging calorimeter to veto charged cosmic rays, which otherwise could be detected.

3.2.2 Operating principles and performance

The CdZnTe Imaging Calorimeter, acting as a standalone Compton telescope with a large field-of-view, enables the coarse-scale measurement of “total” diffuse+point source emission, and also locates point sources with limited angular resolution. The coded-aperture mask provides detection and localization of point sources, otherwise

unresolved, with sub-arcminute angular resolution. With combined “mask + Compton” operation, GECCO will separate diffuse and point-source components in Galactic gamma-radiation with high sensitivity [208]. An iterative analysis approach will enable revealing faint sources and their characteristics as well as measuring actual diffuse radiation.

GECCO can operate in either scanning or pointed mode. In scanning mode, it will observe the Galactic Plane. It will change to pointed mode to either increase observation time for special regions of interest, (e.g. the Galactic Center) or to observe transient events such as flares of various origins or gamma-ray bursts.

The expected GECCO performance is as follows: energy resolution $< 1\%$ at $0.5 - 5$ MeV, angular resolution ~ 0.5 arcmin in mask mode with 5° field-of-view, and $3 - 5^\circ$ in the Compton mode with $\sim 40^\circ$ field-of-view. The effective area varies from 200 cm^2 to $\sim 2000 \text{ cm}^2$ depending on the energy and observation mode.

3.2.3 Instrument Sensitivity

The determination (either by calculations or simulations) of the future mission’s sensitivity is far from trivial, and it always includes a number of critical assumptions. Some of the inputs to the sensitivity estimate are not well known, or not known at all in the early stages of the instrument development. However, as the mission progresses, especially during orbital operation, the assessment of the sensitivity gradually increases due to better understanding of all the critical inputs, and especially due to continuously improving data analysis. Nevertheless, because GECCO’s sensitivity is a

key parameter for the content of this paper, we present here initial sensitivity estimates for GECCO, emphasizing how particular design specifics contributed to the sensitivity improvement.

We separately analyze the instrumental sensitivity in three distinct modes of observation. The first one is the Compton-only mode, which is not especially relevant to the subject of this paper because, while providing capability to measure diffuse radiation, it has a relatively poor angular resolution of a few degrees. The two other modes correspond to measurements employing the coded-aperture mask, which will be used in the observations proposed in this paper. Usually the aperture of the coded-aperture mask instrument is shielded from side-entering radiation (diffuse radiation, all celestial sources, Earth limb, etc.) by either active, or passive layers of material [234, 235]. Such design places the limits on the distance between a coded aperture mask and a focal plane detector due to the spacecraft constraints, limiting the instrumental angular resolution. In GECCO, the coded aperture mask is deployed at 20 m from the detector, yielding higher angular resolution but at the same time creating a problem of side entering background.

The first mask mode for GECCO can be called a *classical* coded mask mode, when the source image on the focal-plane detector (CdZnTe ImCal for GECCO) is deconvoluted with the mask pattern. Useful details of the coded mask operation and its sensitivity can be found in e.g. [216] and [63]. We will leave aside all the issues of the coded mask optimization and effects of imperfections in the mask design, fabrication and analysis issues, and summarize them all in applying a factor of 0.8 (coding power)

to the final sensitivity. Coded masks provide excellent subtraction of the diffuse, spatially uniform background by applying a balanced convolution: the imaging of the same celestial source through a transparent and opaque mask elements provides simultaneous measurement of the background and a source, and a background contribution can be almost completely eliminated. We note, however, that a highly uniform background is a unique situation, which can potentially happen only at high-latitude directions. Non-uniform side-entering background, in particular caused by the instrument structure activation, arguably the most difficult background to control, can potentially be reduced because it is also not modulated by the mask. This is a difficult but doable task, and we anticipate to reach a solution later in the project development. It is important to notice that neither the angular resolution, nor the energy resolution affect the sensitivity in the classical mask-only data analysis, as the latter is a direct result of the mask and detector design, the system's effective area, and the analysis specifics.

Currently we assume for GECCO the Low-Earth equatorial orbit (LEO) with orbital period ~ 91 min, where a background will be rapidly changing. This is where the unique feature of combined Compton-Mask telescope GECCO comes to the play: all radiation in the GECCO FoV (practically unobscured by the deployed Mask) is mapped by the CdZnTe Imaging Calorimeter serving as a Compton telescope, with angular resolution (ARM) 3-5 degrees and effective area from $\sim 200 \text{ cm}^2$ to $\sim 1500 \text{ cm}^2$ (it is larger for the Mask-only mode). This includes practically all radiation, coming from a sky (diffuse and the sources) and from the instrument structure (activation and prompt radiation which was missed by the Anti-Coincidence Detector). Collecting these

spacecraft-position dependent map of all side-entering background, which will be used in the Mask analysis. Similar analysis for IBIS was successfully used in Ref. [156], yielded improvement of the sensitivity by $\sim 44\%$. This is a very complicated analysis and certainly cannot be performed for GECCO until we will start obtaining real data. Important contribution to the background in the Mask data analysis comes from non-uniform response of the CdZnTe Imaging Calorimeter, but accurate pre-flight calibration and development of the flight performance monitoring procedure will allow to significantly reduce it.

GECCO's unique concept of a Compton-plus-Coded Mask telescope provides an opportunity to reduce side-entering background by using for the image reconstruction only the photons which passed Compton reconstruction by the CdZnTe Imaging Calorimeter, and whose event circle intersects with the Mask position (see fig. 3.2). Originally this was considered the main method to work with the deployed mask, however this approach has higher low-energy limit (200-300 keV) compared with the Mask-only mode (50-100 keV). Fig. 3.2 illustrates this case. The blue bold-dashed line shows an incident photon which passed (and so was modulated) through the Mask. Dotted lines show the Compton-scattered photon which was detected by the detector and its incident direction was reconstructed as a blue event circle. This reconstructed circle geometrically intersects with the Mask (red arc), and this is a good event which will be included in the Mask image reconstruction. We note that the width of the circle is the angular resolution of the Compton reconstruction (ARM). The second incident photon shown as a dark-red line does not go through the Mask, but the reconstructed

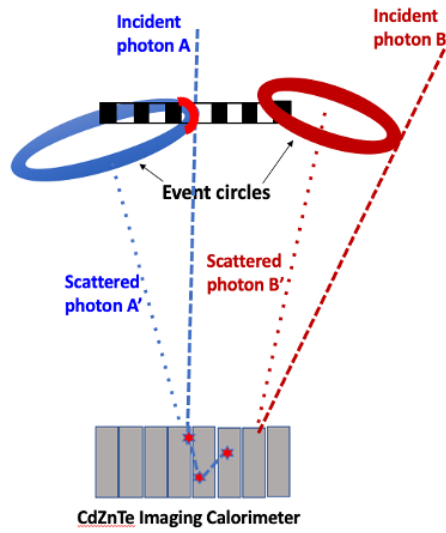


Figure 3.2: Backgrounds in the Compton-Mask combined analysis. The signal event is shown in blue, while the background event is shown in dark red. Dashed lines show the photons' incident direction, while the dotted lines show the reconstructed direction of Compton-scattered photons. The rings illustrate the solid angle of background acceptance. The red arc shows the intersection of the reconstructed event circle with the Mask position for signal events. [183]

event circle does intersect with the Mask, and so this event will be included in the Mask image reconstruction, representing a background event. As a result, the background for this analysis will consist of all celestial and artificial photons which fall in the Compton event circle.

We can illustrate the resulting sensitivity for an incident photon energy of 1 MeV: The sensitivity S can be calculated with the following expression:

$$S = \frac{E}{2 \times A \times T} \left(n^2 + n \times \sqrt{n^2 + 4 \times B} \right), \quad (3.1)$$

where B is the number of background counts, $B = F_{\text{bckg}} \times \Delta\Omega \times T \times A_{\text{eff}}$, E is the incident photon energy, n is a detection confidence level expressed in number of σ , F_{bckg} is the total background flux, $\Delta\Omega$ is a solid angle corresponding to the event circle (as shown in fig. 3.2), and T is the observation time. We use the measured diffuse background F_{bckg} from [133] and [5] and applied an additional “safety” factor of 3 to account for unknown contributors such as activation. We use the very conservative numbers $A_{\text{eff}} = 1,380 \text{ cm}^2$, $\text{ARM} = 60$, $\sigma = 3$, $T = 10^6 \text{ s}$, $\Delta\Omega = 0.14 \text{ sr}$, and arrived to the continuum sensitivity $S \simeq 1.0 \times 10^{-5} \text{ MeV cm}^{-2} \text{ s}^{-1}$. With rather realistic analysis improvements it is feasible to reach sensitivities on the order of $10^{-6} \text{ MeV cm}^{-2} \text{ s}^{-1}$ or better, subject to future project developments. We want to stress that this is a very conservative analysis. Thus, the GECCO performance is particularly promising for searching for dark matter particles with O(MeV)-scale masses as well as for evaporating primordial black holes with O(10^{17} g) masses, as explained in the remainder of this work.

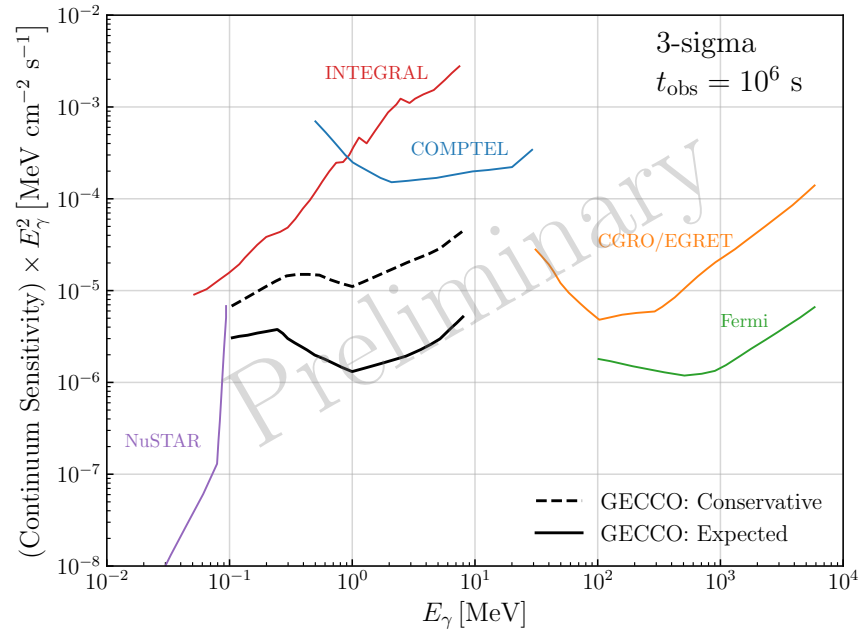


Figure 3.3: A (preliminary) comparison of instrumental sensitivities with GECCO's projected sensitivity, as calculated via Eq. (3.1), see the text for details.

3.3 Searches for Annihilating and Decaying Sub-GeV Dark Matter

In this section we demonstrate that GECCO will be especially well-suited to search for particle dark matter (DM) in the MeV mass range. After reviewing DM indirect detection and explaining how we set limits using existing gamma-ray data and make projections for GECCO, we study the instrument’s capabilities to detect the annihilation and decay of DM into specific Standard-Model final states. We also project GECCO’s sensitivity reach for three specific, well-motivated DM models: one with an additional scalar mediating the DM’s interaction with the Standard Model, a second one with a vector mediator and a third one in which the DM is an unstable right-handed neutrino. Throughout we utilize our code `hazma`, which we previously developed to analyze DM models producing MeV-scale gamma rays [84].

3.3.1 Indirect Detection Constraints and Projections

The prompt gamma-ray flux from DM annihilating or decaying in a region of the sky subtending a solid angle $\Delta\Omega$ is given by

$$\left. \frac{d\Phi}{dE_\gamma} \right|_{\bar{X}X}(E_\gamma) = \frac{\Delta\Omega}{4\pi m_\chi^a} \cdot \left[\frac{1}{\Delta\Omega} \int_{\Delta\Omega} d\Omega \int_{\text{LOS}} dl [\rho(r(l, \psi))]^a \right] \cdot \Gamma \cdot \left. \frac{dN}{dE_\gamma} \right|_{\bar{X}X}(E_\gamma), \quad (3.2)$$

where “LOS” indicates the integral along the observation’s direction line of sight. For decaying (annihilating) DM $a = 1$ ($a = 2$). The integral in the bracketed term ranges over lines of sight within a solid angle $\Delta\Omega$ from the target region direction. This is referred to as the \bar{D} factor for decaying DM and \bar{J} factor for annihilating DM. It is

proportional to the angle-averaged number of particles (pairs of particles) in the target available to decay (annihilate). The third term is the DM interaction rate. This is $1/\tau$ for decaying DM, where τ is the DM’s lifetime. For annihilating DM, $\Gamma = \langle\sigma v\rangle_{\bar{\chi}\chi}/2f_\chi$, where $f_\chi = 1$ if the DM is self-conjugate and 2 otherwise (we assume the latter in this work). The last term is the photon spectrum per decay or annihilation. The calculation of this spectrum in `hazma` accounts for the radiative decay chains of the charged pion and muon as well as model-dependent final-state radiation from annihilations that produce electrons, muons and pions relevant for studying specific particle DM models.

To connect the gamma-ray flux with existing and future gamma-ray observations, we define the “convolved” flux

$$\left.\frac{d\bar{\Phi}}{dE_\gamma}\right|_{\bar{\chi}\chi}(E_\gamma) \equiv \int dE'_\gamma R_\epsilon(E_\gamma|E'_\gamma)\frac{d\Phi}{dE'_\gamma}(E'_\gamma). \quad (3.3)$$

In the equation above, $R_\epsilon(E_\gamma|E'_\gamma)$ is the telescope’s energy resolution function, specifying the probability that a photon with true energy E'_γ is detected with energy E_γ . This is well-approximated as a normal distribution $R_\epsilon(E_\gamma) = N(E_\gamma|E'_\gamma, \epsilon E'_\gamma)$ [55], which defines ϵ .² To set an upper limit on the DM contribution to gamma-ray observations we perform a χ^2 test with the quantity

$$\chi_{\text{obs}}^2 = \sum_i \left(\frac{\max[\bar{\Phi}_{\bar{\chi}\chi}^{(i)} - \Phi_{\text{obs}}^{(i)}, 0]}{\sigma^{(i)}} \right)^2, \quad (3.4)$$

where the sum ranges over energy bins, the flux in the numerator is the integral “convolved” flux over bin i and the denominator is the upper error bar on the observed

²Note that the energy resolution of detectors is also sometimes given in terms of the full width at half maximum of this distribution.

integrated flux. Including an explicit background model would introduce significant systematic uncertainties since there is a paucity of MeV gamma-ray data, and in practice we expect it would only strengthen our constraints by less than an order of magnitude [109].³

We project GECCO’s discovery reach by finding the smallest dark matter interaction rate such that the signal-to-noise for different targets is significant at the 5σ level. We define the signal-to-noise ratio as

$$\frac{S}{N} \equiv \max_{E_{\min}, E_{\max}} \frac{N_{\gamma|\bar{\chi}\chi}}{\sqrt{N_{\gamma|\text{bg}}}}, \quad (3.5)$$

where the numerator and denominator contain the number of signal and background photons respectively, and the energy window used for the analysis is chosen to maximize the ratio. Note that this projection procedure assumes the errors on GECCO’s observations will be purely statistical. In lieu of a detailed understanding of GECCO’s systematics, in addition to our fiducial projections we show how they would vary if $N_{\gamma|\text{bg}}$ was increased by a factor of 25.

The number of signal photons depends on the energy window along with GECCO’s observing time and effective area:

$$N_{\gamma|\bar{\chi}\chi} = \int_{E_{\min}}^{E_{\max}} dE_{\gamma} T_{\text{obs}} A_{\text{eff}}(E_{\gamma}) \frac{d\bar{\Phi}}{dE_{\gamma}}. \quad (3.6)$$

While T_{obs} is in general energy-dependent, we fix it to $10^6 \text{ s} \approx 11.6 \text{ days}$. To model the background in the directions of Draco and M31 we utilize a power law fit to high-latitude

³For final states containing monochromatic gamma rays the resulting constraints depend on the binning of the data. In the figures that follow we manually smooth out constraints in this case to account for different possible ways the data could have been binned.

COMPTEL and EGRET data [41]:

$$\frac{d^2\Phi}{dE_\gamma d\Omega} = 2.74 \times 10^{-3} \left(\frac{E}{\text{MeV}} \right)^{-2} \text{ cm}^{-2} \text{ s}^{-1} \text{ sr}^{-1} \text{ MeV}^{-1}. \quad (3.7)$$

For the Galactic Center we adopt the model from Ref. [32]. This consists of several spectral templates computed with GALPROP⁴ [226] and an analytic component, tailored to fit existing gamma-ray data in the inner part of the Milky Way.⁵ The background fluxes per solid angle can be converted to photon counts using eq. (3.6).

We note that a possible point-source contribution contamination from Sag A* associated with 4FGL J1745.6–2859 is not excluded, but recent studies show that it would significantly dimmer than the extended emission we consider in searching for dark matter in the Galactic center region (see e.g. [60] and references therein).

The \bar{J} and \bar{D} factors for the GECCO targets are shown in table 3.1. These are derived from fits of dark matter density profiles to measurements of the targets rotation curves, surface brightnesses and velocity dispersions. We employ a Navarro-Frenk-White (NFW) density profile [187] for all targets and additionally consider an Einasto profile [106] for the Galactic Center to bracket the uncertainties in our analysis stemming from assumptions about the dark matter distribution. For our analysis of annihilating DM we select a 1′ observing region (roughly GECCO’s angular resolution) to maximize the signal-to-noise ratio. In the case of decaying DM we instead find the best strategy is to use a larger 5° field of view, since the \bar{D} factor depends much less strongly on the observing region’s size. The observing regions and \bar{J}/\bar{D} factors used to

⁴<http://galprop.stanford.edu>

⁵This model’s flux is approximately the one in eq. (3.7) rescaled by a factor of 7.

collect existing gamma-ray data are presented in table 3.2.

Secondary photons are also produced by dark matter processes that create electrons and positrons. These can produce energetic photons via inverse-Compton scattering against ambient CMB, starlight and dust-reprocessed infrared photons [77, 79]. Their spectrum, for upscattered initial photon energy E_γ peaks near $E_{\text{peak}} \simeq E_\gamma (E_e/m_e)^2 \simeq E_\gamma (m_{\text{DM}}/(10 m_e))^2$ which for sub-GeV DM masses and for the highest energy background photon from starlight ($E_\gamma \sim 1$ eV) gives $\lesssim 100$ keV upscattered photon energy, thus well below GECCO’s expected energy threshold. Also, the calculation of the secondary radiation carries inherently difficult systematics ranging from the effects of diffusion to the morphology of the background radiation fields. While Ref. [72] recently studied constraints from INTEGRAL on secondary photons produced by MeV-scale DM, we omit these from our plots. Uncertainties in the astrophysics of secondary emission can relax their bounds by an order of magnitude, bringing them into line with constraints on primary emission obtained using other telescopes.

Observations of the cosmic microwave background (CMB) constrain the amount of power DM annihilations and decays are allowed to inject in the form of ionizing particles during recombination [67, 189, 121, 218, 10]. `hazma` contains functions for calculating this constraint for annihilating DM. To review, given a DM model the constraint is set by

$$p_{\text{ann}} = f_{\text{eff}}^\chi \frac{\langle \sigma v \rangle_{\bar{\chi}\chi, \text{CMB}}}{m_\chi}, \quad (3.8)$$

where f_{eff}^χ is the fraction of energy per DM annihilation imparted to the plasma and p_{ann} is an effective parameter measured from observations bounding the energy that

can be injected per unit volume and time. In turn f_{eff}^χ depends on the photon and electron/positron spectrum per DM annihilation. When DM annihilation is velocity-suppressed (as in the Higgs portal model we will consider in section 3.3.3), the present-day thermally-averaged self-annihilation cross section is related to the one in eq. (3.8) by the squared ratio of the DM velocity at present and at recombination, $(v_{\chi,0}/v_{\chi,\text{CMB}})^2$. Computing $v_{\chi,\text{CMB}}$ requires the DM’s kinetic decoupling temperature as input, which typically falls between $(10^{-6} - 10^{-4})m_\chi$ [109]. While this can be calculated self-consistently for a given DM model, we instead leave it as a parameter in our analysis and fix its value when necessary. For DM masses above ~ 1 MeV the constraints on p -wave annihilation are found to be weaker than for s -wave annihilation. For constraints on decaying DM we reuse the results from Ref. [220].

3.3.2 Model-independent projections

We first consider GECCO’s discovery reach for “simplified” dark matter models where the dark matter particles annihilate or decay into exclusive, single final states, namely the diphoton, dielectron and dimuon final states.⁶ The existing gamma-ray constraints and GECCO projections on the branching fraction times self-annihilation cross section (for annihilating DM) are shown in fig. 3.4 and on the lifetime (for decaying DM) in fig. 3.5. In the figures we shade regions of parameter space ruled out by observations taken with previous or existing telescopes, namely COMPTEL (see ref. [145]), EGRET [224], Fermi-LAT [7], and INTEGRAL [48] (see Tab. 3.2 for details on the re-

⁶The results for annihilation into two pions are weaker than the results for the dimuon final state by an order one factor, but otherwise nearly identical, so we do not plot them separately.

Target	$\bar{J}(1')$	$\bar{J}(5^\circ)$	$\bar{D}(1')$	$\bar{D}(5^\circ)$
Galactic Center (NFW)	6.972×10^{32}	1.782×10^{30}	4.84×10^{26}	1.597×10^{26}
Galactic Center (Einasto)	5.987×10^{34}	4.965×10^{31}	4.179×10^{27}	2.058×10^{26}
Draco (NFW)	3.418×10^{30}	8.058×10^{26}	5.949×10^{25}	1.986×10^{24}
M31 (NFW)	1.496×10^{31}	1.479×10^{27}	3.297×10^{26}	4.017×10^{24}

Table 3.1: \bar{J} and \bar{D} factors for various circular targets, in units of $\text{MeV}^2 \text{cm}^{-5} \text{sr}^{-1}$ and $\text{MeV cm}^{-2} \text{sr}^{-1}$ respectively. The dark matter profile parameters are taken from the Ref. [92] (GC, NFW), Ref. [92] (GC, Einasto), Ref. [99] (Draco, NFW), and Ref. [126] (M31, NFW). For the Milky Way, we use the values from Table III of Ref. [92]. The Einasto profile parameters are adjusted within their 1σ uncertainty bands to maximize the \bar{J} and \bar{D} factors. For all other targets we use the parameters' central values. The distance from Earth to the Galactic Center is set to 8.12 kpc [4, 92]. For reference, the angular extents of the $1'$ and 5° regions are $2.658 \times 10^{-7} \text{sr}$ and $2.39 \times 10^{-2} \text{sr}$ respectively.

Experiment	Region	$\Delta\Omega$ [sr]	\bar{J}	\bar{D}
COMPTEL [145]	$ b < 20^\circ, l < 60^\circ$	1.433	9.308×10^{28}	4.866×10^{25}
EGRET [224]	$20^\circ < b < 60^\circ, l < 180^\circ$	6.585	6.265×10^{27}	1.71×10^{25}
Fermi [7]	$8^\circ < b < 90^\circ, l < 180^\circ$	10.82	8.475×10^{27}	1.782×10^{25}
INTEGRAL [48]	$ b < 15^\circ, l < 30^\circ$	0.5421	2.086×10^{29}	7.301×10^{25}

Table 3.2: \bar{J} and \bar{D} factors for observing regions in the Milky Way used by past experiments, in units of $\text{MeV}^2 \text{cm}^{-5} \text{sr}^{-1}$ and $\text{MeV cm}^{-2} \text{sr}^{-1}$ respectively. The regions are specified in Galactic coordinates. We again use the NFW profile parameters from Table III of ref. [92].

gion of interest and resulting assumed integrated dark matter density). We also indicate constraints from CMB distortions with dashed and dot-dashed black lines (the regions excluded are above those lines).

The GECCO sensitivity is shown for four distinct cases, listed here from top to bottom in the order the lines appear in fig. 3.4 (the order is inverted for the lifetime in the case of decay shown in fig. 3.5): the grey line corresponds to observations, within an angular region of $1'$, of the Draco dSph; the magenta line for observations of M31, within the same angular region of $1'$; finally the brown and purple lines correspond to observations of the Galactic Center, again within $1'$, assuming an NFW profile (brown line) and an Einasto profile (purple line). In all instances, to bracket GECCO's potential systematics, as discussed below eq. (3.5) we include a band showing how the limit would

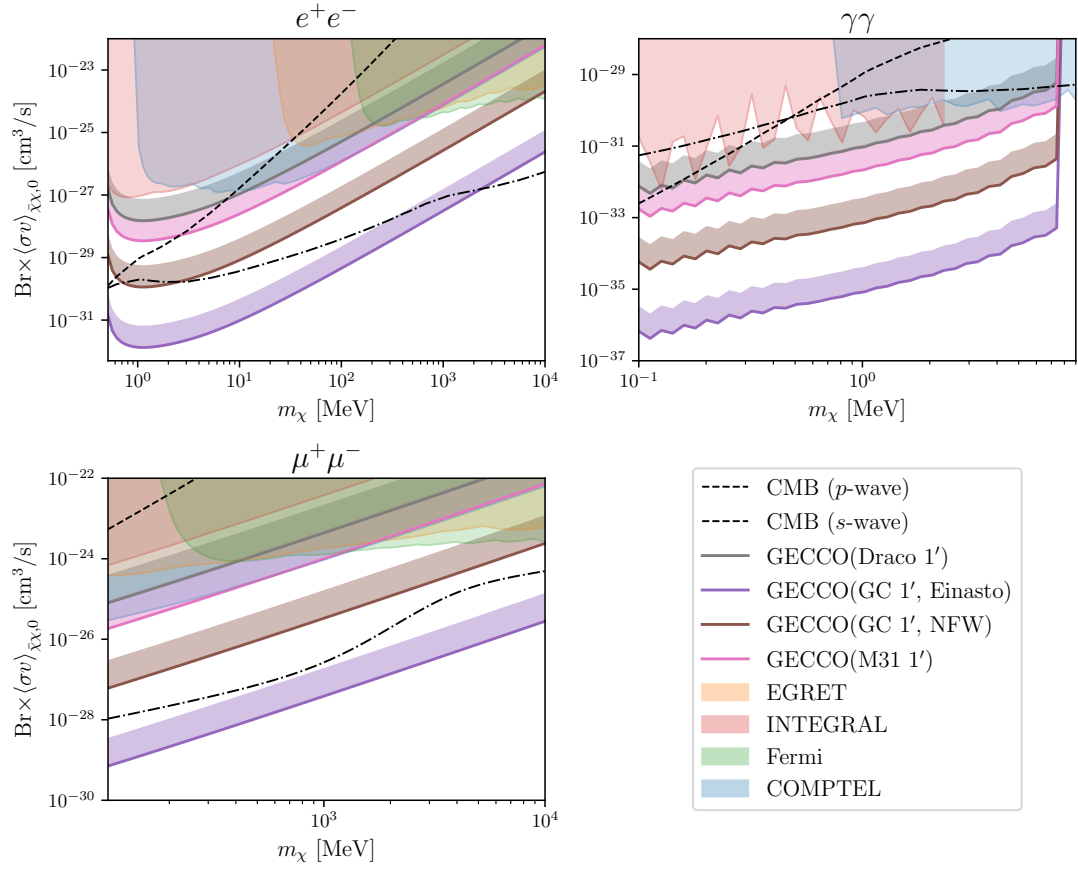


Figure 3.4: Projected constraints on annihilation into different final states (solid lines). To account for the unknown systematics of GECCO, the surrounding bands show how the projections would change if the background photon counts were a factor of 25 higher than the fiducial value. The shaded regions show constraints from existing gamma ray data. The dashed black line shows the CMB constraint assuming the DM annihilation are p -wave and have a kinetic decoupling temperature of $10^{-6} m_\chi$; higher kinetic decoupling temperatures would give weaker constraints. The dot-dashed line gives the CMB constraint for s -wave DM annihilations.

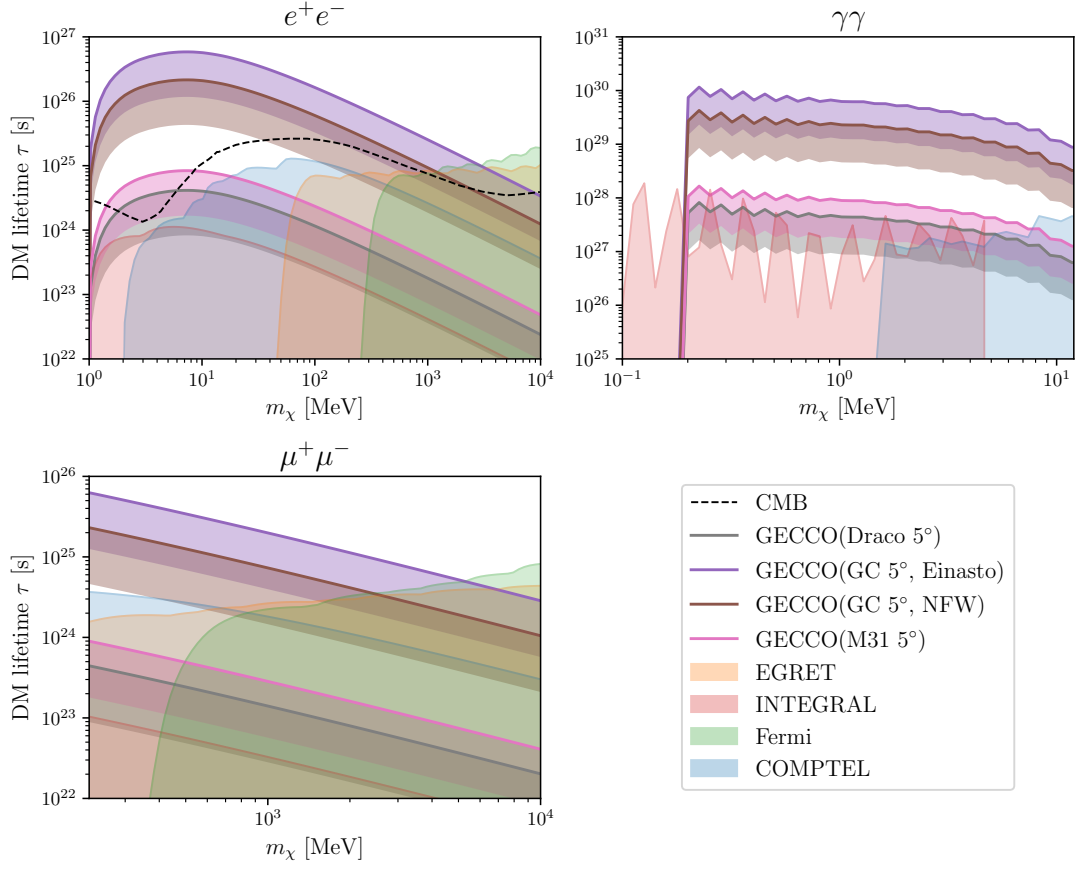


Figure 3.5: Constraints on the DM particle’s lifetime for decays into different final states (solid lines). To account for the unknown systematics of GECCO, the surrounding bands show how the projections would change if the background photon counts were a factor of 25 higher than the fiducial value. The CMB constraint on decays into e^+e^- is taken from Ref. [220]. While constraints for the $\mu^+\mu^-$ final state are not provided, we estimate they lie around $10^{24} - 10^{25}$ s since the subsequent muon decays produces electrons with energy $\sim 1/3m_\chi$. The constraint for decays into $\gamma\gamma$ lies below the axis range.

weaken if the background photon count were 25 times larger than the fiducial value.

We find that the greatest gains a telescope such as GECCO will bring in the search for MeV dark matter are for final states producing monochromatic gamma ray (i.e. lines). In this case the improvements to the sensitivity across the range between 0.1 and 10 MeV are forecast to be as large as four orders of magnitude in the annihilation rate, or over two orders of magnitude in lifetime. Signals will potentially be visible across different targets. The entire parameter space testable with GECCO is compatible with constraints from CMB for p -wave DM annihilations. GECCO observations have the potential to discover DM annihilating in an s -wave to two photons. While the s -wave CMB bounds for the dielectron and dimuon final states are more stringent, GECCO still has the potential to uncover DM annihilation in the Galactic Center depending on the DM mass and spatial distribution. We note that the jagged lines for the GECCO predicted sensitivity are due to the energy window optimization described below eq. (3.5).

The electron-positron final state also offers highly promising prospects, especially at low masses around 1-10 MeV, with improvements to the current sensitivity of up to five orders of magnitude in annihilation rate (two in lifetime) but will improve by almost two orders of magnitude even at large masses, around 10 GeV; detection of an annihilation signal outside the Milky Way center will be possible again, but only for masses below 30 MeV or so, with similar prospects for decay.

Finally, in the muon pair case, the optimal dark matter candidate would have a mass of around the muon mass, offering an improvement of three orders of magnitude

for annihilation, and over one in decay. However, in the $\mu^+\mu^-$ case current constraints exclude the possibility of detecting a signal from M31 or Draco, in either annihilation or decay.

In what follows we illustrate with explicit model realizations the physics reach of GECCO for the detection of dark matter annihilation in the Higgs portal (section 3.3.3) and vector portal/dark photon (section 3.3.4) cases, and of dark matter decay in the case the right-handed neutrino dark matter (section 3.3.5).

3.3.3 Model Example: Higgs Portal

In this model, we extend the Standard Model by adding a new scalar singlet \tilde{S} . The dark matter interacts only with this scalar, through a Yukawa interaction: $\mathcal{L} \supset g_{S\chi}\tilde{S}\bar{\chi}\chi$. The new scalar mixes with the real neutral scalar component of the Higgs with a mixing angle θ providing a portal through which the dark matter can interact with the Standard Model.⁷ This results in a Lagrangian density of the form:

$$\begin{aligned} \mathcal{L} = & \mathcal{L}_{\text{SM}} + \bar{\chi}(i\not{\partial} - m_\chi)\chi - \frac{1}{2}S(\partial^2 + m_S^2)S \\ & - g_{S\chi}(h \sin \theta + S \cos \theta)\bar{\chi}\chi + (h \cos \theta - S \sin \theta) \sum_f m_f \bar{f}f + \dots \end{aligned} \quad (3.11)$$

⁷This is achieved by modifying the scalar potential to be:

$$V(\tilde{S}, H) = -\mu_H^2 H^\dagger H + \lambda(H^\dagger H)^2 + \frac{1}{2}\mu_S^2 \tilde{S}^2 + g_{SH}\tilde{S}H^\dagger H + \dots \quad (3.9)$$

where H is the SM Higgs doublet, \tilde{S} is a new, neutral scalar singlet and the \dots represent interaction terms with more than a single \tilde{S} . After diagonalizing the scalar mass matrix we find two neutral scalars h and S which are related to the original scalars through a mixing angle:

$$\begin{pmatrix} \tilde{h} \\ \tilde{S} \end{pmatrix} = \begin{pmatrix} \cos \theta & -\sin \theta \\ \sin \theta & \cos \theta \end{pmatrix} \begin{pmatrix} h \\ S \end{pmatrix}. \quad (3.10)$$

where f is a massive SM fermion and the \dots contain pure scalar interactions. This Lagrangian density is only valid for energies $E \gtrsim \Lambda_{\text{EW}}$ while our interest lies in sub-GeV energies. To obtain a Lagrangian valid for sub-GeV energies, we first need to find a Lagrangian valid above the QCD confinement scale and then match onto the chiral Lagrangian (see Ref. [206] for a detailed review of chiral perturbation theory). We omit the details here (to be provided in a forthcoming paper) and simply give the result:

$$\begin{aligned}
\mathcal{L}_{\text{Int}(S)} = & \frac{2 \sin \theta}{3v_h} S [(\partial_\mu \pi^0)(\partial^\mu \pi^0) + 2(\partial_\mu \pi^+)(\partial^\mu \pi^-)] \\
& + \frac{4ie \sin \theta}{3v_h} S A^\mu [\pi^-(\partial_\mu \pi^+) - \pi^+(\partial_\mu \pi^-)] \\
& - \frac{m_{\pi^\pm}^2 \sin \theta}{3v_h} \left(\frac{5}{2} S + \frac{\sin \theta}{3v_h} S^2 \right) [(\pi^0)^2 + 2\pi^+\pi^-] \\
& - \frac{10e^2 \sin \theta}{27v_h} S \pi^+\pi^- A_\mu A^\mu \\
& - g_{S\chi} S \bar{\chi}\chi - \sin \theta S \sum_{\ell=e,\mu} \frac{y_\ell}{\sqrt{2}} \bar{\ell}\ell.
\end{aligned} \tag{3.12}$$

In the equation above, we have made the redefinition $g_{S\chi} \cos \theta \rightarrow g_{S\chi}$. The terms relevant for indirect detection are those involving an S field interacting with pions (along with a photon), leptons or dark matter. The $S^2\pi\pi$ and $S\pi\pi AA$ terms are subdominant since they have additional factors of $\sin \theta$, the Higgs vev and/or the electron charge.

As discussed in our previous work [84], this leading-order chiral perturbation theory approach has a limited regime of validity. To avoid the $f_0(500)$ resonance [193] and the resulting final-state interactions between pairs of pions as well as $(500 \text{ MeV}/\Lambda_{\text{QCD}})^2 \sim 20\%$ corrections from the next-to-leading order chiral Lagrangian [195], we restrict $m_\chi < 250 \text{ MeV}$ when the DM annihilates into SM particles, and $m_S < 500 \text{ MeV}$ when it predominantly annihilates into mediators.

The thermally-averaged DM self-annihilation cross section for this model is p -wave suppressed: $\langle\sigma v\rangle_{\bar{\chi}\chi} \propto T_\chi/m$ for low DM temperatures T_χ . Since this assumption holds for all our targets, under the assumption that the DM particles' speeds follow a Maxwell-Boltzmann distribution we can approximate $\langle\sigma v\rangle_{\bar{\chi}\chi} \propto \sigma_v^2$, where σ_v is the velocity dispersion in the target. We take $\sigma_v = 10^{-3} c$ for the Milky Way targets [56] and M31 [241] and $\sigma_v = 3 \times 10^{-5} c$ for Draco [177].⁸

The constraints from current gamma-ray data, our projections for GECCO's reach using different targets and the CMB bounds for this model are displayed in fig. 3.6, with two ratios of m_S to m_χ . We have rescaled the constraints on $\langle\sigma v\rangle_{\bar{\chi}\chi}$ for each target into constraints on $\langle\sigma v\rangle_{\bar{\chi}\chi,0}$, the thermally-averaged self-annihilation cross section in the Milky Way. GECCO's projected reach exceeds the CMB bound for all targets except Draco, on account of the p -wave suppression in the self-annihilation cross section. GECCO observations of M31 and the Galactic Center will improve over previous telescopes by one to four orders of magnitude.

An array of terrestrial, astrophysical and cosmological observations constrain this Higgs portal model (see e.g. Ref. [157]). Depending on the DM and mediator masses the most relevant ones for this work include rare and invisible decays of B and K mesons and beam dumps sensitive to visible S decays. How these complement indirect detection bounds depends strongly on whether the DM annihilates into mediator pairs ($m_\chi > m_S$, left panel) or SM particles ($m_\chi < m_S$, right panel). In the first case, the DM self-annihilation cross section scales as $\langle\sigma v\rangle_{\bar{\chi}\chi,0} \sim g_{S\chi}^4$. As a result, the conservative

⁸A more careful treatment would average over the position-dependent velocity distribution in the target. In the case of the Milky Way, this should only change our results by a factor of $\lesssim 2$ [41].

interpretation of other bounds on this model is that they do not constrain the strength of the possible gamma-ray signals. This is because all other constraints involve the coupling $\sin\theta$, and for each DM and mediator mass combination at least *some* values of $\sin\theta$ are allowed. In the left panel of the figure we show contours of constant $g_{S\chi}$ to give a sense of reasonable values of the cross section. GECCO observations of the Galactic Center will probe down to $g_{S\chi} \sim 5 \times 10^{-5}$ for low DM masses.

When the SS final state is not accessible, the DM's annihilations are strongly suppressed since the cross section scales as $\langle\sigma v\rangle_{\bar{\chi}\chi,0} \sim g_{S\chi}^2 \sin^2\theta y^2$, where $y \ll 1$ is the Yukawa for the heaviest-accessible final state. This means correspondingly large values of the couplings are required to give indirect detection signals. The red line in the right panel of the figure shows the DM self-annihilation cross section for $(g_{S\chi}, \sin\theta) = (4\pi, 1)$ (very roughly the maximum coupling values consistent with unitarity). GECCO can probe this cross section for most masses and targets we consider.

Each point in the $(m_\chi, \langle\sigma v\rangle_{\bar{\chi}\chi,0})$ plane corresponds to a range of possible $\sin\theta$ values. The lower end of this range is determined by setting $g_{S\chi} \sim 4\pi$ while the upper end is $\sin\theta = 1$. We can conservatively map constraints on the Higgs portal model at each point in this plane by checking whether *any* of the $\sin\theta$ values in this range are permitted. Applying this procedure using the constraints from [157] leads to the orange region in the right panel of fig. 3.6. At all points, these constraints are a few orders of magnitude more stringent than GECCO's discovery reach. This conclusion holds for other mediator masses $m_S > m_\chi$ above and below the resonance region around $m_S = 2m_\chi$.

To guide the eye, we also plot curves corresponding to values of the coupling that give the correct DM relic abundance. GECCO can discover this benchmark Higgs portal model when the mediator is lighter than the DM and decays into photons or electrons, depending on the observing region. For both DM-mediator mass ratios shown, the process relevant for the standard relic abundance calculation is $\bar{\chi}\chi \rightarrow SS$. While this is not kinematically permitted for $m_\chi < m_S$ when the DM is nonrelativistic, it contributes dominantly to the thermal average involved in the relic abundance calculation since annihilations into SM final states are Yukawa-suppressed, making this an example of forbidden DM [86]. Translating the value of $g_{S\chi}$ that gives the correct relic abundance for this scenario into $\langle\sigma v\rangle_{\bar{\chi}\chi,0}$ additionally requires fixing $\sin\theta$, which we set to 1 in the right panel of fig. 3.6.⁹ If the DM freezes out purely through annihilations into SM particles (as is the case for $m_S \gg m_\chi$), nonperturbatively large values of the DM-mediator coupling are required to give the correct relic abundance ($g_{S\chi} \gtrsim 100$), even for $\sin\theta = 1$.

Given that we do not know the thermal history of the universe before big bang nucleosynthesis (BBN), the thermal relic cross sections we show can be evaded. For example, if the DM freezes out over-abundantly before BBN ($m_\chi/20 \gtrsim T_{\text{BBN}} \sim 1 \text{ MeV}$), its density can be diluted through mechanisms like entropy injection into the SM bath via the decay of another heavy particle [120, 127, 134] or late-time inflation [89], which have been explored carefully in the context of weakly interacting massive particle DM. For DM whose thermal relic density is lower than the observed cosmological dark matter

⁹Note that there is a weak lower bound on $\sin\theta$ coming from requiring that the DM and mediator thermalize with the SM bath at early times.

density, the dark matter density can be increased through e.g. introducing a field that redshifts faster than radiation and dominates the universe’s energy density at early times [202, 93], or via non-thermal production. Detailed study of various ways of sidestepping the standard relic abundance constraints as well as a full relic abundance calculation that tracks the population of mediators falls outside the scope of this work.

3.3.4 Model Example: Dark Photon

Our vector-portal model is the well-known “dark photon” model in which we add a new $U(1)_D$ gauge group and charge the DM under this group. We connect the dark sector and SM sector by letting the $U(1)_D$ gauge boson mix with the Standard Model photon through $\frac{\epsilon}{2}V_{\mu\nu}F^{\mu\nu}$ where ϵ is a small mixing parameter and $V^{\mu\nu}$ and $F^{\mu\nu}$ are the dark photon and SM photon field strength tensors. The Lagrangian density is:

$$\mathcal{L} = \mathcal{L}_{\text{SM}} - \frac{1}{4}V_{\mu\nu}V^{\mu\nu} + \frac{\epsilon}{2}V_{\mu\nu}F^{\mu\nu} + \bar{\chi}(i\not{\partial} - m_\chi)\chi + g_{\chi V}V_\mu\bar{\chi}\gamma^\mu\chi \quad (3.13)$$

where V_μ is the dark-photon. The kinetic terms for the $U(1)$ fields are diagonalized by shifting the SM-photon field by $A_\mu \rightarrow A_\mu + \epsilon V_\mu$ and ignoring terms $\mathcal{O}(\epsilon^2)$. The result is that all electrically-charged SM fields receive a small dark charge and the DM receives a small electric charge. After integrating out the heavy SM field and matching onto the chiral Lagrangian, we end up with the following interaction Lagrangian between the dark photon and the light SM fields and meson:

$$\mathcal{L}_{V\text{-SM}} = -eV_\mu \sum_\ell \bar{\ell}\gamma^\mu\ell + i\epsilon eV_\mu[\pi^-\partial_\mu\pi^+ - \pi^+\partial_\mu\pi^-] - \frac{e^2}{32\pi^2}\epsilon^{\mu\nu\alpha\beta}F_{\mu\nu}V_{\alpha\beta}\left(\frac{\pi^0}{f_\pi}\right) \quad (3.14)$$

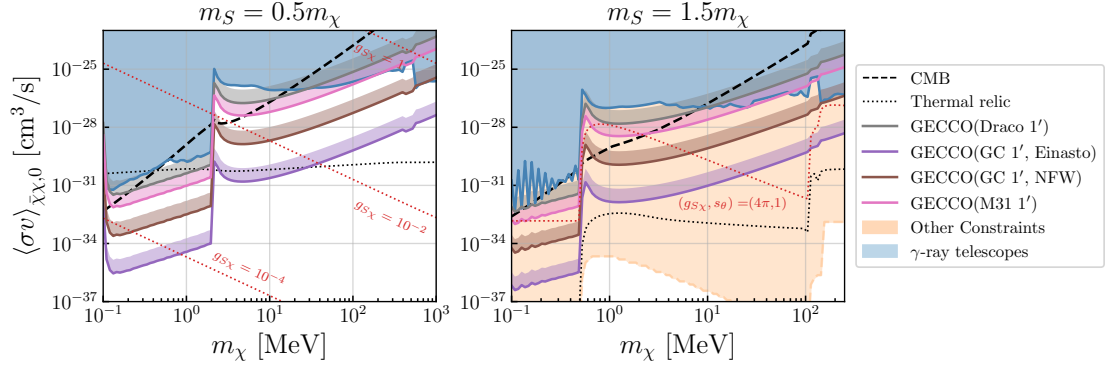


Figure 3.6: Constraints on the thermally-averaged DM self-annihilation cross section in the Milky Way for the Higgs portal model (solid lines). To account for the unknown systematics of GECCO, the surrounding bands show how the projections would change if the background photon counts were a factor of 25 higher than the fiducial value. The case where the indirect detection signal comes from annihilations into mediators (SM particles) is shown on the left (right). The thin red dotted lines are contours of constant coupling strength. The orange region in the right panel is a conservative exclusion region from experiments besides gamma-ray telescopes. The CMB constraint was computed assuming a kinetic decoupling temperature of $10^{-6} m_\chi$; taking this to be higher would weaken the constraint.

where ℓ is either the electron or muon. The first two terms come from the covariant derivatives of the leptons and charge pion. The last term is a shift in the neutral pion decay, stemming from the Wess-Zumino-Witten Lagrangian [240, 245].

In our analysis, we focus on the regime where the mediator is heavier than the dark matter mass, taking $3m_\chi = m_V$. With this choice, we are able to recycle previously studied constraints produced by non-astrophysical experiments. The strongest constraints on dark photon models for the masses we are interested in come from the B -factory BaBar [164] and beam-dump experiments such as LSND [12]. Studies using the datasets of these experiments were able to constraint the dark photon model by looking for the production of dark photons which then decay into dark matter (see, for example Ref. [33, 164, 155]); in the case of BaBar, the relevant process is $\Upsilon(2S), \Upsilon(3S) \rightarrow \gamma + V \rightarrow \gamma + \text{invisible}$, while the relevant process for LSND is $\pi^0 \rightarrow \gamma + V \rightarrow \gamma + \text{invisible}$. We adapt the constraints computed in Ref. [155] (see Fig.(201) for the constraints and the text and references therein for details).

In fig. 3.7, we show the combined constraints from BaBar and LSND in orange. As in section 3.3.3, we show the constraints from existing gamma-ray telescope constraints (in blue), constraints from CMB (dashed black) and a contour where we find the correct relic density for the dark matter through standard thermal freeze-out through annihilation into Standard Model particles (dotted black). While our results show that the dark photon model in which dark matter is produced via standard thermal freeze out is already well excluded, we again point out that there are mechanisms for producing DM through nonthermal processes; see the end of the previous section for

further discussion and Ref. [113] for a specific example using entropy dilution for a dark photon-mediated DM model. The projected constraints for GECCO for various targets and DM profiles are shown with solid lines. Our results demonstrate that GECCO’s potential to significantly extend current constraints, and, more importantly, to offer opportunities for discovery of this class of well-motivated dark matter candidates.

3.3.5 Model Example: Right-Handed Neutrino

The decaying DM model we investigate is one in which the DM is given by a right-handed (RH) neutrino (i.e. a Weyl spinor transforming as a singlet under all Standard Model gauge groups) featuring a non-zero mixing with left-handed “active” neutrinos. We assume the RH neutrino mixes with a single left-handed neutrino flavor, ν_L^k , where ν_L^k is an electron, muon or tau neutrino.¹⁰ The Lagrangian density describing the interactions of the RH-neutrino with the SM is the 4-fermion effective Lagrangian obtained by integrating out the W^\pm and Z :

$$\mathcal{L}_{\text{N(int)}} = -\frac{4G_F}{\sqrt{2}} \left[J_\mu^+ J_\mu^- + (J_\mu^Z)^2 \right] \Big|_{\nu_L^k \rightarrow \sin\theta N - i\cos\theta \nu_L^k} \quad (3.16)$$

¹⁰This can be achieved by the following Lagrangian density:

$$\mathcal{L} = \mathcal{L}_{\text{SM}} + i\hat{N}^\dagger \bar{\sigma}^\mu \partial_\mu N - \frac{1}{2} \hat{m}_N (\hat{N}\hat{N} + \hat{N}^\dagger \hat{N}^\dagger) - y_\ell (\hat{L}_\ell^\dagger \tilde{H} \hat{N} + \text{h.c.}) \quad (3.15)$$

where N is the 2-component Weyl spinor for the RH neutrino and $\hat{L}_\ell = (\hat{\nu}_\ell \hat{e}_\ell)^T$ is one of the SM lepton doublets. For non-zero \hat{m}_N , diagonalizing the neutrino mass matrix yields two majorana spinors. The diagonalization can be performed by constructing a neutrino mass matrix from the neutrino interaction states $\nu = (\hat{\nu}_\ell \hat{N})$ and performing a Takagi diagonalization [98]. The unitary Takagi transformation matrix is:

$$\Omega = \begin{pmatrix} -i\cos\theta & \sin\theta \\ i\sin\theta & \cos\theta \end{pmatrix}, \quad \sin\theta = \frac{vy}{\sqrt{2}\hat{m}_N} - \mathcal{O}\left(\frac{vy}{\hat{m}_N}\right)^3, \quad \cos\theta = 1 - \mathcal{O}\left(\frac{vy}{\hat{m}_N}\right)^2.$$

Where G_F is Fermi's constant and J_μ^\pm and J_μ^Z are the charged and neutral weak fermion currents, given by:

$$\begin{aligned}
J_\mu^+ &= \sum_i \bar{\nu}_L^i \gamma^\mu \ell_L^i + \sum_{i,j} V_{ij}^{\text{CKM}} \bar{u}_L^i \gamma^\mu d_L^j \\
2c_W J_\mu^Z &= \sum_{i=1}^3 \left[\left(1 - \frac{4}{3}s_W^2\right) \bar{u}_i \gamma^\mu u_i + \left(-1 + \frac{2}{3}s_W^2\right) \bar{d}_i \gamma^\mu d_i \right] \\
&\quad + \sum_{i=1}^3 [\bar{\nu}_L^i \gamma^\mu \nu_L^i - (1 + 2s_W^2) \bar{\ell}^i \gamma^\mu \ell^i]
\end{aligned} \tag{3.17}$$

with s_W and c_W being the sine and cosine of the weak mixing angle.

In order to calculate the interactions between the RH neutrino and mesons, we first need to determine the interaction Lagrangian written in terms of light quarks. Grouping the up, down and strange into a light-quark vector $\mathbf{q} = (u \ d \ s)^T$, we can write the relevant interactions terms of the expanded 4-Fermi Lagrangian as:

$$\begin{aligned}
-\frac{\sqrt{2}}{4G_f} \mathcal{L}_{\text{N(int)}} &= \bar{\mathbf{q}} \gamma^\mu [2\mathbf{G}_R(L_\mu^0 + R_\mu^0)] P_R \mathbf{q} + \bar{\mathbf{q}} \gamma^\mu \left[(\mathbf{V}^\dagger L_\mu^- + \text{h.c.}) + 2\mathbf{G}_L(L_\mu^0 + R_\mu^0) \right] P_L \mathbf{q} \\
&\quad + L_\mu^+ L_\mu^- + (L_\mu^0 + R_\mu^0)^2 + \dots
\end{aligned} \tag{3.18}$$

Here the \dots contain terms without the RH-neutrino. The charged and neutral left and right handed currents which the light quarks interact with are given by:

$$R_\mu^0 = \frac{1}{2c_W} (i \cos \theta \bar{\nu}_L^k + \sin \theta \bar{N}) \gamma^\mu (-i \cos \theta \nu_L^k + \sin \theta N) + \dots \tag{3.19}$$

$$L_\mu^0 = \frac{1}{2c_W} (i \cos \theta \bar{\nu}_L^k + \sin \theta \bar{N}) \gamma^\mu (-i \cos \theta \nu_L^k + \sin \theta N) + \dots \tag{3.20}$$

$$L_\mu^- = -i \cos \theta \nu_L^k \gamma^\mu \ell_L^k + \sin \theta \bar{N} \gamma^\mu \ell_L^k + \dots \tag{3.21}$$

The \mathbf{G}_R and \mathbf{G}_L are the right and left light-quark coupling matrices to the Z boson,

given by:

$$\mathbf{G}_R = \frac{1}{2c_W} \text{diag}(1, -1, -1) + \mathbf{G}_L, \quad \mathbf{G}_L = -\frac{s_W^2}{3c_W} \text{diag}(-2, 1, 1) \quad (3.22)$$

and \mathbf{V} is CKM coupling matrix for the light quarks:

$$\mathbf{V} = \begin{pmatrix} 0 & V_{ud} & V_{us} \\ 0 & 0 & 0 \\ 0 & 0 & 0 \end{pmatrix} \quad (3.23)$$

These interactions terms are easily matched onto the chiral Lagrangian. The terms involving the light-quarks that look like $\bar{\mathbf{q}}\gamma_\mu J_{L,R}^\mu P_{L,R}\mathbf{q}$ are matched onto the ‘‘covariant’’ derivative of the meson matrix of the chiral Lagrangian while the terms without quarks simply carry straight over. The result is:

$$\mathcal{L} = \frac{f_\pi^2}{4} \text{Tr} \left[(D_\mu \Sigma)^\dagger (D_\mu \Sigma) \right] + L_\mu^+ L_\mu^- + (L_\mu^0 + R_\mu^0)^2 + \dots \quad (3.24)$$

where f_π is the pion decay constant $f_\pi \sim 92$ MeV and the Σ field is the pseudo-Goldstone matrix containing the meson made from u, d and s quarks:

$$\Sigma = \begin{pmatrix} \pi^0 + \eta/\sqrt{3} & \sqrt{2}\pi^+ & \sqrt{2}K^+ \\ \sqrt{2}\pi^- & -\pi^0 + \eta/\sqrt{3} & \sqrt{2}K^0 \\ \sqrt{2}K^- & \sqrt{2}\bar{K}^0 & -2\eta/\sqrt{3} \end{pmatrix} \quad (3.25)$$

and the covariant derivative is:

$$D_\mu \Sigma = \partial_\mu \Sigma - ir_\mu \Sigma + i\Sigma l_\mu \quad (3.26)$$

$$r_\mu = 2\mathbf{G}_R R_\mu^0 \quad (3.27)$$

$$l_\mu = \left(\mathbf{V}^\dagger L_\mu^- + \text{h.c.} \right) + 2\mathbf{G}_L (L_\mu^0 + R_\mu^0) \quad (3.28)$$

RH neutrinos are well-known and well-motivated DM candidates (for a recent review see e.g. Ref. [51]). For the range of masses and lifetimes of interest here, the mixing angle must be extremely small: the dominant decay widths corresponding to a RH neutrino of mass m_N with mixing angle with active neutrinos θ reads [190]

$$\Gamma(N \rightarrow \pi^0 \nu_\ell) = \frac{f_\pi^2 G_F^2 m_N^3 \theta^2}{8\pi c_W^4} \left(1 - \frac{m_\pi^2}{m_N^2}\right)^2, \quad (3.29)$$

$$\Gamma(N \rightarrow \pi^\pm \ell^\mp) = \frac{f_\pi^2 G_F^2 |V_{ud}|^2 \theta^2}{8\pi m_N^3} \lambda^{1/2}(m_N^2, m_\ell^2, m_{\pi^\pm}^2) \times \left[(m_N^2 - m_\ell^2)^2 - m_{\pi^\pm}^2 (m_\ell^2 + m_N^2) \right], \quad (3.30)$$

$$\Gamma(N \rightarrow \nu_\ell \gamma) = \frac{9\alpha_{\text{EM}} G_F^2 m_N^5 \theta^2}{64\pi^4}, \quad (3.31)$$

$$\Gamma(N \rightarrow 3\nu_\ell) = \frac{G_F^2 m_N^5 \theta^2}{384\pi^3}, \quad (3.32)$$

$$\Gamma(N \rightarrow \nu_\ell \ell^+ \ell^-) = \frac{G_F^2 m_N^5 \theta^2}{192\pi^3} \left[1 + 4s_W^2 + 8s_W^4 - 16\mu_\ell^2 (1 + 3s_W^2 + 6s_W^4) + 24\mu_\ell^4 (1 + 6s_W^2 + 12s_W^4 - 2\log(\mu_\ell)) + \mathcal{O}(\mu_\ell^6) \right], \quad (3.33)$$

where s_W is the sine of the weak mixing angle, $\lambda(a, b, c) = a^2 + b^2 + c^2 - 2ab - 2ac - 2bc$ and $\mu_\ell = m_\ell/m_N$. For RH neutrino masses below the pion threshold, the three-body final state decay modes are dominant. In this regime, photons are produced via the one-loop decay of the RH-neutrino into $\nu\gamma$ and through radiation off a charged lepton, if $N \rightarrow \nu\ell^+\ell^-$ is kinematically accessible. Once the pion threshold is crossed, the two body final states $N \rightarrow \pi^0\nu_\ell$ and $N \rightarrow \pi^\pm\nu_\ell^\mp$ dominate and photons are produced via the decay of pions and radiation off charged states.

We show contours of constant θ on the lifetime versus mass plot in fig. 3.8.

We do not assume here any specific RH neutrino production mechanism in the early universe. In the mass range of interest, the most natural, although by all means not the only, scenario is non-thermal production from the decay of a heavy species ϕ coupled to the RH neutrino via a Yukawa term of the form $y\phi\bar{N}N$ (see e.g. Ref. [209]). The yield depends on a variety of assumptions, including whether the ϕ is in thermal equilibrium or not, which other decay channels it possesses, and the number of degrees of freedom that populate the universe as a function of time/temperature. However, production of RH neutrinos with the right abundance is generically possible across the parameter space we show in fig. 3.8.

The phenomenological constraints for RH neutrinos are weak for the masses and mixing angles of interest here. We refer the Reader to fig. 4 of Ref. [91] for an extensive review. In short, the most stringent constraints occur for mixing with the electron-type active neutrino, for a non-trivial CP phase and lepton-flavor violation structure. The strongest constraints, from neutrino-less double-beta decay, do not constrain values of the mixing angle to be smaller than $\theta \sim 10^{-8}$, even in the most favorable case. In the case of muon mixing, at or below 100 MeV the constraints are never stronger than $\theta \sim 10^{-4}$. Finally, in the weakest constraints case, that with tau neutrino mixing, the constraints on the mixing angle occur only for $\theta \gtrsim 10^{-2}$. We conclude that there are essentially no meaningful phenomenological constraints on the parameter space shown in fig. 3.8, in contrast to the situation for $\mathcal{O}(\text{keV})$ -scale sterile neutrinos (see e.g. Ref. [51]).

Our results in fig. 3.8 indicate that a signal from sterile neutrino dark matter decay will be detectable from the Galactic Center over a wide range of masses and

lifetimes. Limits will improve, for RH neutrinos in the few hundreds of keV range, by up to three orders of magnitude. A signal will also possibly be detectable for masses up to 100 MeV, and from targets different from the Galactic Center, such as M31 and Draco, for short enough lifetimes. Constraints from CMB observations are negligible [109].

3.4 Searches for Light Primordial Black Hole Evaporation

The discovery of gravitational radiation from binary black hole mergers ushered a renewed interest in black holes of primordial rather than stellar origin as dark matter candidates (for recent reviews, see e.g. Refs. [130, 65]). In a recent study, we considered Hawking evaporation from primordial black holes with lifetimes on the order of the age of the universe to 10^6 times the age of the universe [83]. There we corrected shortcomings of similar past analysis pertaining to the treatment of final state radiation and to the extrapolation of hadronization results outside proper energy ranges. We carried out a complete calculation of particle emission for Hawking temperatures in the MeV, and of the resulting gamma-ray and electron-positron spectrum.

Our key finding is that MeV gamma-ray telescopes are ideally poised to potentially discover Hawking radiation from light but sufficiently long-lived primordial black holes, specifically in the mass range between 10^{16} and 10^{18} grams. The Hawking temperature scales with the holes' mass as $T_H \approx (10^{16} \text{ g}/M) \text{ MeV}$. As a result, especially towards the more massive end of that mass range, the bulk of the emission stems from prompt primary photon emission at higher energy, and from secondary emission from

electrons at lower energy.

Emission from the central region of the Galaxy and from nearby astrophysical systems with significant amounts of dark matter can be detectable with GECCO, as we show here. The calculation of the flux from black hole evaporation is as follows: a non-rotating black hole with mass M and corresponding Hawking temperature $T_H = 1/(4\pi G_N M) \simeq 1.06(10^{16} \text{ g}/M) \text{ MeV}$, with G_N Newton's gravitational constant, emits a differential flux of particles per unit time and energy given by

$$\frac{\partial^2 N_i}{\partial E_i \partial t} = \frac{1}{2\pi} \frac{\Gamma_i(E_i, M)}{e^{E_i/T_H} - (-1)^{2s}}, \quad (3.34)$$

where Γ_i is the species-dependent grey-body factor, and E_i indicates the energy of the emitted particle of species i . Unstable particles decay and produce stable *secondary* particles, including photons. The resulting differential photon flux per solid angle from a region parameterized by an angular direction ψ is obtained by summing the photon yield N_γ from all particle species the hole evaporates to:

$$\frac{d\phi_\gamma}{dE_\gamma} = \frac{1}{4\pi M} \int_{\text{LOS}} dl \rho_{\text{DM}}(l, \psi) f_{\text{PBH}} \frac{\partial^2 N_\gamma}{\partial E \partial t}. \quad (3.35)$$

Notice that upon integrating over the appropriate solid angle this expression is analogous to the one for the gamma-ray flux from decaying DM, containing the same \bar{D} factor (c.f. eq. (3.2)).

As for the calculation of the grey-body factors, we employ the publicly available code `BlackHawk` [22]. `BlackHawk` provides primary spectra of photons, electrons and muons. We then model the final-state radiation off the charged final state particles by convolving the primary particle spectrum with the Altarelli-Parisi splitting functions

at leading order in the electromagnetic fine-structure constant α_{EM} [66, 17]. For the unstable particles, such as pions, we use `hazma` to compute the photon spectrum from decays. The total resulting photon spectrum is then given by:

$$\begin{aligned} \frac{\partial^2 N_\gamma}{\partial E_\gamma \partial t} &= \frac{\partial^2 N_{\gamma, \text{primary}}}{\partial E_\gamma \partial t} \\ &+ \sum_{i=e^\pm, \mu^\pm, \pi^\pm} \int dE_i \frac{\partial^2 N_{i, \text{primary}}}{\partial E_i \partial t} \frac{dN_i^{\text{FSR}}}{dE_\gamma} \\ &+ \sum_{i=\mu^\pm, \pi^0, \pi^\pm} \int dE_i \frac{\partial^2 N_{i, \text{primary}}}{\partial E_i \partial t} \frac{dN_i^{\text{decay}}}{dE_\gamma}, \end{aligned} \quad (3.36)$$

where the FSR spectra are given by:

$$\begin{aligned} \frac{dN_i^{\text{FSR}}}{dE_\gamma} &= \frac{\alpha_{\text{EM}}}{\pi Q_f} P_{i \rightarrow i\gamma}(x) \left[\log \left(\frac{(1-x)}{\mu_i^2} \right) - 1 \right], \\ P_{i \rightarrow i\gamma}(x) &= \begin{cases} \frac{2(1-x)}{x}, & i = \pi^\pm \\ \frac{1+(1-x)^2}{x}, & i = \mu^\pm, e^\pm \end{cases}, \end{aligned} \quad (3.37)$$

with $x = 2E_\gamma/Q_f$, $\mu_i = m_i/Q_f$ and $Q_f = 2E_f$. We give for explicit expressions of $dN^{\text{decay}}/dE_\gamma$ for the muon, neutral and charged pions in Ref. [84].

In evaluating GECCO's discovery reach we consider the same targets as in the preceding section: the Galactic Center with an NFW and an Einasto dark matter density profile, M31, and Draco. Assumptions on observing time are identical as before, and we use the same procedures to set limits and make projections as described in section 3.3.1. We additionally refer to our study of the discovery prospects of several proposed MeV gamma-ray telescopes for further details [83]. The strongest existing bounds on evaporating PBHs were derived in that work using COMPTEL data. Other competitive constraints come from INTEGRAL [161], CMB data [74, 198], EDGES 21

cm observations [73], Voyager 1 e^\pm measurements [49], the 511 keV line [95, 160], dwarf galaxy heating [151] and the extragalactic gamma-ray background measurements [64].

In summary, we show in fig. 3.9 that GECCO will enable the revolutionary possibility of directly detecting Hawking evaporation from primordial black holes, for instance if these objects constitute at least 0.001% of the dark matter and have a mass of 10^{16} grams, or if they are a larger fraction of the dark matter and a mass up to 10^{18} grams. Under optimistic circumstances (e.g. the black holes weigh around 10^{17} grams and they are more than 10% of the dark matter), GECCO will detect Hawking evaporation from multiple targets besides the Galactic Center, such as from nearby dSph (e.g. Draco) and galaxies (e.g. M31). This reach in PBH mass is an order-of-magnitude improvement over existing bounds.

3.5 Exploring the Origin of the 511 keV Line

The discovery of 511 keV line emission from positron-electron pair annihilation in the central region of the Galaxy dates back to balloon-borne experiments since the 1970s (see e.g. Ref. [135]). Space telescopes, specifically OSSE on the Compton Gamma-Ray Observatory [215] and, more recently, the SPI spectrometer [237, 143] and the IBIS imager on board INTEGRAL [90] have significantly increased the amount of information about the 511 keV emission. The overall intensity of the line is around 10^{-3} photons $\text{cm}^{-2} \text{s}^{-1}$, and it originates from a region of approximately 10° radius around the Galactic Center. The emission does not appear to have any significant time

variability, and its spatial smoothness, combined with the point-source sensitivity of the IBIS imager, places a lower limit of at least eight discrete sources contributing to the signal [143].

Measurements of the diffuse emission at energies below and above 511 keV constrain the injection energy of the positrons and the properties of the medium where injection and annihilation occur. Most notably for constructing new physics interpretations of the signal, the absence of significant emission at energies higher than 511 keV indicates that the positron injection energy is bounded from above in the few MeV (at most 4 – 8.5 MeV, allowing for a partially ionized medium [211, 212]). In turn this implies an upper limit of around 3 MeV on the mass of putative dark matter particles annihilating to electrons and positrons in a neutral medium [8, 35]. In absence of large-scale magnetic fields [199], the injection sources of positrons are constrained to lie within approximately 250 pc of the annihilation sites [142], thus indicating that the source distribution is quite close to the actual signal distribution in the sky [70, 142].

The origin of the positrons in the Galactic Center is still actively debated. Morphological information, and the mentioned lower limit on the number of contributing sources, rules out as major contributors (although it does not rule out as co-contributors) single sources such as Sgr A* [167] or a single injection event such as a gamma-ray burst or a hypernova in the Galactic Center [168]. The bulk of the signal is however slated to originate from a distributed population of several sources that could not be resolved as individual point sources in prior observations [154].

Much enthusiasm surrounded the possibility that the 511 keV line originate

from sources associated with new physics. Of these, the simplest possibility is perhaps the pair-annihilation of MeV-scale dark matter particles [42]. Other proposed scenarios include the decay of new particles such as sterile neutrinos [194], axions [137], neutralinos [37], Q-balls [147], mirror matter [119], moduli [149], cosmic strings [117], superconducting quark matter [188], MeV-scale excitations of more massive particles [118, 196], or small accreting black holes [232]. The common denominator of all these “exotic” scenarios is a genuinely diffuse emission: the significant detection of point sources at 511 keV would robustly rule out a new physics origin for the signal. Here, we point out that GECCO’s outstanding point source sensitivity would provide an exceptional probe to discriminate between an exotic and a conventional astrophysical origin for the signal.

A variety of conventional astrophysical sources have been considered for the production of positrons in the Galaxy contributing to the 511 keV signal. These include massive stars, pulsars as well as millisecond pulsars, core-collapse supernovae and SNe Ia, Wolf-Rayet stars, and low-mass X-ray binaries (LMXB), especially microquasars [210, 28]. In many instances, these astrophysical objects are also found much closer to the solar system than in the Galactic Center region. For instance, the closest Wolf-Rayet star, in the Gamma Velorum system, is around 350 pc away [182]; the catalogue in Ref. [169] includes an LMXB at a distance of 0.42 kpc (4U 1700+24) as well as at least four candidates closer than 2 kpc. The ATNF catalogue [173] contains several MSPs closer than 0.2 kpc, including J0437-4715 whose distance is 0.16 kpc (see also Ref. [44]), J0605+3757 at 0.21 kpc, J0636+5129 and J1737-0811 also at 0.21 kpc, J2322-2650 at 0.23 kpc, J1017-7156 at 0.26 kpc, and J1400-1431 at 0.28 kpc.

GECCO’s angular resolution and point-source sensitivity make it ideally suited to enable to differentiate between a multiple discrete point sources versus a genuinely diffuse origin for the 511 keV emission. Specifically, if one source class dominated the positron emission, GECCO has a distinct chance to detect nearby members of that source class. To clarify and quantify this statement, we assume for simplicity that the 511 keV signal originates from N_{src} sources each with a luminosity L_{src} at an average distance of 8.5 kpc. Given that the 511 keV signal is approximately $\phi_{511} \simeq 3 \times 10^{-3} \Delta\Omega \text{ cm}^2 \text{ s}^{-1} \text{ sr}^{-1}$ over an angular region of 10 degrees, i.e. $\Delta\Omega \simeq 0.1 \text{ sr}$, the flux expected from a single source at a distance d_{src} reads

$$\phi_{\text{src}} = \frac{L_{\text{src}}}{4\pi d_{\text{src}}^2} \simeq \frac{\phi_{511}}{N_{\text{src}}} \left(\frac{8.5 \text{ kpc}}{d_{\text{src}}} \right)^2. \quad (3.38)$$

We can thus compare the narrow line flux sensitivity of GECCO, which in the best-case scenario is $7.4 \times 10^{-8} \text{ cm}^{-2} \text{ ss}^{-1}$ and in the worse case scenario $3.2 \times 10^{-7} \text{ cm}^{-2} \text{ s}^{-1}$ with the flux expected for a given putative source class point source. Specifically, we calculate the GECCO sensitivity on the plane of N_{src} vs d_{src} . In the plot we indicate with vertical lines the closest known WR star, LMXB, and MSP, and with a horizontal line an estimate for the number of LMXB that could be responsible for the 511 keV line according to Ref. [28] ($N_{\text{LMXB}} \simeq 3000$), the estimate in Ref. [61] for the number of MSP in the Galactic Center region ($N_{\text{MSP}} \simeq (9.2 \pm 3.1) \times 10^3$) and an estimate for the total number of Wolf-Rayet stars in the Milky Way from Ref. [204] ($N_{\text{WR}} \simeq 1900 \pm 250$).

The plot shows that GECCO’s sensitivity should enable the detection of any positron source responsible for a significant fraction of the 511 keV signal closer than 4

kpc.

Additional information on the nature of the origin of the 511 keV signal from the Galactic Center will be provided by observations of nearby systems such as the Andromeda galaxy (M31), the Triangulum galaxy (M33), nearby clusters such as Fornax and Coma, and nearby satellite dwarf galaxies such as Draco and Ursa Minor [246].

The crudest estimate of the predicted 511 keV signal is a simple mass to distance-squared ratio, which we report in table 3.3. According to our predictions, the 511 keV signal from M31 should be detectable by GECCO, as should the signal from the Fornax and (although marginally) the Coma cluster. We predict that instead M33, and local dSph should not be bright enough at 511 keV to be detectable by GECCO. Notice that Integral/SPI already searched for a 511 keV line from Andromeda (M31), reporting an upper limit to the flux of $1 \times 10^{-4} \text{ cm}^{-2} \text{ s}^{-1}$ [28].

Notice that certain types of new physics explanations such as dark matter decay would follow a similar scaling. Other new physics explanations such as e.g. eXcited dark matter [118] would not, a critical factor being the typical velocity dispersion in a given system: no signal at all would be predicted from e.g. small galaxies such as Draco or Ursa Minor. The predictions for galaxies versus clusters of galaxies would depend upon the details of the model, but generally scale similarly to what reported in table 3.3.

We use the estimate of Ref. [166] for the Milky Way bulge total mass, and the flux quoted in Ref. [210] for the 511 keV flux from the bulge. We take the value for the total dynamical mass of M31 from Ref. [114], while the distance is from Ref. [146]; the total mass of M33 is from Ref. [50] and the distance from Ref. [47]. For the dSph

Target	Mass [M_{\odot}]	Distance [kpc]	ϕ_{511} [$\text{cm}^{-2} \text{s}^{-1}$]
Milky Way	$(1.69 \pm 0.12) \times 10^{10}$	8.5	$(9.6 \pm 0.7) \times 10^{-4}$
M31	$(8.5 \pm 5) \times 10^{11}$	778 ± 33	$(5.76 \pm 4.71) \times 10^{-6}$
M33	$(1.75 \pm 0.25) \times 10^{10}$	942 ± 73	$(8.09 \pm 3.58) \times 10^{-8}$
Draco	$(2.1 \pm 0.3) \times 10^7$	76 ± 5	$(1.49 \pm 0.62) \times 10^{-8}$
Ursa Minor	$(5.6 \pm 0.7) \times 10^7$	77 ± 4	$(3.85 \pm 1.44) \times 10^{-8}$
Fornax Cl.	$(7 \pm 2) \times 10^{13}$	$(18.97 \pm 1.33) \times 10^3$	$(7.98 \pm 4.55) \times 10^{-7}$
Coma Cl.	$(5.1 \pm 3.2) \times 10^{14}$	$(106.1 \pm 7.5) \times 10^3$	$(1.86 \pm 1.70) \times 10^{-7}$

Table 3.3: Predicted brightness of a 511 keV signal assuming a scaling proportional to mass over distance squared for a variety of astrophysical targets (see main text for references to the quoted masses, distances, and fluxes).

we take data from Ref. [246]. Data for the Fornax cluster are from Ref. [144], while for the Coma cluster from Ref. [2] and Ref. [125]. We propagate errors including those on masses, distances, and the observed 511 keV flux, and show our results in the right panel of fig. 3.10.

3.6 Discussion and Conclusions

We explored and elucidated the scientific portfolio that would be enabled by the deployment of the proposed mid-scale NASA mission GECCO as it pertains to

dark matter and new physics. GECCO is ideally suited to explore MeV dark matter candidates as long as they decay and/or pair-annihilate. The new instrument would unveil dark matter signals up to four orders of magnitude fainter than the current observational sensitivity, and would make it possible to detect a dark matter signal from multiple astrophysical targets, reducing the intrinsic background and systematic effects that could otherwise obscure a conclusive discovery. GECCO would enable the exciting possible direct detection of Hawking evaporation from primordial black holes with masses in the $10^{16} - 10^{18}$ grams range, if they constitute a sizable fraction of the cosmological dark matter. Under favorable circumstances, GECCO might detect Hawking evaporation from more than one astrophysical target as well.

Finally, we showed the potential of GECCO to elucidate the nature of the 511 keV line, by virtue of its unprecedented line sensitivity and point-source angular resolution. We found that GECCO should be able to observe a 511 keV line from a variety of extra-Galactic targets, such as nearby clusters and massive galaxies and, potentially, even from nearby dwarf galaxies; in addition, GECCO should be able to detect single sources of the 511 keV emission, as long as they are reasonably close.

In summary, we have shown that GECCO would push the observational frontier of MeV gamma rays in ways that would enormously benefit the quest for fundamental questions in cosmology and particle physics, chiefly the nature and particle properties of the cosmological dark matter, and the origin of the mysterious 511 keV line emission from the center of the Galaxy.

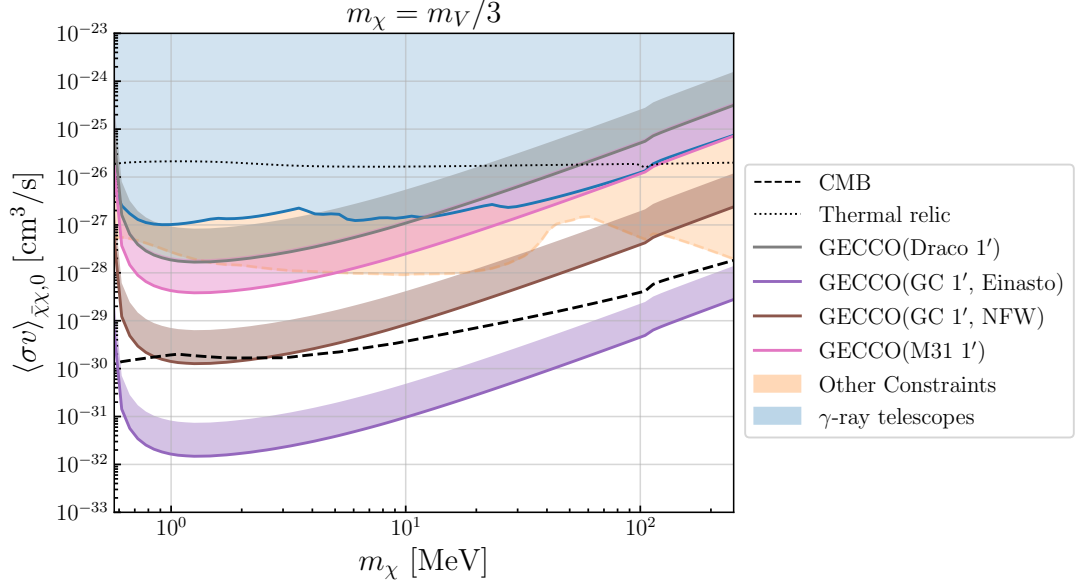


Figure 3.7: Projected constraints on the dark matter annihilation cross section for the dark photon model from GECCO (solid lines). To account for the unknown systematics of GECCO, the surrounding bands show how the projections would change if the background photon counts were a factor of 25 higher than the fiducial value. As before, the bands correspond to increasing or decreasing the background model by a factor of 25. The light blue shaded region shows the combined constraints from COMPTEL, EGRET, FERMI and INTEGRAL. The orange region shows the region excluded by BaBar and LSND. We show the contour yielding the correct dark matter relic density with the dotted black line.

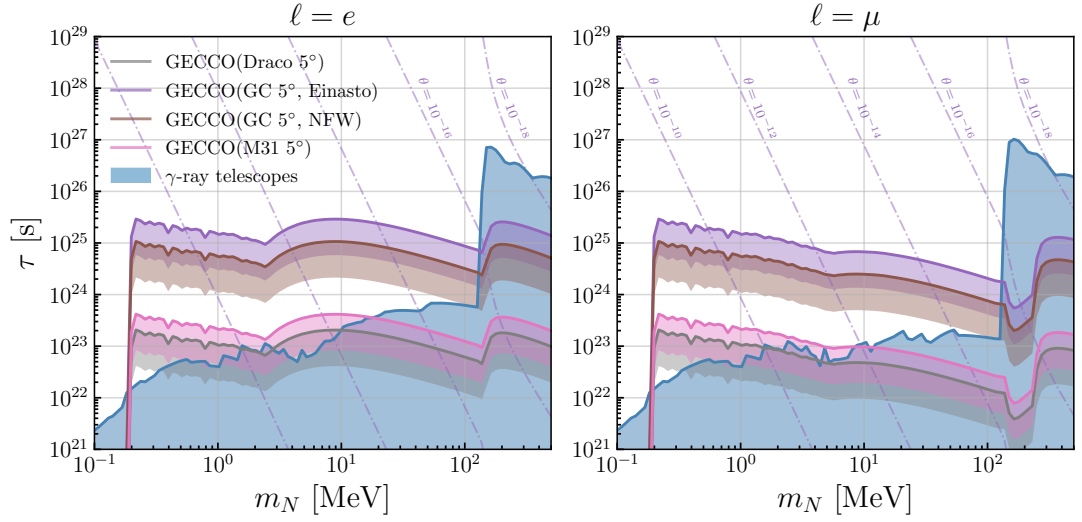


Figure 3.8: Projected constraints on the RH-neutrino lifetime (solid lines). To account for the unknown systematics of GECCO, the surrounding bands show how the projections would change if the background photon counts were a factor of 25 higher than the fiducial value. The area shaded in light blue is excluded by current observations, as in the previous plots. We also show, with dot-dashed contours, the mixing angle corresponding to parameter space shown in the figure.

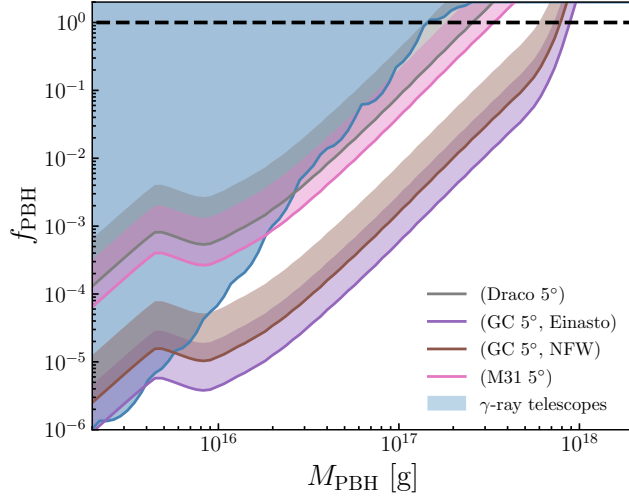


Figure 3.9: GECCO’s 5σ discovery reach for detecting Hawking radiation from evaporating primordial black hole dark matter (solid lines). To account for the unknown systematics of GECCO, the surrounding bands show how the projections would change if the background photon counts were a factor of 25 higher than the fiducial value. The blue region shows existing constraints, the strongest of which comes from COMPTEL data [83]. We assume a monochromatic mass function.

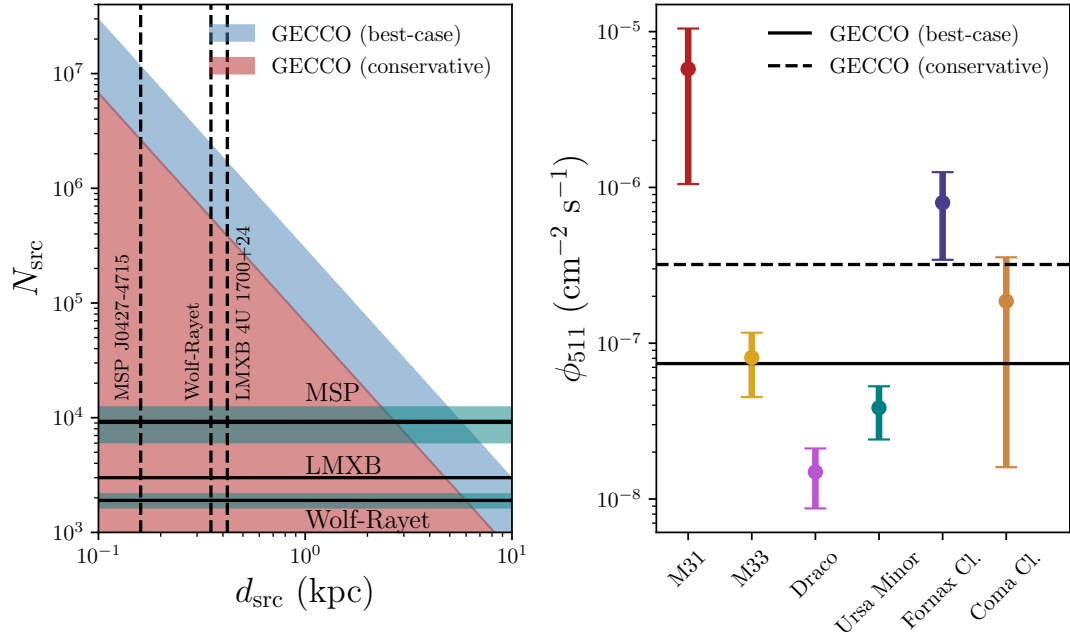


Figure 3.10: Left: the GECCO sensitivity to 511 keV individual point source on the plane defined by the number of sources contributing to the signal at the Galactic Center (assumed to all contribute the same 511 keV luminosity), versus the distance of the closest such source; we also indicate with vertical dashed lines the distance to the closest MSP, Wolf-Rayet star, and LMXB, and with horizontal dark green bands the estimates for the total number of MSP and Wolf-Rayet stars potentially contributing to the signal. Right: predictions for the 511 keV flux from a variety of nearby astrophysical objects, based on a signal scaling proportional to mass over distance squared. The horizontal dashed and solid lines correspond to GECCO’s point source sensitivity best-case and conservative case.

Chapter 4

Direct Detection of Hawking Radiation from Asteroid-Mass Primordial Black Holes

This chapter was adapted from “Direct Detection of Hawking Radiation from Asteroid-Mass Primordial Black Holes” which was published to Physical Review Letters (2021, DOI: 10.1103/PhysRevLett.126.171101). This work was done with Adam Coogan and Stefano Profumo.

4.1 Introduction

Discerning the fundamental nature of the cosmological dark matter (DM) is perhaps the most pressing issue in particle physics. While much is known about the average density of DM in the universe as a whole as well as on the density of DM

in specific structures, the mass of its elementary constituent is largely unconstrained. Roughly, macroscopic quantum effects, such as the DM featuring a De Broglie wavelength comparable to the size of the smallest gravitationally collapsed structures, bound the DM mass from below. The stability of structures such as galactic disks and the existence of relatively old, stable, unperturbed systems such as globular clusters and dwarf spheroidal galaxies constrains the DM mass from above, since a large point mass would measurably disrupt such structures. Most of the roughly ninety orders of magnitude in between these two model-independent constraints could well accommodate the mass of the elementary objects making up (most of the) DM (see [201] for a review).

Essentially all information about what the DM is therefore stems from gravitational interactions. As far as observations are concerned, the DM need not be “charged” under any other additional interaction besides gravity. An extensive experimental and observational program has for many years assumed that the DM is charged under the Standard Model’s weak nuclear interactions. This program, however, has thus far failed to bear positive fruit. The class of DM candidates known as weakly interacting massive particles (WIMPs), while remaining solidly theoretically motivated, does not appear to be supported by any uncontroversial experimental evidence [23].

The successful detection of gravitational waves [1] has ushered a renewed interest in DM candidates with masses of the order of the black holes whose binary mergers were directly detected [38]. The somewhat surprising mass and spin distributions of such black holes, as inferred from observations, brought further momentum to the notion that the black holes might in fact not be all of stellar origin, but that some (or all)

of them be of *primordial* origin [116] (see e.g. [65, 130] for recent reviews on primordial black holes, or PBHs). At the same time, closer scrutiny of the range of viable masses for PBHs has unveiled that previously-thought excluded regions are in fact perfectly viable [130].

Stellar-mass black holes, such as those whose binary mergers are detected via gravitational wave telescopes, could well be a significant fraction of the DM. Constraints from CMB distortions [197, 75] and dynamical effects on small-scale structures [52] are subject to significant debate and systematic issues, while constraints dependent on their merger rates might also have been overestimated (see e.g. the recent study [43]). Lighter black holes with horizon sizes comparable to visible light and masses around $10^{-11} M_{\odot}$ or 10^{22} grams are constrained by microlensing of stars. Again, recent work has shown how finite-size source effects must be very carefully taken into account to avoid overestimating the constrained parameter space [221].

Much lighter black holes are extremely challenging to detect. Femtolensing constraints [30], employing much shorter wavelengths than visible light, turned out to also have neglected the impact of finite source size [148, 185] and do not set any meaningful constraints. Destruction of white dwarfs and neutron stars was also found to be plagued by issues with the black hole capture rate, and does not set any strong constraints at present (see e.g. [185]).

Lighter and lighter black holes have increasingly large Hawking temperatures ($T_H \approx (10^{10} \text{ g}/M) \text{ TeV}$) and evaporate much more efficiently and quickly, with a lifetime $\tau \approx 10^{66} (M/M_{\odot})^3$ years. Black holes lighter than $\approx 5 \times 10^{14}$ g have a lifetime compa-

rable to the age of the universe, while slightly more massive black holes are currently evaporating. Constraints can thus be set from searches for the evaporation products of these $10^{16} - 10^{17}$ g holes, assuming they are a fraction f_{PBH} of the cosmological DM. Evaporation of black holes at all redshifts and in all structures can be constrained by the requirement not to overproduce the extragalactic gamma-ray background (EGRB) [64]. Evaporation can also lead to CMB distortions [197, 75], heating of neutral hydrogen [73], and of the interstellar medium in dwarf galaxies [151]. The local density of PBH, in the mass range where evaporation is significant, is also constrained by measurements of the abundance of electrons and positrons in the cosmic radiation from Voyager 1 [49]. Positrons from evaporation are additionally constrained by the 511 keV annihilation line with electrons as observed by INTEGRAL [95, 160]. INTEGRAL data also directly constrain the abundance of PBH in the Galaxy, as shown in Ref. [162]. Finally, there exist constraints from the diffuse neutrino background as measured by Super-Kamiokande from evaporation to neutrinos [88].

In this work, we find that observations with COMPTEL give the *strongest constraints currently available* over a broad range of black hole masses. We study the prospects for discovering these PBHs with next-generation MeV gamma-ray telescope observations of the Milky Way, Andromeda (M31) and nearby dwarf spheroidal galaxies. In deriving these constraints we present a robust, semianalytical calculation of the secondary photon spectrum from evaporating PBHs with MeV-scale temperatures. This is required for correctly assessing the sensitivity of telescopes to PBHs at the low end of the mass range we consider.

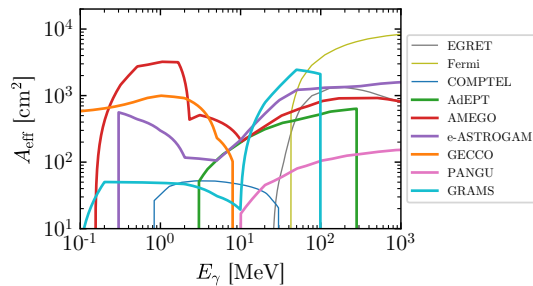


Figure 4.1: **The effective area, as a function of energy, of existing and proposed MeV gamma-ray telescopes.** Thin lines mark existing telescopes and thick lines mark proposed ones. The effective area of MAST (not shown) ranges from $\sim 7 \times 10^4 - 10^5 \text{ cm}^2$ over $E_\gamma = 10 \text{ MeV} - 60 \text{ GeV}$.

The remainder of this study is as follows: after describing the current observational status, we list future telescopes relevant for the detection of Hawking radiation, and describe the salient features that would enable detection of black hole evaporation. We then describe the details of Hawking evaporation and its detection, present our results, and conclude.

4.2 MeV gamma-ray telescopes.

The Hawking temperature T_H of interest for black holes of mass M whose lifetimes are within a few orders of magnitude of the age of the universe τ_U falls in the MeV scale:

$$\tau(M) \simeq 200 \tau_U \left(\frac{M}{10^{15} \text{ g}} \right)^3 \simeq 200 \tau_U \left(\frac{10 \text{ MeV}}{T_H} \right)^3. \quad (4.1)$$

PBH with a Hawking temperature in the GeV would have a lifetime of less than 3×10^6 years. At present they cannot comprise a significant fraction of the cosmological DM since that would imply too large a DM abundance at early times, in conflict with CMB and BBN observations. Instead, PBHs evaporating at present are generically expected to be producing photons in the MeV range. This limits the available observational capabilities relevant for constraining PBH evaporation to the low-energy range of the Fermi Large Area Telescope (Fermi-LAT) [26], and to its predecessors EGRET [140] and COMPTEL [145] on board the Compton Gamma Ray Observatory, and the International Gamma-Ray Astrophysics Laboratory (INTEGRAL) [242]. We show in fig. 4.1 the relevant effective areas, in cm^2 , as a function of energy, with solid lines.

Several missions with capabilities in the MeV are in the proposal, planning, or construction phase. Here, we consider the following: ADEPT [138], AMEGO [179], eASTROGAM [229]¹, GECCO [184], MAST [101], PANGU [248, 247] and GRAMS [21, 20]. For future missions, we will assume dedicated observation times of $T_{\text{obs}} = 10^8 \text{ s} \approx 3 \text{ yr}$. We note that in searching for Hawking evaporation products, energy and angular resolution are not critical. The spectra, to be discussed below, consist of a fairly broad peak with a long, low-energy tail. As long as the target's angular size is larger than the telescope's angular resolution, the latter does not enhance detection capabilities either.

¹This has since been scaled back to All-Sky-ASTROGAM [172].

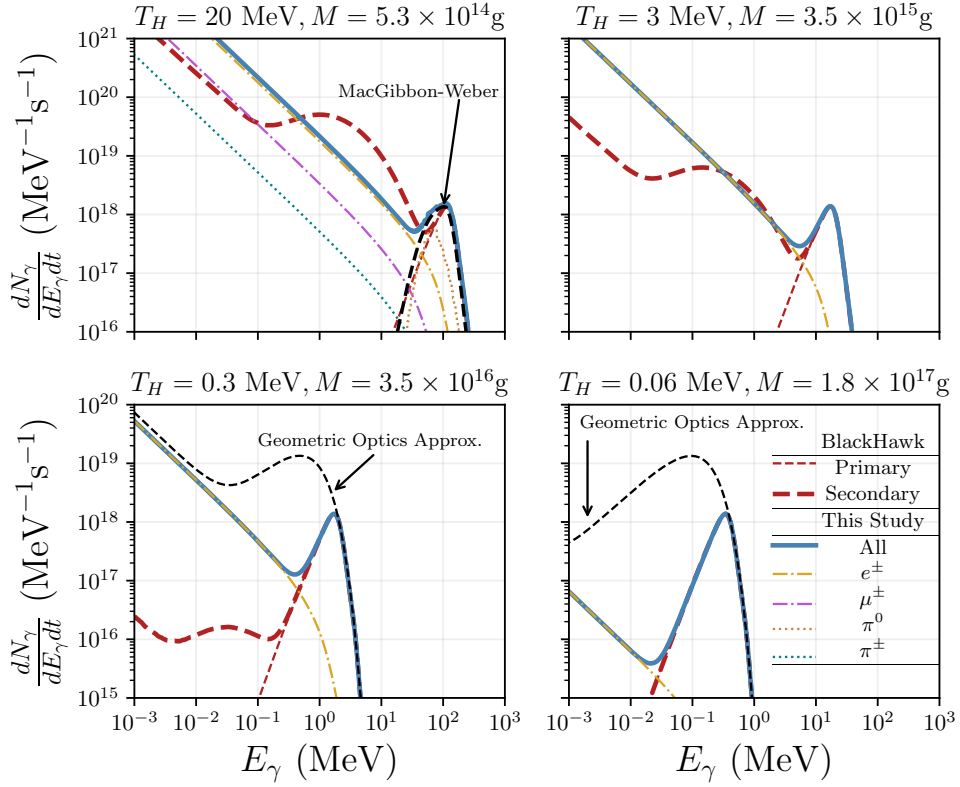


Figure 4.2: **Photon emission from light black hole evaporation.** We consider Hawking temperatures of 20, 3, 0.3 and 0.06 MeV (from top left to bottom right), corresponding to masses $M = 5.3 \times 10^{14}$, 3.5×10^{15} , 3.5×10^{16} , 1.8×10^{17} grams. The thick blue lines show the spectra computed in this work; the dashed red curves correspond to the primary (thin lines) and secondary-plus-primary (thick lines) output from `BlackHawk`. We also show contributions from π^0 decay (magenta dotted lines) and from final state radiation off of electrons and muons (dot dashed yellow and magenta lines) and charged pions (dotted green lines). The upper-left panel shows the results from MacGibbon and Weber [171] as a dashed black line. In the two lower panel we also show what results from adopting the geometric optics approximation for the grey-body factors.

4.3 Photons from evaporating PBHs.

A non-rotating black hole with mass M and corresponding Hawking temperature $T_H = 1/(4\pi G_N M) \simeq 1.06(10^{16} \text{ g}/M) \text{ MeV}$, with G_N Newton's gravitational constant, emits a differential flux of particles per unit time and energy given by (in natural units $\hbar = c = 1$)

$$\frac{\partial^2 N_i}{\partial E_i \partial t} = \frac{1}{2\pi} \frac{\Gamma_i(E_i, M)}{e^{E_i/T_H} - (-1)^{2s}}, \quad (4.2)$$

where Γ_i is the species-dependent grey-body factor, and E_i indicates the energy of the emitted particle of species i . Unstable particles decay and produce stable *secondary* particles, including photons. The resulting differential photon flux per solid angle from a region parametrized by angular direction ψ is obtained by summing the photon yield N_γ from all particle species the hole evaporates to:

$$\frac{d\phi_\gamma}{dE_\gamma} = \frac{1}{4\pi} \int_{\text{LOS}} dl \frac{\partial^2 N_\gamma}{\partial E \partial t} \frac{f_{\text{PBH}} \rho_{\text{DM}}(l, \psi)}{M}. \quad (4.3)$$

We assume the PBHs have a monochromatic mass function, comprise a fraction f_{PBH} of the DM and trace the DM's spatial distribution.

Notice that upon integrating over the appropriate solid angle, the expression above contains a factor identical to what found in decaying DM searches, which we denote by

$$\bar{J}_D \equiv \frac{1}{\Delta\Omega} \int_{\Delta\Omega} d\Omega \int_{\text{LOS}} dl \rho_{\text{DM}}(r(l, \psi)). \quad (4.4)$$

We list \bar{J}_D in table 4.1 for the inner 5° of the Milky Way, Draco, and M31, assuming the PBH spatial density is described by a Navarro-Frenk-White (NFW) profile [186].

Target	\bar{J}_D (MeV cm ⁻² sr ⁻¹)
Draco (NFW) [99]	1.986×10^{24}
M31 (NFW) [126]	4.017×10^{24}
Galactic Center (NFW) [92]	1.597×10^{26}
Galactic Center (Einasto) [92]	2.058×10^{26}
$ b < 20^\circ, \ell < 60^\circ$ (NFW) [92]	4.866×10^{25}

Table 4.1: \bar{J}_D factors for various circular targets and the COMPTEL observing region from Ref. [145]. The DM profile parameters are taken from the indicated references. For the Milky Way targets, we use the values from Table III of Ref. [92]. The Einasto profile parameters are adjusted within their 1σ uncertainty bands to maximize \bar{J}_D . For all other targets we use the parameters' central values. The distance from Earth to the Galactic Center is set to 8.12 kpc [4, 92]. For reference, the angular extent of a 5° region is 2.39×10^{-2} sr.

We find that a 5° observing angle provides a close-to-optimal balance of signal to background. To bracket uncertainties in the Galactic DM distribution, we also consider the possibility that it follows an Einasto profile [107]. We include the \bar{J}_D factor from galactic PBHs for the region $|b| < 20^\circ, |\ell| < 60^\circ$ observed by COMPTEL [145, 109], assuming an NFW Galactic DM halo.

To generate the gamma-ray spectra from a decaying PBH, we employ the

greybody factors calculated by the publicly available code `BlackHawk` [22]. `BlackHawk` generates primary spectra for all fundamental SM particles using the standard Hawking evaporation spectrum given in eq. (4.2). The code also uses `PYTHIA` [213] and `HERWIG` [27]² to hadronize and shower strongly-interacting and unstable particles, producing the full (primary and secondary) spectra of all stable SM particles. However, the hadronization routines in both of these codes are only reliable for energies $\gtrsim 5$ GeV. In fact, `BlackHawk` uses *extrapolation tables* to compute spectra from particles with energies below the range where `PYTHIA` and `HERWIG` are computed for, which result in unreliable and unphysical spectra.³

In addition, since `PYTHIA` is designed for collider physics, it rejects photons which are sufficiently collinear to the radiating charged particle. This is because events in which the photon and charged particle are not well separated cannot be distinguished from events with no photon in collider detectors. However, on cosmic scales, the propagation lengths of the photon and charged particle are large enough to completely separate the two, making `PYTHIA`'s isolation cut too restrictive.

Instead, we use `BlackHawk` to generate primary spectra of photons, electrons and muons, and we use `BlackHawk`'s tables of greybody factors to compute the primary Hawking radiation of neutral and charged pions. We model the final-state radiation off the charged final state particles by “convolving” the primary spectrum with the

²`BlackHawk` has options of use either `PYTHIA` or `Herwig` at the BBN epoch (using concrete lifetimes for various unstable particles) or `PYTHIA` at the present epoch, where all unstable particles are decayed. We exclusively use `PYTHIA` at the current epoch.

³The `BlackHawk` authors are aware of this, and the code raises the following warning when a user attempts to compute the secondary spectra below 5 GeV: `WARNING ENERGY BOUNDARIES ARE NOT COMPATIBLE WITH THE NEW PYTHIA HADRONIZATION TABLES! NEW PYTHIA HADRONIZATION TABLES WERE COMPUTED FOR 5.00e+00 GeV < E < 1.00e+05 GeV EXTRAPOLATION WILL BE USED.`

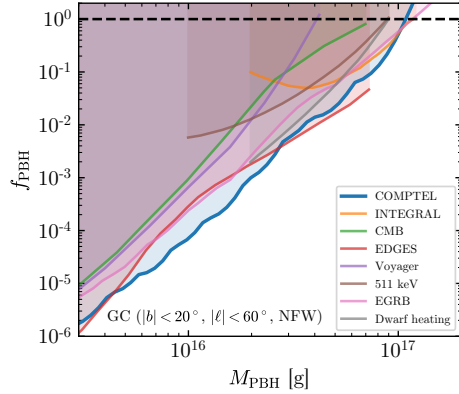


Figure 4.3: **New bounds on the PBH abundance based on COMPTEL observations of the Milky Way.** Assuming the PBHs follow an Einasto rather than NFW distribution gives a slightly stronger bound. Existing bounds collected in Ref. [130] from INTEGRAL observations of galactic diffuse emission [162], CMB [197, 75], EDGES 21 cm [73], Voyager 1 [49], the 511 keV gamma-ray line [95, 160], the extragalactic gamma-ray background [64] and dwarf galaxy heating [151] are also shown.

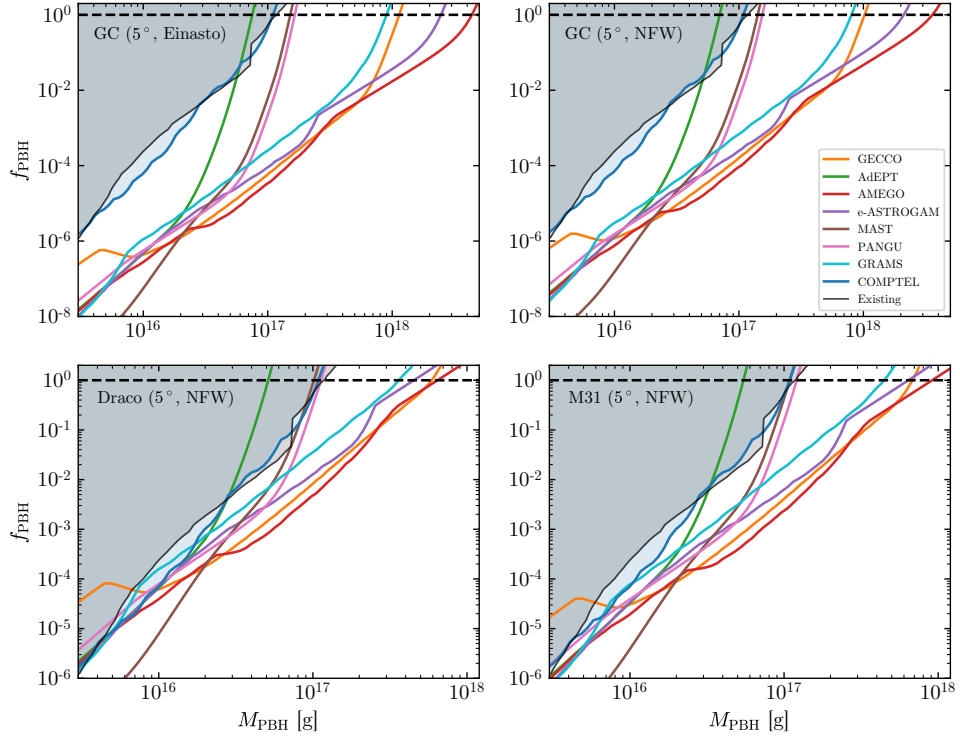


Figure 4.4: **Discovery reach for PBHs with future MeV gamma ray telescopes.**

In the top row, the PBH density is assumed to track an Einasto density profile (left) and an NFW profile (right) fit to the Milky Way’s DM distribution. In the lower panels we consider the Draco dwarf spheroidal and M31 as targets. For all targets we assume a 5° circle around the central region.

Altarelli-Parisi splitting functions at leading order in the electromagnetic fine-structure constant α_{EM} [66, 17]. For the unstable particles, such as pions, we use **Hazma** [84] to compute the photon spectrum from decays. Our total photon spectrum is then:

$$\begin{aligned} \frac{\partial^2 N_\gamma}{\partial E_\gamma \partial t} &= \frac{\partial^2 N_{\gamma, \text{primary}}}{\partial E_\gamma \partial t} \\ &+ \sum_{i=e^\pm, \mu^\pm, \pi^\pm} \int dE_i \frac{\partial^2 N_{i, \text{primary}}}{\partial E_i \partial t} \frac{dN_i^{\text{FSR}}}{dE_\gamma} \\ &+ \sum_{i=\mu^\pm, \pi^0, \pi^\pm} \int dE_i \frac{\partial^2 N_{i, \text{primary}}}{\partial E_i \partial t} \frac{dN_i^{\text{decay}}}{dE_\gamma}, \end{aligned} \quad (4.5)$$

where the FSR spectra are given by:

$$\begin{aligned} \frac{dN_i^{\text{FSR}}}{dE_\gamma} &= \frac{\alpha_{\text{EM}}}{\pi Q_f} P_{i \rightarrow i\gamma}(x) \left[\log \left(\frac{(1-x)}{\mu_i^2} \right) - 1 \right], \\ P_{i \rightarrow i\gamma}(x) &= \begin{cases} \frac{2(1-x)}{x}, & i = \pi^\pm \\ \frac{1+(1-x)^2}{x}, & i = \mu^\pm, e^\pm \end{cases}, \end{aligned} \quad (4.6)$$

with $x = 2E_\gamma/Q_f$, $\mu_i = m_i/Q_f$ and $Q_f = 2E_f$. (See Ref. [84] for explicit expressions of $dN^{\text{decay}}/dE_\gamma$ for the muon, neutral and charged pions.)

We illustrate the issues mentioned above in fig. 4.2, where we show secondary spectra computed with **BlackHawk**, which, as mentioned, include unphysical extrapolations of the QCD fragmentation results outside their range of validity, evident in the unphysical bumps at low energy. Note that the bump is likely a remnant of what is expected from neutral pion decay. However, on a log scale in energy the emission from $\pi \rightarrow \gamma\gamma$ is symmetric around $m_{\pi^0}/2$, which is not the case in the extrapolated spectra. Additionally, we note that while the bump over- or undershoots the actual photon emission, the asymptotic low-energy behavior is also incorrect, as explained above, because

of the lack of soft collinear photons. Finally, we note that for the largest masses/lowest Hawking temperatures, the treatment of final state radiation off of electrons and positrons leads to a significant underestimate of the emission in the keV range. We also show in the two lower panels the spectra that would result from adopting the geometric optics approximation, as done e.g. in Ref. [49], which leads to a significant overestimate of the particles' fluxes. In this current work, correctly accounting for the secondary spectrum impact constraints on low-mass PBHs from telescopes sensitive to low-energy gamma rays (e.g. GECCO; c.f. fig. 4.1).

COMPTEL Bounds & discovery reach. To set constraints with COMPTEL data, we find the largest value of f_{PBH} such that the photon flux from PBHs in the region $|b| < 20^\circ$, $|\ell| < 60^\circ$ does not exceed the observed flux plus twice the upper error bar in any energy bin:

$$\left[\int_{E_{\text{low}}^{(i)}}^{E_{\text{high}}^{(i)}} dE_\gamma \frac{d\Phi_\gamma}{dE_\gamma} \right] \leq \Phi_\gamma^{(i)} + 2\Delta\Phi_\gamma^{(i)}, \quad i = 1, \dots, n_{\text{bins}}. \quad (4.7)$$

The integral ranges from the lower to upper bound of each bin, indexed by i . This procedure yields conservative limits since it makes no assumptions about the astrophysical background. However, with background modeling we expect the constraints to improve by less than an order of magnitude [109].

For analyzing the discovery potential for future telescopes, we require the signal-to-noise ratio over the observing period to be larger than five: $N_\gamma|_{\text{PBH}} = 5\sqrt{N_\gamma|_{\text{bg}}}$.

Given a signal or background flux $\frac{d\Phi}{dE}$, the number of photons detected is given by

$$N_\gamma = T_{\text{obs}} \int_{E_{\text{min}}}^{E_{\text{max}}} dE_\gamma A_{\text{eff}}(E_\gamma) \int dE'_\gamma R_\epsilon(E_\gamma|E'_\gamma) \frac{d\Phi}{dE_\gamma}. \quad (4.8)$$

Here A_{eff} is the energy-dependent telescope's effective area (c.f. fig. 4.1). The function $R_\epsilon(E|E')$ is a Gaussian with mean E' and standard deviation $\epsilon(E') E'$ that accounts for the telescope's finite energy resolution. We ignore energy dependence in T_{obs} .

For targets oriented away from the Galactic center (Draco and M31), we adopt an empirical power law background model fit to high-latitude COMPTEL and EGRET data [41]:

$$\frac{d\Phi_\gamma}{dE_\gamma} = 2.74 \times 10^{-3} \left(\frac{E}{\text{MeV}} \right)^{-2} \text{cm}^{-2} \text{s}^{-1} \text{sr}^{-1} \text{MeV}^{-1}. \quad (4.9)$$

In the case of targets focused on the Galactic center, we use a more sophisticated model [32]. It consists of bremsstrahlung, π^0 and inverse-Compton spectral components computed with GALPROP [227] and calibrated against data in the window $|\ell| < 30^\circ$ $|b| < 10^\circ$, as well an additional power law component required to fit COMPTEL data. This flux predicted by this model is roughly a factor of 7 larger than in eq. (4.9).

We carry out this analysis by implementing a new model for PBH dark matter in our code `hazma` [84].

4.4 Results and discussion

The PBH abundance bound we derive from COMPTEL data is displayed in fig. 4.3, along with a host of existing evaporation constraints. The COMPTEL bound

is the most stringent constraint by a factor of ~ 3 for PBH masses near 10^{16} g and in line with other constraints over the rest of the mass range we consider.

The discovery reach for selected planned MeV gamma-ray telescope using observations of the Galactic center, Draco and M31 are shown in fig. 4.4. We highlight that AMEGO, e-ASTROGAM and GECCO observations of the Galactic center are capable of discovering PBH DM up to a mass of $\sim 10^{18}$ g, an order of magnitude larger than current constraints. Note that neglecting the secondary evaporation spectrum computed above would lead to underprojecting GECCO's discovery reach by an order of magnitude at the lower bound of the mass range in our plots. All of the experiments considered herein could discover PBHs with an abundance an order of magnitude below current constraints in part of the mass range $5 \times 10^{15} - 3 \times 10^{18}$ g. We emphasize that having a low energy threshold is important for pushing the discovery reach into the asteroid mass window, as can be seen by comparing the effective areas in fig. 4.1 with the curves in fig. 4.4. Due to the relative large observing region (5°), these projections are not particularly sensitive to whether the Galactic PBH distribution follows an Einasto or NFW profile. In the case of M31 or Draco observations we predict a fainter signal, but expect PBHs with masses up to $\sim 10^{18}$ g to be discoverable.

4.5 Summary & conclusions.

We considered bounds on the fractional contribution that primordial black holes with lifetimes comparable to the age of the universe make to the cosmological

dark matter. We pointed out that since the relevant Hawking temperature is around the MeV scale, computing their secondary evaporation spectra requires appropriately treating the final state radiation off of charged leptons and light hadrons, as well the production and decays of light mesons. We showed that at present and across a large swath of black hole masses the best constraints stem from COMPTEL observations of the central region of the Galaxy. We considered an optimistic range of possible future telescopes with MeV-band coverage, and pointed out that many of those will have a distinct opportunity to discover Hawking evaporation from evaporating PBH making up a large fraction of the DM with masses in the $10^{17} \lesssim M/g \lesssim \text{few} \times 10^{18}$. Direct detection of black hole evaporation would have enormous consequences for the quest to discern the nature of the cosmological DM, for understanding the early universe, and for black hole physics.

Chapter 5

Hazma: A Python Toolkit for Studying Indirect Detection of Sub-GeV Dark Matter

This chapter was adapted from “Hazma: A Python Toolkit for Studying Indirect Detection of Sub-GeV Dark Matter” which was published to the Journal of Cosmology and Astroparticle Physics, Volume 2020. This work was done in collaboration with Adam Coogan and Stefano Profumo with significant contributions from Francesco D’Eramo.

5.1 Introduction

The search for particle debris from dark matter (DM) annihilation or decay has thus far largely centered on DM masses in the GeV-TeV scale, for a variety of

reasons. First, if the DM shares electroweak interactions with the Standard Model, as in the weakly-interacting massive particle (WIMP) scenario, then, by the Lee-Weinberg limit, its mass is expected to be more than a few GeV [163]¹. Second, the general expectation for the scale of new physics based on the “small hierarchy problem” is that new physics, and thus new massive particles possibly including the particle making up the cosmological DM, should appear around the electroweak scale. Finally, the GeV scale is testable with an array of currently-operating gamma-ray and cosmic-ray observatories, including, but not limited to, the Fermi Large Area Telescope (LAT) [25], Cherenkov Telescope Arrays such as MAGIC [16], HESS [3], VERITAS [136], and the Alpha-Magnetic Spectrometer (AMS-02) [13].

On the theory front, the calculation of the detailed expected *particle spectrum* of the debris resulting from DM annihilation or decay has thus focused on the GeV-TeV regime. State-of-the-art codes utilize simulations describing the results of high-energy collisions of elementary particles yielding jets and leptons, which in turn decay and produce stable final-state particles. Many such codes, such as DarkSUSY [128], micrOmegas [36] and PPPC4DM [71] utilize tabulated results from PYTHIA [214], one of the most widely-used programs for performing these simulations. Such results are reliable at center-of-mass energy scales at or above roughly 5 GeV [214], but not at lower energies, where, for instance, strongly-interacting particles form hadronic bound states and are no longer described by parton showers, fragmentation and decay. It is well known that the resulting spectra of gamma rays, electrons and positrons and

¹Note that exceptions exist to the Lee-Weinberg limit, see e.g. [200]

antiprotons, are dramatically different in that case.

For a variety of reasons it is now quite timely to offer the community a reliable computational package that provides the spectra of particles resulting from lighter, sub-GeV DM annihilation or decay. First and foremost, MeV astronomy will soon be revolutionized with a new generation of telescopes such as e-ASTROGAM [203, 230], AMEGO [178] and others, including concept telescopes such as the Advanced Energetic Pair Telescope (AdEPT) [138], the PAir-productioN Gamma-ray Unit (PANGU) [248], and the Gamma-Ray Imaging, Polarimetry and Spectroscopy (“GRIPS”) [100]. Second, the persistent absence of any conclusive astrophysical signal from DM in the GeV-TeV range has furthered theoretical and phenomenological interest in the mass range below the GeV, providing additional motivation to investigate the details of DM decay or annihilation processes. Lastly, at present no code exists that allows users to readily study gamma-ray and cosmic-ray production from DM particles annihilating dominantly into hadronic bound states.

With these motivations, we here introduce a Python toolkit, `hazma`², that computes spectra of gamma rays and cosmic-ray electrons and positrons from the decay of muons and pions, calculates constraints from gamma-ray observations and the cosmic microwave background, and allows users to compute composite spectra for selected built-in models of DM-parton interactions.

²Hazma is a small rounded Pokemon, with light green spikes running down its back and tail, making it appear somewhat dinosaurian. Its body resembles a yellow hazardous materials suit, with a face resembling a respirator or gas mask, and a zipper-like marking running down its stomach. It has two stubby legs, the feet of which are green. Hazma is one of the few stable Nuclear types, the others being Nucleon and Urayne. Its leaded skin makes it immune to nuclear radiation. In the aftermath of a nuclear accident, groups of Hazma will appear and feed on the radioactive gas, eventually cleaning the air of the area over time. [81]

From a field theoretic standpoint, the description of the interactions of fundamental fields with hadrons is performed in the context of chiral perturbation theory (ChPT, see e.g. Ref. [205] for a review). A full account of mapping a fundamental, parton-level Lagrangian onto its ChPT counterpart will be given elsewhere [85]; here, however, we do provide selected examples of how models where the DM interacts with a *mediator* of specified spin and parity produces ChPT vertices.

As for any effective theory, ChPT possesses a certain range of validity which depends upon the size of some dimensionless parameter, here the ratio of the meson momentum to a scale $\Lambda_{\text{ChPT}} \equiv 4\pi f_\pi \sim 1 \text{ GeV}$. Below we will describe the range of dark matter and mediator masses for which our EFT framework can be reliably used to compute annihilation cross sections and mediator decay rates. The mass ranges dictate which combination of mesons we include in the computational package we hereby present.

In the light DM mass limit, we also found that the standard approach for studying radiative emission from leptonic final states is problematic. In short, utilizing the Altarelli-Parisi splitting function to calculate the final state radiation spectrum assumes that radiating particle's center-of-mass frame energy is much larger than its mass. For $\mathcal{O}(100 \text{ MeV})$ dark matter annihilating into muons, this is not the case. As a result we compute the *exact* spectrum for a few model cases. We also provide spectra for the final state radiation off of charged pions, and account for radiative decays of all relevant particles (e.g. $\pi^+ \rightarrow \mu^+ \nu \gamma$, $\pi^+ \rightarrow e^+ \nu \gamma$ etc).

A general issue with light, sub-GeV DM models is that constraints from per-

turbations to the cosmic microwave background (CMB) are generically very strong if the DM freezes out as a thermal relic. Of course there exist a broad variety of workarounds and caveats (see e.g. [94]), but any light DM model is prone to CMB constraints. `hazma` implements such constraints by including functionality for computing electron and positron spectra from dark matter annihilation.

The remainder of this paper is structured as follows. Sec. (5.2) offers a high-level overview of the `hazma` code and introduces the `Theory` class, the main user-facing component of `hazma`. Section (5.3) describes the effective field theory framework used to study sub-GeV dark matter, provides details of the scalar mediator (sec. (5.3.1) and vector mediator (sec. (5.3.2)) models, and describes the particle physics outputs of `hazma`, including cross section, decay widths, and branching fractions. Section (5.4) explains how to calculate gamma-ray spectra from individual annihilation final states, while Sec. (5.5) combines the latter with the scalar- and vector-mediator models to obtain the *overall* gamma-ray spectra from DM annihilation. Section (5.6) describes the calculation of the positron spectra, and, finally, Sec. (5.7) and Sec. (5.8) describe, respectively, gamma-ray and CMB limits. Section (5.9) concludes. Examples of how to use `hazma` are woven throughout the text. Appendix (A) describes the installation process for `hazma`, App. (B) review the basics of using `hazma`, and App. (C) gives examples of more advanced applications of the code, such as incorporating new models. Appendices (D-E) describe modules provided with `hazma` for convenience which can perform arbitrary phase-space integrations and compute photon spectrum for ≥ 3 -body final states.

5.2 Structure of hazma

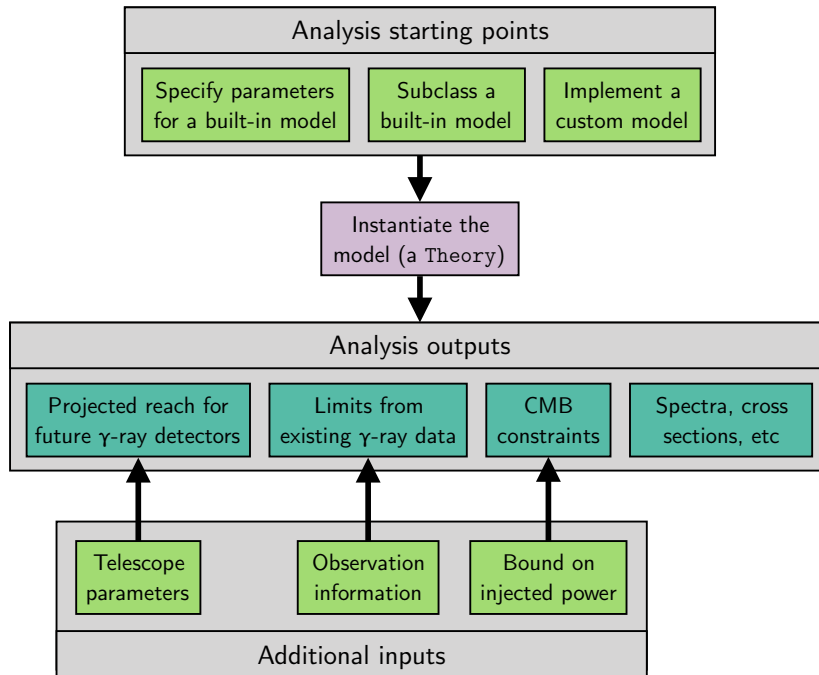


Figure 5.1: **Overview of the hazma workflow, showing different starting points for analyzing sub-GeV dark matter models and possible outputs.** The light green boxes show different types of models the user can analyze. After a model has been instantiated (purple box), various functions can be called to compute the outputs in the dark green boxes.

In this section, we describe the structure of the `hazma` codebase and the intended workflow. The general workflow for a user of `hazma` is shown in Fig. (5.1). The light green boxes at the top indicate the types of physics models a user can study, the dark green boxes show possible analysis outputs, and the light green boxes at the bottom denoting inputs required for these outputs.

The user has several options for tapping into the resources provided by `hazma`. The easiest is to use one of the built-in models, where a user only needs to specify the parameters of the model (see below and Sec. (5.3.1) and Sec. (5.3.2) for details on the built-in models and their corresponding parameters). Alternatively, if the user is working with a model which is a specific version one of the included models (e.g., where the mediator’s couplings to Standard Model particles are interrelated), they can define their own subclass of that model. By using inheritance, one retains all of the functionality of the built-in model (such as functions for computing final state radiation spectra, cross sections, mediator decay widths, etc.) while supplying the user with a simpler, more specialized interface to the underlying models. For a detailed explanations of how to set model parameters and make subclasses of built-in models, see App. (B). Another option is for the user to define their own model. To do this, they need to define a class which contains functions for the gamma-ray and positron spectra, as well as the annihilation cross sections and branching fractions. In App. (C) we provide a detailed example of how to do this for a toy model, utilizing various helper modules provided by `hazma`.

After choosing a model, the user represents it in `hazma` by creating an instance of the `Theory` class (purple box in Fig. (5.1)). Various particle physics quantities (the DM self-annihilation cross section, gamma-ray spectra per DM annihilation, etc) can be computed using the values of the masses and couplings in the `Theory`. Computing constraints on the DM self-annihilation cross section requires additional inputs (green boxes at bottom of Fig. 5.1). To make it straightforward for the user to constrain

models using existing data, `hazma` comes with flux measurements from several gamma-ray telescopes, along with Planck’s upper bound on how much energy DM annihilations could inject into the CMB. For projecting the reach of future gamma-ray telescopes, the user must provide information characterizing the detector.

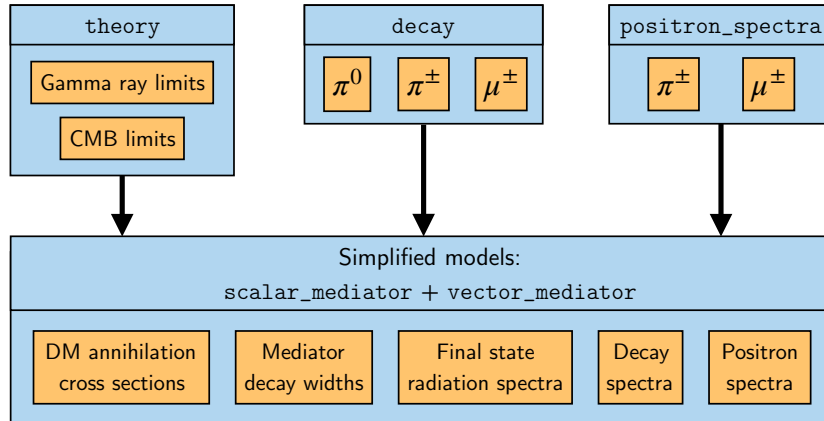


Figure 5.2: **Structure of hazma.** At the core of `hazma` are modules for computing gamma-ray and positron spectra: `decay`, `positron_spectra` and `gamma_ray` `hazma` comes with predefined models located in the `scalar_mediator` and `vector_mediator` modules.

Fig. (5.2) displays the modules contained in `hazma` as well as the general structure of the code, which are explained in detail below.

theory The primary goal of `hazma` is to provide users with a simple interface for setting indirect detection constraints on $\langle\sigma v\rangle$ as a function of DM mass for sub-GeV dark matter models. This is done using the `Theory` abstract base class, which every dark matter model in `hazma` should inherit from. At a high level, it contains three

methods for determining these constraints: one that uses existing gamma-ray data (`Theory.binned_limit`), one for computing the discovery reach for planned gamma-ray detectors (`Theory.unbinned_limit`), and one for deriving CMB constraints (`Theory.cmb_limit`). The class also provides methods for computing particle physics quantities such as annihilation cross sections (with `annihilation_cross_sections`), mediator decay widths (`partial_widths`), the continuum and monochromatic gamma-ray spectra from DM annihilation (`total_spectrum`, `gamma_ray_lines`), and the same for positron spectra (`total_positron_spectrum`, `positron_lines`), and more.

Custom models must implement functions for computing gamma-ray spectra, positron spectra and branching fractions to gain use of the methods in `Theory`. Appendix (C) shows how to implement a simple custom model.

decay This contains high-performance functions for computing the decay spectra from π^\pm, π^0 and μ^\pm . Details of how these are computed are found in Sec. (5.4.3). The functions in this module allow the user to compute the decay spectra for particles decaying with arbitrary lab-frame energies. This requires computing the decay spectra in the rest frame of the parent-particle and performing a Lorentz boost, amounting to performing a change-of-variables along with a convolution integral. To achieve high computational performance, we perform all integrations in `c` using `cython` and build extension modules to interface with `python`.

positron_spectra This module computes the electron/positron spectra from decays of π^\pm and μ^\pm , which are critical inputs for constraining dark matter models using CMB

observations. See Sec. (5.6) for details on how these spectra are computed. As in the `decay` module, the `positron_spectra` module allows users to compute the electron/positron spectra for arbitrary energies of the parent-particle. The procedure for computing the spectra for arbitrary parent-particle energies is identical to the procedure used for `decay`.

`hazma` also ships with various particle physics models of sub-GeV DM. These models are located in the modules `scalar_mediator` and `vector_mediator`, and contain all the relevant annihilation cross sections, branching fractions, decay spectra, FSR spectra and positron spectra. They can be used by instantiating the appropriate class (for example, the `HiggsPortal` class from `scalar_mediator` for the Higgs-portal model.) The user only needs to specify the parameters of the model. The particle physics frameworks used to construct these models, the specialized subclasses of these models included with `hazma`, and accessing functions to compute their annihilation cross sections and other particle physics quantities is the topic of the following section.

5.3 Particle physics framework

Each of the models distributed with `hazma` contain two BSM particles: a dark matter particle χ and a mediator M that interacts with the DM as well as Standard Model particles. The Lagrangian can be expressed as

$$\mathcal{L} = \mathcal{L}_{\text{SM}} + \mathcal{L}_{\text{DM}} + \mathcal{L}_M + \mathcal{L}_{\text{Int}(M)}, \quad (5.1)$$

which consists of the SM Lagrangian, the free Lagrangians for the Dark Matter (DM) and mediator (M), and the mediator's interactions with the DM and SM fields, collectively included in the term $\mathcal{L}_{\text{Int}(M)}$. For the models currently available in `hazma` the DM is taken to be a Dirac fermion, so that

$$\mathcal{L}_{\text{DM}} = \bar{\chi}(i\not{\partial} - m_{\chi})\chi. \quad (5.2)$$

Both the dark matter and the mediator are taken to be uncharged under the Standard Model gauge group. The Lagrangian is defined in terms of the microscopic degrees of freedom of the Standard Model. However, at the energy scale of interest for self-annihilations of non-relativistic MeV dark matter ($\sqrt{s} \sim 1 - 100$ MeV), quarks and gluons are not the correct strongly-interacting degrees of freedom. We thus match our microscopic Lagrangian onto the effective Lagrangian for pions and other mesons using the techniques of chiral perturbation theory (ChPT) [238, 123, 124, 104, 205]. The models currently implemented in `hazma` utilize leading-order ChPT.

Before describing these models, we review the range of validity of ChPT, which is limited since it is an effective theory. ChPT is organized as an expansion in a small parameter, the meson momentum squared p^2 divided by the squared mass scale associated with loop diagrams, $\Lambda_{\text{ChPT}} \sim 4\pi f_{\pi} \approx 1.2$ GeV, where $f_{\pi} = 92.2$ MeV is the pion decay constant. Derivatives of the meson fields and factors of the meson masses are counted as $\mathcal{O}(p)$. The expansion parameter p^2 is used in two ways. First, the chiral Lagrangian is organized as a sum of terms of decreasing importance

$$\mathcal{L}_{\text{ChPT}} = \mathcal{L}^{(2)} + \mathcal{L}^{(4)} + \mathcal{L}^{(6)} + \dots, \quad (5.3)$$

where the superscript indicates the number of derivatives or powers of meson masses. Second, the expansion parameter can be used to assess the relative size of an individual Feynman diagram's contribution in the calculation of a given observable. This is quantified using the *chiral dimension*, which is lower for more important diagrams. Generally the tree-level diagrams from $\mathcal{L}^{(2)}$ have the lowest chiral dimension and provide the largest contributions to observables, followed by tree-level diagrams from $\mathcal{L}^{(4)}$ and one-loop diagrams from $\mathcal{L}^{(2)}$, and so on. As $p^2 \rightarrow \Lambda_{\text{ChPT}}^2$, this scheme for organizing calculations in terms of the chiral dimension breaks down and ChPT becomes unreliable.

Assessing the precise range of validity of leading-order ChPT is complicated. A simple estimate suggests that for processes with meson energies of e.g. 500 MeV the leading-order observables receive $\sim (500 \text{ MeV}/\Lambda_{\text{ChPT}})^2 \sim 20\%$ corrections from next-to-leading-order (NLO) contributions [195]. In reality, the magnitude of NLO corrections is larger for annihilation final states with the same quantum numbers as resonances such as the ρ [180] and $f_0(500)$ [192], since the final state particles can rescatter. While resonances can be accounted for with unitarization techniques [233, 192] or as explicit resonance fields [103, 222], we instead use leading-order ChPT, restricting to DM masses below 250 MeV in the case of annihilation into Standard-Model particles and mediator masses below 500 MeV for analysis of their decays to avoid resonances. An important consequence is that annihilation into kaons and heavier mesons is not considered herein since that would require DM masses far above this range. User-defined models (see App. (C.0.2)) need not use leading-order ChPT, and this is an interesting topic for

future work.

While the preceding discussion is quite general, we now specialize to the two models that come with `hazma`: `scalar_mediator`, which contains a real scalar mediator S , and `vector_mediator`, where the mediator is a vector V ³. These are subclasses of the abstract class `Theory`, and thus implement a variety of functions for computing physical quantities. In the following two subsections, we present $\mathcal{L}_{\text{Int}(S)}$ and $\mathcal{L}_{\text{Int}(V)}$ at the level of quarks and gluons as well as the Lagrangians obtained by performing the ChPT matching.⁴ Snippets are provided to demonstrate how to construct each model and change its parameters. The third subsection shows how to access various particle physics quantities in `hazma`.

5.3.1 Scalar Mediator

The free Lagrangian for a real scalar is

$$\mathcal{L}_S = \frac{1}{2}(\partial_\mu S)(\partial^\mu S) - \frac{1}{2}m_S^2 S^2, \quad (5.4)$$

where m_S is the scalar's mass. The interactions with the light fundamental SM degrees of freedom read

$$\begin{aligned} \mathcal{L}_{\text{Int}(S)} = -S & \left(g_{S\chi} \bar{\chi}\chi + g_{Sf} \sum_f \frac{y_f}{\sqrt{2}} \bar{f}f \right) \\ & + \frac{S}{\Lambda} \left(g_{SG} \frac{\alpha_{\text{EM}}}{4\pi} F_{\mu\nu} F^{\mu\nu} + g_{SF} \frac{\alpha_s}{4\pi} G_{\mu\nu}^a G^{a\mu\nu} \right). \end{aligned} \quad (5.5)$$

3

⁴The interaction Lagrangians, matching procedure and a review of the chiral Lagrangian are explained in detail in a forthcoming companion paper [85].

The sum runs over fermions with mass below the GeV scale ($f = e, \mu, u, d, s$). Note that the coupling g_{Sf} is outside the sum. The Yukawa couplings are defined to be $y_f = \sqrt{2}m_f/v_h$, with the Higgs vacuum expectation value (vev) defined as $v_h = 246$ GeV. The parameter Λ is the mass scale at which S acquires (non-renormalizable) interactions with the photon and gluon.

After performing the matching onto the chiral Lagrangian and expanding to leading order in the pion fields, the resulting interaction Lagrangian is

$$\begin{aligned}
\mathcal{L}_{\text{Int}(S)} = & \frac{2g_{SG}}{9\Lambda} S [(\partial_\mu \pi^0)(\partial^\mu \pi^0) + 2(\partial_\mu \pi^+)(\partial^\mu \pi^-)] \\
& + \frac{4ie g_{SG}}{9\Lambda} S A^\mu [\pi^-(\partial_\mu \pi^+) - \pi^+(\partial_\mu \pi^-)] \\
& - \frac{B(m_u + m_d)}{6} \left(\frac{3g_{Sf}}{v_h} + \frac{2g_{SG}}{3\Lambda} \right) S [(\pi^0)^2 + 2\pi^+\pi^-] \\
& + \frac{B(m_u + m_d)g_{SG}}{81\Lambda} \left(\frac{2g_{SG}}{\Lambda} - \frac{9g_{Sf}}{v_h} \right) S^2 [(\pi^0)^2 + 2\pi^+\pi^-] \\
& + \frac{4e^2 g_{SF}}{9\Lambda} S \pi^+ \pi^- A_\mu A^\mu \\
& - g_{S\chi} S \bar{\chi} \chi - g_{Sf} S \sum_{\ell=e,\mu} \frac{y_\ell}{\sqrt{2}} \bar{\ell} \ell.
\end{aligned} \tag{5.6}$$

where $B = m_{\pi^\pm}^2 / (m_u + m_d) \approx 2800$ MeV [104].

The parameters for the scalar model are attributes of the `scalar_mediator` class. Their names in `hazma` are

$$(m_\chi, m_S, g_{S\chi}, g_{Sf}, g_{SG}, g_{SF}, \Lambda) \leftrightarrow (\text{mx}, \text{ms}, \text{gsxx}, \text{gsff}, \text{gsGG}, \text{gsFF}, \text{lam}).$$

The following snippet shows how to instantiate `scalar_mediator`, change the value of a parameter, and print its new value:

```

>>> from hazma.scalar_mediator import ScalarMediator

>>> sm = ScalarMediator(mx=150., ms=1e3, gsxx=1., gsff=0.1,

...                               gsGG=0.1, gsFF=0.1, lam=2e5)

>>> sm.gsff

0.1

>>> sm.gsff = 0.5

>>> sm.gsff

0.5

```

In addition to the general `scalar_mediator` model, `hazma` also comes with two subclasses of `scalar_mediator`, which represent UV completions: a Higgs-portal model [157] (`HiggsPortal`) and a model containing a heavy quark (`HeavyQuark`.) The Higgs-portal model assumes the scalar mediator interacts with the Higgs through gauge-invariant interactions resulting in the scalar mediator mixing with the Higgs. After diagonalizing the scalar-mediator/Higgs mass matrix, the scalar mediator and Higgs are replaced with:

$$h \rightarrow h \cos \theta - S \sin \theta, \quad S \rightarrow h \sin \theta + S \cos \theta \quad (5.7)$$

where θ is the scalar-mediator/Higgs mixing angle. This replacement results in the following cutoff scale and couplings of the scalar mediator with the Standard Model fermions, gluons and photon, the later of which require integrating out the τ , c , b , t , W

and Z [174]:

$$g_{Sf} = \sin \theta, \quad g_{SG} = 3 \sin \theta, \quad g_{SF} = -\frac{5}{6} \sin \theta, \quad \Lambda = v_h. \quad (5.8)$$

where $v_h = 246$ GeV is the Higgs vacuum expectation value. For this model we define $g_{S\chi\chi} \cos \theta \rightarrow g_{S\chi\chi}$ so that

$$\mathcal{L}_{\text{Int}(S)} \supset -g_{S\chi\chi} S \bar{\chi} \chi - g_{S\chi\chi} \frac{\sin \theta}{\cos \theta} h \bar{\chi} \chi. \quad (5.9)$$

The parameters for the **HiggsPortal** class are:

$$(m_\chi, m_S, g_{S\chi}, \sin \theta) \leftrightarrow (\mathbf{m}_\chi, \mathbf{m}_S, \mathbf{g}_{\text{SXX}}, \mathbf{s}\theta). \quad (5.10)$$

The heavy-quark model assumes the existence a new heavy, colored and charged fermion which enters the Lagrangian as:

$$\mathcal{L} \supset i \bar{Q} \not{D} Q - m_Q \bar{Q} Q - \frac{m_Q}{v_h} h \bar{Q} Q - g_{SQ} S \bar{Q} Q \quad (5.11)$$

with $D_\mu = \partial_\mu - ie Q_Q A_\mu - ig_s G_\mu^a \lambda^a / 2$ where Q_Q is the $U_{\text{EM}}(1)$ charge of the heavy-quark. Integrating out the heavy quark induces a cutoff scale and effective couplings of the scalar mediator with gluons and photons:

$$g_{SG} = g_{SQ}, \quad g_{SF} = 2Q_Q^2 g_{SQ}, \quad \Lambda = m_Q. \quad (5.12)$$

Note that integrating out the heavy-quark also induced effective couplings to the SM fermions, but at two-loop order. We do not include these interactions. The parameters for the **HeavyQuark** class are:

$$(m_\chi, m_S, g_{S\chi}, g_{SQ}, m_Q, Q_Q) \leftrightarrow (\mathbf{m}_\chi, \mathbf{m}_S, \mathbf{g}_{\text{SXX}}, \mathbf{g}_{\text{SQ}}, \mathbf{m}_Q, \mathbf{Q}_Q). \quad (5.13)$$

Both of these models can be imported and used in a similar fashion to the generic `ScalarMediator` class. The following snippet displays how to initialize these sub-classes:

```
>>> from hazma.scalar_mediator import HiggsPortal, HeavyQuark
>>> hp = HiggsPortal(mx=150., ms=1e3, gsxx=1., stheta=1e-3)
>>> hq = HeavyQuark(mx=150., ms=1e3, gsxx=1., gsQ=1.0, mQ=1e6, QQ=1.)
```

Trying to set the underlying `ScalarMediator` model's attributes will result in an error when these are fully determined by the attributes of the subclass:

```
>>> hp.gsff          # can only be accessed
0.001
>>> hp.gsff = 0.1  # fully determined by hp.stheta
AttributeError: Cannot set gsff
```

5.3.2 Vector Mediator

For the vector mediator the free part of the Lagrangian is

$$\mathcal{L}_V = -\frac{1}{4}V_{\mu\nu}V^{\mu\nu} + \frac{1}{2}m_V^2V_\mu V^\mu, \quad (5.14)$$

where m_V is the mass of the vector. The interactions considered are

$$\mathcal{L}_{\text{Int}(V)} = V_\mu \left(g_{V\chi} \bar{\chi} \gamma^\mu \chi + \sum_f g_{Vf} \bar{f} \gamma^\mu f \right). \quad (5.15)$$

The sum again runs over the light fermions ($f = e, \mu, u, d, s$), and V may have different couplings to each of these.

A kinetic mixing term between the mediator and photon is also possible:

$$\mathcal{L}_{\text{Int}(V)} \supset -\frac{\epsilon}{2} V^{\mu\nu} F_{\mu\nu}. \quad (5.16)$$

However, this can be eliminated by redefining the photon field using $A_\mu \rightarrow A_\mu - \epsilon V_\mu$. Upon this field redefinition V acquires an ϵ -suppressed interaction with the SM fermions, which is captured by changing the fermion couplings

$$g_{Vf} \rightarrow g_{Vf} - \epsilon e Q_f, \quad (5.17)$$

where Q_f is the electric charge of the fermion f and $e > 0$ is the electron's charge. Because of this, we do not include ϵ as a coupling in the vector model, and instead provide a subclass `KineticMixing` to handle this case.

Matching onto the chiral Lagrangian and isolating the terms contributing at leading order to the quantities computed in `hazma` gives

$$\begin{aligned} \mathcal{L}_{\text{Int}(V)} = & -i(g_{Vu} - g_{Vd})V^\mu (\pi^+ \partial_\mu \pi^- - \pi^- \partial_\mu \pi^+) \quad (5.18) \\ & + (g_{Vu} - g_{Vd})^2 V_\mu V^\mu \pi^+ \pi^- \\ & + 2e(Q_u - Q_d)(g_{Vu} - g_{Vd})A_\mu V^\mu \pi^+ \pi^- \\ & + V_\mu (g_{Ve} \bar{e} \gamma^\mu e + g_{V\mu} \bar{\mu} \gamma^\mu \mu) \\ & + \frac{1}{8\pi^2 f_\pi} \epsilon^{\mu\nu\rho\sigma} (\partial_\mu \pi^0) \\ & \quad \times \{e(2g_{Vu} + g_{Vd}) [(\partial_\nu A_\rho) V_\sigma + (\partial_\nu V_\rho) A_\sigma] \\ & \quad + 3(g_{Vu}^2 - g_{Vd}^2) (\partial_\nu V_\rho) V_\sigma\}. \end{aligned}$$

The contributions in the last three lines come from matching onto the anomalous terms in the chiral Lagrangian [244, 239, 205, 123], which is explained in detail in our compan-

ion paper [85]. While these terms come from the NLO chiral Lagrangian, the resulting final states contribute significantly to the gamma-ray spectra, so we include them here. In particular, in the case where V couples only to quarks, the *only* final state accessible below the two-pion threshold is $\pi^0\gamma$. In contrast, other terms from the NLO chiral Lagrangian only lead to corrections for scattering rates into final states accessible at tree-level, and are thus not included.

The correspondence between the microscopic parameters for the vector model and attributes of the base `vector_mediator` class is⁵

$$(m_\chi, m_V, g_{V\chi}, g_{Vu}, g_{Vd}, g_{Vs}, g_{Ve}, g_{V\mu}) \\ \leftrightarrow (\text{mx}, \text{mv}, \text{gvxx}, \text{gvuu}, \text{gvdd}, \text{gvss}, \text{gvee}, \text{gvmumu}).$$

The following snippet shows how to instantiate `vector_mediator`:

```
>>> from hazma.vector_mediator import VectorMediator
>>> vm = VectorMediator(mx=150., mv=1e3, gvxx=1., gvuu=0.1,
...                       gvdd=0.2, gvss=0.0, gvee=0.4,
...                       gvmumu=0.5)
```

For the subclass `KineticMixing` which handles the important case of a kinetically-mixed mediator, the parameters are

$$(m_\chi, m_V, g_{V\chi}, \epsilon) \leftrightarrow (\text{mx}, \text{mv}, \text{gvxx}, \text{eps}).$$

While the underlying parameters `gvuu`, \dots , `gvmumu` can be accessed by instances of `KineticMixing`, they cannot be set directly since they are fully determined by `eps`:

⁵Note that `gvss` is not currently used since `vector_mediator` is based on leading-order ChPT.

```

>>> from hazma.vector_mediator import KineticMixing

>>> km = KineticMixing(mx=150., mv=1e3, gvxx=1., eps=0.1)

>>> km.gvuu

-0.020187846690459792 # = -0.1 * 2/3 * sqrt(4 pi / 137)

>>> km.gvuu = 0.1

AttributeError: Cannot set gvuu

```

Finally, the subclass `QuarksOnly` is provided for analyzing the case where the mediator is hadrophilic and has only couplings to quarks. The parameters are those for the full vector-mediator model, with the leptonic couplings set to zero.

5.3.3 Computing Particle physics quantities

Every model in `hazma` is required to implement functions listing the available annihilation final states and providing corresponding functions for computing annihilation cross sections. For example, for the models described above we have:

```

>>> ScalarMediator.list_annihilation_final_states()

['mu mu', 'e e', 'g g', 'pi0 pi0', 'pi pi', 's s']

>>> VectorMediator.list_annihilation_final_states()

['mu mu', 'e e', 'pi pi', 'pi0 g', 'pi0 v', 'v v']

```

These lists *exclude* final states where the annihilation is extremely suppressed by couplings or phase-space factors (e.g., $\pi^+\pi^-\gamma\gamma$, $S\pi^0\pi^0$, $S\pi^+\pi^-$ for the scalar model). They also exclude final states arising from radiative processes (such as $e^+e^-\gamma$). Depending

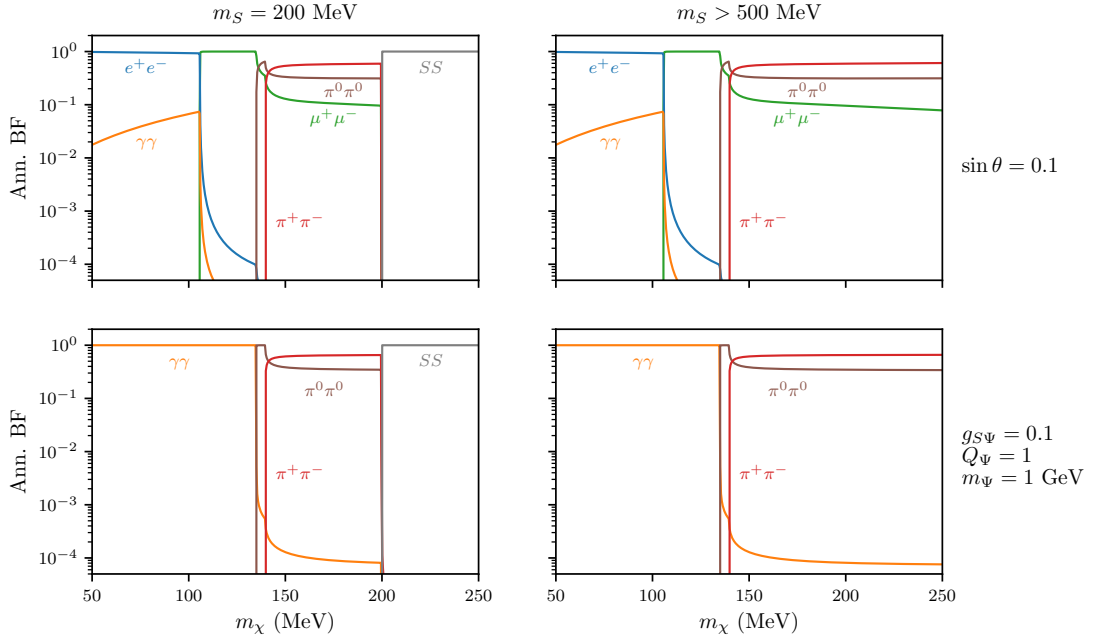

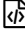


Figure 5.3: **Annihilation branching fractions for the scalar mediator model.**

The coupling $g_{S\chi\chi}$ between the DM and mediator is set to one. The rows correspond to the Higgs portal and heavy quark UV completions and the columns are for a light (left) and heavy (right) mediator.  

on the couplings' values and the center of mass energy of the DM, some of these final state may be inaccessible.

The corresponding annihilation cross sections and branching fractions can be accessed using the `annihilation_cross_sections` function:

```

>>> from hazma.scalar_mediator import ScalarMediator

>>> sm = ScalarMediator(mx=180., ms=190., gsxx=1., gsff=0.1,
...
                           gsGG=0.1, gsFF=0.1, lam=2e5)

```

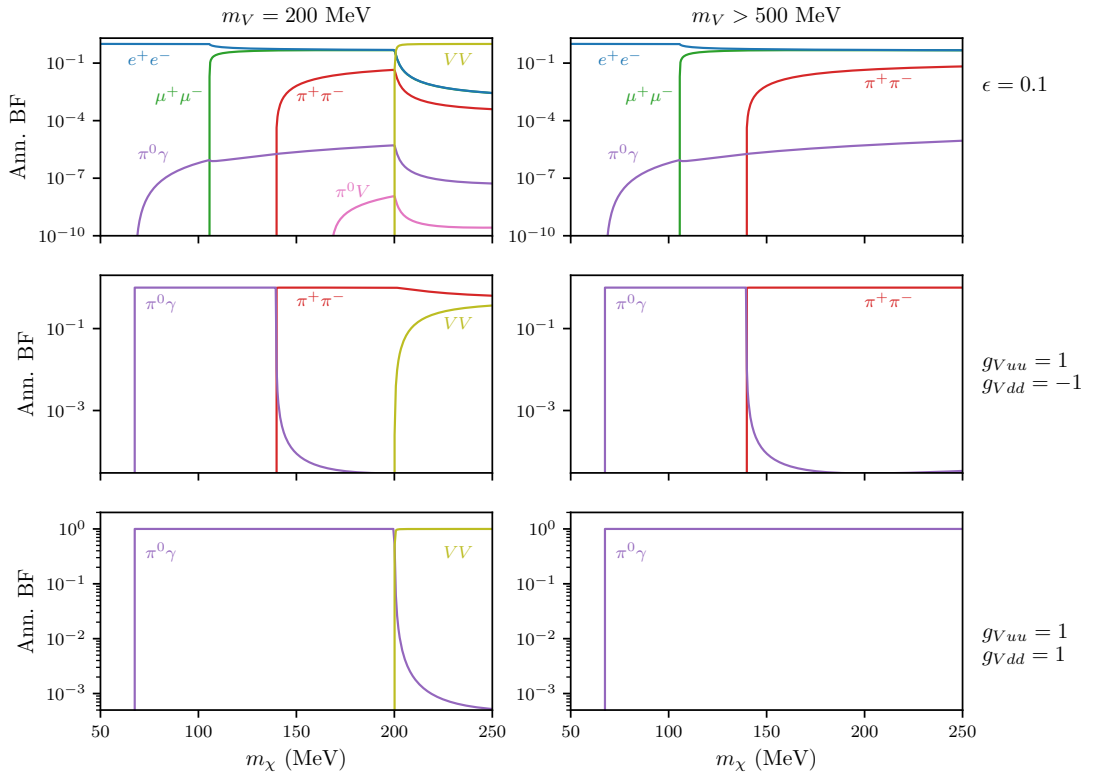




Figure 5.4: **Annihilation branching fractions for the vector mediator model.**

The coupling $g_{S\chi\chi}$ between the DM and mediator is set to one. The rows correspond to a kinetically mixed mediator and a mediator with couplings only to quarks, and the columns are for a light (left) and heavy (right) mediator.  

```

>>> e_cm = 400.

>>> sm.annihilation_cross_sections(e_cm) # MeV^-2

{'mu mu': 1.018678054222354e-16,
 'e e': 3.892649866478948e-21,
 'g g': 2.4381469306302895e-21,

```

```

'pi0 pi0': 7.975042237472552e-17,
'pi pi': 1.5169347389281449e-16,
's s': 1.78924656025887e-07,
'total': 1.7892465635920504e-07}

```

Note that in this example $m_\chi < m_S$, but the center of mass energy is large enough to allow the process $\bar{\chi}\chi \rightarrow SS$. The function

`Theory.annihilation_branching_fractions()` is invoked the same way and returns a `dict` of branching fractions for annihilation into each final state X :

$$\text{BF}(\bar{\chi}\chi \rightarrow X) = \frac{\sigma_{\bar{\chi}\chi \rightarrow X}}{\sum_Y \sigma_{\bar{\chi}\chi \rightarrow Y}} \quad (5.19)$$

Fig. (5.3) shows the annihilation branching fractions for the scalar model. The different rows exhibit results for the Higgs portal and heavy quark UV completions discussed above, which will be referred to throughout this work. In the first case, the branching fraction is largest into whichever final state is closest to threshold since S couples to Standard Model states roughly proportionally to their Yukawas. The branching fraction into $\gamma\gamma$ is small for non-relativistic DM annihilations due to the derivative coupling between S and the photon field. For the heavy quark coupling pattern only hadronic final states are accessible since the mediator couplings exclusively to photons and gluons.

Fig. (5.4) collects the branching fractions for the vector model, assuming it kinetically mixes with the photon (top row) or couples only to quarks (middle and bottom rows). The coupling-dependence of the vector's cross sections can be understood

without performing detailed calculations. Since the vector model can be recast as a U(1) gauge theory (by using the Stuckelberg mechanism to generate the mass term and decoupling the Stuckelberg field), the vector's couplings to pions are the sums of its couplings to their constituents: $g_{V\pi^\pm\pi^\pm} = g_{Vuu} - g_{Vdd}$, $g_{V\pi^0\pi^0} = 0$. The cross section $\sigma_{\tilde{\chi}\chi \rightarrow \pi^+\pi^-}$ is thus proportional to $(g_{Vuu} - g_{Vdd})^2$, explaining why that final state has a branching fraction of zero in the bottom row of the figure. The vector's coupling to $\pi^0\gamma$ and π^0V come from the anomalous part of the chiral Lagrangian. Since the anomaly is exact at one loop, the relevant diagrams in the former case can be evaluated with a proton running in the loop, making it clear that $\sigma_{\tilde{\chi}\chi \rightarrow \pi^0\gamma} \propto (2g_{Vuu} + g_{Vdd})^2$. This cross section is suppressed due to the loop factors, but provides an important contribution to the gamma-ray spectrum. For the coupling choices used for the plots in this work, the spectrum contribution from the π^0V final state is either negligible or identically zero.

Finally, the mediator decay partial widths are easily obtained with the `partial_widths` function:

```
>>> from hazma.scalar_mediator import ScalarMediator
>>> sm = ScalarMediator(mx=120., ms=280., gsxx=1., gsff=0.1,
...                       gsGG=0.1, gsFF=0.1, lam=2e5)
>>> sigmas = sm.partial_widths()
>>> sigmas # MeV
{'g g': 1.472617003459079e-13,
 'pi0 pi0': 3.261686997076484e-09,
```



```

'pi pi': 1.8664869506864194e-09,
'x x': 1.522436123428156,
'e e': 4.798160511838726e-13,
'mu mu': 5.792897882600423e-09,
'total': 1.522436134349855}

```

5.4 Building Blocks of MeV Gamma-Ray Spectra

The total gamma-ray spectrum for dark matter annihilation consists of three parts:

$$\left. \frac{dN}{dE_\gamma} \right|_{\bar{\chi}\chi} = \left. \frac{dN}{dE_\gamma} \right|_{\bar{\chi}\chi,\text{line}} + \left. \frac{dN}{dE_\gamma} \right|_{\bar{\chi}\chi,\text{dec.}} + \left. \frac{dN}{dE_\gamma} \right|_{\bar{\chi}\chi,\text{FSR}}. \quad (5.20)$$

The first term accounts for photons from final states containing one or more monochromatic gamma rays, which result in spectral lines. The second term is the spectrum of photons produced through the radiative decays of final state particles. Decays can produce dramatic spectral features such as the neutral pion “box” as well as E_γ^{-1} spectra. FSR generically produces spectra that scale as $dN/dE_\gamma \propto E_\gamma^{-1}$ at low energies, in accordance with Low’s theorem [170, 59], which could be distinguished from the softer $dN/dE_\gamma \propto E_\gamma^{-\Gamma}$, with $\Gamma \sim 2$ for typical astrophysical background.

The calculations required to account for these contributions are described in detail in this section, beginning with the trivial case of spectral lines and the associated `hazma` functions. The model-dependent FSR spectra are explained in detail since we compute them exactly for leptonic and hadronic final states. With regard to radiative

decays, we present a comprehensive overview of the contributions to the π^\pm decay spectrum, which is currently absent from the literature and thus has not been considered in prior work on sub-GeV DM. Code snippets for computing different decay spectra are included throughout.

The section concludes by showing how to compute FSR and radiative decay spectra in `hazma` for the built-in models. A key feature of `hazma` is that the spectrum functions can be employed to analyze user-defined models, as demonstrated in a detailed example in App. (C.0.2).

5.4.1 Monochromatic Gamma Rays

The only final states containing monochromatic photons that are relevant for this work are $\pi^0\gamma$ and $\gamma\gamma$:

$$\left. \frac{dN}{dE_\gamma} \right|_{\bar{\chi}\chi, \text{line}}(E_\gamma) = \text{Br}(\bar{\chi}\chi \rightarrow \pi^0\gamma) \delta(E_{\pi^0\gamma} - E_\gamma) + 2 \text{Br}(\bar{\chi}\chi \rightarrow \gamma\gamma) \delta(E_{\text{CM}}/2 - E_\gamma), \quad (5.21)$$

where the energy of the line from the $\pi^0\gamma$ final state is $E_{\pi^0\gamma} \equiv (E_{\text{CM}}^2 - m_{\pi^0}^2)/(2E_{\text{CM}})$ and E_{CM} is the center of mass energy. This contribution to the DM annihilation spectrum is thus obtained by computing the branching fractions appearing in this expression.

The `Theory.gamma_ray_lines()` method returns a `dict` with information about monochromatic gamma-ray lines produced in dark matter annihilations. For example, the scalar mediator model has a 2γ line and the vector model has a line from the $\pi^0\gamma$ final state. Assuming heavy quark-type couplings for the former and quark-only couplings for the later, the line energies and branching fractions are found to be

```

>>> from hazma.scalar_mediator import HeavyQuark

>>> sm = HeavyQuark(mx=140., ms=1e3, gsxx=1., gsQ=0.1, mQ=1e3,
↳ QQ=0.1)

>>> sm.gamma_ray_lines(e_cm=300.)

{'g g': {'energy': 150.0, 'bf': 1.285653242415087e-08}}

>>> from hazma.vector_mediator import QuarksOnly

>>> vm = QuarksOnly(mx=140., mv=1e3, gvxx=1., gvuu=0.1, gvdd=0.1,
↳ gvss=0.)

>>> vm.gamma_ray_lines(e_cm=300.)

{'pi0 g': {'energy': 119.63552908740002, 'bf': 1.0}}

```

5.4.2 Final State Radiation

Dark matter annihilating into charged SM particles generically produces photons via final state radiation (FSR), which is accounted for by computing

$$\left. \frac{dN}{dE_\gamma} \right|_{\bar{\chi}\chi, \text{FSR/IB}} = \frac{1}{\sigma_{\bar{\chi}\chi}} \sum_A \frac{d\sigma_{\bar{\chi}\chi \rightarrow A\gamma}(E_\gamma)}{dE_\gamma} \quad (5.22)$$

$$\approx \sum_A \left[\frac{\sigma_{\bar{\chi}\chi \rightarrow A}}{\sigma_{\bar{\chi}\chi}} \right] \left[\frac{1}{\sigma_{\bar{\chi}\chi \rightarrow A}} \frac{d\sigma_{\bar{\chi}\chi \rightarrow A\gamma}(E_\gamma)}{dE_\gamma} \right] \quad (5.23)$$

$$\equiv \sum_A \text{Br}(\bar{\chi}\chi \rightarrow A) \left. \frac{dN}{dE_\gamma} \right|_{\bar{\chi}\chi \rightarrow A}(E_\gamma), \quad (5.24)$$

where in the second line we assumed $\sigma_{\bar{\chi}\chi \rightarrow A\gamma} \ll \sigma_{\bar{\chi}\chi \rightarrow A}$ and the sum is over final states containing electromagnetically-charged particles. The required branching fractions were computed in Sec. (5.3.3).

This spectrum, which we call the Altarelli-Parisi (AP) approximation, has been employed in prior studies of indirect detection of sub-GeV DM [31, 34, 175, 53, 111]. However, the AP approximation is insufficient for our analysis since it is only valid near the mass singularity, i.e. for $\mu_X \ll 1$. This does not hold for MeV DM in the Milky Way halo annihilating non-relativistically into $\mu^+\mu^-$ (or $\pi^+\pi^-$), since in this case $Q \sim m_\mu \sim \mathcal{O}(100 \text{ MeV})$. As a result of this assumption, the AP spectrum cuts off at $x = 1 - \exp(1)\mu^2$, which is different from the exact kinematic threshold $x = 1 - 4\mu^2$.

In this section we instead exactly compute the model-dependent FSR spectra for the e^+e^- and $\mu^+\mu^-$ final states, as well as the $\pi^+\pi^-$ final state. The resulting spectra for leptonic final states are (see chapter 20 of [207] for details of how these calculations can be performed)

$$\left. \frac{dN}{dE_\gamma} \right|_{\bar{\chi}\chi \rightarrow S^* \rightarrow \bar{\ell}\ell} = \frac{\alpha}{E_\gamma \pi (1 - 4\mu^2)^{3/2}} \left[\begin{aligned} & (2(1 - x - 6\mu^2) + (x + 4\mu^2)^2) \log\left(\frac{1 + S(x, \mu)}{1 - S(x, \mu)}\right) \\ & - 2(1 - 4\mu^2)(1 - x)S(x, \mu) \end{aligned} \right] \quad (5.25)$$

$$\left. \frac{dN}{dE_\gamma} \right|_{\bar{\chi}\chi \rightarrow V^* \rightarrow \bar{\ell}\ell} = \frac{\alpha}{E_\gamma \pi \sqrt{1 - 4\mu^2}(1 + 2\mu^2)} \left[\begin{aligned} & (1 + (1 - x)^2 - 4\mu^2(x + 2\mu^2)) \log\left(\frac{1 + S(x, \mu)}{1 - S(x, \mu)}\right) \\ & - (1 + (1 - x)^2 + 4\mu^2(1 - x))S(x, \mu) \end{aligned} \right] \quad (5.26)$$

where $S(x, \mu) = \sqrt{1 - 4\mu^2/(1 - x)}$. The FSR spectrum for the $\pi^+\pi^-$ final state can be computed using the interaction Lagrangians derived in our companion paper [85] and

reproduced in Eqn. (5.6) and (5.18). The final expressions for the spectra are

$$\frac{dN}{dE_\gamma} \Big|_{\bar{\chi}\chi \rightarrow S^* \rightarrow \pi^+ \pi^-} = \frac{2\alpha}{E_\gamma \pi \sqrt{1-4\mu^2}} \left[(1-x-2\mu^2) \log\left(\frac{1+S(x,\mu)}{1-S(x,\mu)}\right) - (1-x)S(x,\mu) \right] \quad (5.27)$$

$$\frac{dN}{dE_\gamma} \Big|_{\bar{\chi}\chi \rightarrow V^* \rightarrow \pi^+ \pi^-} = \frac{2\alpha}{E_\gamma \pi (1-4\mu^2)^{3/2}} \left[(1-x-2\mu^2)(1-4\mu^2) \log\left(\frac{1+S(x,\mu)}{1-S(x,\mu)}\right) - ((1-x)(1-4\mu^2) - x^2) S(x,\mu) \right] \quad (5.28)$$

In Fig. (5.5) we plot the spectra for FSR in the scalar and vector models as well as the AP spectrum (blue, red and yellow curves respectively). As can be seen from the above equations, the specific values of the couplings, mediator masses and DM mass do not impact the shape of the spectrum since they cancel when dividing by $\sigma_{\bar{\chi}\chi \rightarrow \bar{\ell}\ell}$. As expected, the AP approximation performs poorly near the dimuon threshold (upper left panel). The photon energy at which the spectrum cuts off is an order of magnitude too large, and while the normalization is within a factor of two for the scalar model's spectrum, it is an order of magnitude larger than the vector model's one. The situation improves at larger center of mass energies, and just above the $\pi\pi$ threshold the spectra all agree to within a factor of two. The pion FSR spectra are shown in Fig. (5.6).

We demonstrate how to compute these spectra in `hazma` at the end of this section.

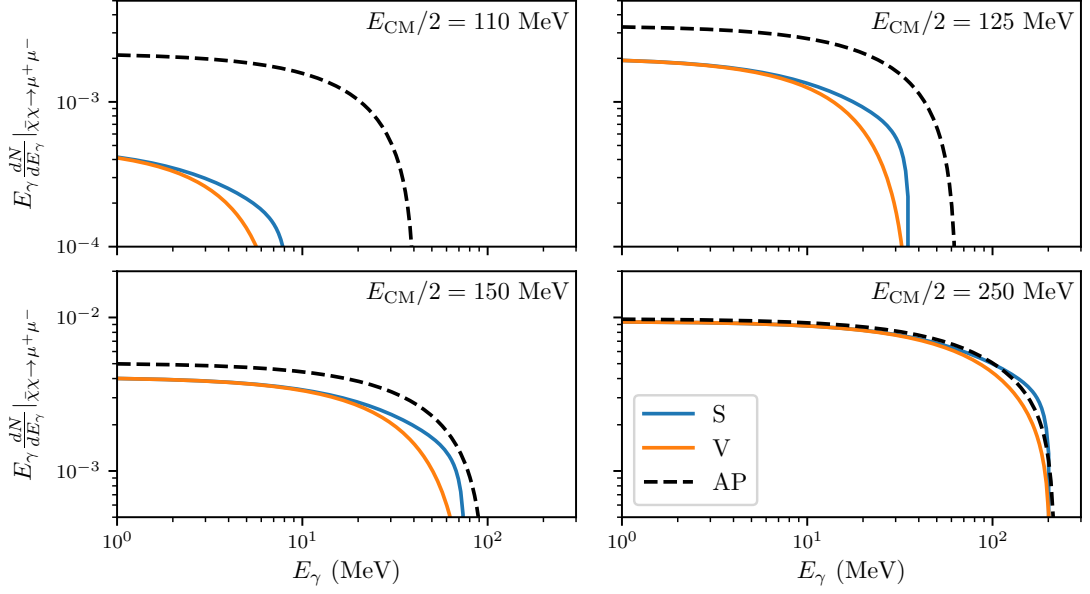




Figure 5.5: **Final state radiation spectrum for dark matter annihilating into $\mu^+\mu^-$.** The curves correspond to the scalar (blue curve) and vector (orange curve) models, with the indicated center of mass energies. The Altarelli-Parisi spectrum from Eqn. (??) is also shown (dashed black curve), illustrating the limiting behavior of the spectra as $m_\ell \ll Q$.  

5.4.3 Radiative Decay Spectra

Photons are produced when dark matter annihilates into a state A that subsequently undergoes radiative decay $A \rightarrow B\gamma$:

$$\left. \frac{dN}{dE_\gamma} \right|_{\tilde{\chi}\tilde{\chi}, \text{dec.}}(E_\gamma) = \sum_A \text{Br}(\tilde{\chi}\tilde{\chi} \rightarrow A) \left. \frac{dN}{dE_\gamma} \right|_A(E_\gamma). \quad (5.29)$$

In addition to collecting well-known expressions for the neutral pion and muon radiative decay spectra, we carefully account for the three dominant contributions to the charge

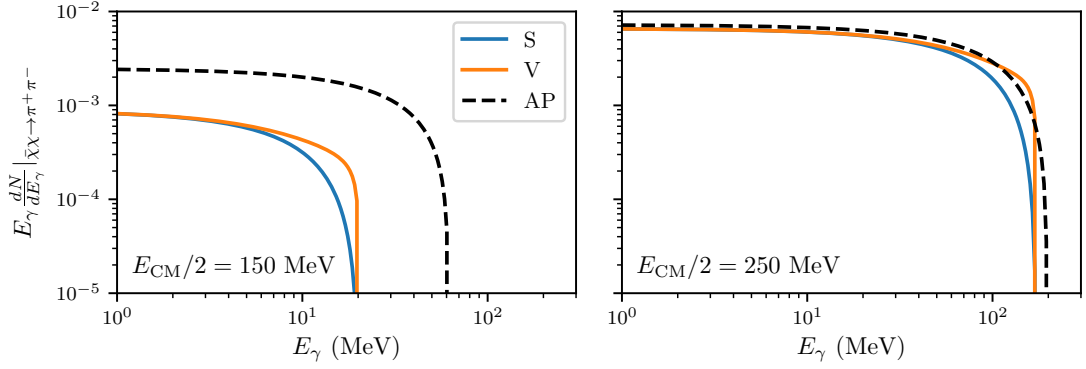




Figure 5.6: **Final state radiation spectrum for dark matter annihilating into $\pi^+\pi^-$.** The blue curve corresponds to the scalar-mediator model and the orange to the vector-mediator case. The dashed black curve shows the Altarelli-Parisi spectrum. The panels are labeled with the annihilation’s center of mass energy.  

pion’s radiative decay spectrum. Functions for computing radiative decay spectra are contained in the `decay` module, and described below. These can be utilized to compute the decay contribution to the annihilation spectrum for arbitrary final states.

5.4.3.1 Decay Spectra in Different Frames

Before computing the radiative decay spectra for the μ^\pm , π^0 and π^\pm , we review how to boost a spectrum dN/dE_R from the parent particle’s rest frame to obtain the “lab frame” spectrum dN/dE_L , where the particle has boost $\gamma = E/m$ along the z -axis. Let the photon phase space coordinates be $(E_R, \cos\theta_R)$ in the rest frame and $(E_L, \cos\theta_L)$ in the lab frame, where θ_R and θ_L are the angles with respect to the z axis and we have assumed azimuthal symmetry. Since the number of photons in a small

patch of phase space does not depend on which coordinates we choose, we have

$$dN = f(E_R, \cos \theta_R) dE_R d \cos \theta_R \quad (5.30)$$

$$= \left| \begin{array}{cc} \frac{dE_R}{dE_L} & \frac{dE_R}{d \cos \theta_L} \\ \frac{d \cos \theta_R}{dE_L} & \frac{d \cos \theta_R}{d \cos \theta_L} \end{array} \right| f(E_R(E_L, \cos \theta_L), \cos \theta_R(E_L, \cos \theta_L)) dE_L d \cos \theta_L, \quad (5.31)$$

where we recognize the partial phase space density as $f(E, \cos \theta) \equiv dN/(dE d \cos \theta)$ and the term with the two vertical lines is the Jacobian factor for the change of variables. If $f(E_R, \cos \theta_R)$ is independent of $c\theta_R$ (which is the case for all the spectra we will consider), we can write:

$$f(E_R, c\theta_R) = \frac{1}{2} \frac{dN}{dE_R}. \quad (5.32)$$

The variables $E_1, E_2, c\theta_1$ and $c\theta_2$ are related via a Lorentz boost. The relationships are

$$E_R = \gamma E_L (1 - \beta c\theta_L), \quad \cos \theta_R = \frac{\beta - \cos \theta_L}{1 - \beta \cos \theta_L}, \quad (5.33)$$

where $\beta = \sqrt{1 - 1/\gamma^2}$ is the particle's velocity in natural units. The spectrum in the lab frame is then obtained by integrating Eqn. (5.30) over $\cos \theta_L$:

$$\frac{dN}{dE_L} = \int \cos \theta_L \frac{1}{2\gamma(\beta \cos \theta_L - 1)} \frac{dN}{dE_R}. \quad (5.34)$$

5.4.3.2 Neutral Pions

The dominant decay mode for neutral pions is $\pi^0 \rightarrow \gamma\gamma$ with a branching fraction of about 99%. Due to this decay modes' large branching fraction and the fact that it has two photons in the final state, we ignore the π^0 's other decay modes. In the

pion's rest frame, the gamma-ray spectrum is trivial:

$$\left. \frac{dN}{dE_\gamma} \right|_{\pi^0} (E_{\pi^0} = m_{\pi^0}) = 2 \times \delta \left(E_R - \frac{m_\pi}{2} \right) \quad (5.35)$$

where the factor of 2 comes from the fact that there are two photons in the final state.

Applying Eqn. (5.34) gives that the gamma ray spectrum in the laboratory frame is

$$\left. \frac{dN}{dE_\gamma} \right|_{\pi^0} (E_{\pi^0}) = \int \cos \theta_L \frac{1}{2\gamma(\beta \cos \theta_L - 1)} 2 \times \delta \left(E_R - \frac{m_{\pi^0}}{2} \right) \quad (5.36)$$

$$= \frac{2}{\gamma\beta m_{\pi^0}} [\theta(E_\gamma - E_-) - \theta(E_\gamma - E_+)] \quad (5.37)$$

with $E_\pm = m_{\pi^0}/2\gamma(1 \mp \beta)$, which is the characteristic box spectrum centered at $m_{\pi^0}/2$.

The boosted spectrum can be computed in `hazma` as follows:

```
>>> from hazma.decay import neutral_pion as dnnde_pi0
>>> e_gams = np.array([100., 125., 150]) # photon energies
>>> e_pi0 = 180. # pion energy
>>> dnnde_pi0(e_gams, e_pi0)
array([0.0165965, 0.0165965, 0.] )
```

5.4.3.3 Muons

The primary muon decay channel is $\mu^- \rightarrow e^- \bar{\nu}_e \nu_\mu$. The photon in the corresponding radiative decay $\mu^- \rightarrow e^- \bar{\nu}_e \nu_\mu \gamma$ has the following spectrum in the muon's rest

frame [159]:

$$\frac{dN}{dE_\gamma} \Big|_{\mu^\pm}(E_\mu = m_\mu) = \frac{\alpha(1-x)}{36\pi E_\gamma} \left[12 \left(3 - 2x(1-x)^2 \right) \log\left(\frac{1-x}{r}\right) + x(1-x)(46 - 55x) - 102 \right], \quad (5.38)$$

where $r \equiv (m_e/m_\mu)^2$, $x \equiv 2E_\gamma/m_\mu$ and the kinematic bounds on E_γ translate into $0 \leq x \leq (1-r)$. To obtain the spectrum in the lab frame we substitute the above expression into Eqn. (5.34) and evaluate the integral numerically.

The lab-frame decay spectrum can be compute for arbitrary muon energies using:

```
>>> from hazma.decay import muon as dnnde_mu

>>> e_gams = np.array([1., 10., 100.]) # photon energies

>>> e_mu = 130. # muon energy

>>> dnnde_mu(e_gams, e_mu)

array([1.76076858e-02, 1.34063877e-03, 4.64775301e-08])
```

5.4.3.4 Charged Pions

The dominant pion decay is $\pi^+ \rightarrow \ell^+ \nu_\ell$, where $\ell = e, \mu$ and ℓ is produced approximately on shell, thanks to the narrow width approximation when $\ell = \mu$. Contributions to the pion’s radiative decay spectrum come from initial state radiation from the photon or FSR from the lepton, as well as emission from virtual hadronic states (the “structure-dependent” component). An expression for $d^2\Gamma_{\pi^+ \rightarrow \ell^+ \nu_\ell \gamma}/dx dy$ is given

in Eqn. (72) of [57] and Eq. (68.3) in the Review of Particle Physics [228]⁶, where $x \equiv 2E_\gamma/m_{\pi^+}$ and $y \equiv 2E_\ell/m_{\pi^+}$. After changing to the Mandelstam variables

$$s \equiv (p_\pi - p_\gamma)^2 = m_{\pi^+}^2(1 - x),$$

$$t \equiv (p_\pi - p_\ell)^2 = m_{\pi^+}^2 \left(1 - y + \frac{m_\ell^2}{m_{\pi^+}^2} \right),$$

integrating over $0 \leq t \leq (m_{\pi^+}^2 - s)(s - m_\ell^2)/s$, and dividing by the total π^+ decay width, we obtain an analytic expression for this channel's contribution to the π^+ decay spectrum:

$$\text{Br}(\pi^+ \rightarrow \ell^+ \nu_\ell) \cdot \left. \frac{dN}{dE_\gamma} \right|_{\pi^+ \rightarrow \ell^+ \nu_\ell} (E_{\pi^+} = m_{\pi^+}) \quad (5.39)$$

$$= \frac{\Gamma_{\pi^+ \rightarrow \ell^+ \nu_\ell}}{\Gamma_{\pi^+}} \cdot \frac{\alpha(f(x) + g(x))}{24\pi m_{\pi^+} f_\pi^2 (r-1)^2 (x-1)^2 r x}, \quad (5.40)$$

where $r \equiv m_\ell^2/m_{\pi^+}^2$ and

$$f(x) = (r + x - 1) [m_{\pi^+}^2 x^4 (F_A^2 + F_V^2) (r^2 - rx + r - 2(x-1)^2)$$

$$- 12\sqrt{2} f_\pi m_{\pi^+} r (x-1) x^2 (F_A(r - 2x + 1) + x F_V)$$

$$- 24 f_\pi^2 r (x-1) (4r(x-1) + (x-2)^2)], \quad (5.41)$$

$$g(x) = 12\sqrt{2} f_\pi r (x-1)^2 \log \left(\frac{r}{1-x} \right) [m_{\pi^+}^2 x^2 (F_A(x-2r) - x F_V)$$

$$+ \sqrt{2} f_\pi (2r^2 - 2rx - x^2 + 2x - 2)]. \quad (5.42)$$

The vector form factor is $F_V(q^2) = F_V(0)(1 + aq^2)$ with $F_V(0) = 0.0254$, slope parameter $a = 0.10$ and $q^2 = 1 - x$; the axial form factor is $F_A = 0.0119$ [228].

⁶Note that the Particle Data Group uses the convention $f_\pi = 130$ MeV, which is a factor of $\sqrt{2}$ larger than the value used in this work.

When $\ell = \mu$, the muon's subsequent radiative decay also contributes significantly to the pion's decay spectrum. Since we can take the muon to be on shell by the narrow width approximation, this decay path's contribution is simply the product of the branching fraction for $\pi^+ \rightarrow \mu^+ \nu_\mu$ and the muon decay spectrum Eqn. (5.38) evaluated at the muon's energy. Our final expression for the charged pion decay spectrum is thus

$$\begin{aligned} \left. \frac{dN}{dE_\gamma} \right|_{\pi^+} (E_{\pi^+} = m_{\pi^+}) &= \sum_{\ell=e,\mu} \text{Br}(\pi^+ \rightarrow \ell^+ \nu_\ell) \cdot \left. \frac{dN}{dE_\gamma} \right|_{\pi^+ \rightarrow \ell^+ \nu_\ell} (E_{\pi^+} = m_{\pi^+}) \\ &+ \text{Br}(\pi^+ \rightarrow \mu^+ \nu_\mu) \cdot \left. \frac{dN}{dE_\gamma} \right|_{\mu^\pm} \left(E_\mu = \frac{m_{\pi^+}^2 + m_\mu^2}{2m_{\pi^+}} \right). \end{aligned} \quad (5.43)$$

This rest frame spectrum can be substituted into Eqn. (5.34) and numerically integrated to obtain the total charged pion radiative decay spectrum.

Fig. (5.7) shows the contributions of each term and the total spectrum in the pion's rest frame. The muon's radiative decay is by far the most important component due to its large branching fraction. There is also more phase space available for the photon in comparison with $\pi^+ \rightarrow \mu^+ \nu_\mu \gamma$ since the other final state particles are massless: the former spectrum cuts off at ~ 69 MeV and the latter at $(m_{\pi^+}^2 - m_\mu^2)/(2m_{\pi^+}) \approx 27$ MeV. The contribution from $\pi^+ \rightarrow e^+ \nu_e \gamma$ is smaller than the others due to helicity suppression.

The charged pion decay spectrum is included in `hazma.decay`:

```
>>> from hazma.decay import charged_pion as dn_de_pi
>>> e_gams = np.array([1., 10., 100.]) # photon energies
>>> e_pi = 150. # pion energy
```

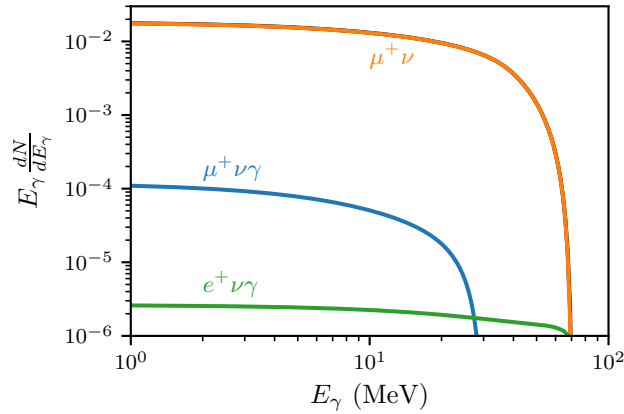

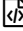


Figure 5.7: **Contributions to the charged pion radiative decay spectrum in the pion's rest frame.** The decay $\pi^+ \rightarrow \mu^+ \nu_\mu$ followed by radiative muon decay is plotted in orange. The other curves show the spectra for $\pi^+ \rightarrow \ell^+ \nu_\ell$, where the photon is produced via initial/final state radiation from the lepton or emission from virtual hadronic states. The total spectrum completely overlaps with the orange curve.  

```
>>> dnnde_pi(e_gams, e_pi)
array([1.76949944e-02, 1.32675207e-03, 1.16607174e-09])
```

The individual contributions can also be computed by setting the `mode` argument. The orange, blue and green curves are obtained using `mode="munu"`, `"munug"` and `"enug"` respectively.

5.4.4 Continuum Gamma-Ray Spectra in `hazma`

Models in `hazma` provide a few methods for computing gamma-ray spectra at different levels of detail. The `total_spectrum` method gives the total *continuum* gamma-ray spectrum at specified photon energies and fixed center-of-mass energy:

```

>>> from hazma.scalar_mediator import HiggsPortal

>>> e_cm = 305. # DM center of mass energy

>>> e_gams = np.array([1., 10., 100.]) # photon energies

>>> hp = HiggsPortal(mx=150., ms=1e3, gsxx=0.7, stheta=0.1)

>>> hp.total_spectrum(e_gams, e_cm)

array([0.02484114, 0.00186874, 0.01827828])

```

Underlying this are methods for computing the gamma-ray spectra for individual final states. These are accessible through the `spectra` method, which also accepts a list of photon energies and a center of mass energies. It returns the total continuum spectrum and the contribution from each final state (ie, dN/dE_γ multiplied by the final state's branching fraction):

```

>>> hp.spectra(e_gams, e_cm)

{'mu mu': array([4.87977497e-03, 3.83154301e-04, 1.22977086e-06]),
 'e e': array([4.19129970e-07, 3.93151015e-08, 2.22413275e-09]),
 'pi0 pi0': array([0.          , 0.          , 0.01827702]),
 'pi pi': array([1.99609455e-02, 1.48554303e-03, 2.28115016e-08]),
 's s': array([0., 0., 0.]),
 'total': array([0.02484114, 0.00186874, 0.01827828])}

```

The `spectra` and `total_spectrum` methods are provided by the `Theory` class, and are driven by the method `spectrum_funcs` which classes inheriting from `Theory` are required to implement. This returns a `dict` whose keys are strings corresponding to

annihilation final states and whose values are methods returning the continuum gamma-ray spectrum for annihilations into that final state (ie, omitting the branching fraction factor).

The models built into `hazma` provide more fine-grained methods for studying different channels' spectra. Each of these has a name corresponding to the final state and takes an additional string argument specifying the spectrum type ("`decay`", "`fsr`" or "`all`", the default). The return value depends on the spectrum type argument. In the first case, the returned spectrum only accounts for the final state particles' radiative decays, which are model-independent. In the second case, the method returns the radiative decay spectrum, which is model-dependent. In the third, default case, the method returns the total continuum spectrum.

For example, in the scalar mediator model, the annihilation final states e^+e^- , $\mu^+\mu^-$, $\pi^0\pi^0$, $\pi^+\pi^-$ and SS contribute to the continuum annihilation spectrum. The following snippet shows how to call the spectrum methods for the instance of `HiggsPortal` created above. The methods all follow the same naming conventions and return dN/dE_γ in MeV^{-1} :

```
>>> from hazma.scalar_mediator import HiggsPortal
>>> e_cm = 305. # DM center of mass energy
>>> e_gams = np.array([1., 10., 100.]) # photon energies
>>> hp = HiggsPortal(mx=150., ms=1e3, gsxx=0.7, stheta=0.1)
>>> hp.dnde_ee(e_gams, e_cm, spectrum_type="fsr")
```

```

>>> array([0.05435176, 0.00509829, 0.00028842])
>>> hp.dnde_ee(e_gams, e_cm, spectrum_type="decay")
>>> array([0., 0., 0.]) # electrons don't decay
>>> hp.dnde_pipi(e_gams, e_cm, spectrum_type="fsr")
>>> array([1.01492577e-03, 5.00245201e-05, 0.00000000e+00])
>>> hp.dnde_pipi(e_gams, e_cm, spectrum_type="decay")
>>> array([3.53972084e-02, 2.65985674e-03, 4.16120296e-08])
>>> hp.dnde_pipi(e_gams, e_cm)
>>> array([3.64121342e-02, 2.70988126e-03, 4.16120296e-08])

```

5.5 Gamma Ray Spectra from DM annihilation

Using the ingredients described in the previous section, we now compute the photon spectra from DM annihilation for the scalar and vector models with the same couplings as in Fig. (5.3) and Fig. (5.4). In what follows, the center of mass energy is set to the non-relativistic approximation $E_{CM} = 2m_\chi (1 + \frac{1}{2}v_{MW}^2)$, where $v_{MW} = 10^{-3}c$ is the fiducial velocity dispersion for the Milky Way.

Fig. (5.8) displays the spectrum for the scalar model when annihilation into the mediator is kinematically prohibited ($m_S \gtrsim m_\chi$). The dark matter mass is fixed for each column and the model parameters in each row. Individual final states' spectra are indicated by the colored curves. To visualize the di-photon final state's contribution, the black curve shows the total spectrum convolved with a 5% energy resolution function (the case for COMPTEL [145]), with a vertical dashed line highlighting the photons'

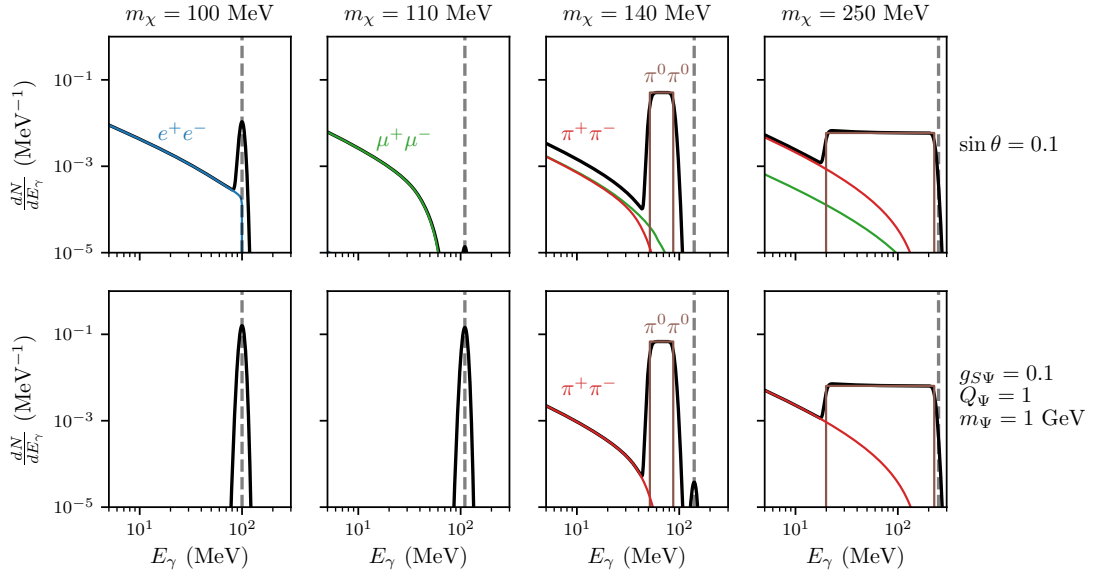




Figure 5.8: **Spectra from DM annihilation into Standard Model particles for scalar-mediator models.** The two-mediator final state is kinematically forbidden.

The black curve is the total spectrum as seen by an instrument with 5% energy resolution. The labeled colored curves are the spectra for individual final states, and the vertical dashed line marks the photons' energies in the $\gamma\gamma$ final state. The rows correspond to Higgs portal and heavy quark coupling patterns. The DM mass is fixed to the indicated value in each column.  

energies ($E_{\text{CM}}/2$).

For low DM masses, the electron and di-photon line are responsible for the spectrum. Above the muon threshold the Yukawa-suppressed electron contribution is negligible. Since the branching fractions into different pion species are identical (up to isospin-breaking corrections proportional to $m_{\pi^\pm} - m_{\pi^0}$), the charged pion spectrum is

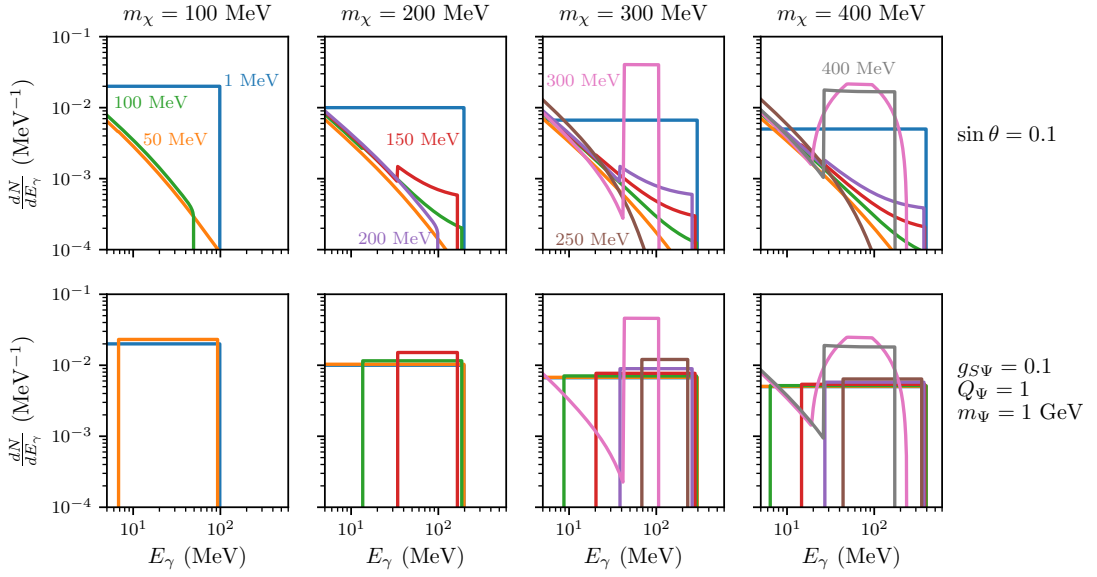

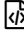


Figure 5.9: **Spectra from DM annihilation into mediators for scalar-mediator models.** Curves are only shown when $E_{\text{CM}} \geq 2m_S$, and are labeled with the corresponding mediator mass. The spectra have not been convolved with an energy resolution function since the SS final state does not produce gamma-ray lines.  

always sub-dominant to the neutral pion box for $E_{\text{CM}} > 2m_\pi$. Depending on the ratio of the microscopic coupling to photons (g_{SF}) with the couplings to gluons and fermions (g_{SG} and g_{Sf}), the neutral pion box or di-photon line are generally the most distinctive spectral features for large DM masses, which can also be seen in the figure. Note that if g_{Sff} and g_{SGG} are considered as independent parameters, they can take values such that the cross section for annihilation into pions is zero, though this scenario is very fine-tuned.

Spectra for annihilation into *mediators* are shown in Fig. (5.9). The panels are

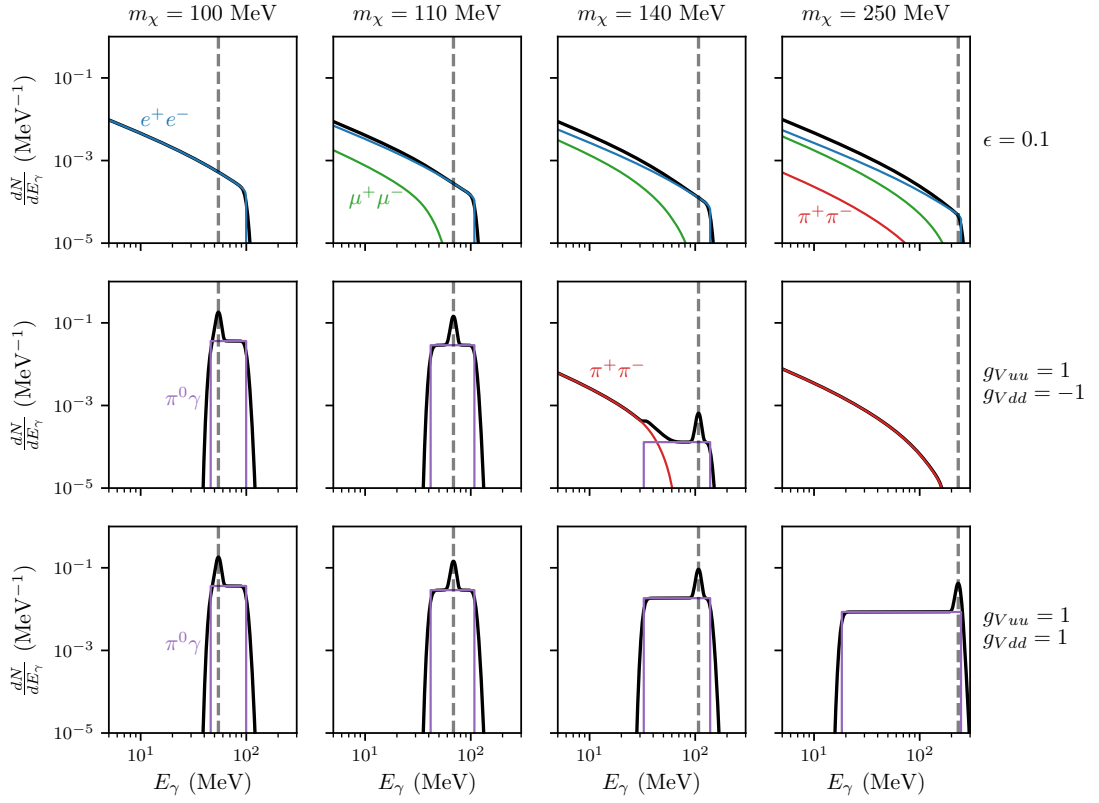

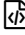


Figure 5.10: **Spectra from DM annihilation into Standard Model particles for vector-mediator models.** The two-mediator final state is taken to be kinematically forbidden. The black curve is the total spectrum as seen by an instrument with 5% energy resolution. The rows correspond to the case where the mediator kinetically mixes with the photon and where it couples only to quarks. The vertical dashed line indicates the energy of the photon in the $\pi^0\gamma$ final state.  

labeled with the DM mass and the different colored curves are the spectra computed with the scalar's mass set to the indicated values. For different mediator masses, the following processes dictate the shape of the spectrum:

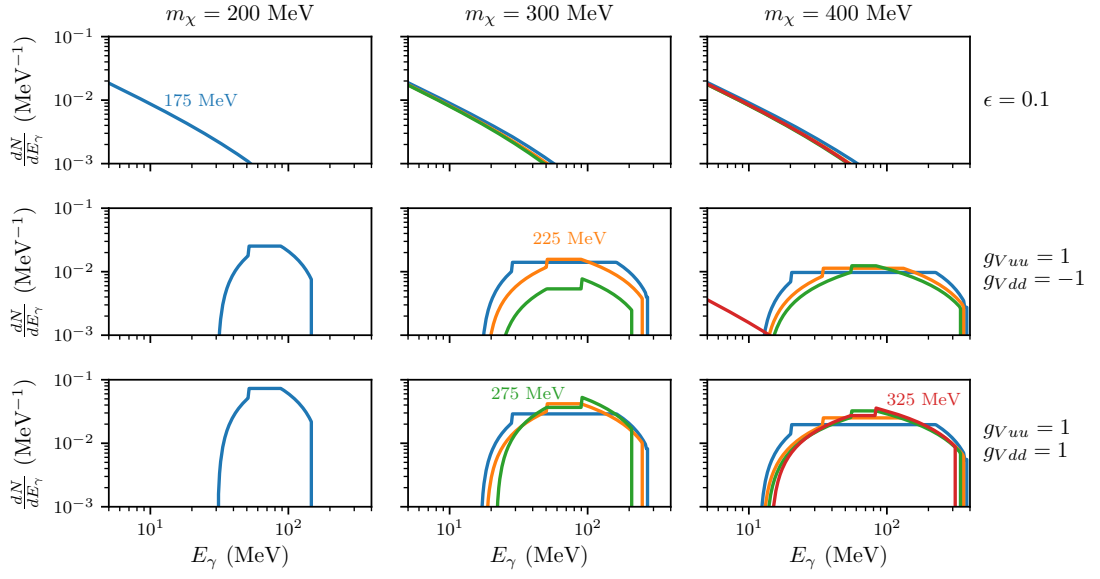

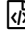


Figure 5.11: **Spectra from DM annihilation into mediators for vector-mediator models.** The labels and colors indicate the value of m_V for each curve.  

- $m_S < 2m_e$: the mediator can only decay to two photons, so the annihilation spectrum is a box centered at $m_S/2$, just like for the neutral pion.
- $2m_e < m_S < 2m_\mu$: the spectrum is a superposition of the box and the electron FSR spectra, and when the scalar can decay into two muons this dominates the spectrum.
- $m_S > 2m_\pi$: the spectrum consists of a peak from boosting the π^0 decay spectrum and a softer component from FSR and decays from the other final states into which S decays. The peak is more rounded if the scalar is highly boosted ($m_S \ll E_{\text{CM}}/2$) and boxy for $m_S \sim E_{\text{CM}}/2$. The difference in the case of heavy quark microscopic couplings is that the muon and electron final states are not present.

The components of the spectrum for DM annihilation into SM final states in the vector model are illustrated in Fig. (5.10). In the kinetic mixing case the spectrum consists purely of a continuum, since the branching fraction for annihilation into $\pi^0\gamma$ is highly suppressed. In contrast, if the vector couples only to quarks the spectrum is composed of a monochromatic gamma ray line and box from the π^0 decay at low energies. If not forbidden by the vector's couplings (as is the case for the bottom row), as the center-of-mass energy grows above the two-pion threshold the continuum of photons from the $\pi^+\pi^-$ final state overwhelm those from $\pi^0\gamma$.

Fig. (5.11) exhibits spectra from DM annihilating into VV followed by the vectors' decays for a kinetically mixed vector (top row) and couplings to quarks only. As in the case of annihilations directly into SM particles, a power law spectrum is obtained in the kinetically mixed case. For the spectrum for quark-only couplings (middle and bottom rows) is sourced exclusively by the vector's decay to $\pi^0\gamma$. The resulting spectrum is comprised of a box (from the boosting the monochromatic photon) and a rounded peak (from boosting the neutral pion's decay spectrum). This feature would only be observable at a detector with very good energy resolution.

The colored curves in the Fig. (5.8)-(5.11) can be reproduced using the `Theory.spectra()` function described in Sec. (5.4.4). The total spectrum convolved with an energy resolution function can be obtained using `Theory.total_conv_spectrum_fn()`. The arguments specify the range of photon energies over which to perform the convolved spectrum, the center of mass energy of the DM annihilation, the energy resolution function, and the number of points to use when

computing the convolution:

```
>>> from hazma.scalar_mediator import HiggsPortal
>>> e_cm = 305. # DM center of mass energy
>>> e_min, e_max = 1., 100. # define energy range
>>> energy_res = lambda e: 0.05 # 5% energy resolution function
>>> hp = HiggsPortal(mx=150., ms=1e3, gsxx=0.7, stheta=0.1)
>>> dn_de_conv = hp.total_conv_spectrum_fn(
...     e_min, e_max, e_cm, energy_res, n_pts=1000)
```

Decreasing `n_pts` from its default value of 1000 increases speed at the cost of accuracy.

The return value (`dn_de_conv` above) is an interpolator of type

`InterpolatedUnivariateSpline` from the `scipy.interpolate` module. This can be used to compute the spectrum at a particular photon energy:

```
>>> dn_de_conv(25.)
array(0.00048767)
```

This spectrum is can easily and efficiently be integrated over a range of photon energies between `e_min` and `e_max`:

```
>>> dn_de_conv.integral(25., 85.)
0.815998464406668
```

5.6 Electron and Positron Spectra from DM annihilation

Dark matter annihilation in the mass range under consideration produces relativistic electrons and positrons. Such particles could be in principle directly detected as part of the cosmic radiation, albeit at energies well below the GeV solar modulation strongly affects cosmic-ray electron spectra. Additionally, relativistic electrons and positrons can be indirectly detected through (1) effects on photons of the cosmic microwave background and (2) the secondary emission of radiation via e.g. up-scattering of background photons (inverse Compton processes), synchrotron radiation, and bremsstrahlung. The calculation of the electron-positron spectra for MeV dark matter is therefore needed to reliably compute CMB limits and the spectrum of secondary radiation.

In this section we compute the positron spectrum for MeV dark matter, which follows along the lines of the gamma-ray ones.⁷ The spectrum consists of a line-like spectrum from $\bar{\chi}\chi \rightarrow e^+e^-$ and a continuum piece from the decays of unstable particles:

$$\left. \frac{dN}{dE_{e^+}} \right|_{\bar{\chi}\chi} (E_{e^+}) = \text{Br}(\bar{\chi}\chi \rightarrow e^+e^-) \delta(E_{\text{CM}}/2 - E_{e^+}) + \left. \frac{dN}{dE_{e^+}} \right|_{\bar{\chi}\chi, \text{dec}} (E_{e^+}) \quad (5.44)$$

For the scalar and vector model, the decay piece receives contributions from the $\mu^+\mu^-$ and $\pi^+\pi^-$ final states.

The muon decays nearly 100% of the time through $\mu^+ \rightarrow e^+\nu_e\bar{\nu}_\mu$. In the muon's rest frame, the positron's energy spectrum is [181]

⁷The electron spectrum looks identical to the positron one since our dark matter particles do not carry lepton number.

$$\frac{dN}{dE_{e^+}} = -\frac{4\sqrt{x^2 - 4r^2} (r^2(4 - 3x) + x(2x - 3))}{m_\mu} \quad (5.45)$$

where $r = m_e/m_\mu$ and $x = 2E_{e^+}/m_\mu$. The spectrum can be boosted to other frames using Eqn. (5.34). It is accessible in `hazma` using:

```
>>> from hazma.positron_spectra import muon as dn_de_p_mu
>>> e_mu = 150. # muon energy
>>> e_p = np.array([1., 10., 100.]) # positron energies
>>> dn_de_p_mu(e_p, e_mu)
array([4.86031362e-05, 4.56232320e-03, 4.45753994e-03])
```

The charged pion primarily decays through $\pi^+ \rightarrow \mu^+ \nu_\mu$, which yields a positron when the muon decays. The energy spectrum is thus obtained by boosting the muon spectrum from Eqn. (5.45). An additional contribution comes from the monochromatic positron produced through $\pi^+ \rightarrow e^+ \nu_e$, which has a helicity suppressed branching fraction $\text{Br}(\pi^+ \rightarrow e^+ \nu_e) = 1.23 \times 10^{-4}$. The total spectrum can be computed in `hazma` with

```
>>> from hazma.positron_spectra import charged_pion as dn_de_p_pi
>>> e_pi = 150. # charged pion energy
>>> e_p = np.array([1., 10., 100.]) # positron energies
>>> dn_de_p_pi(e_p, e_pi)
array([3.84163631e-05, 3.85242442e-03, 2.55578895e-05])
```

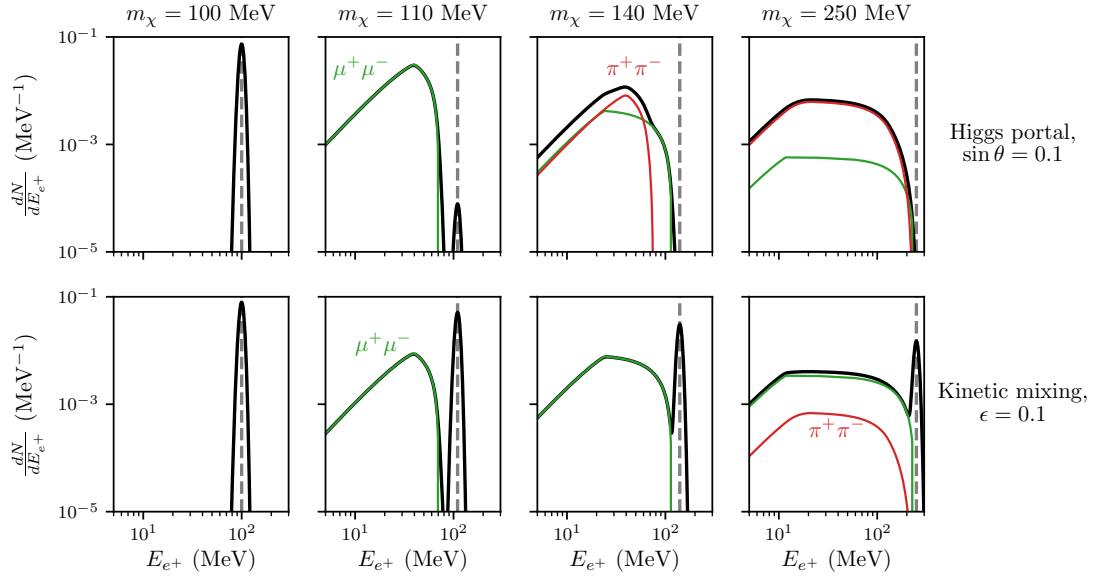





Figure 5.12: **Positron spectra for DM annihilating into Standard Model final states.** Results for the scalar model with Higgs portal couplings are shown in the top row and for the vector model with a kinetically-mixed mediator in the bottom. The grey vertical dashed line indicates the location of the monochromatic $\bar{\chi}\chi \rightarrow e^+e^-$ final state. The total spectrum (black curve) is convolved with a 5% energy resolution function.  

Fig. (5.12) exhibits representative positron annihilation spectra from the scalar model with , and several DM masses (different columns). Changing the couplings to prohibit annihilation into leptons has a straightforward impact on the total spectrum. Here annihilation into mediators is kinematically forbidden. Positron spectra for annihilation into mediators are shown for these models in Fig. (5.13). When the mediator is light the spectrum is box-shaped since the mediator can only produce electrons by

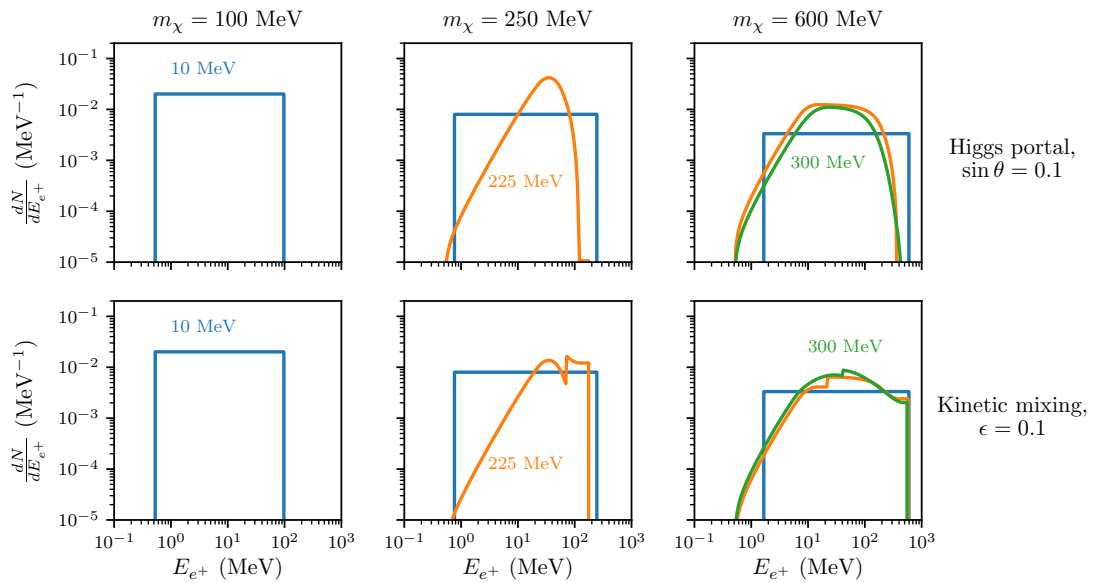




Figure 5.13: **Positron spectra for DM annihilating into two mediators.**  

decaying into them directly. At higher energies the spectrum is a superposition of the rounded spectra from mediator decays into muons and pions and this box spectrum.

The interface for computing positron spectra mirrors the gamma-ray spectrum interface. The `total_positron_spectrum` and `positron_spectra` methods in `Theory` give the total positron spectrum and individual channels’ contributions (scaled by branching fraction). The `positron_lines` method gives information about final states producing monochromatic positrons:

```
>>> from hazma.scalar_mediator import HiggsPortal

>>> e_cm = 305. # DM center of mass energy

>>> e_ps = np.array([1., 10., 100.]) # positron energies

>>> hp = HiggsPortal(mx=150., ms=1e3, gsxx=0.7, stheta=0.1)
```

```

>>> hp.total_positron_spectrum(e_ps, e_cm)

array([2.60677406e-05, 2.58192085e-03, 4.09383294e-04])

>>> hp.positron_spectra(e_ps, e_cm)

{'mu mu': array([6.10588051e-06, 5.70145391e-04, 5.78482356e-04]),
 'pi pi': array([2.14034924e-05, 2.13725359e-03, 9.48371777e-05]),
 's s': array([0., 0., 0.]),
 'total': array([2.75093729e-05, 2.70739898e-03, 6.73319534e-04])}

>>> hp.positron_lines(e_cm)

{'e e': {'energy': 152.5, 'bf': 7.711433862697906e-06}}

```

For the built-in models, functions computing the positron spectra for annihilations into particular final states follow a similar naming scheme to the gamma-ray ones, and can be called directly.

A method (more precisely, an `InterpolatedUnivariateSpline`) to compute the total positron spectrum convolved with an energy resolution function is obtained using:

```

>>> e_cm = 305. # DM center of mass energy

>>> e_p_min, e_p_max = 1., 100. # define energy range

>>> energy_res = lambda e: 0.05

>>> dnnde_p_conv = hp.total_conv_positron_spectrum_fn(
...     e_p_min, e_p_max, e_cm, energy_res)

>>> dnnde_p_conv(20.)

```

```
0.00864851382906508
```

```
>>> dnnde_p_conv.integral(10, 100) # integrate spectrum
```

```
0.6538810882108401
```

5.7 Gamma Ray Limits

In `hazma` we include two routines to set constraints on the DM self-annihilation cross section $\langle\sigma v\rangle_{\bar{\chi}\chi}$ using current gamma-ray flux measurements and to make projections for planned detectors.

As is well-known, the primary gamma-ray flux from DM annihilating in a region of the sky subtending a solid angle $\Delta\Omega$ is

$$\left.\frac{d\Phi}{dE_\gamma}\right|_{\bar{\chi}\chi}(E) = \frac{\Delta\Omega}{4\pi} \cdot \frac{\langle\sigma v\rangle_{\bar{\chi}\chi}}{2f_\chi m_\chi^2} \cdot J \cdot \left.\frac{dN}{dE_\gamma}\right|_{\bar{\chi}\chi}(E). \quad (5.46)$$

The factor f_χ is 1 if the DM is self-conjugate and 2 otherwise (2 for the models currently included with `hazma`). The J factor counts the number of pairs of DM particles in the observing region:

$$J \equiv \frac{1}{\Delta\Omega} \int_{\Delta\Omega} d\Omega \int_{\text{LOS}} dl \rho(r(l, \psi))^2, \quad (5.47)$$

where $\rho(r)$ is the DM density profile. The annihilation spectrum $dN/dE_\gamma|_{\bar{\chi}\chi}$ was computed in detail in the previous section. A detector with finite energy resolution observes the smoothed flux

$$\left.\frac{d\Phi_\epsilon}{dE_\gamma}\right|_{\bar{\chi}\chi}(E) \equiv \int dE' R_\epsilon(E|E') \left.\frac{d\Phi}{dE_\gamma}\right|_{\bar{\chi}\chi}(E'), \quad (5.48)$$

where the spectral resolution function is the probability that a gamma ray with true energy E' is reconstructed with energy E , and can be approximated as a Gaussian [54]:

$$R_\epsilon(E|E') \equiv \frac{1}{\sqrt{2\pi} \epsilon(E') E'} \exp \left[-\frac{(E - E')^2}{2(\epsilon(E') E')^2} \right]. \quad (5.49)$$

In the limit-setting procedure for *existing* experiments, the integral of the smoothed spectrum in each energy bin is required not to exceed the observed value plus twice the upper error bar: $\Phi_\epsilon^{(i)}|_{\bar{X}X} < \Phi^{(i)}|_{\text{obs}} + 2\sigma^{(i)}$. While better limits can be obtained by assuming a background model, this introduces significant systematic uncertainties since the model is derived from precisely the observations under consideration and would thus only marginally improve the limits on $\langle\sigma v\rangle_{\bar{X}X}$ [109].

For assessing the discovery reach by *upcoming* experiments, **hazma** uses an unbinned procedure. A detector can be characterized by an effective area $A_{\text{eff}}(E)$ and an (energy-independent) observing time T_{obs} . Over the energy range $[E_{\text{min}}, E_{\text{max}}]$, the number of photons observed is then

$$N_\gamma|_{\bar{X}X} = \int_{E_{\text{min}}}^{E_{\text{max}}} dE T_{\text{obs}} A_{\text{eff}}(E) \left. \frac{d\Phi_\epsilon}{dE_\gamma} \right|_{\bar{X}X}(E). \quad (5.50)$$

Assuming Poisson statistics, the minimum-detectable $\langle\sigma v\rangle_{\bar{X}X}$ is obtained by requiring the signal-to-noise ratio to be significant at the $n_\sigma = 5$ level: $N_\gamma|_{\bar{X}X}/\sqrt{N_\gamma|_{\text{bg}}} = n_\sigma$. Holding the DM mass fixed, the lowest-possible value of $\langle\sigma v\rangle_{\bar{X}X}$ is found by optimizing over E_{min} and E_{max} to maximize $N_\gamma|_{\bar{X}X}/\sqrt{N_\gamma|_{\text{bg}}}$. This energy range does not completely align with spectra features. For example, in the case of the π^0 spectrum, setting E_{min} equal to the left boundary of the “box” would include too much of the $d\Phi/dE_\gamma|_{\text{bg}} \propto E_\gamma^{-2}$ spectrum.

The unbinned analysis requires a background model, two of which are included with `hazma`. The simplest was obtained by fitting a power law to COMPTEL and EGRET data from high galactic latitudes over the energy range 0.8 MeV – 10 GeV [40]. This is suitable for projecting limits on $\langle\sigma v\rangle_{\bar{\chi}\chi}$ from dwarf galaxy observations. A model derived using `GALPROP` to fit existing MeV gamma-ray data in the region $|b| < 10^\circ$, $|l| < 30^\circ$ is also included to assess the sensitivity to emission from the Galactic Center.

Detector	Energy range	A_{eff} (cm ²)	ϵ
COMPTEL [145]	0.7 – 27 MeV	50	5%
EGRET [231]	27 MeV – 8.6 GeV	$10 - 10^3$	18%
Fermi-LAT [25]	150 MeV – 95 GeV	$10^3 - 10^4$	7.5%
e-ASTROGAM [18]	0.3 MeV – 3 GeV	$10^2 - 10^3$	$\lesssim 2\%$, $E_\gamma < 10$ MeV 20–30%, $E_\gamma \geq 10$ MeV

Table 5.1: **Figures of merit for the detectors used in hazma.** Note that the effective area is only used in `hazma` for projecting limits for e-ASTROGAM.

These two limit-setting procedures can currently be applied in `hazma` to data from three existing experiments (COMPTEL, EGRET and Fermi-LAT) and one proposed detector (e-ASTROGAM). The energy ranges, approximate effective areas and energy resolutions for these are supplied in Tab. (5.1). Each gamma-ray data set is paired with a target region, defined by the galactic coordinate ranges, solid angles and J -factors (assuming an NFW distribution for the galactic DM halo) in Tab. (5.2). These

Detector	Region	$\Delta\Omega$ (sr)	J ($\text{MeV}^2 \text{ cm}^{-5} \text{ sr}^{-1}$)
COMPTEL [145]	$ b < 20^\circ, l < 60^\circ$	1.433	3.725×10^{28}
EGRET [225]	$20^\circ < b < 60^\circ, l < 180^\circ$	6.585	3.79×10^{27}
Fermi-LAT [6]	$8^\circ < b < 90^\circ, l < 180^\circ$	10.817	4.698×10^{27}
e-ASTROGAM [18]	$ b < 10^\circ, l < 10^\circ$	0.121	1.795×10^{29}

Table 5.2: **Target regions and data references (first column) for detectors included in hazma.** The J -factors for COMPTEL, EGRET and Fermi-LAT are taken from [109] and the value for e-ASTROGAM is from ref. [71]. All assume an NFW profile for the galactic DM distribution [71].

are packaged into `FluxMeasurements` objects in `hazma`.

The limit-setting procedures are methods in the `Theory` class. For example, the following snippet imports a `FluxMeasurement` object containing information about EGRET observations and computes the $\langle\sigma v\rangle_{\bar{\chi}\chi}$ limits for the Higgs portal model at three DM masses in cm^3/s :

```
>>> from hazma.scalar_mediator import ScalarMediator
>>> from hazma.gamma_ray_parameters import egret_diffuse, TargetParams
>>> egret_diffuse.target # target region information
TargetParams(J=3.79e+27, dOmega=6.584844306798711)
>>> sm = ScalarMediator(mx=150., ms=1e4, gsxx=1., gsff=0.1, gsGG=0.5,
```

```

...                gsFF=0, lam=1e5)

>>> sm.binned_limit(egret_diffuse)

7.890021123433229e-27 # cm^3 / s

```

It is important to note that `hazma` only uses the model parameters (m_S , $g_{S\chi\chi}$, g_{Sff} , g_{SGG} , g_{SFF} and Λ) to compute the *shape* of the spectrum and treats $\langle\sigma v\rangle_{\bar{\chi}\chi}$ as an independent parameter (c.f. 5.46). To relate the model parameters to $\langle\sigma v\rangle_{\bar{\chi}\chi}$, the user can employ the method `Theory.annihilation_cross_sections()`. The `FluxMeasurement` objects for COMPTEL and Fermi-LAT observations are named `comptel_diffuse` and `fermi_diffuse` and can be imported similarly. App. (C.0.1) describes how to create new flux measurement objects.

Computing unbinned limits requires specifying several quantities :

- An effective area function returning $A_{\text{eff}}(E)$ in cm^2 ;
- An energy resolution function returning $\epsilon(E')$ in %;
- An observing time in seconds;
- An object of type `TargetParams` containing the J -factor and $\Delta\Omega$ for the target region;
- A `BackgroundModel` object, which has a method `dPhi_dEdOmega()` returning the differential gamma-ray flux per solid angle for the background model, and an attribute `e_range` specifying the range of E_γ values for which the model is valid.

Using the same instance of `scalar_mediator` and DM masses as above, we can compute

the projected limits for e-ASTROGAM using the $10^\circ \times 10^\circ$ window around the Galactic Center from Tab. (5.2) as the target:

```

>>> from hazma.gamma_ray_parameters import A_eff_e_astrogam
>>> from hazma.gamma_ray_parameters import energy_res_e_astrogam
>>> from hazma.gamma_ray_parameters import T_obs_e_astrogam
>>> from hazma.gamma_ray_parameters import gc_target, gc_bg_model

>>> gc_target.J                                # target J-factor
1.795e+29

>>> gc_target.dOmega                            # target extent
0.12122929761504078

>>> sm.unbinned_limit(A_eff_e_astrogam,        # effective area
...                   energy_res_e_astrogam,   # energy resolution
...                   T_obs_e_astrogam,        # observing time
...                   gc_target,              # target region
...                   gc_bg_model)            # background model
5.6701062876845636e-30 # cm^3 / s

```

Modifying these ingredients to study other planned gamma-ray detectors is described in App. (C.0.1).

We do not currently use secondary radiation to set limits on our models. Such limits are highly dependent on (for example) the choice of observational target, the magnetic field intensity and spatial structure [76, 78]; Ref. ([31]) calculates the secondary emission for select MeV dark matter annihilation final states. Since `hazma` can

already compute the relevant input spectra for determining secondary spectra, we plan to incorporate this into future versions of the code.

5.8 Cosmic Microwave Background limits

Dark matter annihilations at recombination inject ionizing particles into the photon-baryon plasma. The resulting changes in the residual ionization fraction and baryon temperature modify the CMB temperature and polarization power spectra, particularly at small scales, which puts a constraint on $\langle\sigma v\rangle_{\bar{\chi}\chi,\text{CMB}}$, the DM self-annihilation cross section at recombination [67, 189, 121, 219, 217, 9]. The size of the effect of the changes depend on the energy per unit volume per unit time, which is related to the effective parameter

$$p_{\text{ann}} \equiv f_{\text{eff}}^{\chi} \frac{\langle\sigma v\rangle_{\bar{\chi}\chi,\text{CMB}}}{m_{\chi}}. \quad (5.51)$$

The current 95% upper limit on p_{ann} from Planck is $3.5 \times 10^{-31} \text{ cm}^3 \text{ s}^{-1} \text{ MeV}^{-1}$ [9]. f_{eff}^{χ} is the fraction of energy per DM annihilation imparted to the plasma. This depends on how many electrons/positrons and photons are produced per DM annihilation (ie, the spectra computed earlier in this work) and how efficiently these particles re-ionize the CMB (quantified by the factors f_{eff}^{γ} and $f_{\text{eff}}^{e^+e^-}$) [217]:

$$f_{\text{eff}}^{\chi} = \frac{1}{E_{\text{CM}}} \int_0^{E_{\text{CM}}/2} dE \left(2f_{\text{eff}}^{e^+e^-} E \left. \frac{dN}{dE_{e^+}} \right|_{\bar{\chi}\chi} + f_{\text{eff}}^{\gamma} E \left. \frac{dN}{dE_{\gamma}} \right|_{\bar{\chi}\chi} \right). \quad (5.52)$$

If the DM self-annihilation cross section is velocity dependent (as is the case for the scalar mediator model, where the annihilation is p -wave), the DM velocity $v_{\chi,\text{CMB}}$

at recombination is required to relate $\langle\sigma v\rangle_{\bar{\chi}\chi,\text{CMB}}$ to the present-day value of $\langle\sigma v\rangle_{\bar{\chi}\chi}$ in indirect detection targets. This velocity is also required for computing the center of mass energy in DM self-annihilation events at recombination. The velocity depends on the kinetic decoupling temperature, T_{KD} . Before kinetic decoupling DM initially is coupled to the plasma so that $v_{\chi,\text{CMB}} = \sqrt{3T_{\gamma}/m_{\chi}}$, but afterwards it cools more quickly ($T_{\chi} \propto z^2$). The DM velocity is thus [109]

$$v_{\chi,\text{CMB}} = \sqrt{\frac{3T_{\chi}}{m_{\chi}}} \approx 2 \times 10^{-4} \left(\frac{T_{\gamma}}{1 \text{ eV}}\right) \left(\frac{1 \text{ MeV}}{m_{\chi}}\right) \left(\frac{10^{-4}}{x_{\text{kd}}}\right)^{1/2}, \quad (5.53)$$

where $x_{\text{kd}} \equiv T_{\text{KD}}/m_{\chi}$ generally lies in the range $10^{-6} - 10^{-4}$. Since this velocity is much smaller than the characteristic velocity in the Milky Way, the CMB constraints on $\langle\sigma v\rangle_{\bar{\chi}\chi}$ for models with p -wave suppression are in general much weaker than the gamma-ray ones. The CMB constraints in the s -wave case are generally much stronger, but can be evaded in models where the DM is partially produced through the decay of a heavier dark-sector degree of freedom after recombination [94].

The quantity f_{eff}^{χ} as well as the separate e^{\pm} and γ terms in Eqn. (5.52) can be computed for a given kinetic decoupling temperature:

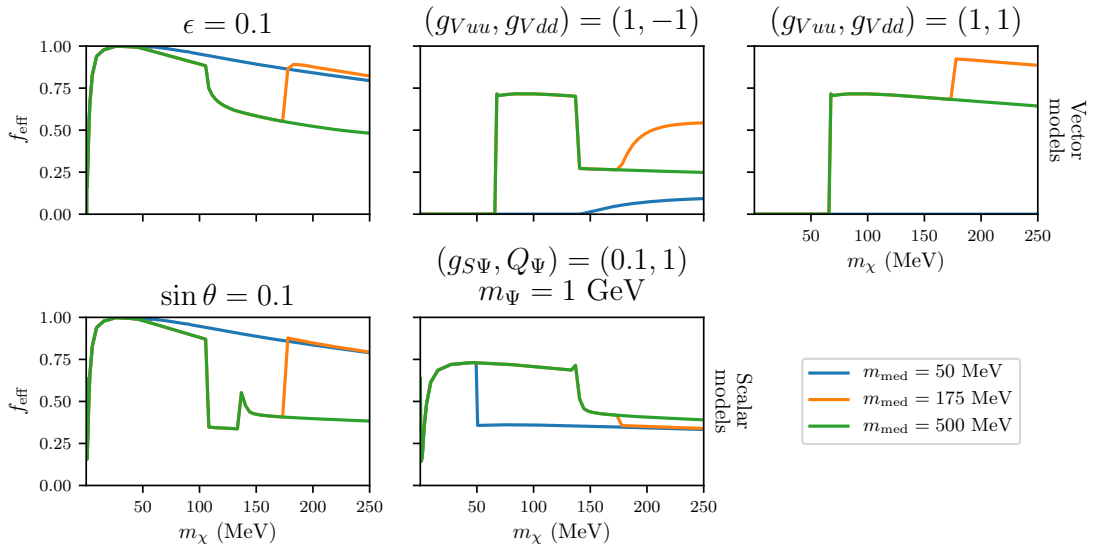




Figure 5.14: **Efficiency of energy injection into the CMB by dark matter annihilation.** The top panels are for the vector model with kinetic mixing and two possible values for mediator couplings to quarks only. The bottom row shows f_{eff}^{χ} for the scalar mediator with Higgs portal and heavy quark-type couplings. The DM-mediator coupling is fixed to one in all panels. Note that the curves for different mediator masses have some overlap.  

```

>>> from hazma.scalar_mediator import ScalarMediator
>>> sm = ScalarMediator(mx=150., ms=1e4, gsxx=1., gsff=0.1,
↳ gsGG=0.5,gsFF=0, lam=1e5)
>>> x_kd = 1e-4
>>> sm.f_eff(x_kd), sm.f_eff_ep(x_kd), sm.f_eff_g(x_kd)
(0.436, 0.167, 0.270)

```

Fig. (5.14) shows this factor as a function of DM and mediator mass for the scalar and vector models with the couplings we have been using as benchmarks. There are sharp variations in f_{eff}^{χ} arising from SM or two-mediator final states becoming accessible as the DM mass changes. Deriving the kinetic decoupling temperature for particular models rather than leaving it as a free parameter is left for future work (or the user).

The `Theory.cmb_limit()` function computes the constraint on $\langle\sigma v\rangle_{\bar{\chi}\chi,\text{CMB}}$ given a value of x_{kd} and upper limit on p_{ann} :

```

>>> from hazma.cmb import p_ann_planck_temp_pol as p_ann
>>> p_ann
3.5e-31 # cm^3 / MeV / s
>>> x_kd = 1e-4
>>> sm = HiggsPortal(mx=150., ms=1e4, gsxx=1., stheta=0.01)
>>> sm.cmb_limit(x_kd, p_ann)
1.2398330863024796e-28 # cm^3 / s

```

As with the gamma-ray limits described in the previous section, the parameters of the theory (here m_S , $g_{S\chi\chi}$ and s_θ) determine the *shapes* of the photon and e^\pm spectra, and `Theory.cmb_limit()` treats $\langle\sigma v\rangle_{\bar{\chi}\chi,\text{CMB}}$ as a free parameter. The user can find which model parameters reproduce this cross section using `Theory.annihilation_cross_sections()`.

5.9 Conclusion

We have introduced `hazma`, a code for the calculation of gamma-ray and electron-positron spectra as well as constraints and projected reach for future telescopes for sub-GeV dark matter models. `hazma` is timely both because of forthcoming new observational capabilities at sub-GeV gamma-ray energies, and because of renewed interest in dark matter models beyond the WIMP paradigm and at lower-than-usually-considered masses. In future work we will use `hazma` to study the complementarity between indirect and other probes of sub-GeV dark matter.

`hazma` allows users to compute both spectra of gamma rays, electrons and positrons for individual annihilation final states containing arbitrarily many particles, as well as for user-implemented or a set of built-in dark matter models. In the latter case, the code computes the relevant branching fractions and the ensuing decay chains leading to photons, electrons and positrons, and calculates model-dependent emission processes such as e.g. internal bremsstrahlung. The interactions between the mediator particles in these models and the final state mesons is implemented using chiral perturbation

theory techniques.

`hazma` contains several updates and refinements over how gamma-ray spectra have been calculated in the recent literature. These include several radiative decay spectra, such as from charged pion decay or from muon decay, final state radiation calculations going beyond the Altarelli-Parisi splitting function approximation for the built-in models, and the ability to include arbitrarily many mesons and leptons in the final states.

We presented numerous snippets of code, and all code used to produce the figures shown herein manuscript is available through clickable links. We also showed a few advanced usage features, such as adding new gamma-ray experiments for deriving constraints from existing data or assessing projected reach for planned detectors, and implementing user-defined models.

Appendix A

Installation

`hazma` was developed for python3. Before installing `hazma`, the user needs to install several well-established python packages: `cython`, `scipy`, `numpy`, and `scikit-image`. These are easily installed by using PyPI. If the user has PyPI installed on their system, then these packages can be installed using

```
pip install cython, scipy, numpy, scikit-image, matplotlib
```

`hazma` can be installed in the same way, using:

```
pip install hazma
```

This will download a tarball from the PyPI repository, compile all the c-code and install `hazma` on the system. Alternatively, the user can install `hazma` by downloading the package from <https://github.com/LoganAMorrison/Hazma.git>. Once downloaded, navigate to the package directory using the command line and run either


```
pip install .
```

or

```
python setup.py install
```

Note that since `hazma` makes extensive usage of the package `cython`, the user will need to have a `c` and `c++` compiler installed on their system (for example `gcc` and `g++` on unix-like systems or Microsoft Visual Studios 2015 or later on Windows). For more information, see the `cython` installation guide: <https://cython.readthedocs.io/en/latest/src/quickstart/install.html>

Appendix B

Basic Usage

B.0.1 Using the Built-In Models

Throughout the text, we gave usage examples of how to use the models built into `hazma`. Here we give a compact review of how to use these models in `hazma`. All the models built into `hazma` have identical interfaces. The only difference in the interfaces is the parameters which need to be specified for the particular model being used. Thus, we will only show the usage of one of the models. The others can be used in an identical fashion. The example we will use is the `KineticMixing` model. First, we import the model:

```
from hazma.vector_mediator import KineticMixing
```

The kinetic mixing model takes four parameters: the dark matter mass, vector mediator mass, dark matter charge and the kinetic mixing parameters. To create the kinetic mixing model with $m_\chi = 250$ MeV, $m_V = 1$ TeV, $g_{V\chi} = 1$ and $\epsilon = 10^{-3}$, we use:

```
km = KineticMixing(mx=250.0, mv=1e6, gvxx=1.0, eps=1e-3)
```

Now we can use `km` to compute properties of our model. For examples, to list all of the available final states for which the dark matter can annihilate into, we use:

```
>>> km.list_annihilation_final_states()
['mu mu', 'e e', 'pi pi', 'pi0 g', 'pi0 v', 'v v']
```

This tells us that we can potentially annihilate through: $\chi\bar{\chi} \rightarrow \mu^+\mu^-, e^+e^-, \pi^+\pi^-, \pi^0\gamma, \pi^0V$ or $V^\mu V^\mu$. However, which of these final states is actually available depends on the center of mass energy. We can see this fact by looking at the annihilation cross sections or branching fractions. For example, if we set the center of mass energy to be $\sqrt{s} = 2m_\chi(1 + v_\chi^2/2)$ with dark matter velocity $v_\chi = 10^{-3}$, we find:

```
#  $\sqrt{s} = 2m_\chi(1 + v_\chi^2/2)$ 
>>> cme = 2.0 * km.mx * (1.0 + 0.5 * 1e-6)
>>> km.annihilation_cross_sections(cme)
{'mu mu': 8.998735387276086e-25,
 'e e': 9.115024836416874e-25,
 'pi pi': 1.3013263970304e-25,
 'pi0 g': 1.7451483984993156e-29,
 'pi0 v': 0.0,
```

```
'v v': 0.0,  
'total': 1.941526113556321e-24}
```

with similar results for `km.annihilation_branching_fractions(cme)`. Here we have chosen a realistic center of mass energy for dark matter in our galaxy, which as a velocity dispersion of $\delta v \sim 10^{-3}$. We can see that the $V^\mu V^\mu$ final state is unavailable, as it should be since the vector mediator mass is too heavy. In this theory, the vector mediator can decay. If we would like to know the decay width and the partial widths, we can use:

```
>>> km.partial_widths()  
{'pi pi': 0.0006080948890354345,  
'pi0 g': 0.23374917012731816,  
'x x': 26525.823848648604,  
'e e': 0.0024323798404358825,  
'mu mu': 0.0024323798404358803,  
'total': 26526.0630706733}
```

If we would like to know the gamma-ray spectrum from dark matter annihilations, we can use

```
# Specify photon energies to compute spectrum at  
>>> photon_energies = np.array([cme / 4])  
>>> km.spectra(photon_energies, cme)  
{'mu mu': array([2.8227189e-05]),
```

```

'e e': array([0.00013172]),
'pi pi': array([2.1464018e-06]),
'pi0 g': array([7.66452627e-08]),
'pi0 v': array([0.]),
'v v': array([0.]),
'total': array([0.00016217])}

```

Note that we only used a single photon energy because of display purposes, but in general the user can specify any number of photon energies. If the user would like access to the underlying spectrum functions, they can use:

```

>>> spec_funs = km.spectrum_functions()
>>> spec_funs['mu mu'](photon_energies, cme)
array([6.09016958e-05])
>>> mumu_bf = km.annihilation_branching_fractions(cme)['mu mu']
>>> mumu_bf * spec_funs['mu mu'](photon_energies, cme)
array([2.8227189e-05])

```

Notice that the direct call to the spectrum function for $\chi\bar{\chi} \rightarrow \mu^+\mu^-$ doesn't give the same result as `km.spectra(photon_energies, cme)['mu mu']`. This is because the branching fractions are not applied for the `spec_funs = km.spectrum_functions()`. If the user doesn't care about the underlying components of the gamma-ray spectra, they can simply call

```
>>> km.total_spectrum(photon_energies, cme)

array([0.00016217])
```

to get the total gamma-ray spectrum. The reader may have caught the fact that there is a gamma-ray line in the spectrum for $\chi\bar{\chi} \rightarrow \pi^0\gamma$. To get the location of this line, the user can use:

```
>>> km.gamma_ray_lines(cme)

{'pi0 g': {'energy': 231.78145156177675, 'bf': 8.988539408840104e-06}}
```

This tells us the process which produces the line, the location of the line and the branching fraction for the process. We do not include the line in the total spectrum since the line produces a Dirac-delta function. In order to get a realistic spectrum including the line, we need to convolve the gamma-ray spectrum with an energy resolution. This can be achieved using:

```
>>> min_photon_energy = 1e-3

>>> max_photon_energy = cme

>>> energy_resolution = lambda photon_energy : 1.0

>>> number_points = 1000

>>> spec = km.total_conv_spectrum_fn(min_photon_energy,
  ↳ max_photon_energy, cme, energy_resolution, number_points)

>>> spec(cme / 4) # compute the spectrum at a photon energy of
  ↳ `cme/4`
```

```
array(0.00167605)
```

The `km.total_conv_spectrum_fn` computes and returns an interpolating function of the convolved function. An important thing to note here is that the `km.total_conv_spectrum_fn` takes in a *function* for the energy resolution. This allows the user to define the energy resolution to depend on the specific photon energy, which is often the case for gamma-ray telescopes.

Next we present the positron spectra. These have an identical interface to the gamma-ray spectra, so we only show how to call the functions and we suppress the output

```
from hazma.parameters import electron_mass as me

positron_energies = np.logspace(np.log10(me), np.log10(cme),
    ↪ num=100)

km.positron_spectra(positron_energies, cme)

km.positron_lines(cme)

km.total_positron_spectrum(positron_energies, cme)

dnde_pos = km.total_conv_positron_spectrum_fn(
    min(positron_energies),
    max(positron_energies),
    cme,
    energy_resolution,
```

```
    number_points
)
```

The last thing that we would like to demonstrate is how to compute limits. In order to compute the limits on the annihilation cross section of a model from a gamma-ray telescope, say EGRET, we can use:

```
from hazma.gamma_ray_parameters import egret_diffuse

# Choose DM masses from half the electron mass to 250 MeV

mxs = np.linspace(me/2., 250., num=100)

# Compute limits from e-ASTROGAM

limits = np.zeros(len(mxs), dtype=float)

for i, mx in enumerate(mxs):

    km.mx = mx

    limits[i] = km.binned_limit(egret_diffuse)
```

Similarly, if we would like to set constraints using e-ASTROGAM, one can use:

```
# Import target and background model for the e-ASTROGAM telescope

from hazma.gamma_ray_parameters import gc_target, gc_bg_model

# Import telescope parameters

from hazma.gamma_ray_parameters import A_eff_e_astrogam

from hazma.gamma_ray_parameters import energy_res_e_astrogam

from hazma.gamma_ray_parameters import T_obs_e_astrogam

# Choose DM masses from half the electron mass to 250 MeV
```



```

mxs = np.linspace(me/2., 250., num=100)

# Compute limits

limits = np.zeros(len(mxs), dtype=float)

for i, mx in enumerate(mxs):

    km.mx = mx

    limits[i] = km.unbinned_limit(

        A_eff_e_astrogam,

        energy_res_e_astrogam,

        T_obs_e_astrogam,

        gc_target,

        gc_bg_model

    )

```

B.0.2 Subclassing the Built-In Models

As mentioned in Sec. (5.2), the user may not be interested in the generic models built into `hazma`, but instead a more specialized model. In this case, it makes sense for the user to subclass one of the models (i.e. create a class which inherits from one of the models.) As an example, we illustrate how to do this with the Higgs-portal model (of course this model is already built into `hazma`, but it works nicely as an example.) Recall that the full set of parameters for the scalar mediator model are:

1. m_χ : dark matter mass,
2. m_S : scalar mediator mass,

3. $g_{S\chi}$: coupling of scalar mediator to dark matter,
4. g_{Sf} : coupling of scalar mediator to standard model fermions,
5. g_{SG} : effective coupling of scalar mediator to gluons,
6. g_{SF} : effective coupling of scalar mediator to photons and
7. Λ : cut-off scale for the effective interactions.

In the case of the Higgs-portal model, the scalar mediator talks to the standard model only through the Higgs boson, i.e. it mixes with the Higgs. Therefore, the scalar mediator inherits its interactions with the standard model fermions, gluons and photon through the Higgs. In Sec. (5.3.1), we gave the relationships between the couplings $g_{Sf}, g_{SG}, g_{SF}, \Lambda$ and $\sin \theta, v_h$, where $\sin \theta$ is the mixing angle for the scalar and Higgs and v_h is the Higgs vacuum expectation value. These relationships are:

$$g_{Sf} = \sin \theta, \quad g_{SG} = 3 \sin \theta, \quad g_{SF} = -\frac{5}{6} \sin \theta, \quad \Lambda = v_h. \quad (\text{B.1})$$

Therefore, the Higgs-portal model doesn't need to know about all of the couplings of the generic scalar mediator model. It only needs to know about $m_\chi, m_S, g_{S\chi}$ and $\sin \theta$. Below, we construct a class which subclasses the scalar mediator class to implement the Higgs-portal model.

```
from hazma.scalar_mediator import ScalarMediator
from hazma.parameters import vh
```

```

class HiggsPortal(ScalarMediator):

    def __init__(self, mx, ms, gsxx, stheta):

        self._lam = vh

        self._stheta = stheta

        super(HiggsPortal, self).__init__(

            mx,

            ms,

            gsxx,

            stheta,

            3.0 * stheta,

            -5.0 * stheta / 6.0,

            vh

        )

    @property

    def stheta(self):

        return self._stheta

    @stheta.setter

    def stheta(self, stheta):

        self._stheta = stheta

```

```

self.gsff = stheta

self.gsGG = 3. * stheta

self.gsFF = - 5. * stheta / 6.

# Hide underlying properties' setters

@ScalarMediator.gsff.setter

def gsff(self, gsff):

    raise AttributeError("Cannot set gsff")

@ScalarMediator.gsGG.setter

def gsGG(self, gsGG):

    raise AttributeError("Cannot set gsGG")

@ScalarMediator.gsFF.setter

def gsFF(self, gsFF):

    raise AttributeError("Cannot set gsFF")

```

There are a couple things to note about our above implementation. First, our model only takes in $m_\chi, m_S, g_{S\chi}$ and $\sin\theta$, as desired. But the underlying model, i.e. the `ScalarMediator` model only knows about $m_\chi, m_S, g_{S\chi}, g_{Sf}, g_{SG}, g_{SF}$ and Λ . So if we update $\sin\theta$, we additionally need to update the underlying parameters, g_{Sf}, g_{SG}, g_{SF} and Λ . The easiest way to do this is using getters and setters by defining $\sin\theta$ to be

a `property` through the `@property` decorator. Then every time we update $\sin \theta$, we can also update the underlying parameters. The second thing to note is that we want to make sure we don't accidentally change the underlying parameters directly, since in this model, they are only defined through $\sin \theta$. We can ensure that we cannot change the underlying parameters directly by overriding the getters and setters for `gsff`, `gsGG` and `gsGG` and raising an error if we try to change them. This isn't strictly necessary (as long as the user is careful), but can help avoid confusing behavior.

Appendix C

Advanced Usage

C.0.1 Adding New Gamma-Ray Experiments

Currently `hazma` only includes information for producing projected unbinned limits with e-ASTROGAM, using the dwarf Draco or inner $10^\circ \times 10^\circ$ region of the Milky Way as a target. Adding new detectors and target regions is straightforward. As described in Sec. (5.7), a detector is characterized by the effective area $A_{\text{eff}}(E)$, the energy resolution $\epsilon(E)$ and observation time T_{obs} . In `hazma`, the first two can be any callables (functions) and the third must be a float. The region of interest is defined by a `TargetParams` object, which can be instantiated with:

```
>>> from hazma.gamma_ray_parameters import TargetParams
>>> tp = TargetParams(J=1e29, dOmega=0.1)
```

The background model should be packaged in an object of type `BackgroundModel`. This light-weight class has a function `dPhi_dEdOmega()` for computing the differential photon flux per solid angle (in $\text{MeV}^{-1} \text{sr}$) and an attribute `e_range` specifying the energy range

over which the model is valid (in MeV). New background models are defined by passing these two the initializer:

```
>>> from hazma.background_model import BackgroundModel

>>> bg = BackgroundModel(e_range=[0.5, 1e4],
...                        dPhi_dEdOmega=lambda e: 2.7e-3 / e**2)
```

As explained in Sec. (5.7), gamma-ray observation information from Fermi-LAT, EGRET and COMPTEL is included with `hazma`, and other observations can be added using the container class `FluxMeasurement`. The initializer requires:

- The name of a CSV file containing gamma-ray observations. The file's columns must contain:
 1. Lower bin edge (MeV)
 2. Upper bin edge (MeV)
 3. $E^n d^2\Phi/dE d\Omega$ (in $\text{MeV}^{n-1} \text{cm}^{-2} \text{s}^{-1} \text{sr}^{-1}$)
 4. Upper error bar (in $\text{MeV}^{n-1} \text{cm}^{-2} \text{s}^{-1} \text{sr}^{-1}$)
 5. Lower error bar (in $\text{MeV}^{n-1} \text{cm}^{-2} \text{s}^{-1} \text{sr}^{-1}$)

Note that the error bar values are their y -coordinates, not their relative distances from the central flux.

- The detector's energy resolution function.
- A `TargetParams` object for the target region.

For example, a CSV file `obs.csv` containing observations

```
150.0,275.0,0.0040,0.0043,0.0038
650.0,900.0,0.0035,0.0043,0.003
```

with $n = 2$ for an instrument with energy resolution $\epsilon(E) = 0.05$ observing the target region `tp` defined above can be loaded using¹

```
>>> from hazma.flux_measurement import FluxMeasurement
>>> obs = FluxMeasurement("obs.dat", lambda e: 0.05, tp)
```

The attributes of the `FluxMeasurement` store all of the provide information, with the E^n prefactor removed from the flux and error bars, and the errors converted from the positions of the error bars to their sizes. These are used internally by the `Theory.binned_limit()` method, and can be accessed as follows:

```
>>> obs.e_lows, obs.e_highs
(array([150., 650.]), array([275., 900.]))
>>> obs.target
<hazma.gamma_ray_parameters.TargetParams at 0x1c1bbbafd0>
>>> obs.fluxes
array([8.85813149e-08, 5.82726327e-09])
>>> obs.upper_errors
array([6.64359862e-09, 1.33194589e-09])
>>> obs.lower_errors
```

¹If the CSV containing the observations uses a different power of E than $n = 2$, this can be specified using the `power` keyword argument to the initializer for `FluxMeasurement`.


```
array([4.42906574e-09, 8.32466181e-10])

>>> obs.energy_res(10.)

0.05
```

C.0.2 User-Defined Models

In this subsection, we demonstrate how to implement new models in Hazma. A notebook containing all the code in this appendix can be downloaded from GitHub [\[1\]](#). The model we will consider is an effective field theory with a Dirac fermion DM particle which talks to neutral and charged pions through gauge-invariant dimension-5 operators. The Lagrangian for this model is:

$$\mathcal{L} \supset \frac{c_1}{\Lambda} \bar{\chi} \chi \pi^+ \pi^- + \frac{c_2}{\Lambda} \bar{\chi} \chi \pi^0 \pi^0 \quad (\text{C.1})$$

where c_1, c_2 are dimensionless Wilson coefficients and Λ is the cut-off scale of the theory. In order to implement this model in Hazma, we need to compute the annihilation cross sections and the FSR spectra. The annihilation channels for this model are simply $\bar{\chi} \chi \rightarrow \pi^0 \pi^0$ and $\bar{\chi} \chi \rightarrow \pi^+ \pi^-$. The computations for the cross sections are straight forward and yield:

$$\sigma(\bar{\chi} \chi \rightarrow \pi^+ \pi^-) = \frac{c_1^2 \sqrt{1 - 4\mu_\pi^2} \sqrt{1 - 4\mu_\chi^2}}{32\pi\Lambda^2} \quad (\text{C.2})$$

$$\sigma(\bar{\chi} \chi \rightarrow \pi^0 \pi^0) = \frac{c_2^2 \sqrt{1 - 4\mu_{\pi^0}^2} \sqrt{1 - 4\mu_\chi^2}}{8\pi\Lambda^2} \quad (\text{C.3})$$

where Q is the center of mass energy, $\mu_\chi = m_\chi/Q$, $\mu_\pi = m_{\pi^\pm}/Q$ and $\mu_{\pi^0} = m_{\pi^0}/Q$. In addition to the cross sections, we need the FSR spectrum for $\bar{\chi}\chi \rightarrow \pi^+\pi^-\gamma$. This is:

$$\frac{dN(\bar{\chi}\chi \rightarrow \pi^+\pi^-\gamma)}{dE_\gamma} = \frac{\alpha \left(2f(x) - 2(1-x-2\mu_\pi^2) \log\left(\frac{1-x-f(x)}{1-x+f(x)}\right) \right)}{\pi \sqrt{1-4\mu_\pi^2} x} \quad (\text{C.4})$$

where

$$f(x) = \sqrt{1-x} \sqrt{1-x-4\mu_\pi^2} \quad (\text{C.5})$$

We are now ready to set up the Hazma model. For `hazma` to work properly, we will need to define the following functions in our model:

- `annihilation_cross_section_funcs()`: A function returning a dictionary of the annihilation cross sections functions, each of which take a center of mass energy.
- `spectrum_funcs()`: A function returning a dictionary of functions which take photon energies and a center of mass energy and return the gamma-ray spectrum contribution from each final state.
- `gamma_ray_lines(e_cm)`: A function returning a dictionary of the gamma-ray lines for a given center of mass energy.
- `positron_spectrum_funcs()`: Like `spectrum_funcs()`, but for positron spectra.
- `positron_lines(e_cm)`: A function returning a dictionary of the electron/positron lines for a center of mass energy.

In the interests of compartmentalization, we find it easiest place each of these components in its own class (a mixin in python terminology) which are then combined into a

master class representing our model. Before we begin writing the classes, we need to import a few helper functions and constants from `hazma`:

```
import numpy as np # NumPy is heavily used

import matplotlib.pyplot as plt # Plotting utilities

# neutral and charged pion masses

from hazma.parameters import neutral_pion_mass as mpi0

from hazma.parameters import charged_pion_mass as mpi

from hazma.parameters import qe # Electric charge

# Positron spectra for neutral and charged pions

from hazma.positron_spectra import charged_pion as pspec_charged_pion

# Decay spectra for neutral and charged pions

from hazma.decay import neutral_pion, charged_pion

# The `Theory` class which we will ultimately inherit from

from hazma.theory import Theory
```

Now, we implement a cross section class:

```
class HazmaExampleCrossSection:

    def sigma_xx_to_pipi(self, Q):

        mupi = mpi / Q

        mux = self.mx / Q

        if Q > 2 * self.mx and Q > 2 * mpi:
```

```

        sigma = (self.c1**2 * np.sqrt(1 - 4 * mupi**2) *
                 np.sqrt(1 - 4 * mux**2)**2 /
                 (32.0 * self.lam**2 * np.pi))

    else:

        sigma = 0.0

    return sigma

def sigma_xx_to_pi0pi0(self, Q):

    mupi0 = mpi0 / Q

    mux = self.mx / Q

    if Q > 2 * self.mx and Q > 2 * mpi0:

        sigma = (self.c2**2 * np.sqrt(1 - 4 * mux**2) *
                 np.sqrt(1 - 4 * mupi0**2) /
                 (8.0 * self.lam**2 * np.pi))

    else:

        sigma = 0.0

    return sigma

```

```

def annihilation_cross_section_funcs(self):
    return {'pi0 pi0': self.sigma_xx_to_pi0pi0,
           'pi pi': self.sigma_xx_to_pipi}

```

The key function is `annihilation_cross_section_funcs`, which is **required** to be implemented. Next, we implement the spectrum functions which will produce the FSR and decay spectra:

```

class HazmaExampleSpectra:

    def dnde_pi0pi0(self, e_gams, e_cm):
        # Decay spectra for the neutral pions
        return 2.0 * neutral_pion(e_gams, e_cm / 2.0)

    def __dnde_xx_to_pipig(self, e_gam, Q):
        # Unvectorized function for computing FSR spectrum

        mupi = mpi / Q

        mux = self.mx / Q

        x = 2.0 * e_gam / Q

        if 0.0 < x and x < 1. - 4. * mupi**2:

            dnde = (
                qe ** 2
                * (

```

```

2 * np.sqrt(1 - x) * np.sqrt(1 - 4 * mupi ** 2 -
↳ x)
+ (-1 + 2 * mupi ** 2 + x)
* np.log(
    (-1 + np.sqrt(1 - x) *
    np.sqrt(1 - 4 * mupi ** 2 - x) + x) ** 2
    / (1 + np.sqrt(1 - x) *
    np.sqrt(1 - 4 * mupi ** 2 - x) - x) ** 2
    )
)
) / (Q * 2.0 * np.sqrt(1 - 4 * mupi ** 2) * np.pi ** 2 *
↳ x)
else:
    dnde = 0

return dnde

def dnde_pipi(self, e_gams, e_cm):
    # Sum the FSR and decay spectra for the charged pions
    return (np.vectorize(self.__dnde_xx_to_pipig)(e_gams, e_cm)
↳ +

```

```

        2. * charged_pion(e_gams, e_cm / 2.0))

def spectrum_funcs(self):
    return {'pi0 pi0': self.dnde_pi0pi0,
           'pi pi': self.dnde_pipi}

def gamma_ray_lines(self, e_cm):
    return {}

```

The required functions here are `spectrum_funcs` and `gamma_ray_lines`. Note the second `__dnde_xx_to_pipig` is an unvectorized helper function, which is not to be used directly.

Next we implement the positron spectra:

```

class HazmaExamplePositronSpectra:
    def dnde_pos_pipi(self, e_ps, e_cm):
        return pspec_charged_pion(e_ps, e_cm / 2.)

    def positron_spectrum_funcs(self):
        return {"pi pi": self.dnde_pos_pipi}

    def positron_lines(self, e_cm):
        return {}

```

Lastly, we group all of these classes into a master class and we're done:

```

class HazmaExample(HazmaExampleCrossSection,
                   HazmaExamplePositronSpectra,
                   HazmaExampleSpectra,
                   Theory):

    # Model parameters are DM mass: mx,

    # Wilson coefficients: c1, c2 and

    # cutoff scale: lam

    def __init__(self, mx, c1, c2, lam):

        self.mx = mx

        self.c1 = c1

        self.c2 = c2

        self.lam = lam

    @staticmethod

    def list_annihilation_final_states():

        return ['pi pi', 'pi0 pi0']

```

Now we can easily compute gamma-ray spectra, positron spectra and limit on our new model from gamma-ray telescopes. To implement our new model with $m_\chi = 200$ MeV, $c_1 = c_2 = 1$ and $\Lambda = 100$ GeV, we can use:


```
>>> model = HazmaExample(200.0, 1.0, 1.0, 100e3)
```

To compute a gamma-ray spectrum:

```
# Photon energies from 1 keV to 1 GeV

>>> e_gams = np.logspace(-3.0, 3.0, num=150)

# Assume the DM is moving with a velocity of  $10^{-3}$ 

>>> vdm = 1e-3

# Compute CM energy assuming the above velocity

>>> Q = 2.0 * model.mx * (1 + 0.5 * vdm**2)

# Compute spectra

>>> spectra = model.spectra(e_gams, Q)
```

Then we can plot the spectra using:

```
>>> plt.figure(dpi=100)

>>> for key, val in spectra.items():

...     plt.plot(e_gams, val, label=key)

>>> plt.xlabel(r'$E_{\gamma}$ (\mathrm{MeV})$', fontsize=16)

>>> plt.ylabel(r'$\frac{dN}{dE_{\gamma}}$ (\mathrm{MeV}^{-1})$',

↪     fontsize=16)

>>> plt.xscale('log')
```

```
>>> plt.yscale('log')
>>> plt.legend()
```

Additionally, we can compute limits on the thermally-averaged annihilation cross section of our model for various DM masses using

```
# Import target and background model for the E-Astrogam telescope
>>> from hazma.gamma_ray_parameters import gc_target, gc_bg_model

# Choose DM masses from half the pion mass to 250 MeV
>>> mxs = np.linspace(mpi/2., 250., num=100)

# Compute limits from E-Astrogam
>>> limits = np.zeros(len(mxs), dtype=float)

>>> for i, mx in enumerate(mxs):
...     model.mx = mx
...     limits[i] = model.unbinned_limit(target_params=gc_target,
...                                     bg_model=gc_bg_model)
```

Appendix D

Multi-particle phase space integration:

`rambo`

The `rambo` module implements the RAMBO algorithm, developed by Kleiss, Stirling and Ellis [152], for generating phase-space points using a Monte Carlo procedure. We advise the interested reader to consult the original paper for details on how this algorithm works. We will only described how the algorithm works at a high-level.

The RAMBO algorithm works by first democratically generations random, independent, isotropic, massless four-momenta, q_i^μ , with i running from 1 to N , N being the number of final state particles. The momenta q_i^μ are generated with energies distributed according to $q_i^0 \exp(-q_i^0) dq_i^0$. These four momenta are then transformed into four-momenta p_i^μ by performing a particular Lorentz boost such that $\sum_i p_i^\mu = P^\mu$ where P^μ is the total four-momenta of the given process in the center-of-mass frame (i.e. $P^0 = E_{\text{CM}}$ and $\vec{P} = \vec{0}$.) At this stage, a corresponding weight $W_0(p_i)$ is computed to

give the probability of the event with the particular four-momenta p_i^μ . Lastly, the four-momenta p_i^μ are transformed into four-momenta k_i^μ such that the k_i^μ have the correct masses (i.e. $k_i^\mu k_{i,\mu} = m_i^2$) and a new weight $W(k_i)$ is computed. This completes the algorithm. Below we give pseudo-code for the algorithm:

1. Generate the q_i^μ 's with energies distributed according to $q_i^0 \exp(-q_i^0) dq_i^0$ using:

$$q_i^0 = -\log(\rho_i^{(3)} \rho_i^{(4)}), \quad q_i^x = q_i^0 \sqrt{1 - c_i^2} \cos \phi_i, \quad q_i^y = q_i^0 \sqrt{1 - c_i^2} \sin \phi_i, \quad q_i^z = q_i^0 c_i. \quad (\text{D.1})$$

where $c_i = 2\rho_i^{(1)} - 1$, $\phi_i = 2\pi\rho_i^{(2)}$ and $\rho_i^{(1,2,3,4)}$ are uniform random numbers on $(0,1)$. See [152] for a proof that these are indeed distributed according to $q_i^0 \exp(-q_i^0) dq_i^0$.

2. Transform the q_i^μ 's into p_i^μ 's such that the $\sum_i p_i^\mu = P^\mu$ with $P^0 = E_{\text{CM}}$ and $\vec{P} = \vec{0}$.

This is done using:

$$p_i^0 = x(\gamma q_i^0 + \vec{b} \cdot \vec{q}_i), \quad \vec{p}_i = x(\vec{q}_i + \vec{b} q_i^0 + a(\vec{b} \cdot \vec{q}_i) \vec{b}). \quad (\text{D.2})$$

where

$$\begin{aligned} \vec{b} &= -\vec{Q}/M, & x &= E_{\text{CM}}/M, & \gamma &= Q^0/M, & a &= 1/\sqrt{1 + \gamma}, \\ Q^\mu &= \sum_i q_i^\mu, & M &= \sqrt{Q_\mu Q^\mu} \end{aligned} \quad (\text{D.3})$$

Assign the following weight to the event:

$$W_0 = \left(\frac{\pi}{2}\right)^{N-1} E_{\text{CM}}^{2N-4} \frac{(2\pi)^{4-3N}}{\Gamma(N)\Gamma(N-1)} \quad (\text{D.4})$$

3. Next we transform the p_i^μ 's to k_i^μ 's such that $k_i^\mu k_{i,\mu} = m_i$. This is done via:

$$\vec{k}_i = \xi \vec{p}_i, \quad k_i^0 = \sqrt{m_i + (\xi p_i^0)^2} \quad (\text{D.5})$$

where ξ is the solution to

$$E_{\text{CM}} = \sum_{i=1}^N \sqrt{m_i^2 + (\xi p_i^0)^2} \quad (\text{D.6})$$

This equation can be solved efficiently using Newton's method with the initial guess $\xi_0 = \sqrt{1 - \left(\sum_{i=1}^N m_i/E_{\text{CM}}\right)^2}$. Lastly, we re-weight the probability of the event using:

$$W = W_0 E_{\text{CM}} \left(\sum_{i=1}^N \frac{|\vec{k}_i|}{E_{\text{CM}}} \right)^{2N-3} \left(\sum_{i=1}^N \frac{|\vec{k}_i|^2}{k_i^0} \right)^{-1} \left(\prod_{i=1}^N \frac{|\vec{k}_i|}{k_i^0} \right) \quad (\text{D.7})$$

We note that this fixes a typo from the original paper, where the overall factor of E_{CM} was missing. Additionally, we note that the weights clearly don't take into account the matrix element of the particle physics process. The matrix elements are included by simply multiplying the weights by the corresponding matrix element.

This completes the pseudo-code for the RAMBO algorithm.

In `hazma`, the `rambo` module can be used to perform various tasks. At the highest level, the function `compute_annihilation_cross_section(compute_decay_width)` is provided for computing cross-sections (decay widths) for $2 \rightarrow N$ ($1 \rightarrow N$) processes. For example, consider computing the partial decay width of $\mu^- \rightarrow e^- \bar{\nu}_e \nu_\mu$. One first declares a function that takes a list of the final state particles' four-momenta and muon's four-momentum, and returns the matrix element squared for the reaction:

```

# Import the fermi constant

>>> from hazma.parameters import GF

# Import a helper function for scalar products of four-vectors

>>> from hazma.field_theory_helper_functions.common_functions import
↳   minkowski_dot as MDot

# Declare the matrix element

>>> def msqrd_mu_to_enunu(momenta):

...     pe = momenta[0] # electron four-momentum

...     pve = momenta[1] # electron-neutrino four-momentum

...     pvmu = momenta[2] # muon-neutrino four-momentum

...     pmu = sum(momenta) # muon four-momentum

...     # squared matrix element

...     return 64. * GF**2 * MDot(pe, pvmu) * MDot(pmu, pve)

```

Then, the partial decay width can be computed using:

```

# Import function to compute decay width

>>> from hazma.rambo import compute_decay_width

# import masses of muon and electron

>>> from hazma.parameters import muon_mass as mmu

>>> from hazma.parameters import electron_mass as me

```

```

# Specify the masses of the electron and neutrinos

>>> fsp_masses = np.array([me, 0., 0.])

# compute the partial width

>>> partial_width = compute_decay_width(fsp_masses, mmu,
↳ num_ps_pts=50000,
...
↳ mat_elem_sqrd=msqrd_mu_to_enunu)

```

Using 50000 phase-space points gives a result within 5% of the analytical value.

In addition, `rambo` includes a function for performing integrations over all variables except the energy of one of the final-state particles called `generate_energy_histogram`. This is useful for computing energy spectra for FSR from final states with large numbers of particles. The following demonstrates how it can be used:

```

>>> from hazma.rambo import generate_energy_histogram

>>> import numpy as np

>>> num_ps_pts = 100000 #number of phase-space points to use

# masses of final-state particles

>>> masses = np.array([100., 100., 0.0, 0.0])

>>> cme = 1000. # center-of-mass energy

>>> num_bins = 100 # number of energy bins to use

```

```

# computing energy histograms

>>> eng_hist = generate_energy_histogram(num_ps_pts, masses, cme,
...                                     num_bins=num_bins)

# plot the results

>>> import matplotlib as plt

>>> for i in range(len(masses)):

...     # pts[i, 0] are the energies of particle i

...     # pts[i, 1] are the probabilities

...     plt.loglog(pts[i, 0], pts[i, 1])

```

At the lowest level, `rambo` includes a function for generating phase-space points called `generate_phase_space`. We also include a function `integrate_over_phase_space` which will perform the integral

$$\int \left(\prod_{i=1}^N \frac{d^3 \vec{p}_i}{(2\pi)^3} \frac{1}{2E_i} \right) (2\pi)^4 \delta^4 \left(P - \sum_{i=1}^N p_i \right) |\mathcal{M}|^2 \quad (\text{D.8})$$

where P^μ is the total four-momentum, p_i^μ are the individual four-momenta for each of the N final-state particles and \mathcal{M} is the matrix element.

Appendix E

Gamma-ray Spectra from many final state particles: `gamma_ray`

Since computing gamma-ray spectra is a model-dependent process, we include in `hazma` tools for computing gamma-ray spectra from both FSR and the decay of final state-particles. The `gamma_ray` module contains two functions called `gamma_ray_decay` and `gamma_ray_fsr`. The `gamma_ray_decay` function accepts a list of the final-state particles, the center-of-mass energy, the gamma-ray energies to compute the spectrum at and optionally the matrix element squared. Currently, the final-state particles can be $\pi^0, \pi^\pm, \mu^\pm, e^\pm, K^\pm, K_L$ and K_S where K stands for kaon. We caution that when including many final-state mesons, one needs to take care to supply a matrix element squared that is valid at the reaction's center-of-mass energy (see Sec. (5.1) for a discussion on the validity of ChPT for large energies).

The `gamma_ray_decay` function works by first computing the energies distri-

butions of all the final-state particles and convolving these with the decay spectra of the final-state particles. It can be used as follows:

```

>>> from hazma.gamma_ray_decay import gamma_ray_decay

>>> import numpy as np

# specify the final-state particles

>>> particles = np.array(['muon', 'charged_kaon', 'long_kaon'])

# choose the center of mass energy

>>> e_cm = 5000.

# choose list of the gamma-ray energies to compute spectra at

>>> e_gams = np.logspace(0., np.log10(e_cm), num=200,
    ↪ dtype=np.float64)

# compute the gamma-ray spectra assuming a constant matrix element

>>> spec = gamma_ray_decay(particles, e_cm, e_gams)

```

The `gamma_ray_fsr` function computes the gamma-ray spectrum from $X \rightarrow Y\gamma$, i.e.:

$$\frac{dN(X \rightarrow Y\gamma)}{dE_\gamma} = \frac{1}{\sigma(X \rightarrow Y)} \frac{d\sigma(X \rightarrow Y\gamma)}{dE_\gamma} \quad (\text{E.1})$$

where X and Y are any particles excluding the photon. As input this function takes a list of the initial state particle masses (either 1 or 2 particles), the final state particle masses, the center-of-mass energy, a function for the tree-level matrix element squared (for $X \rightarrow Y$) and a function for the radiative matrix element squared ($X \rightarrow Y\gamma$). The

functions for the squared matrix elements must take is a single argument which is a list of the four-momenta for the final state particles. As an example, we consider the process of two dark-matter particles annihilating into charged pions, $\chi\bar{\chi} \rightarrow \pi^+\pi^-(\gamma)$ using the model from App. (C.0.2). In App (C.0.2), we gave the analytic expressions for the gamma-ray spectra. The tree-level and radiative matrix elements squared for this process are:

$$|\mathcal{M}(\chi\bar{\chi} \rightarrow \pi^+\pi^-)|^2 = \frac{c_1^2 (s - 4m_\chi^2)}{2\Lambda^2} \quad (\text{E.2})$$

$$|\mathcal{M}(\chi\bar{\chi} \rightarrow \pi^+\pi^-\gamma)|^2 = \frac{2c_1^2 (4\mu_\chi^2 - 1) Q^2 e^2}{\Lambda^2 (t - \mu_\pi^2 Q^2)^2 (u - \mu_\pi^2 Q^2)^2} \times \left((\mu_\pi Q(t + u) - 2\mu_\pi^3 Q^3)^2 + s (t - \mu_\pi^2 Q^2) (\mu_\pi^2 Q^2 - u) \right) \quad (\text{E.3})$$

where Q is the center-of-mass energy, e is the electromagnetic coupling, $\mu_{\pi,\chi} = m_{\pi,\chi}/Q$ and

$$s = (p_{\pi,1} + p_{\pi,2})^2, \quad t = (p_{\pi,1} + k)^2, \quad u = (p_{\pi,2} + k)^2 \quad (\text{E.4})$$

with $p_{\pi,1,2}$ are the four-momenta of the two final-state pions and k is the four-momenta of the final-state photon. Below, we create a class to implement functions for the tree and radiative squared matrix elements. Note that these functions take in an array of four-momenta.

```
from hazma.field_theory_helper_functions.common_functions import
↪ minkowski_dot as MDot
```

```

class Msqrd(object):

    def __init__(self, mx, c1, lam):

        self.mx = mx # DM mass

        self.c1 = c1 # effective coupling of DM to charged pions

        self.lam = lam # cut off scale for effective theory

    def tree(self, momenta):

        ppi1 = momenta[0] # first charged pion four-momentum

        ppi2 = momenta[1] # second charged pion four-momentum

        Q = ppi1[0] + ppi2[0] # center-of-mass energy

        return -((self.c1**2 * (4 * self.mx**2 - Q**2)) / (2 *
        ↪ self.lam**2))

    def radiative(self, momenta):

        ppi1 = momenta[0] # first charged pion four-momentum

        ppi2 = momenta[1] # second charged pion four-momentum

        k = momenta[2] # photon four-momentum

        Q = ppi1[0] + ppi2[0] + k[0] # center-of-mass energy

        mux = self.mx / Q

        mupi = mpi / Q

```

```

s = MDot(ppi1 + ppi2, ppi1 + ppi2)

t = MDot(ppi1 + k, ppi1 + k)

u = MDot(ppi2 + k, ppi2 + k)

return ((2*self.c1**2*(-1 + 4*mux**2)*Q**2*qe**2 *
        (s*(-(mupi**2*Q**2) + t)*(mupi**2*Q**2 - u) +
        (-2*mupi**3*Q**3 + mupi*Q*(t + u)**2)) /
        (self.lam**2*(-(mupi**2*Q**2) + t)**2*
        (-mupi**2*Q**2) + u)**2))

```

Next, we can compute the gamma-ray spectrum for $\chi\bar{\chi} \rightarrow \pi^+\pi^-\gamma$ using:

```

>>> from hazma.gamma_ray import gamma_ray_fsr

# specify the parameters of the model

>>> params = {'mx': 200.0, 'c1': 1.0, 'lam': 1e4}

# create instance of our Msqrd class

>>> msqrds = Msqrd(**params)

# specify the initial and final state masses

>>> isp_masses = np.array([msqrds.mx, msqrds.mx])

>>> fsp_masses = np.array([mpi, mpi, 0.0])

# choose the center-of-mass energy

```

```

>>> e_cm = 4.0 * msqrds.mx

# compute the gamma-ray spectrum

>>> spec = gamma_ray_fsr(isp_masses, fsp_masses, e_cm, msqrds.tree,
                          msqrds.radiative, num_ps_pts=500000,
                          ↪ num_bins=50)

# plot the spectrum

>>> import matplotlib.pyplot as plt

>>> plt.figure(dpi=100)

>>> plt.plot(spec[0], spec[1])

>>> plt.yscale('log')

>>> plt.xscale('log')

>>> plt.ylabel(r'$dN/dE_{\gamma} \ (\mathrm{MeV})^{-1}$',
               ↪ fontsize=16)

>>> plt.xlabel(r'$E_{\gamma} \ (\mathrm{MeV})$', fontsize=16)

```

Bibliography

- [1] B. P. Abbott et al. Observation of Gravitational Waves from a Binary Black Hole Merger. *Phys. Rev. Lett.*, 116(6):061102, 2016.
- [2] George O. Abell, Jr. Corwin, Harold G., and Ronald P. Olowin. A Catalog of Rich Clusters of Galaxies. *Astrophysical Journal, Supplement*, 70:1, May 1989.
- [3] A. Abramowski et al. Search for dark matter annihilation signatures in H.E.S.S. observations of Dwarf Spheroidal Galaxies. *Phys. Rev.*, D90:112012, 2014.
- [4] R. Abuter et al. Detection of the gravitational redshift in the orbit of the star S2 near the Galactic centre massive black hole. *Astron. Astrophys.*, 615:L15, 2018.
- [5] M. Ackermann, M. Ajello, A. Albert, W. B. Atwood, L. Baldini, J. Ballet, G. Barbiellini, D. Bastieri, K. Bechtol, R. Bellazzini, E. Bissaldi, R. D. Blandford, E. D. Bloom, E. Bottacini, T. J. Brandt, J. Bregeon, P. Bruel, R. Buehler, S. Buson, G. A. Caliandro, R. A. Cameron, M. Caragiulo, P. A. Caraveo, E. Cavazzuti, C. Cecchi, E. Charles, A. Chekhtman, J. Chiang, G. Chiaro, S. Ciprini, R. Claus, J. Cohen-Tanugi, J. Conrad, A. Cuoco, S. Cutini, F. D'Ammando, A. de Angelis, F. de Palma, C. D. Dermer, S. W. Digel, E. do Couto e. Silva, P. S. Drell,

C. Favuzzi, E. C. Ferrara, W. B. Focke, A. Franckowiak, Y. Fukazawa, S. Funk, P. Fusco, F. Gargano, D. Gasparrini, S. Germani, N. Giglietto, P. Giommi, F. Giordano, M. Giroletti, G. Godfrey, G. A. Gomez-Vargas, I. A. Grenier, S. Guiriec, M. Gustafsson, D. Hadasch, K. Hayashi, E. Hays, J. W. Hewitt, P. Ippoliti, T. Jogler, G. Jóhannesson, A. S. Johnson, W. N. Johnson, T. Kamae, J. Kataoka, J. Knödlseider, M. Kuss, S. Larsson, L. Latronico, J. Li, L. Li, F. Longo, F. Loparco, B. Lott, M. N. Lovellette, P. Lubrano, G. M. Madejski, A. Manfreda, F. Massaro, M. Mayer, M. N. Mazziotta, J. E. McEnery, P. F. Michelson, W. Mitthumsiri, T. Mizuno, A. A. Moiseev, M. E. Monzani, A. Morselli, I. V. Moskalenko, S. Murgia, R. Nemmen, E. Nuss, T. Ohsugi, N. Omodei, E. Orlando, J. F. Ormes, D. Paneque, J. H. Panetta, J. S. Perkins, M. Pesce-Rollins, F. Piron, G. Pivato, T. A. Porter, S. Rainò, R. Rando, M. Razzano, S. Razzaque, A. Reimer, O. Reimer, T. Reposeur, S. Ritz, R. W. Romani, M. Sánchez-Conde, M. Schaal, A. Schulz, C. Sgrò, E. J. Siskind, G. Span-dre, P. Spinelli, A. W. Strong, D. J. Suson, H. Takahashi, J. G. Thayer, J. B. Thayer, L. Tibaldo, M. Tinivella, D. F. Torres, G. Tosti, E. Troja, Y. Uchiyama, G. Vianello, M. Werner, B. L. Winer, K. S. Wood, M. Wood, G. Zaharijas, and S. Zimmer. The Spectrum of Isotropic Diffuse Gamma-Ray Emission between 100 MeV and 820 GeV. *ApJ*, 799(1):86, January 2015.

- [6] M. Ackermann, M. Ajello, W. B. Atwood, L. Baldini, J. Ballet, G. Barbiellini, D. Bastieri, K. Bechtol, R. Bellazzini, B. Berenji, R. D. Blandford, E. D. Bloom,

E. Bonamente, A. W. Borgland, T. J. Brandt, J. Bregeon, M. Brigida, P. Bruel, R. Buehler, S. Buson, G. A. Caliendo, R. A. Cameron, P. A. Caraveo, E. Cavazuti, C. Cecchi, E. Charles, A. Chekhtman, J. Chiang, S. Ciprini, R. Claus, J. Cohen-Tanugi, J. Conrad, S. Cutini, A. de Angelis, F. de Palma, C. D. Dermer, S. W. Digel, E. do Couto e Silva, P. S. Drell, A. Drlica-Wagner, L. Falletti, C. Favuzzi, S. J. Fegan, E. C. Ferrara, W. B. Focke, P. Fortin, Y. Fukazawa, S. Funk, P. Fusco, D. Gaggero, F. Gargano, S. Germani, N. Giglietto, F. Giordano, M. Giroletti, T. Glanzman, G. Godfrey, J. E. Grove, S. Guiriec, M. Gustafsson, D. Hadasch, Y. Hanabata, A. K. Harding, M. Hayashida, E. Hays, D. Horan, X. Hou, R. E. Hughes, G. Jóhannesson, A. S. Johnson, R. P. Johnson, T. Kamae, H. Katagiri, J. Kataoka, J. Knödseder, M. Kuss, J. Lande, L. Latronico, S.-H. Lee, M. Lemoine-Goumard, F. Longo, F. Loparco, B. Lott, M. N. Lovellette, P. Lubrano, M. N. Mazziotta, J. E. McEnery, P. F. Michelson, W. Mitthumsiri, T. Mizuno, C. Monte, M. E. Monzani, A. Morselli, I. V. Moskalenko, S. Murgia, M. Naumann-Godo, J. P. Norris, E. Nuss, T. Ohsugi, A. Okumura, N. Omodei, E. Orlando, J. F. Ormes, D. Paneque, J. H. Panetta, D. Parent, M. Pesce-Rollins, M. Pierbattista, F. Piron, G. Pivato, T. A. Porter, S. Rainò, R. Rando, M. Razzano, S. Razzaque, A. Reimer, O. Reimer, H. F.-W. Sadrozinski, C. Sgrò, E. J. Siskind, G. Spandre, P. Spinelli, A. W. Strong, D. J. Suson, H. Takahashi, T. Tanaka, J. G. Thayer, J. B. Thayer, D. J. Thompson, L. Tibaldo, M. Tinivella, D. F. Torres, G. Tosti, E. Troja, T. L. Usher, J. Vandenbroucke, V. Vasileiou, G. Vianello, V. Vitale, A. P. Waite, P. Wang, B. L. Winer, K. S.

- Wood, M. Wood, Z. Yang, M. Ziegler, and S. Zimmer. FERMI-LAT OBSERVATIONS OF THE DIFFUSE γ -RAY EMISSION: IMPLICATIONS FOR COSMIC RAYS AND THE INTERSTELLAR MEDIUM. *The Astrophysical Journal*, 750(1):3, apr 2012.
- [7] M. Ackermann et al. Fermi-LAT Observations of the Diffuse Gamma-Ray Emission: Implications for Cosmic Rays and the Interstellar Medium. *Astrophys. J.*, 750:3, 2012.
- [8] F. A. Agaronyan and A. M. Atoyan. On the Origin of the Galactic Annihilation Radiation. *Soviet Astronomy Letters*, 7:395–398, August 1981.
- [9] N. Aghanim et al. Planck 2018 results. VI. Cosmological parameters. 2018.
- [10] N. Aghanim et al. Planck 2018 results. VI. Cosmological parameters. *Astron. Astrophys.*, 641:A6, 2020.
- [11] P. Agnes et al. Constraints on Sub-GeV Dark-Matter-Electron Scattering from the DarkSide-50 Experiment. *Phys. Rev. Lett.*, 121(11):111303, 2018.
- [12] A. Aguilar, L. B. Auerbach, R. L. Burman, D. O. Caldwell, E. D. Church, A. K. Cochran, J. B. Donahue, A. Fazely, G. T. Garvey, R. M. Gunasingha, and et al. Evidence for neutrino oscillations from the observation of ν_{e^-} appearance in a ν_{μ^-} beam. *Physical Review D*, 64(11), Nov 2001.
- [13] M. Aguilar et al. Precision Measurement of the Boron to Carbon Flux Ratio in

Cosmic Rays from 1.9 GV to 2.6 TV with the Alpha Magnetic Spectrometer on the International Space Station. *Phys. Rev. Lett.*, 117(23):231102, 2016.

- [14] A. Aguilar-Arevalo, D. Amidei, D. Baxter, G. Canelo, B. A. Cervantes Vergara, A. E. Chavarria, E. Darragh-Ford, J. R. T. de Mello Neto, J. C. D’Olivo, J. Estrada, R. Gaïor, Y. Guardincerri, T. W. Hossbach, B. Kilminster, I. Lawson, S. J. Lee, A. Letessier-Selvon, A. Matalon, V. B. B. Mello, P. Mitra, J. Molina, S. Paul, A. Piers, P. Privitera, K. Ramanathan, J. Da Rocha, Y. Sarkis, M. Settimo, R. Smida, R. Thomas, J. Tiffenberg, D. Torres Machado, R. Vilar, and A. L. Virto. Constraints on light dark matter particles interacting with electrons from cosmic at snolab. *Phys. Rev. Lett.*, 123:181802, Oct 2019.
- [15] Torsten Akesson, Asher Berlin, Nikita Blinov, Owen Colegrove, Giulia Collura, Valentina Dutta, Bertrand Echenard, Joshua Hiltbrand, David G Hitlin, Joseph Incandela, et al. Light dark matter experiment (ldmx). *arXiv preprint arXiv:1808.05219*, 2018.
- [16] J. Aleksić et al. The major upgrade of the MAGIC telescopes, Part II: A performance study using observations of the Crab Nebula. *Astropart. Phys.*, 72:76–94, 2016.
- [17] Guido Altarelli and G. Parisi. Asymptotic Freedom in Parton Language. *Nucl. Phys. B*, 126:298–318, 1977.

- [18] A. De Angelis et al. Science with e-astrogam (a space mission for mev-gev gamma-ray astrophysics). Technical report, April 2018.
- [19] E. Aprile et al. Light dark matter search with ionization signals in xenon1t. 2019.
- [20] Tsuguo Aramaki et al. Snowmass 2021 Letter of Interest: The GRAMS Project: MeV Gamma-Ray Observations and Antimatter-Based Dark Matter Searches. 9 2020.
- [21] Tsuguo Aramaki, Per Hansson Adrian, Georgia Karagiorgi, and Hirokazu Odaka. Dual MeV Gamma-Ray and Dark Matter Observatory - GRAMS Project. *Astropart. Phys.*, 114:107–114, 2020.
- [22] Alexandre Arbey and Jérémy Auffinger. Blackhawk: a public code for calculating the hawking evaporation spectra of any black hole distribution. *The European Physical Journal C*, 79(8):1–26, 2019.
- [23] Giorgio Arcadi, Maíra Dutra, Pradipta Ghosh, Manfred Lindner, Yann Mambrini, Mathias Pierre, Stefano Profumo, and Farinaldo S. Queiroz. The waning of the WIMP? A review of models, searches, and constraints. *Eur. Phys. J. C*, 78(3):203, 2018.
- [24] W. B. Atwood et al. The large area telescope on the fermi gamma-ray space telescope mission. *The Astrophysical Journal*, 697(2):1071, 2009.
- [25] W. B. Atwood et al. The Large Area Telescope on the Fermi Gamma-ray Space Telescope Mission. *Astrophys. J.*, 697:1071–1102, 2009.

- [26] W.B. Atwood et al. The Large Area Telescope on the Fermi Gamma-ray Space Telescope Mission. *Astrophys. J.*, 697:1071–1102, 2009.
- [27] M. Bahr et al. Herwig++ Physics and Manual. *Eur. Phys. J. C*, 58:639–707, 2008.
- [28] Reba M. Bandyopadhyay, Joseph Silk, James E. Taylor, and Thomas J. Maccarone. On the Origin of the 511 keV Emission in the Galactic Centre. *Mon. Not. Roy. Astron. Soc.*, 392:1115, 2009.
- [29] Liron Barak, Itay M. Bloch, Mariano Cababie, Gustavo Canelo, Luke Chaplinsky, Fernando Chierchie, Michael Crisler, Alex Drlica-Wagner, Rouven Essig, Juan Estrada, Erez Etzion, Guillermo Fernandez Moroni, Daniel Gift, Sravan Mungalalasa, Aviv Orly, Dario Rodrigues, Aman Singal, Miguel Sofo Haro, Leandro Stefanazzi, Javier Tiffenberg, Sho Uemura, Tomer Volansky, and Tien-Tien Yu. Sensei: Direct-detection results on sub-gev dark matter from a new skipper-ccd, 2020.
- [30] A. Barnacka, J.-F. Glicenstein, and R. Moderski. New constraints on primordial black holes abundance from femtolensing of gamma-ray bursts. *Physical Review D*, 86(4), Aug 2012.
- [31] Richard Bartels, Daniele Gaggero, and Christoph Weniger. Prospects for indirect dark matter searches with mev photons. *Journal of Cosmology and Astroparticle Physics*, 2017(05):001, 2017.

- [32] Richard Bartels, Daniele Gaggero, and Christoph Weniger. Prospects for indirect dark matter searches with MeV photons. *JCAP*, 05:001, 2017.
- [33] Brian Batell, Maxim Pospelov, and Adam Ritz. Exploring portals to a hidden sector through fixed targets. *Physical Review D*, 80(9):095024, 2009.
- [34] John F. Beacom, Nicole F. Bell, and Gianfranco Bertone. Gamma-ray constraint on galactic positron production by meV dark matter. *Phys. Rev. Lett.*, 94:171301, May 2005.
- [35] John F. Beacom and Hasan Yüksel. Stringent Constraint on Galactic Positron Production. *Physical Review Letters*, 97(7):071102, August 2006.
- [36] G. Belanger, F. Boudjema, A. Pukhov, and A. Semenov. micrOMEGAs: A program for calculating dark matter observables. *Comput. Phys. Commun.*, 185:960–985, 2014.
- [37] C. Bird, R. Kowalewski, and M. Pospelov. Dark Matter Pair-Production in $b \rightarrow s$ Transitions. *Modern Physics Letters A*, 21(6):457–478, January 2006.
- [38] Simeon Bird, Ilias Cholis, Julian B. Muñoz, Yacine Ali-Haïmoud, Marc Kamionkowski, Ely D. Kovetz, Alvise Raccanelli, and Adam G. Riess. Did LIGO detect dark matter? *Phys. Rev. Lett.*, 116(20):201301, 2016.
- [39] Deirdre Black, Amir H. Fariborz, and Joseph Schechter. Chiral Lagrangian treatment of pi eta scattering. *Phys. Rev.*, D61:074030, 2000.

- [40] Kimberly K. Boddy and Jason Kumar. Indirect detection of dark matter using mev-range gamma-ray telescopes. *Phys. Rev. D*, 92:023533, Jul 2015.
- [41] Kimberly K. Boddy and Jason Kumar. Indirect Detection of Dark Matter Using MeV-Range Gamma-Ray Telescopes. *Phys. Rev. D*, 92(2):023533, 2015.
- [42] Céline Boehm, Dan Hooper, Joseph Silk, Michel Casse, and Jacques Paul. MeV Dark Matter: Has It Been Detected? *Physical Review Letters*, 92(10):101301, March 2004.
- [43] Celine Boehm, Archil Kobakhidze, Ciaran A.J. O’Hare, Zachary S.C. Picker, and Mairi Sakellariadou. Eliminating the LIGO bounds on primordial black hole dark matter. 8 2020.
- [44] Slavko Bogdanov. The Nearest Millisecond Pulsar Revisited with XMM-Newton: Improved Mass-Radius Constraints for PSR J0437-4715. *Astrophys. J.*, 762:96, 2013.
- [45] Steven E. Boggs et al. The Advanced Compton Telescope Mission. *New Astron. Rev.*, 50:604–607, 2006.
- [46] A. E. Bolotnikov, G. S. Camarda, G. De Geronimo, J. Fried, D. Hodges, A. Hosain, K. Kim, G. Mahler, L. Ocampo Giraldo, E. Vernon, G. Yang, and R. B. James. A 4 x 4 array module of position-sensitive virtual Frisch-grid CdZnTe detectors for gamma-ray imaging spectrometers. *Nuclear Instruments and Methods in Physics Research A*, 954:161036, February 2020.

- [47] A. Z. Bonanos, K. Z. Stanek, R. P. Kudritzki, L. Macri, D. D. Sasselov, J. Kaluzny, D. Bersier, F. Bresolin, T. Matheson, B. J. Mochejska, N. Przybilla, A. H. Szentgyorgyi, J. Tonry, and G. Torres. The First DIRECT Distance to a Detached Eclipsing Binary in M33. *Astrophysics and Space Science*, 304(1-4):207–209, August 2006.
- [48] Laurent Bouchet, Andrew W. Strong, Troy A. Porter, Igor V. Moskalenko, Elisabeth Jourdain, and Jean-Pierre Roques. Diffuse emission measurement with INTEGRAL/SPI as indirect probe of cosmic-ray electrons and positrons. *Astrophys. J.*, 739:29, 2011.
- [49] Mathieu Boudaud and Marco Cirelli. Voyager 1 e^\pm Further Constrain Primordial Black Holes as Dark Matter. *Phys. Rev. Lett.*, 122(4):041104, 2019.
- [50] J. Boulesteix and G. Monnet. Mass distribution and a stellar population model in the spiral galaxy M33. *Astronomy and Astrophysics*, 9:350–355, December 1970.
- [51] A. Boyarsky, M. Drewes, T. Lasserre, S. Mertens, and O. Ruchayskiy. Sterile neutrino Dark Matter. *Prog. Part. Nucl. Phys.*, 104:1–45, 2019.
- [52] Timothy D. Brandt. Constraints on MACHO Dark Matter from Compact Stellar Systems in Ultra-Faint Dwarf Galaxies. *Astrophys. J. Lett.*, 824(2):L31, 2016.
- [53] Torsten Bringmann, Lars Bergstrom, and Joakim Edsjo. New gamma-ray contributions to supersymmetric dark matter annihilation. *Journal of High Energy Physics*, 2008(01):049, 2008.

- [54] Torsten Bringmann, Michele Doro, and Mattia Fornasa. Dark matter signals from draco and willman 1: prospects for magic ii and cta. *Journal of Cosmology and Astroparticle Physics*, 2009(01):016, 2009.
- [55] Torsten Bringmann, Michele Doro, and Mattia Fornasa. Dark Matter signals from Draco and Willman 1: Prospects for MAGIC II and CTA. *JCAP*, 01:016, 2009.
- [56] Warren R. Brown, Margaret J. Geller, Scott J. Kenyon, and Antonaldo Diaferio. Velocity Dispersion Profile of the Milky Way Halo. *Astronomical Journal*, 139(1):59–67, January 2010.
- [57] DA Bryman, P Depommier, and C Leroy. $\pi \rightarrow e\nu$, $\pi \rightarrow e\nu\gamma$ decays and related processes. *Physics Reports*, 88(3):151–205, 1982.
- [58] A. J. Buras, P. Gambino, M. Gorbahn, S. Jager, and L. Silvestrini. Universal unitarity triangle and physics beyond the standard model. *Phys. Lett.*, B500:161–167, 2001.
- [59] T. H. Burnett and Norman M. Kroll. Extension of the low soft-photon theorem. *Phys. Rev. Lett.*, 20(2), January 1968.
- [60] Fabio Cafardo and Rodrigo Nemmen. Fermi LAT observations of Sagittarius A*: Imaging Analysis. 7 2021.
- [61] Francesca Calore, Mattia Di Mauro, Fiorenza Donato, Jason W. T. Hessels, and Christoph Weniger. Radio detection prospects for a bulge population of mil-

- lisecond pulsars as suggested by Fermi LAT observations of the inner Galaxy. *Astrophys. J.*, 827(2):143, 2016.
- [62] Regina Caputo et al. All-sky Medium Energy Gamma-ray Observatory: Exploring the Extreme Multimessenger Universe. 7 2019.
- [63] E. Caroli, J. B. Stephen, G. Di Cocco, L. Natalucci, and A. Spizzichino. Coded Aperture Imaging in X-Ray and Gamma-Ray Astronomy. *Space Sci. Rev.*, 45(3-4):349–403, September 1987.
- [64] B. J. Carr, Kazunori Kohri, Yuuiti Sendouda, and Jun’ichi Yokoyama. New cosmological constraints on primordial black holes. *Phys. Rev.*, D81:104019, 2010.
- [65] Bernard Carr, Kazunori Kohri, Yuuiti Sendouda, and Jun’ichi Yokoyama. Constraints on Primordial Black Holes. 2 2020.
- [66] Junmou Chen, Tao Han, and Brock Tweedie. Electroweak Splitting Functions and High Energy Showering. *JHEP*, 11:093, 2017.
- [67] Xue-Lei Chen and Marc Kamionkowski. Particle decays during the cosmic dark ages. *Phys. Rev. D*, 70:043502, 2004.
- [68] Chen Cheng, Pengwei Xie, Abdusalam Abdukerim, Wei Chen, Xun Chen, Yunhua Chen, Xiangyi Cui, Yingjie Fan, Deqing Fang, Changbo Fu, Mengting Fu, Lisheng Geng, Karl Giboni, Linhui Gu, Xuyuan Guo, Ke Han, Changda He, Shengming He, Di Huang, Yan Huang, Yanlin Huang, Zhou Huang, Xiangdong

Ji, Yonglin Ju, Shuaijie Li, Qing Lin, Huaxuan Liu, Jianglai Liu, Liqiang Liu, Xiaoying Lu, Wenbo Ma, Yugang Ma, Yajun Mao, Yue Meng, Parinya Namwongsa, Kaixiang Ni, Jinhua Ning, Xuyang Ning, Xiangxiang Ren, Nasir Shaheed, Changsong Shang, Guofang Shen, Lin Si, Andi Tan, Anqing Wang, Hongwei Wang, Meng Wang, Qiuhong Wang, Siguang Wang, Wei Wang, Xiuli Wang, Zhou Wang, Mengmeng Wu, Shiyong Wu, Weihao Wu, Jingkai Xia, Mengjiao Xiao, Xiang Xiao, Binbin Yan, Jijun Yang, Yong Yang, Chunxu Yu, Jumin Yuan, Ying Yuan, Xinning Zeng, Dan Zhang, Tao Zhang, Li Zhao, Qibin Zheng, Jifang Zhou, Ning Zhou, and Xiaopeng Zhou. Search for light dark matter-electron scattering in the pandax-ii experiment. *Phys. Rev. Lett.*, 126:211803, May 2021.

- [69] R Sekhar Chivukula, Andrew Cohen, Howard Georgi, Benjamin Grinstein, and Aneesh V Manohar. Higgs decay into goldstone bosons. *Annals of Physics (New York);(USA)*, 192(1), 1989.
- [70] E. Churazov, R. Sunyaev, S. Sazonov, M. Revnivtsev, and D. Varshalovich. Positron annihilation spectrum from the Galactic Centre region observed by SPI/INTEGRAL. *Monthly Notices of the Royal Astronomical Society*, 357(4):1377–1386, March 2005.
- [71] Marco Cirelli, Gennaro Corcella, Andi Hektor, Gert Hutsi, Mario Kadastik, Paolo Panci, Martti Raidal, Filippo Sala, and Alessandro Strumia. PPPC 4 DM ID: A Poor Particle Physicist Cookbook for Dark Matter Indirect Detection. *JCAP*, 1103:051, 2011. [Erratum: JCAP1210,E01(2012)].

- [72] Marco Cirelli, Nicolao Fornengo, Bradley J. Kavanagh, and Elena Pinetti. Integral X-ray constraints on sub-GeV Dark Matter. 7 2020.
- [73] Steven Clark, Bhaskar Dutta, Yu Gao, Yin-Zhe Ma, and Louis E. Strigari. 21 cm limits on decaying dark matter and primordial black holes. *Phys. Rev. D*, 98(4):043006, 2018.
- [74] Steven Clark, Bhaskar Dutta, Yu Gao, Louis E. Strigari, and Scott Watson. Planck Constraint on Relic Primordial Black Holes. *Phys. Rev. D*, 95(8):083006, 2017.
- [75] Steven J. Clark, Bhaskar Dutta, Yu Gao, Louis E. Strigari, and Scott Watson. Planck constraint on relic primordial black holes. *Physical Review D*, 95(8), Apr 2017.
- [76] Sergio Colafrancesco, S. Profumo, and P. Ullio. Multi-frequency analysis of neutralino dark matter annihilations in the Coma cluster. *Astron. Astrophys.*, 455:21, 2006.
- [77] Sergio Colafrancesco, S. Profumo, and P. Ullio. Multi-frequency analysis of neutralino dark matter annihilations in the Coma cluster. *Astron. Astrophys.*, 455:21, 2006.
- [78] Sergio Colafrancesco, S. Profumo, and P. Ullio. Detecting dark matter WIMPs in the Draco dwarf: A multi-wavelength perspective. *Phys. Rev.*, D75:023513, 2007.
- [79] Sergio Colafrancesco, S. Profumo, and P. Ullio. Detecting dark matter WIMPs in the Draco dwarf: A multi-wavelength perspective. *Phys. Rev. D*, 75:023513, 2007.

- [80] EDELWEISS Collaboration, Q. Arnaud, E. Armengaud, C. Augier, A. Benoît, L. Bergé, J. Billard, A. Broniatowski, P. Camus, A. Cazes, M. Chapellier, F. Charlieux, M. De Jésus, L. Dumoulin, K. Eitel, E. Elkhoury, J. B. Fillipini, D. Filosofov, J. Gascon, A. Giuliani, M. Gros, Y. Jin, A. Juillard, M. Kleifges, H. Lattaud, S. Marnieros, D. Misiak, X. F. Navick, C. Nones, E. Olivieri, C. Oriol, P. Pari, B. Paul, D. Poda, S. Rozov, T. Salagnac, V. Sanglard, B. Siebenborn, L. Vagneron, M. Weber, E. Yakushev, and A. Zolotarova. First germanium-based constraints on sub-meV dark matter with the edelweiss experiment, 2020.
- [81] Pokemon Uranium Wiki Contributors. Hazma, 2019.
- [82] Adam Coogan, Alexander Moiseev, Logan Morrison, and Stefano Profumo. Hunting for Dark Matter and New Physics with (a) GECCO. 1 2021.
- [83] Adam Coogan, Logan Morrison, and Stefano Profumo. Direct Detection of Hawking Radiation from Asteroid-Mass Primordial Black Holes. 10 2020.
- [84] Adam Coogan, Logan Morrison, and Stefano Profumo. Hazma: A Python Toolkit for Studying Indirect Detection of Sub-GeV Dark Matter. *JCAP*, 01:056, 2020.
- [85] Coogan, Adam and Morrison, Logan and Profumo, Stefano. The effective theory of sub-gev dark matter interactions with hadrons. to appear.
- [86] Raffaele Tito D’Agnolo and Joshua T. Ruderman. Light Dark Matter from Forbidden Channels. *Phys. Rev. Lett.*, 115(6):061301, 2015.

- [87] G. D’Ambrosio, G. F. Giudice, G. Isidori, and A. Strumia. Minimal flavor violation: An Effective field theory approach. *Nucl. Phys.*, B645:155–187, 2002.
- [88] Basudeb Dasgupta, Ranjan Laha, and Anupam Ray. Neutrino and positron constraints on spinning primordial black hole dark matter. *Phys. Rev. Lett.*, 125(10):101101, 2020.
- [89] Hooman Davoudiasl, Dan Hooper, and Samuel D. McDermott. Inflatable Dark Matter. *Phys. Rev. Lett.*, 116(3):031303, 2016.
- [90] Giovanni De Cesare, A. Bazzano, F. Capitanio, M. Del Santo, V. Lonjou, L. Natalucci, P. Ubertini, and P. Von Ballmoos. INTEGRAL/IBIS search for $e^- e^+$ annihilation radiation from the Galactic Center region. *Adv. Space Res.*, 38:1457, 2006.
- [91] André de Gouvêa and Andrew Kobach. Global Constraints on a Heavy Neutrino. *Phys. Rev. D*, 93(3):033005, 2016.
- [92] P.F. de Salas, K. Malhan, K. Freese, K. Hattori, and M. Valluri. On the estimation of the Local Dark Matter Density using the rotation curve of the Milky Way. *JCAP*, 10:037, 2019.
- [93] Francesco D’Eramo, Nicolas Fernandez, and Stefano Profumo. When the Universe Expands Too Fast: Relentless Dark Matter. *JCAP*, 05:012, 2017.
- [94] Francesco D’Eramo and Stefano Profumo. Sub-GeV Dark Matter Shining at Future MeV γ -Ray Telescopes. *Phys. Rev. Lett.*, 121(7):071101, 2018.

- [95] William DeRocco and Peter W. Graham. Constraining Primordial Black Hole Abundance with the Galactic 511 keV Line. *Phys. Rev. Lett.*, 123(25):251102, 2019.
- [96] Matthew J. Dolan, Felix Kahlhoefer, Christopher McCabe, and Kai Schmidt-Hoberg. A taste of dark matter: Flavour constraints on pseudoscalar mediators. *JHEP*, 03:171, 2015. [Erratum: *JHEP*07,103(2015)].
- [97] John F. Donoghue, J. Gasser, and H. Leutwyler. The Decay of a Light Higgs Boson. *Nucl. Phys. B*, 343:341–368, 1990.
- [98] Herbi K Dreiner, Howard E Haber, and Stephen P Martin. Two-component spinor techniques and feynman rules for quantum field theory and supersymmetry. *Physics Reports*, 494(1-2):1–196, 2010.
- [99] Leanna Dugger, Tesla E. Jeltema, and Stefano Profumo. Constraints on Decaying Dark Matter from Fermi Observations of Nearby Galaxies and Clusters. *JCAP*, 12:015, 2010.
- [100] Nicole Duncan et al. First flight of the Gamma-Ray Imager/Polarimeter for Solar flares (GRIPS) instrument. *Proc. SPIE Int. Soc. Opt. Eng.*, 9905:99052Q, 2016.
- [101] Timur Dzhathdov and Egor Podlesnyi. Massive Argon Space Telescope (MAST): A concept of heavy time projection chamber for γ -ray astronomy in the 100 MeV–1 TeV energy range. *Astropart. Phys.*, 112:1–7, 2019.

- [102] G. Ecker, J. Gasser, A. Pich, and E. de Rafael. The Role of Resonances in Chiral Perturbation Theory. *Nucl. Phys.*, B321:311–342, 1989.
- [103] G. Ecker, J. Gasser, A. Pich, and E. De Rafael. The role of resonances in chiral perturbation theory. *Nuclear Physics B*, 321(2):311 – 342, 1989.
- [104] Gerhard Ecker. Chiral perturbation theory. *Progress in Particle and Nuclear Physics*, 35:1–80, 1995.
- [105] Andrey E. Egorov, Nikolay P. Topchiev, Arkadiy M. Galper, Oleg D. Dalkarov, Alexey A. Leonov, Sergey I. Suchkov, and Yuriy T. Yurkin. Dark matter searches by the planned gamma-ray telescope GAMMA-400. *JCAP*, 11:049, 2020.
- [106] J. Einasto. On the Construction of a Composite Model for the Galaxy and on the Determination of the System of Galactic Parameters. *Trudy Astrofizicheskogo Instituta Alma-Ata*, 5:87–100, January 1965.
- [107] J. Einasto. On the Construction of a Composite Model for the Galaxy and on the Determination of the System of Galactic Parameters. *Trudy Astrofizicheskogo Instituta Alma-Ata*, 5:87–100, 1965.
- [108] Rafel Escribano, Pere Masjuan, and Juan Jose Sanz-Cillero. Chiral dynamics predictions for $\eta' \rightarrow \eta \pi \pi$. *JHEP*, 05:094, 2011.
- [109] Rouven Essig, Eric Kuflik, Samuel D. McDermott, Tomer Volansky, and Kathryn M. Zurek. Constraining Light Dark Matter with Diffuse X-Ray and Gamma-Ray Observations. *JHEP*, 11:193, 2013.

- [110] Rouven Essig, Jeremy Mardon, and Tomer Volansky. Direct Detection of Sub-GeV Dark Matter. aug 2011.
- [111] Rouven Essig, Neelima Sehgal, and Louis E. Strigari. Bounds on cross sections and lifetimes for dark matter annihilation and decay into charged leptons from gamma-ray observations of dwarf galaxies. *Phys. Rev. D*, 80:023506, Jul 2009.
- [112] Rouven Essig, Mukul Sholapurkar, and Tien-Tien Yu. Solar Neutrinos as a Signal and Background in Direct-Detection Experiments Searching for Sub-GeV Dark Matter With Electron Recoils. *Phys. Rev.*, D97(9):095029, 2018.
- [113] Jared A. Evans, Akshay Ghalsasi, Stefania Gori, Michele Tammaro, and Jure Zupan. Light Dark Matter from Entropy Dilution. *JHEP*, 02:151, 2020.
- [114] N. Wyn Evans, Mark I. Wilkinson, Puragra Guhathakurta, Eva K. Grebel, and Steven S. Vogt. Dynamical mass estimates for the halo of m31 from keck spectroscopy. *The Astrophysical Journal*, 540(1):L9–L12, Sep 2000.
- [115] Jonathan L. Feng and Jason Kumar. The WIMPless Miracle: Dark-Matter Particles without Weak-Scale Masses or Weak Interactions. *Phys. Rev. Lett.*, 101:231301, 2008.
- [116] Nicolas Fernandez and Stefano Profumo. Unraveling the origin of black holes from effective spin measurements with LIGO-Virgo. *JCAP*, 08:022, 2019.
- [117] Francesc Ferrer and Tanmay Vachaspati. 511 keV Photons from Superconducting Cosmic Strings. *Physical Review Letters*, 95(26):261302, December 2005.

- [118] Douglas P. Finkbeiner and Neal Weiner. Exciting Dark Matter and the INTEGRAL/SPI 511 keV signal. *Phys. Rev. D*, 76:083519, 2007.
- [119] R. Foot and Z. K. Silagadze. Supernova Explosions, 511 keV Photons, Gamma Ray Bursts and Mirror Matter. *International Journal of Modern Physics D*, 14(1):143–151, January 2005.
- [120] N. Fornengo, A. Riotto, and S. Scopel. Supersymmetric dark matter and the reheating temperature of the universe. *Phys. Rev. D*, 67:023514, 2003.
- [121] Silvia Galli, Fabio Iocco, Gianfranco Bertone, and Alessandro Melchiorri. CMB constraints on Dark Matter models with large annihilation cross-section. *Phys. Rev. D*, 80:023505, 2009.
- [122] A. M. Galper et al. The GAMMA-400 space observatory: status and perspectives. 2014.
- [123] J. Gasser and H. Leutwyler. Chiral Perturbation Theory to One Loop. *Annals Phys.*, 158:142, 1984.
- [124] J. Gasser and H. Leutwyler. Chiral perturbation theory: Expansions in the mass of the strange quark. *Nuclear Physics B*, 250(1):465 – 516, 1985.
- [125] R. Gavazzi, C. Adami, F. Durret, J.-C. Cuillandre, O. Ilbert, A. Mazure, R. Pelló, and M. P. Ulmer. A weak lensing study of the coma cluster. *Astronomy & Astrophysics*, 498(2):L33–L36, Apr 2009.

- [126] J.J. Geehan, Mark A. Fardal, A. Babul, and P. Guhathakurta. Investigating the Andromeda Stream. 1. Simple analytic bulge-disk-halo model for M31. *Mon. Not. Roy. Astron. Soc.*, 366:996–1011, 2006.
- [127] Graciela Gelmini, Paolo Gondolo, Adrian Soldatenko, and Carlos E. Yaguna. The Effect of a late decaying scalar on the neutralino relic density. *Phys. Rev. D*, 74:083514, 2006.
- [128] P. Gondolo, J. Edsjo, P. Ullio, L. Bergstrom, Mia Schelke, and E. A. Baltz. Dark-SUSY: Computing supersymmetric dark matter properties numerically. *JCAP*, 0407:008, 2004.
- [129] Alma X. Gonzalez-Morales, Stefano Profumo, and Javier Reynoso-Córdova. Prospects for indirect MeV Dark Matter detection with Gamma Rays in light of Cosmic Microwave Background Constraints. *Phys. Rev.*, D96(6):063520, 2017.
- [130] Anne M. Green and Bradley J. Kavanagh. Primordial Black Holes as a dark matter candidate. 7 2020.
- [131] Benjamin Grinstein and Lisa Randall. The Renormalization of g^2 . *Phys. Lett. B*, 217:335–340, 1989.
- [132] Eilam Gross and Ofer Vitells. Trial factors for the look elsewhere effect in high energy physics. *Eur. Phys. J. C*, 70:525–530, 2010.
- [133] D. E. Gruber, J. L. Matteson, L. E. Peterson, and G. V. Jung. The Spectrum of

- Diffuse Cosmic Hard X-Rays Measured with HEAO 1. *ApJ*, 520(1):124–129, July 1999.
- [134] Edward Hardy. Higgs portal dark matter in non-standard cosmological histories. *JHEP*, 06:043, 2018.
- [135] R. C. Haymes, G. D. Walraven, C. A. Meegan, R. D. Hall, F. T. Djuth, and D. H. Shelton. Detection of nuclear gamma rays from the galactic center region. *Astrophysical Journal*, 201:593–602, November 1975.
- [136] Jamie Holder, RW Atkins, HM Badran, G Blaylock, SM Bradbury, JH Buckley, KL Byrum, DA Carter-Lewis, O Celik, YCK Chow, et al. The first veritas telescope. *Astroparticle Physics*, 25(6):391–401, 2006.
- [137] Dan Hooper and Lian-Tao Wang. Possible evidence for axino dark matter in the galactic bulge. *Physical Review D*, 70(6):063506, September 2004.
- [138] S. D. Hunter, P. F. Bloser, M. P. Dion, M. L. McConnell, G. A. de Nolfo, S. Son, J. M. Ryan, and F. W. Stecker. Development of the Advance Energetic Pair Telescope (AdEPT) for medium-energy gamma-ray astronomy. In *Space Telescopes and Instrumentation 2010: Ultraviolet to Gamma Ray*, volume 7732 of *Proceedings of the SPIE*, page 773221, July 2010.
- [139] S. D. Hunter et al. EGRET observations of the diffuse gamma-ray emission from the galactic plane. *Astrophys. J.*, 481:205–240, 1997.

- [140] S.D. Hunter et al. EGRET observations of the diffuse gamma-ray emission from the galactic plane. *Astrophys. J.*, 481:205–240, 1997.
- [141] Stanley D. Hunter et al. A Pair Production Telescope for Medium-Energy Gamma-Ray Polarimetry. *Astropart. Phys.*, 59:18–28, 2014.
- [142] P. Jean, J. Knödlseider, W. Gillard, N. Guessoum, K. Ferrière, A. Marcowith, V. Lonjou, and J. P. Roques. Spectral analysis of the Galactic e^+e^- annihilation emission. *Astronomy and Astrophysics*, 445(2):579–589, January 2006.
- [143] P. Jean, J. Knödlseider, V. Lonjou, M. Allain, J. P. Roques, G. K. Skinner, B. J. Teegarden, G. Vedrenne, P. von Ballmoos, B. Cordier, P. Caraveo, R. Diehl, Ph. Durouchoux, P. Mandrou, J. Matteson, N. Gehrels, V. Schönfelder, A. W. Strong, P. Ubertini, G. Weidenspointner, and C. Winkler. Early SPI/INTEGRAL measurements of 511 keV line emission from the 4th quadrant of the Galaxy. *Astronomy and Astrophysics*, 407:L55–L58, August 2003.
- [144] Andres Jordan, John P. Blakeslee, Patrick Cote, Laura Ferrarese, Leopoldo Infante, Simona Mei, David Merritt, Eric W. Peng, John L. Tonry, and Michael J. West. The acs fornax cluster survey. i. introduction to the survey and data reduction procedures. *The Astrophysical Journal Supplement Series*, 169(2):213–224, Apr 2007.
- [145] S. Cheenu Kappadath. *Measurement of the Cosmic Diffuse Gamma-Ray Spectrum from 800 keV to 30 MeV*. PhD thesis, University of New Hampshire, May 1993.

- [146] I. D. Karachentsev and O. G. Kashibadze. Masses of the local group and of the M81 group estimated from distortions in the local velocity field. *Astrophysics*, 49(1):3–18, January 2006.
- [147] Shinta Kasuya and Fuminobu Takahashi. 511 keV line from Q balls in the galactic center. *Physical Review D*, 72(8):085015, October 2005.
- [148] Andrey Katz, Joachim Kopp, Sergey Sibiryakov, and Wei Xue. Femtolensing by Dark Matter Revisited. *JCAP*, 12:005, 2018.
- [149] M. Kawasaki and T. Yanagida. 511 keV gamma ray from moduli decay in the Galactic bulge. *Physics Letters B*, 624(3-4):162–165, September 2005.
- [150] Carolyn A. Kierans. AMEGO: Exploring the Extreme Multimessenger Universe. *Proc. SPIE Int. Soc. Opt. Eng.*, 11444:1144431, 2020.
- [151] Hyungjin Kim. A constraint on light primordial black holes from the interstellar medium temperature. 7 2020.
- [152] R. Kleiss, W. James Stirling, and S. D. Ellis. A new monte carlo treatment of multiparticle phase space at high-energies. *Comput. Phys. Commun.*, 40:359, 1986.
- [153] Simon Knapen, Tongyan Lin, and Kathryn M. Zurek. Light Dark Matter: Models and Constraints. *Phys. Rev.*, D96(11):115021, 2017.
- [154] J. Knödseder, P. Jean, V. Lonjou, G. Weidenspointner, N. Guessoum, W. Gillard, G. Skinner, P. von Ballmoos, G. Vedrenne, J. P. Roques, S. Schanne, B. Teegar-

den, V. Schönfelder, and C. Winkler. The all-sky distribution of 511 keV electron-positron annihilation emission. *Astronomy and Astrophysics*, 441(2):513–532, October 2005.

- [155] E Kou, P Urquijo, W Altmannshofer, F Beaujean, G Bell, M Beneke, I I Bigi, F Bishara, M Blanke, C Bobeth, M Bona, N Brambilla, V M Braun, J Brod, A J Buras, H Y Cheng, C W Chiang, M Ciuchini, G Colangelo, A Crivellin, H Czyz, A Datta, F De Fazio, T Deppisch, M J Dolan, J Evans, S Fajfer, T Feldmann, S Godfrey, M Gronau, Y Grossman, F K Guo, U Haisch, C Hanhart, S Hashimoto, S Hirose, J Hisano, L Hofer, M Hoferichter, W S Hou, T Huber, T Hurth, S Jaeger, S Jahn, M Jamin, J Jones, M Jung, A L Kagan, F Kahlhoefer, J F Kamenik, T Kaneko, Y Kiyo, A Kokulu, N Kosnik, A S Kronfeld, Z Ligeti, H Logan, C D Lu, V Lubicz, F Mahmoudi, K Maltman, S Mishima, M Misiak, K Moats, B Moussallam, A Nefediev, U Nierste, D Nomura, N Offen, S L Olsen, E Passemar, A Paul, G Paz, A A Petrov, A Pich, A D Polosa, J Pradler, S Prelovsek, M Procura, G Ricciardi, D J Robinson, P Roig, J Rosiek, S Schacht, K Schmidt-Hoberg, J Schwichtenberg, S R Sharpe, J Shigemitsu, D Shih, N Shimizu, Y Shimizu, L Silvestrini, S Simula, C Smith, P Stoffer, D Straub, F J Tackmann, M Tanaka, A Tayduganov, G Tetlalmatzi-Xolocotzi, T Teubner, A Vairo, D van Dyk, J Virto, Z Was, R Watanabe, I Watson, S Westhoff, J Zupan, R Zwicky, F Abudinén, I Adachi, K Adamczyk, P Ahlburg, H Aihara, A Aloisio, L Andricek, N Anh Ky, M Arndt, D M Asner, H Atmacan, T Aushev, V Aushev, R Ayad, T Aziz,

S Baehr, S Bahinipati, P Bambade, Y Ban, M Barrett, J Baudot, P Behera, K Belous, M Bender, J Bennett, M Berger, E Bernieri, F U Bernlochner, M Bessner, D Besson, S Bettarini, V Bhardwaj, B Bhuyan, T Bilka, S Bilmis, S Bilokin, G Bonvicini, A Bozek, M Bračko, P Branchini, N Braun, R A Briere, T E Browder, L Burmistrov, S Bussino, L Cao, G Caria, G Casarosa, C Cecchi, D Červenkov, M-C Chang, P Chang, R Cheaib, V Chekelian, Y Chen, B G Cheon, K Chilikin, K Cho, J Choi, S-K Choi, S Choudhury, D Cinabro, L M Cremaldi, D Cuesta, S Cunliffe, N Dash, E de la Cruz Burelo, E de Lucia, G De Nardo, M De Nuccio, G De Pietro, A De Yta Hernandez, B Deschamps, M Destefanis, S Dey, F Di Capua, S Di Carlo, J Dingfelder, Z Doležal, I Domínguez Jiménez, T V Dong, D Dossett, S Duell, S Eidelman, D Epifanov, J E Fast, T Ferber, S Fiore, A Fodor, F Forti, A Frey, O Frost, B G Fulsom, M Gabriel, N Gabyshev, E Ganiev, X Gao, B Gao, R Garg, A Garmash, V Gaur, A Gaz, T Geßler, U Gebauer, M Gelb, A Gellrich, D Getzkow, R Giordano, A Giri, A Glazov, B Gobbo, R Godang, O Gogota, P Goldenzweig, B Golob, W Gradl, E Graziani, M Greco, D Greenwald, S Griбанov, Y Guan, E Guido, A Guo, S Halder, K Hara, O Hartbrich, T Hauth, K Hayasaka, H Hayashii, C Hearty, I Heredia De La Cruz, M Hernandez Villanueva, A Hershenhorn, T Higuchi, M Hoek, S Hollitt, N T Hong Van, C-L Hsu, Y Hu, K Huang, T Iijima, K Inami, G Inguglia, A Ishikawa, R Itoh, Y Iwasaki, M Iwasaki, P Jackson, W W Jacobs, I Jaegle, H B Jeon, X Ji, S Jia, Y Jin, C Joo, M Künzel, I Kadenko, J Kahn, H Kakuno, A B Kaliyar, J Kandra, K H Kang, Y Kato, T Kawasaki, C Ketter, M Khasmidatul, H Kichimi, J B Kim,

K T Kim, H J Kim, D Y Kim, K Kim, Y Kim, T D Kimmel, H Kindo, K Kinoshita, T Konno, A Korobov, S Korpar, D Kotchetkov, R Kowalewski, P Križan, R Kroeger, J-F Krohn, P Krokovny, W Kuehn, T Kuhr, R Kulasiri, M Kumar, R Kumar, T Kumita, A Kuzmin, Y-J Kwon, S Lacaprara, Y-T Lai, K Lalwani, J S Lange, S C Lee, J Y Lee, P Leitl, D Levit, S Levonian, S Li, L K Li, Y Li, Y B Li, Q Li, L Li Gioi, J Libby, Z Liptak, D Liventsev, S Longo, A Loos, G Lopez Castro, M Lubej, T Lueck, F Luetticke, T Luo, F Müller, Th Müller, C MacQueen, Y Maeda, M Maggiora, S Maity, E Manoni, S Marcello, C Marinas, M Martinez Hernandez, A Martini, D Matvienko, J A McKenna, F Meier, M Merola, F Metzner, C Miller, K Miyabayashi, H Miyake, H Miyata, R Mizuk, G B Mohanty, H K Moon, T Moon, A Morda, T Morii, M Mrvar, G Muroyama, R Mussa, I Nakamura, T Nakano, M Nakao, H Nakayama, H Nakazawa, T Nanut, M Naruki, K J Nath, M Nayak, N Nellikunnummel, D Neverov, C Niebuhr, J Ninkovic, S Nishida, K Nishimura, M Nouxman, G Nowak, K Ogawa, Y Onishchuk, H Ono, Y Onuki, P Pakhlov, G Pakhlova, B Pal, E Paoloni, H Park, C-S Park, B Paschen, A Passeri, S Paul, T K Pedlar, M Perelló, I M Peruzzi, R Pestotnik, L E Piilonen, L Podesta Lerma, V Popov, K Prasanth, E Prencipe, M Prim, M V Purohit, A Rabusov, R Rasheed, S Reiter, M Remnev, P K Resmi, I Ripp-Baudot, M Ritter, M Ritzert, G Rizzo, L Rizzuto, S H Robertson, D Rodriguez Perez, J M Roney, C Rosenfeld, A Rostomyan, N Rout, S Rummel, G Russo, D Sahoo, Y Sakai, M Salehi, D A Sanders, S Sandilya, A Sangal, L Santelj, J Sasaki, Y Sato, V Savinoy, B Scavino, M Schram, H Schreeck, J Schueler, C Schwanda, A J Schwartz,

R M Seddon, Y Seino, K Senyo, O Seon, I S Seong, M E Sevier, C Sfienti, M Shapkin, C P Shen, M Shimomura, J-G Shiu, B Shwartz, A Sibidanov, F Simon, J B Singh, R Sinha, S Skambraks, K Smith, R J Sobie, A Soffer, A Sokolov, E Solovieva, B Spruck, S Stanič, M Starič, N Starinsky, U Stolzenberg, Z Stottler, R Stroili, J F Strube, J Stypula, M Sumihama, K Sumisawa, T Sumiyoshi, D Summers, W Sutcliffe, S Y Suzuki, M Tabata, M Takahashi, M Takizawa, U Tamponi, J Tan, S Tanaka, K Tanida, N Taniguchi, Y Tao, P Taras, G Tejada Munoz, F TENCHINI, U Tippawan, E Torassa, K Trabelsi, T Tsuboyama, M Uchida, S Uehara, T Uglov, Y Unno, S Uno, Y Ushiroda, Y Usov, S E Vahsen, R van Tonder, G Varner, K E Varvell, A Vinokurova, L Vitale, M Vos, A Vossen, E Waheed, H Wakeling, K Wan, M-Z Wang, X L Wang, B Wang, A Warburton, J Webb, S Wehle, C Wessel, J Wiechczynski, P Wieduwilt, E Won, Q Xu, X Xu, B D Yabsley, S Yamada, H Yamamoto, W Yan, W Yan, S B Yang, H Ye, I Yeo, J H Yin, M Yonenaga, T Yoshinobu, W Yuan, C Z Yuan, Y Yusa, S Zakharov, L Zani, M Zeyrek, J Zhang, Y Zhang, Y Zhang, X Zhou, V Zhukova, V Zhulanov, and A Zupanc. The Belle II Physics Book. *Progress of Theoretical and Experimental Physics*, 2019(12), 12 2019. 123C01.

- [156] R. Krivonos, M. Revnivitsev, S. Tsygankov, S. Sazonov, A. Vikhlinin, M. Pavlinsky, E. Churazov, and R. Sunyaev. INTEGRAL/IBIS 7-year All-Sky Hard X-ray Survey. I. Image reconstruction. *Astronomy and Astrophysics*, 519:A107, September 2010.

- [157] Gordan Krnjaic. Probing Light Thermal Dark-Matter With a Higgs Portal Mediator. *Phys. Rev. D*, 94(7):073009, 2016.
- [158] Jason Kumar. Indirect Detection of Sub-GeV Dark Matter Coupling to Quarks. 2018.
- [159] Yoshitaka Kuno and Yasuhiro Okada. Muon decay and physics beyond the standard model. *Rev. Mod. Phys.*, 73:151–202, Jan 2001.
- [160] Ranjan Laha. Primordial Black Holes as a Dark Matter Candidate Are Severely Constrained by the Galactic Center 511 keV γ -Ray Line. *Phys. Rev. Lett.*, 123(25):251101, 2019.
- [161] Ranjan Laha, Julian B. Muñoz, and Tracy R. Slatyer. INTEGRAL constraints on primordial black holes and particle dark matter. *Phys. Rev. D*, 101(12):123514, 2020.
- [162] Ranjan Laha, Julian B. Muñoz, and Tracy R. Slatyer. Integral constraints on primordial black holes and particle dark matter. *Physical Review D*, 101(12), Jun 2020.
- [163] Benjamin W. Lee and Steven Weinberg. Cosmological Lower Bound on Heavy Neutrino Masses. *Phys. Rev. Lett.*, 39:165–168, 1977. [,183(1977)].
- [164] JP Lees, V Poireau, V Tisserand, E Grauges, A Palano, G Eigen, David Nathan Brown, M Derdzinski, A Giuffrida, Yu G Kolomensky, et al. Search for invisible

- decays of a dark photon produced in $e^+ e^-$ collisions at $b \bar{a} b \bar{a}$. *Physical review letters*, 119(13):131804, 2017.
- [165] Benjamin V. Lehmann and Stefano Profumo. Cosmology and prospects for sub-MeV dark matter in electron recoil experiments. *Phys. Rev. D*, 102(2):023038, 2020.
- [166] Enbang Li. Modelling mass distribution of the milky way galaxy using gaia billion-star map, 2016.
- [167] R. E. Lingenfelter and R. Ramaty. On the Origin of the positron annihilation radiation from the direction of the Galactic Center. In G. R. Riegler and R. D. Blandford, editors, *The Galactic Center*, volume 83 of *American Institute of Physics Conference Series*, pages 148–159, May 1982.
- [168] Richard E. Lingenfelter and Geoffrey J. Hueter. Gamma ray burst emission: A jet and fireball model. In S. E. Woosley, editor, *High Energy Transients in AstroPhysics*, volume 115 of *American Institute of Physics Conference Series*, pages 558–567, May 1984.
- [169] Q.Z. Liu, J. van Paradijs, and E.P.J.van den Heuvel. A catalogue of low-mass X-ray binaries in the Galaxy, LMC, and SMC. 4th Edition. *Astron. Astrophys.*, 469:807, 2007.
- [170] F. E. Low. *Phys. Rev.*, 110, 1958.
- [171] Jane H. MacGibbon and B. R. Webber. Quark- and gluon-jet emission from

- primordial black holes: The instantaneous spectra. *Phys. Rev. D*, 41:3052–3079, May 1990.
- [172] Manuela Mallamaci et al. All-Sky-ASTROGAM: a MeV Companion for Multi-messenger Astrophysics. *PoS, ICRC2019:579*, 2020.
- [173] R N Manchester, G B Hobbs, A Teoh, and M Hobbs. The Australia Telescope National Facility pulsar catalogue. *Astron. J.*, 129:1993, 2005.
- [174] William J. Marciano, Cen Zhang, and Scott Willenbrock. Higgs Decay to Two Photons. *Phys. Rev.*, D85:013002, 2012.
- [175] Jeremy Mardon, Yasunori Nomura, Daniel Stolarski, and Jesse Thaler. Dark matter signals from cascade annihilations. *Journal of Cosmology and Astroparticle Physics*, 2009(05):016, 2009.
- [176] STEPHEN P. MARTIN. A supersymmetry primer. *Advanced Series on Directions in High Energy Physics*, page 1–98, Jul 1998.
- [177] D. Massari, A. Helmi, A. Mucciarelli, L. V. Sales, L. Spina, and E. Tolstoy. Stellar 3D kinematics in the Draco dwarf spheroidal galaxy. *Astronomy and Astrophysics*, 633:A36, January 2020.
- [178] Julie McEnery, Juan Abel Barrio, Ivan Agudo, Marco Ajello, José-Manuel Álvarez, Stefano Ansoldi, Sonia Anton, Natalia Auricchio, John B Stephen, Luca Baldini, et al. All-sky medium energy gamma-ray observatory: Exploring the extreme multimessenger universe. *arXiv preprint arXiv:1907.07558*, 2019.

- [179] Julie McEnery et al. Amego: A multimessenger mission for the extreme universe, 2019.
- [180] Ulf G. Meissner. Recent developments in chiral perturbation theory. *Rept. Prog. Phys.*, 56:903–996, 1993.
- [181] L. Michel. Interaction between four half spin particles and the decay of the μ meson. *Proc. Phys. Soc.*, A63:514–531, 1950. [,45(1949)].
- [182] F. Millour, R. G. Petrov, O. Chesneau, D. Bonneau, L. Dessart, C. Bechet, I. Tallon-Bosc, M. Tallon, E. Thiébaud, F. Vakili, and et al. Direct constraint on the distance of γ^2 velorum from amber/vlti observations. *Astronomy & Astrophysics*, 464(1):107–118, Nov 2006.
- [183] A. Moiseev and *et al.* New Mission Concept: Galactic Explorer with a Coded Aperture Mask Compton Telescope (GECCO). *PoS, 2021 International Cosmic Ray Conference*, Berlin, 2021.
- [184] Alexander Moiseev, Stefano Profumo, Adam Coogan, and Logan Morrison. Snowmass 2021 Letter of Interest: Searching for Dark Matter and New Physics with GECCO, 2020. https://www.snowmass21.org/docs/files/summaries/CF/SNOWMASS21-CF3_CF1_Stefano_Profumo-007.pdf.
- [185] Paulo Montero-Camacho, Xiao Fang, Gabriel Vasquez, Makana Silva, and Christopher M. Hirata. Revisiting constraints on asteroid-mass primordial black holes

- as dark matter candidates. *Journal of Cosmology and Astroparticle Physics*, 2019(08):031–031, Aug 2019.
- [186] J. F. Navarro, C. S. Frenk, and S. D. M. White. The Structure of Cold Dark Matter Halos. *The Astrophysical Journal*, 462:563, May 1996.
- [187] Julio F. Navarro, Carlos S. Frenk, and Simon D.M. White. The Structure of cold dark matter halos. *Astrophys. J.*, 462:563–575, 1996.
- [188] David H. Oaknin and Ariel R. Zhitnitsky. 511 keV Photons from Color Superconducting Dark Matter. *Physical Review Letters*, 94(10):101301, March 2005.
- [189] Nikhil Padmanabhan and Douglas P. Finkbeiner. Detecting dark matter annihilation with CMB polarization: Signatures and experimental prospects. *Phys. Rev. D*, 72:023508, 2005.
- [190] Palash B. Pal and Lincoln Wolfenstein. Radiative decays of massive neutrinos. *Phys. Rev. D*, 25:766–773, Feb 1982.
- [191] J. R. Pelaez. From controversy to precision on the sigma meson: a review on the status of the non-ordinary $f_0(500)$ resonance. *Phys. Rept.*, 658:1, 2016.
- [192] J. R. Pelaez. From controversy to precision on the sigma meson: a review on the status of the non-ordinary $f_0(500)$ resonance. *Phys. Rept.*, 658:1, 2016.
- [193] J.R. Pelaez. From controversy to precision on the sigma meson: a review on the status of the non-ordinary $f_0(500)$ resonance. *Phys. Rept.*, 658:1, 2016.

- [194] Charles Picciotto and Maxim Pospelov. Unstable relics as a source of galactic positrons. *Physics Letters B*, 605(1-2):15–25, January 2005.
- [195] A. Pich. Chiral perturbation theory. *Rept. Prog. Phys.*, 58:563–610, 1995.
- [196] Maxim Pospelov and Adam Ritz. The galactic 511 keV line from electroweak scale WIMPs. *Physics Letters B*, 651(2-3):208–215, July 2007.
- [197] Vivian Poulin, Julien Lesgourgues, and Pasquale D. Serpico. Cosmological constraints on exotic injection of electromagnetic energy. *Journal of Cosmology and Astroparticle Physics*, 2017(03):043–043, Mar 2017.
- [198] Vivian Poulin, Julien Lesgourgues, and Pasquale D. Serpico. Cosmological constraints on exotic injection of electromagnetic energy. *JCAP*, 03:043, 2017.
- [199] N. Prantzos. On the intensity and spatial morphology of the 511 keV emission in the Milky Way. *Astronomy and Astrophysics*, 449(3):869–878, April 2006.
- [200] Stefano Profumo. Hunting the lightest lightest neutralinos. *Phys. Rev.*, D78:023507, 2008.
- [201] Stefano Profumo. *An Introduction to Particle Dark Matter*. World Scientific, 2017.
- [202] Stefano Profumo and Piero Ullio. SUSY dark matter and quintessence. *JCAP*, 11:006, 2003.

- [203] R. Rando, A. De Angelis, and M. Mallamaci. e-ASTROGAM: a space mission for MeV-GeV gamma-ray astrophysics. *J. Phys. Conf. Ser.*, 1181(1):012044, 2019.
- [204] C. K. Rosslowe and P. A. Crowther. Spatial distribution of Galactic Wolf-Rayet stars and implications for the global population. *Monthly Notices of the Royal Astronomical Society*, 447(3):2322–2347, 01 2015.
- [205] Stefan Scherer. *Introduction to Chiral Perturbation Theory*, pages 277–538. Springer US, Boston, MA, 2003.
- [206] Stefan Scherer and Matthias R Schindler. A chiral perturbation theory primer. *arXiv preprint hep-ph/0505265*, 2005.
- [207] Matthew Dean. Schwartz. *Quantum field theory and the standard model*. Cambridge University Press, 2017.
- [208] Marco Selig, Valentina Vacca, Niels Oppermann, and Torsten A. Enßlin. The denoised, deconvolved, and decomposed Fermi γ -ray sky. An application of the D³PO algorithm. *Astronomy and Astrophysics*, 581:A126, September 2015.
- [209] Mikhail Shaposhnikov and Igor Tkachev. The ν msm, inflation, and dark matter. *Physics Letters B*, 639(5):414–417, Aug 2006.
- [210] Thomas Siegert, Roland Diehl, Gerasim Khachatryan, Martin G.H. Krause, Fabrizia Guglielmetti, Jochen Greiner, Andrew W. Strong, and Xiaoling Zhang. Gamma-ray spectroscopy of Positron Annihilation in the Milky Way. *Astron. Astrophys.*, 586:A84, 2016.

- [211] P. Sizun, M. Cassé, and S. Schanne. Continuum γ -ray emission from light dark matter positrons and electrons. *Physical Review D*, 74(6):063514, September 2006.
- [212] P. Sizun, M. Cassé, S. Schanne, and B. Cordier. Constraints on the Injection Energy of Positrons in the Galactic Centre Region. In *The Obscured Universe. Proceedings of the VI INTEGRAL Workshop*, volume 622 of *ESA Special Publication*, page 61, January 2007.
- [213] Torbjorn Sjostrand, Stephen Mrenna, and Peter Z. Skands. PYTHIA 6.4 Physics and Manual. *JHEP*, 05:026, 2006.
- [214] Torbjorn Sjostrand, Stephen Mrenna, and Peter Z. Skands. A Brief Introduction to PYTHIA 8.1. *Comput. Phys. Commun.*, 178:852–867, 2008.
- [215] J.G. Skibo, W.N. Johnson, J.D. Kurfess, R.L. Kinzer, G. Jung, J.E. Grove, W.R. Purcell, M.P. Ulmer, N. Gehrels, and J. Tueller. Osse observations of the soft gamma-ray continuum from the galactic plane at longitude 95 degrees. *Astrophys. J. Lett.*, 483:L95, 1997.
- [216] Gerald K. Skinner. Sensitivity of coded mask telescopes. *Appl. Opt.*, 47(15):2739–2749, May 2008.
- [217] Tracy R. Slatyer. Indirect dark matter signatures in the cosmic dark ages. i. generalizing the bound on s -wave dark matter annihilation from planck results. *Phys. Rev. D*, 93:023527, Jan 2016.
- [218] Tracy R. Slatyer. Indirect dark matter signatures in the cosmic dark ages. I.

- Generalizing the bound on s-wave dark matter annihilation from Planck results. *Phys. Rev. D*, 93(2):023527, 2016.
- [219] Tracy R. Slatyer, Nikhil Padmanabhan, and Douglas P. Finkbeiner. CMB Constraints on WIMP Annihilation: Energy Absorption During the Recombination Epoch. *Phys. Rev.*, D80:043526, 2009.
- [220] Tracy R. Slatyer and Chih-Liang Wu. General Constraints on Dark Matter Decay from the Cosmic Microwave Background. *Phys. Rev. D*, 95(2):023010, 2017.
- [221] Nolan Smyth, Stefano Profumo, Samuel English, Tesla Jeltema, Kevin McKinnon, and Puragra Guhathakurta. Updated Constraints on Asteroid-Mass Primordial Black Holes as Dark Matter. *Phys. Rev. D*, 101(6):063005, 2020.
- [222] J. Soto, P. Talavera, and J. Tarrus. Chiral Effective Theory with A Light Scalar and Lattice QCD. *Nucl. Phys.*, B866:270–292, 2013.
- [223] A. W. Strong, H. Bloemen, R. Diehl, W. Hermsen, and V. Schoenfelder. Comptel skymapping: A New approach using parallel computing. *Astrophys. Lett. Commun.*, 39:209, 1999.
- [224] Andrew W. Strong, Igor V. Moskalenko, and Olaf Reimer. Diffuse galactic continuum gamma rays: A model compatible with EGRET data and cosmic-ray measurements. *The Astrophysical Journal*, 613(2):962–976, oct 2004.
- [225] Andrew W. Strong, Igor V. Moskalenko, and Olaf Reimer. Diffuse galactic contin-

- uum gamma rays. A Model compatible with EGRET data and cosmic-ray measurements. *Astrophys. J.*, 613:962–976, 2004.
- [226] A.W. Strong and I.V. Moskalenko. Models for galactic cosmic ray propagation. *Adv. Space Res.*, 27:717–726, 2001.
- [227] A.W. Strong, I.V. Moskalenko, T.A. Porter, G. Johannesson, E. Orlando, and S.W. Digel. The GALPROP Cosmic-Ray Propagation Code. 7 2009.
- [228] M. Tanabashi, K. Hagiwara, K. Hikasa, K. Nakamura, Y. Sumino, F. Takahashi, J. Tanaka, K. Agashe, G. Aielli, C. Amsler, M. Antonelli, D. M. Asner, H. Baer, Sw. Banerjee, R. M. Barnett, T. Basaglia, C. W. Bauer, J. J. Beatty, V. I. Belousov, J. Beringer, S. Bethke, A. Bettini, H. Bichsel, O. Biebel, K. M. Black, E. Blucher, O. Buchmuller, V. Burkert, M. A. Bychkov, R. N. Cahn, M. Carena, A. Ceccucci, A. Cerri, D. Chakraborty, M.-C. Chen, R. S. Chivukula, G. Cowan, O. Dahl, G. D’Ambrosio, T. Damour, D. de Florian, A. de Gouvêa, T. DeGrand, P. de Jong, G. Dissertori, B. A. Dobrescu, M. D’Onofrio, M. Doser, M. Drees, H. K. Dreiner, D. A. Dwyer, P. Eerola, S. Eidelman, J. Ellis, J. Erler, V. V. Ezhela, W. Fetscher, B. D. Fields, R. Firestone, B. Foster, A. Freitas, H. Gallagher, L. Garren, H.-J. Gerber, G. Gerbier, T. Gershon, Y. Gershtein, T. Gherghetta, A. A. Godizov, M. Goodman, C. Grab, A. V. Gribsan, C. Grojean, D. E. Groom, M. Grünewald, A. Gurtu, T. Gutsche, H. E. Haber, C. Hanhart, S. Hashimoto, Y. Hayato, K. G. Hayes, A. Hebecker, S. Heinemeyer, B. Heltsley, J. J. Hernández-Rey, J. Hisano, A. Höcker, J. Holder, A. Holtkamp, T. Hyodo, K. D. Irwin,

K. F. Johnson, M. Kado, M. Karliner, U. F. Katz, S. R. Klein, E. Klempt, R. V. Kowalewski, F. Krauss, M. Kreps, B. Krusche, Yu. V. Kuyanov, Y. Kwon, O. Lahav, J. Laiho, J. Lesgourgues, A. Liddle, Z. Ligeti, C.-J. Lin, C. Lippmann, T. M. Liss, L. Littenberg, K. S. Lugovsky, S. B. Lugovsky, A. Lusiani, Y. Makida, F. Maltoni, T. Mannel, A. V. Manohar, W. J. Marciano, A. D. Martin, A. Masoni, J. Matthews, U.-G. Meißner, D. Milstead, R. E. Mitchell, K. Mönig, P. Molaro, F. Moortgat, M. Moskovic, H. Murayama, M. Narain, P. Nason, S. Navas, M. Neubert, P. Nevski, Y. Nir, K. A. Olive, S. Pagan Griso, J. Parsons, C. Patrignani, J. A. Peacock, M. Pennington, S. T. Petcov, V. A. Petrov, E. Pianori, A. Piepke, A. Pomarol, A. Quadt, J. Rademacker, G. Raffelt, B. N. Ratcliff, P. Richardson, A. Ringwald, S. Roesler, S. Rolli, A. Romaniouk, L. J. Rosenberg, J. L. Rosner, G. Rybka, R. A. Ryutin, C. T. Sachrajda, Y. Sakai, G. P. Salam, S. Sarkar, F. Sauli, O. Schneider, K. Scholberg, A. J. Schwartz, D. Scott, V. Sharma, S. R. Sharpe, T. Shutt, M. Silari, T. Sjöstrand, P. Skands, T. Skwarnicki, J. G. Smith, G. F. Smoot, S. Spanier, H. Spieler, C. Spiering, A. Stahl, S. L. Stone, T. Sumiyoshi, M. J. Syphers, K. Terashi, J. Terning, U. Thoma, R. S. Thorne, L. Tiator, M. Titov, N. P. Tkachenko, N. A. Törnqvist, D. R. Tovey, G. Valencia, R. Van de Water, N. Varelas, G. Venanzoni, L. Verde, M. G. Vincter, P. Vogel, A. Vogt, S. P. Wakely, W. Walkowiak, C. W. Walter, D. Wands, D. R. Ward, M. O. Wascko, G. Weiglein, D. H. Weinberg, E. J. Weinberg, M. White, L. R. Wiencke, S. Willocq, C. G. Wohl, J. Womersley, C. L. Woody, R. L. Workman, W.-M. Yao, G. P. Zeller, O. V. Zenin, R.-Y. Zhu, S.-L. Zhu, F. Zimmermann,

- P. A. Zyla, J. Anderson, L. Fuller, V. S. Lugovsky, and P. Schaffner. Review of particle physics. *Phys. Rev. D*, 98:030001, Aug 2018.
- [229] M. Tavani et al. Science with e-ASTROGAM: A space mission for MeV–GeV gamma-ray astrophysics. *JHEAp*, 19:1–106, 2018.
- [230] M. Tavani et al. Science with e-ASTROGAM: A space mission for MeV–GeV gamma-ray astrophysics. *JHEAp*, 19:1–106, 2018.
- [231] D. J. Thompson et al. Calibration of the Energetic Gamma-Ray Experiment Telescope (EGRET) for the Compton Gamma-Ray Observatory. *Astrophys. J. Suppl.*, 86:629–656, 1993.
- [232] Lev Titarchuk and Pascal Chardonnet. The Observed Galactic Annihilation Line: Possible Signature of Accreting Small-Mass Black Holes in the Galactic Center. *Astrophysical Journal*, 641(1):293–301, April 2006.
- [233] Tran N. Truong. Chiral perturbation theory and final-state theorem. *Phys. Rev. Lett.*, 61:2526–2529, Nov 1988.
- [234] P. Ubertini, F. Lebrun, G. Di Cocco, A. Bazzano, A. J. Bird, K. Broenstad, A. Goldwurm, G. La Rosa, C. Labanti, P. Laurent, I. F. Mirabel, E. M. Quadrini, B. Ramsey, V. Reglero, L. Sabau, B. Sacco, R. Staubert, L. Vigroux, M. C. Weiskopf, and A. A. Zdziarski. IBIS: The Imager on-board INTEGRAL. *Astronomy and Astrophysics*, 411:L131–L139, November 2003.
- [235] G. Vedrenne, J. P. Roques, V. Schönfelder, P. Mandrou, G. G. Lichti, A. von

- Kienlin, B. Cordier, S. Schanne, J. Knödlseher, G. Skinner, P. Jean, F. Sanchez, P. Caraveo, B. Teegarden, P. von Ballmoos, L. Bouchet, P. Paul, J. Matteson, S. Boggs, C. Wunderer, P. Leleux, G. Weidenspointner, Ph. Durouchoux, R. Diehl, A. Strong, M. Cassé, M. A. Clair, and Y. André. SPI: The spectrometer aboard INTEGRAL. *Astronomy and Astrophysics*, 411:L63–L70, November 2003.
- [236] Kenneth M. Watson. Some general relations between the photoproduction and scattering of π mesons. *Phys. Rev.*, 95:228–236, Jul 1954.
- [237] Georg Weidenspointner et al. An asymmetric distribution of positrons in the Galactic disk revealed by gamma-rays. *Nature*, 451:159–162, 2008.
- [238] Steven Weinberg. Phenomenological lagrangians. *Physica A: Statistical Mechanics and its Applications*, 96(1):327 – 340, 1979.
- [239] J. Wess and B. Zumino. Consequences of anomalous Ward identities. *Phys. Lett.*, 37B:95–97, 1971.
- [240] Julius Wess and Bruno Zumino. Consequences of anomalous ward identities. *Physics Letters B*, 37(1):95–97, 1971.
- [241] B. C. Whitmore. Velocity dispersions in M31 and M32. *The Astrophysical Journal*, 242:53–62, November 1980.
- [242] C. Winkler et al. The INTEGRAL mission. *Astron. Astrophys.*, 411:L1–L6, 2003.
- [243] Christoph Winkler, Roland Diehl, Pietro Ubertini, and Jorn Wilms. INTEGRAL: science highlights and future prospects. *Space Sci. Rev.*, 161:149–177, 2011.

- [244] Edward Witten. Global Aspects of Current Algebra. *Nucl. Phys.*, B223:422–432, 1983.
- [245] Edward Witten. Global aspects of current algebra. *Nuclear Physics B*, 223(2):422–432, 1983.
- [246] Joe Wolf, Gregory D. Martinez, James S. Bullock, Manoj Kaplinghat, Marla Geha, Ricardo R. Munoz, Joshua D. Simon, and Frank F. Avedo. Accurate Masses for Dispersion-supported Galaxies. *Mon. Not. Roy. Astron. Soc.*, 406:1220, 2010.
- [247] Xin Wu. PANGU: A High Resolution Gamma-Ray Space Telescope. *PoS, ICRC2015:964*, 2016.
- [248] Xin Wu, Meng Su, Alessandro Bravar, Jin Chang, Yizhong Fan, Martin Pohl, and Roland Walter. PANGU: A High Resolution Gamma-ray Space Telescope. *Proc. SPIE Int. Soc. Opt. Eng.*, 9144:91440F, 2014.
- [249] P. A. Zyla et al. Review of Particle Physics. *PTEP*, 2020(8):083C01, 2020.